Print edition ISSN 2615-5109

Electronic edition ISSN 2621-0541

Publisher:
Center of Technology, Fakultas Teknik, Universitas Hasanuddin

Address:
Engineering Faculty Campus, Hasanuddin University
Jl. Poros Malino km. 6, Bontomarannu
Kabupaten Gowa, Sulawesi Selatan, Indonesia, 92171
Email : epi-ije@unhas.ac.id
Website : cot.unhas.ac.id/journals/index.php/epiije
Telp/Fax : +62-(0)411-58601

EPI International Journal of Engineering

Foreword

We are pleased that EPI International Journal of Engineering (EPI-IJE) is presenting its 2nd issue. We are also excited that authors' country of origin who published their papers in this issue has also increased. The country variety of submission will help to promote the journal globally. We are also delighted that this issue contains a special topic on railway engineering. The special topic is included as a response to the starting of a railway project in South Sulawesi (Trans-Sulawesi railway project). It is hoped that the research results published in this journal will have a contribution to the quality improvement of the railway project in Indonesia, especially in South Sulawesi area.

Besides the special issue on railway engineering, this issue also contains 4 (four) other major topics which are Mechanical and Industrial Engineering, Naval, Ocean, and Marine Engineering, Electrical and Informatics Engineering, and Civil and Environmental Engineering. The first 2 (two) papers in railway engineering group conduct a literature survey and a review on railway work in Japan. The last paper in this group studies approximation of bending stiffness of car body panels. The group of Mechanical and Industrial engineering contains 5 (five) papers. The first 2 (two) papers discuss vibration analysis of cracked structures and moment of inertia effect on mass natural frequencies. The last 3 (three) papers conduct an experimental study and device prototyping utilizing heat energy.

In the next group which is Naval Architecture, Ocean, and Marine Engineering group, 4 (four) papers are published. The first 2 (two) papers also perform experimental study on submarine propeller and ship autopilot system maneuver, respectively. The third paper in this group studies the reduction of sediment transport using permeable groin, while the last paper investigates the longitudinal ship strength on the upper deck side. The group of electrical and informatics contains only one paper which investigates the performance of silicon rubber insulation. The last group contains 2 (two) papers. The first paper conducts a review on earthquake damage and disaster prevention of aboveground storage tanks, while the second paper conducts a model test on Bakau piles foundation.

As the Editor-in-Chief of this promising journal, I am greatly grateful to all authors for their outstanding papers and remarkable work. We hope these high-quality papers would give a contribution to knowledge development of their respective field of study. I also would like to express my gratitude to JICA C-BEST Project team, reviewers, editors, and all other people who have contributed to the publishing of this issue.

Warm regards,

Prof. Baharuddin Hamzah
Editor-in-Chief of EPI-IJE

TABLE OF CONTENTS

EPI International Journal of Engineering
Volume 1, Number 2, August 2018, pp. 1-12
DOI: 10.25042/epi-ije.082018.01

*p*ISSN 2615-5109
*e*ISSN 2621-0541

Research Topics on Railway Vehicle Dynamics - A Literature Survey Focusing on the Works from Japan -

Takahiro Tomioka[a,*]

[a]Department of Mechanical Engineering, Faculty of Systems, Science and Technology, Akita Prefectural University.
Email:tomioka@akita-pu.ac.jp

Abstract

Engineering research subjects relating railway vehicle dynamics are described as a literature survey in this paper. Research works concerning to the motion of wheelset; pantograph-catenary interaction; aerodynamic relating problems on the vehicle; and application of control techniques are introduced firstly as the most distinctive subjects of railway vehicle dynamics. The topics on safety assessment and ride comfort evaluation are also dealt with since those are important research area in railway dynamics as public transportation system. The subject concerning to carbody elastic vibration, which is important relating to ride comfort, is also described. The effect of passengers on the elastic vibration of carbody has been introduced as the interesting (and something surprising) topic. The focuses in the literature survey are particularly on the research works from Japan, in this paper.

Keywords: Dynamics of railway vehicles; mechanical engineering; ride comfort; safety assessment; vibration problems

1. Introduction

As widely known, railway system is one of the origin of mechanical engineering; the first president of the world's oldest society of mechanical engineers (Institution of Mechanical Engineers: IMechE), which was founded in 1847 in Birmingham, UK, was George Stephenson who is famous as *the Father of Railways*. (And the second president of IMechE was Robert Stephenson; the son of George and he was also a railway engineer.) It is obvious that railway was one of the most important object for study in mechanical engineering at that time. Many engineering subjects e.g. tribology, fatigue of metals, fracture mechanics, heat treatment of metals, development of materials like steels and aluminum alloys, were raised or developed together with the advancement of railways. Problems relating dynamics such as vibrations and sound have also been closely connected to railways. And even now, railway still remains one of the most interesting subjects of research in engineering. This paper intends to introduce the engineering research topics relating railway vehicles from the view of dynamics as a literature survey.

*Corresponding author. Tel.: +81-184-27-2131
84-4, Tsuchiya-ebinokuchi,
Yurihonjo, Akita, Japan, 015-0055

About the dynamics of railway vehicles, a lot of research works have been carried out in Europe for a long time, and several good books are available (e.g. [1, 2]). On the other hand, there are also a long history in this field in Japan; a number of great achievements were made from Japan and the Shinkansen is one of the fine fruits of those researches. However, in the author's view, such research activities are lesser-known versus their importance. One reason of this is considered that many of them are written in Japanese; though, not a few works are published in English. This paper focuses the research works from Japan.

2. Characteristic Dynamics in Railway Vehicles

2.1. Wheelset motion

One of major features of railway vehicles is using wheelsets with conical wheels. A wheelset is a set of a pair of wheels and an axle; the wheels are tightly pressed into a common axle, so the right and left wheels rotate with a common angular velocity. Figure 1 shows the schematic illustration of a wheelset. Each wheel's tread has a slope such as the radius of the wheel becomes smaller to the outer side of the axle. It is called coning, conicity or wheel tread gradient. The typical conicity is, for instance, 1/20 or 1/40. Due to the conicity of the wheels, there are some

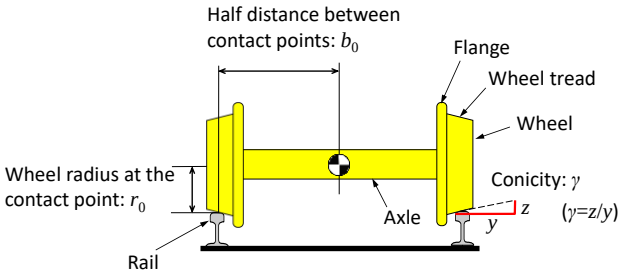

Figure 1. Wheelset of railway vehicles

characteristic dynamics such as self-steering ability and hunting motion. Leaving their detailed theoretical treatments up to the published books [1, 2], some results are described here as follows.

The self-steering ability is the function to return automatically to the center of the track when a wheelset moves to one side of the track without using intentional steering manipulation. Railway vehicles don't have steering wheels like automobiles: the self-steering ability is produced by the difference of the radii of both side wheels in a wheelset. As shown in Fig. 2(a) when a wheelset goes into curve section, the wheelset moves to the outer side of the curve and the wheel on the outer rail contacts with the rail head in larger radius. Since both wheels rotate with the same angular velocity, the outer side wheel runs faster than the other wheel, and thus the wheelset can pass the curve smoothly. When a wheelset running on straight section is displaced to one side of the track as shown in Fig. 2(b), the wheel of the displaced side contacts with the rail head in larger radius and the wheel runs faster than the other one; and the wheelset returns to the center of the track. It should be noted that the flanges shown in Fig. 1 are not usually needed in order to pass curves or return to the track center. The flanges are necessary in case such as passing sharper curves or prevent derailment caused by extraordinary lateral force.

The trajectory of the center of a wheelset passing a curve purely by the self-steering ability is called pure rolling line. The wheelset running on the pure rolling line don't generate

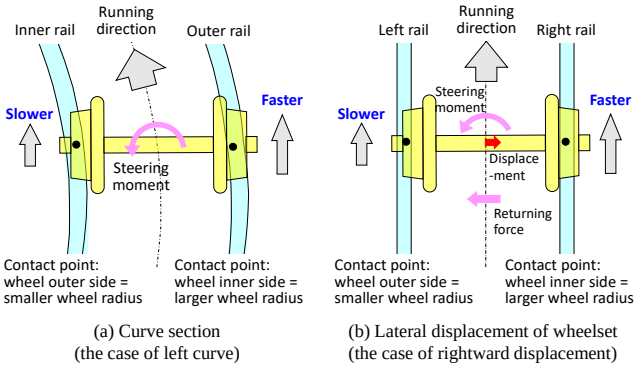

Figure 2. Self-steering ability of wheelsets

longitudinal force (longitudinal creep force). The lateral displacement y_0 to sustain pure rolling during passing a curve with radius R can be expressed using conicity γ (see Fig. 1) and the radius of the wheel in the neutral position r_0 and the half distance between rails b_0 as,

$$y_0 = \frac{b_0 r_0}{R\gamma} \tag{1}$$

This formula is obtained by the simple geometric relationship between parameters shown in Fig. 3.

According to the self-steering ability, if pure rolling is maintained, a wheelset can move back toward the center of the track when it displaces slightly to one side of the track. However, during the regaining motion, the wheelset overshoots the center and this causes oscillatory motion called kinematic hunting. The trajectory of the wheelset kinematic hunting can be expressed a sinusoidal curve as shown in Fig. 4 and its wavelength S_1 can be described as,

$$S_1 = 2\pi\sqrt{\frac{b_0 r_0}{\gamma}} \tag{2}$$

Although the kinematic hunting motion of wheelsets is known since early times [3], the fact that the kinematic hunting is an unstable oscillation and elastically supported two-axled bogie also have similar unstable hunting

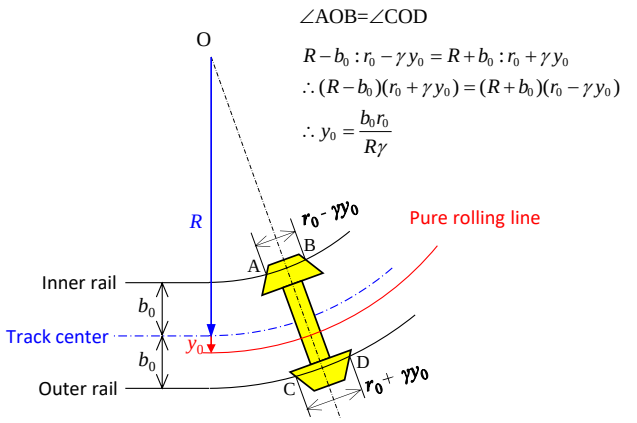

Figure 3. Pure rolling of a wheelset in a curve

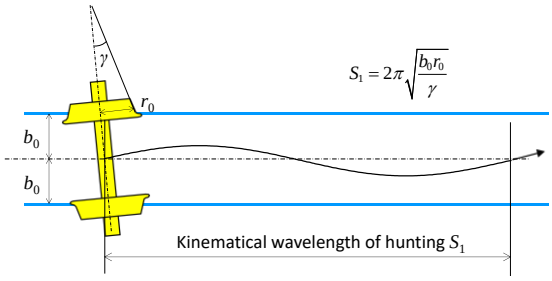

Figure 4. Kinematic hunting of a wheelset

characteristics was firstly found out by Matsudaira shortly after World War II (WWII). He showed the hunting problem is one of the self-excited vibration and not occurred by external cause such as track irregularity. Thanks to the series of his research, design method of high-speed bogies was established and led to the realization of Shinkansen [4-8]. Unfortunately, since many of his research were published in Japanese, it is pointed out that "his research had little impact in the West" according to reference [2], however his works are widely known among researchers in the world in this field now.

The abilities of curving and hunting stability often require opposing properties on the bogie components. For instance, large conicity is advantageous to pass sharp curves, but leads to less hunting stability. To satisfy both of curving performance and running stability is one of important research topics in the railway vehicle dynamics.

Reducing the angle of attack (yaw angle of the wheelset relative to the track) in curve sections is a major strategy to improve curving performance. A number of theoretical and experimental studies have been carried out to realize bogies with small attack angle during curving. As one well known examples of these efforts, Suda [9] proved theoretically that unsymmetrical longitudinal supports of the two axles in a bogie can greatly reduce attack angle (zero attack angle can be realized, ideally) and the concept was adopted in the bogies of an EMU (electric multiple unit) limited express. Sato et al. [10] proposed a mechanically steering bogie with link mechanism and used in a DMU (diesel multiple unit) limited express. Recently, single axle steering bogie (one of the two axles in a bogie has steering mechanism) has been proposed and used in Tokyo Metro [11, 12].

2.2. Dynamics of pantograph-catenary system

As another characteristic topic concerning railway vehicle dynamics, interactions of the pantograph and catenary can be taken. A pantograph is a device to collect electricity from overhead contact line (called catenary here). The contact loss of pantograph and catenary causes problems not only collection loss of electricity but also severe damage of pantograph and catenary, acoustical and radio noise problems, etc. by the generation of arc. Therefore, the effort to reduce the contact loss is important.

The contact loss tends to occur as the vehicle speed becomes higher. After WWII, prior to the construction of Tokaido Shinkansen, speedup of trains of conventional lines were conducted and the dynamics of pantograph-catenary system was studied in detail. Shibata modelled the system as a mass supported by a periodically variable spring stiffness, which represents the effect of supporting span of catenary, with constant upward force. He showed its equation of motion can be expressed as a Mathieu's equation, and derived the critical velocity V_c to arise contact loss as [13],

$$V_c = \frac{l}{2\pi}\sqrt{\frac{k_0}{M}}\sqrt{1-\frac{\varepsilon^2}{2}} \tag{3}$$

where l is the supporting span of the catenary, k_0 is average spring stiffness of the catenary, M is mass of the pantograph and ε is the parameter representing the variation of spring stiffness of catenary. This formula denotes increasing M, ε and increasing k_0 are beneficial to improve the critical velocity V_c. It was also suggested that applying damping in the pantograph is effective. These results were reflected in the design of pantographs for Shinkansen vehicles.

The pantograph-catenary system is also modelled as a string under tensile force suffering a moving upward force, and relation between wave propagation velocity in the string and moving velocity of the upward force are analyzed in Manabe's book [14]. According to the book, following results are demonstrated by the string and moving force model; a large displacement occur at the contact point on the string as the velocity of the moving force approaches to the velocity of wave propagation of the string; when the moving force exceeded the wave propagation velocity, no forward wave propagates and regressive wave with very large amplitude will be generated. Actually, in the real field of rail industry, increasing tensile force in the catenary is widely conducted in case of speedup of vehicles.

To improve the performance of pantograph, efforts to know the contact force between pantograph and catenary [15, 16] or to optimize the shape of pantograph head [17] have been carried out.

The problem of corrugation (periodical wear or undulating wear, see Fig. 5) of catenary has also long been research topics. Corrugation occurs not only high-speed railway but also conventional line, and this problem leads to contact loss. Manabe [19] has been trying to approach to this problem in terms of wave propagation. He modelled a catenary as an Euler beam excited by two moving forces representing pantographs. Using the model, he showed interaction of the waves, which is generated by the moving forces, is strongly relating to the growth of the corrugation in the catenary.

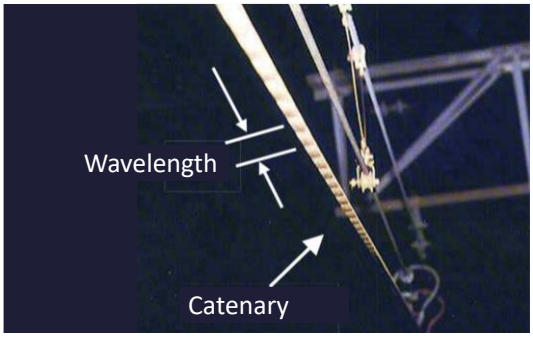

Figure 5. Example of corrugation of catenary [18]

The corrugation problem is also important in the rail-wheel system. According to Manabe's book [14], more than 1000 research papers have been published on the topic of rail corrugation. Manabe also applied his wave interaction theory to the rail corrugation growing mechanism [20, 21].

2.3. Aerodynamic interaction to the vehicles

As the disturbance input acting on the railway vehicle relating to the vehicle dynamics, aerodynamic forces are necessary to be taken into consideration under certain conditions; e.g. strong side wind and aerodynamic force fluctuation during train passage or running in tunnel. The influence of strong side wind will be taken up in sub-section 3.1 in this paper, so the research relating aerodynamic force fluctuation is described here.

As the speed of a vehicle becomes higher, aerodynamic force also increases greatly. As the aerodynamic interaction to the vehicle dynamics, the problem of lateral vibration in tunnel has been received much interest in Japan from the view of ride comfort. Fujimoto et al. [22] revealed from the running test data of a Shinkansen that the lateral vibration of tail car becomes larger than the others in tunnel. They also conducted vehicle dynamics numerical simulation focusing on the relation of tail car lateral vibration and hunting motion, and proposed inter-car yaw damper to reduce tail car's vibration. The inter-car yaw dampers are widely used in Shinkansen and express trains in Japan.

Suzuki et al. studied the aerodynamic force fluctuation from the aspect of experimental and computational fluid dynamics [23, 24]. They proposed to change external parts attached to carbody such as pantograph covers, bogie side covers, etc. to reduce unsteady aerodynamic force acting on the vehicle in tunnel [25]. Sakuma et al. also conducted theoretical [26] and experimental [27] studies about aerodynamic force problem of high-speed trains in tunnel.

2.4. Application of control techniques

The demand for the ride comfort of passengers has been getting higher than ever. In addition, as the increase of vehicle speed, to maintain good ride quality by adjusting suspension parameters in the bogie is getting harder. For example, lateral vibration of a high-speed vehicle is mainly caused by long wavelength track irregularity in open section; on the other hand, aerodynamic excitation force acting directly to the carbody is major cause of disturbance in tunnel section. Lateral connection between bogie and carbody should be weak to reduce excitation from track; in contrast it is favorable to connect carbody tightly with bogies to reduce the effect by aerodynamic excitation: that is, parameter settings of lateral suspension for open and tunnel sections contradict each other.

To solve problems under such conflicting situation, control techniques are applied in the suspension system of railway vehicles. Sasaki et al. proposed to apply variable damper in lateral connection between bogie and car body

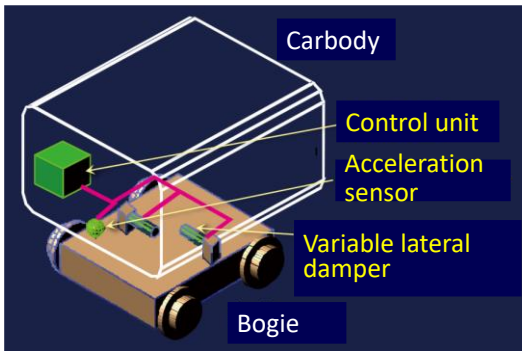

Figure 6. Schematic illustration of lateral semi-active suspension [30]

[28, 29]. Figure 6 illustrates the lateral semi-active suspension system. The variable damper can change its damping coefficient electrically. This system is called semi-active suspension system since no active force is applied. The semi-active suspension has been used many of Shinkansen and some limited express trains in Japan.

In the beginning of this century, active suspension system was also put into practical use in Japan. The active suspension system uses hydric, pneumatic or electric actuators to apply control force. Active suspensions with pneumatic actuators are firstly used in Shinkansen and electro mechanical actuator (EMA) has recently been getting higher share [31].

Above mentioned semi-active and active suspensions are used mainly to reduce lateral vibration in lateral direction. The concept to apply variable dampers in the vertical suspension was proposed by Sugahara et al. [32] and has been used in some cruise trains running on conventional lines [33].

To shorten traveling time, it is important not only improvement of maximum speed but also speedup in curves, particularly for conventional lines through mountainside. Tilting trains, which have tilting mechanism of carbody to compensate for the shortage of cant when speed-up on sharp curves, are introduced for such purpose; in early times, natural pendulum type mechanisms using centrifugal force itself for tilting action were applied to commercial trains in Japan. Although the natural pendulum type of tilting trains contributed to increase speed in curved sections, it was found that they had matters to induce some passengers' comfort in curved section [36, 37] and high-performance actuator [38, 39] with good response to the tilting command are both important in improving performance and ride quality of tilting trains.motion sickness. This was considered caused by the delay of tilting motion at the entry and exit of a curve due to mechanical non-ideality such as friction. To improve the tilting performance and ride comfort, control techniques are used in recent tilting systems [34, 35]. It should be also noted that development of control law to consider passengers'

Recently, air-spring inclination control systems have been widely applied including Shinkansen in Japan as tilting mechanism. By using this system, the tilting angle of

carbody is limited usually within 2 degrees which is lesser than the above mentioned system with tilting beam (more than 5 degrees of tilting angle is possible); however it needs only a little additional parts in implementation to a vehicle and less maintenance costs [40].

3. Safety Assessments and Ride Comfort Evaluation

3.1. Derailment and overturn

As shown in Fig.7, the force acting at the contact area of a wheel and a rail in the cross section of the rail can be expressed by vertical and lateral components. They are usually denoted *P* and *Q*, respectively in Japan, in which the vertical force *P* is called wheel load. If the wheel load becomes small and/or lateral force becomes large, the risk of derailment will increase, therefore, the ratio *Q*/*P* can be used to evaluate safety margin against derailment. The ratio is called *the derailment quotient*. (Note that the symbols *Y* and *Q* respectively are traditionally used for lateral force and wheel load in Europe, so the derailment quotient is expressed as *Y*/*Q* there; while in North America the quotient is often described as *L*/*V*.) Running tests to measure *P* and *Q* using actual vehicle are necessarily conducted in order to confirm sufficiently small derailment quotient when; a new type of vehicles or bogies are developed; speedup of existing vehicles is conducted; or a new line has been constructed. These values are measured using special wheels in which strain gauges are installed in the web of the wheels.

As the vehicle running speed increase, wheel load fluctuation tend to be larger and its frequency becomes higher. Exact evaluation of the derailment quotient under such high-frequency fluctuation condition is needed to promise the running safety of Shinkansen vehicles. Ishida et al. proposed the continuous measurement method of the derailment quotient valid at high speed [41, 42], and it is used widely in Japan.

Derailment assessment is also important at low speed since the risk of flange climb exists in sharp curve [43, 44]. To clarify more detailed derailment phenomena at low speed on sharp curves was conducted and a new assessment levels against derailment on curved track has been proposed [44].

Strong side wind may cause the overturn of a vehicle. In Japan, the critical wind speed of overturning proposed by Kunieda [45] is used to evaluate the safety of vehicle running under strong side wind. It is defined as the wind speed when the windward wheel load becomes zero by solving the equation of static balance of external forces acting on the vehicle. Hibino et al. proposed revised version of the formula to include detailed effects of bogie parts and aerodynamic forces [46, 47].

Stability assessment against extremely large external input such as by earthquake is important in Japan. Miyamoto et al. built numerical model to simulate the dynamic response of running vehicles due to earthquake [48, 49]. They also conducted a full-scale experiment of a bogie under large amplitude track vibration as shown in Fig. 8 and compared with the numerical results [50].

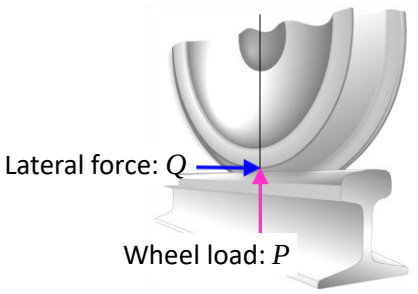

Figure 7. The forces acting in the contact area of a wheel and the rail

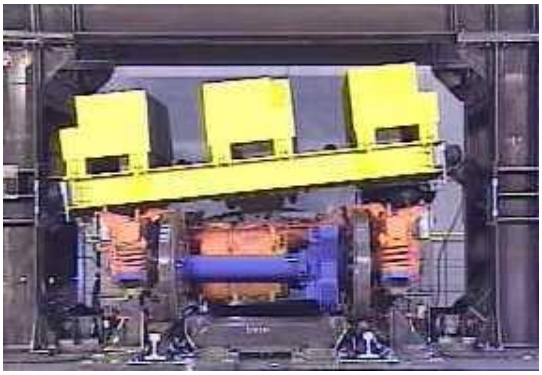

Figure 8. Full-scale shaking experiment of a bogie

3.2. Ride comfort

The riding comfort of railway vehicles is relating many factors such as vibration, noise, smell, temperature, humidity, seat design, etc. However, in the aspect of vehicle dynamics, ride comfort evaluation is based on the vibration acceleration measured on the floor (or sometimes on the seat) of running vehicles.

The international standard ISO 2631 [51] is widely referred as the method for evaluating the effect of vibration on human body. On the other hand, in Japan, the riding comfort coefficient and the ride comfort level have been applied to evaluate ride comfort of railway vehicles [52]. Both of them were determined by Japan National Railways (JNR) and are used for more than 35 years without any modification.

Figure 9 shows the diagram used for the ride comfort evaluation based on the ride comfort coefficient. The peak value of acceleration time series measured in the selected test section is plotted versus its frequency on the diagram and the degree of riding comfort is evaluated according to the position of the plot in five ranks. The evaluation diagram is defined for each acceleration direction. This method has the merit to be able to obtain information about frequency together with acceleration amplitude; however the process is difficult to be automated.

Rank	Riding comfort coefficient	Evaluation
①	~ 1	Very good
②	1 ~ 1.5	Good
③	1.5 ~ 2	Indifferent
④	2 ~ 3	Poor
⑤	3 ~	Very poor

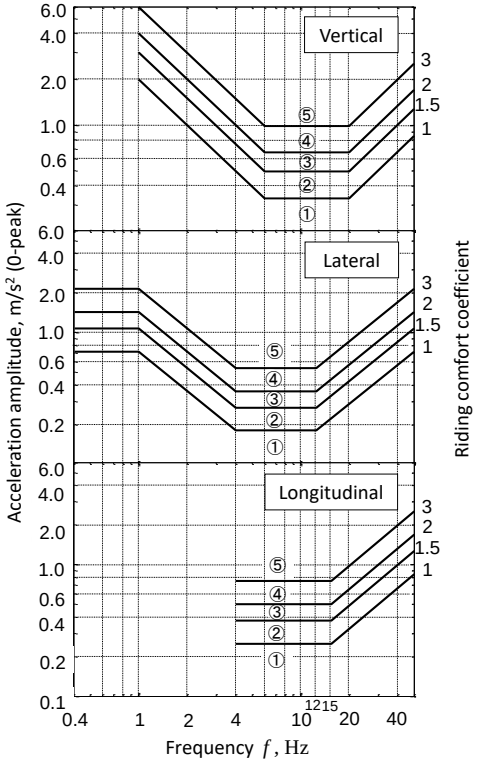

Figure 9. Diagram for the riding comfort coefficient and the ranks of evaluation

Rank	Riding comfort level [dB]	Evaluation
①	RCL < 83	Good ↑
②	83≦RCL<88	
③	88≦RCL<93	
④	93≦RCL<98	↓ Poor
⑤	98≦RCL	

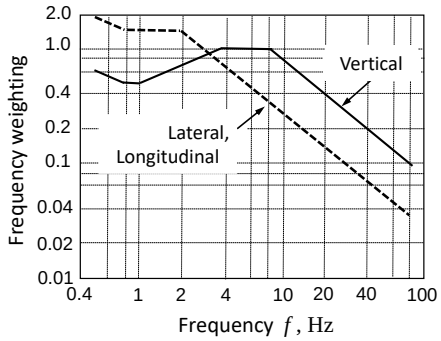

Figure 10. Frequency weightings for the evaluation of ride comfort level and the ranks of evaluation

The ride comfort level (RCL, in dB) is defined as,

$$\mathrm{RCL} = 20\log_{10}\left(\frac{A_w}{A_0}\right) \tag{4}$$

$$A_w = \sqrt{\frac{1}{T}\int_0^T a_w{}^2(t)dt} \tag{5}$$

where A_w is the root mean square (RMS) value of weighted acceleration $a_w(t)$ which is obtained by applying frequency weighting shown in Fig. 10 to the measured acceleration, and A_0 is the reference acceleration ($=10^{-5}$ m/s^2). The frequency weighting curves represent equivalent sensibility contours, which are originally based on the ISO 2631: 1974 with some modification by JNR. They are considered to reflect human sensitivity for vibration acceleration according to frequency. The evaluation duration T of the RMS value is normally set as $T = 3 \pm 2$ min, and five ranks of ride comfort are defined alike the riding comfort coefficient. The RCL value can be easily calculated using computers, though, the information about frequency is lost.

These ride comfort evaluations are mainly applied for the vehicles running at constant speed on a straight section. There are also evaluation criteria for the other running situation; e.g. stationary lateral acceleration at curved section; jerk (changing ratio of acceleration) in transition curves; roll motion of tilt trains; and longitudinal acceleration at accelerating or braking of vehicles [52].

4. Elastic Vibrations of Carbody

4.1. Characteristics of elastic vibrations of carbodies

Due to weight reduction and structural simplification of recent railway vehicles, elastic vibrations of carbody tend to become conspicuous. It is known that such elastic vibrations in vertical direction often occur in the high sensitivity frequency range for human. Figure 11 shows the power spectral density (PSD) measured at the center of floor of a Shinkansen running at 300 km/h [53]. The peak around 1-2 Hz is due to rigid body vibrations and the sharp peak around 8.5 Hz corresponds to the elastic vibration. It can be understood by considering the human sensitivity for vertical

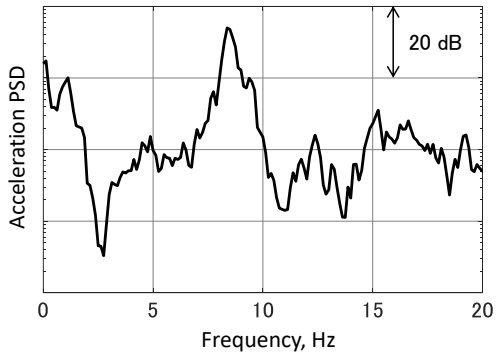

Figure 11. Example of acceleration PSD measured at the center of floor of a Shinkansen. (Running at 300 km/h.)

acceleration shown in Fig. 10 that the carbody elastic vibration has certain impact on the ride comfort. Therefore, it is important to reduce or suppress those elastic vibrations to improve ride comfort of a vehicle. The first step to take appropriate measure is to know detailed modal vibration characteristics of carbody [53-55].

The characteristics of mode shapes are different according to the body construction mainly by the material of carbody shell. In Japan, aluminum alloys and stainless steels are major materials for carbody shells. The mode shapes of actual vehicles obtained by experimental modal analysis [54] for a Shinkansen with aluminum alloy body shell and a commuter vehicle with stainless steel body shell are illustrated in Figs. 12 and 13, respectively [53]. We can see that the characteristics of elastic vibration modes are different. Recent aluminum alloy carbody shells are constructed by continuous welding of long hollow extruded members; therefore, the mode shapes have tendency to show the roof and floor deforms similar manner, and some of them looked like that of a simple free-supported beam. For the case of stainless steel carbody, each part of the carbody shell is constructed separately into a panel and each panel is connected discretely using small joint plates called gusset plates, so each surface of carbody tends to vibrate independently.

4.2. Modelling for analyzing carbody elastic vibrations

As the mathematical treatment of the carbody elastic vibration, beam models in which the carbody is modelled as a simple free-supported (uniform) beam have been used traditionally [e.g. 56-58]. This analytical approach is valid for the case that the objective vehicle has the bending mode similar to the beam, such as Fig. 12(b), and only for the first mode of bending of the beam. Although this model seems too simple to express actual vehicles, it is often used even now [59, 60]. As pointed out in ref. [61], the bending mode of carbody is excited by track irregularity not only through vertical suspension (such as air springs that support carbody on the bogie frames), but also through longitudinal connecting members between bogie and carbody such as traction links or yaw dampers. Although many of the beam models are not taken into account of such longitudinal connection, the author considers the effect must be included since the carbody response may be changed largely due to the longitudinal coupling [63].

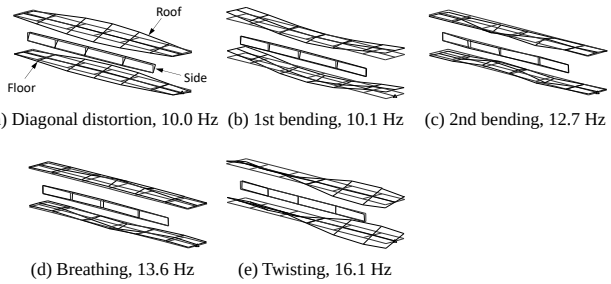

(a) Diagonal distortion, 10.0 Hz (b) 1st bending, 10.1 Hz (c) 2nd bending, 12.7 Hz

(d) Breathing, 13.6 Hz (e) Twisting, 16.1 Hz

Figure 12. Mode shapes and their natural frequencies of a Shinkansen vehicle carbody measured in a stationary excitation test. (Aluminum alloy carbody shell.)

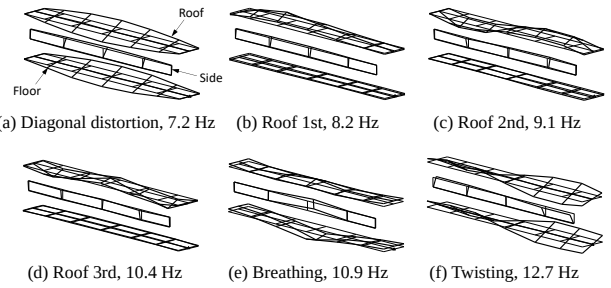

(a) Diagonal distortion, 7.2 Hz (b) Roof 1st, 8.2 Hz (c) Roof 2nd, 9.1 Hz

(d) Roof 3rd, 10.4 Hz (e) Breathing, 10.9 Hz (f) Twisting, 12.7 Hz

Figure 13. Mode shapes and their natural frequencies of a commuter-type vehicle carbody measured in a stationary excitation test. (Stainless-steel carbody shell.)

In order to express the detailed vibration characteristics including many complicated modes like Figs 12 and 13, finite element (FE) models are the most powerful tool, and many commercial software are available now. A number of research are done by using FE models [e.g. 63-65].

A numerical model should be validated by measured data, and in many case, some iterative effort to modify and/or adjust the numerical model are needed. This modification process is called correlation or model update. As a numerical model becomes detailed, the difficulty of model update usually increases. Tomioka et al. [66] proposed a simple model considering the carbody as a three-dimensional (3D) structure consisting of plates and beams as shown in Fig. 14.

The condition to connect these components (plates and beams) is satisfied by introducing artificial springs at their joints. The biggest merit of this model is that the degree of freedom of the model is quite small (less than 1,000) in comparison to FE models (usually more than 500,000); and therefore numerical optimization algorithms such as genetic algorithm (GA) can be applied in model update process [67]. This simple 3D vibration model is called the Box-type model.

4.3. Measures for the elastic vibrations of carbody

Several efforts have been carried out to reduce elastic vibration for a long time in Japan. As mentioned former, elastic vibration of carbody is often modelled as a first mode

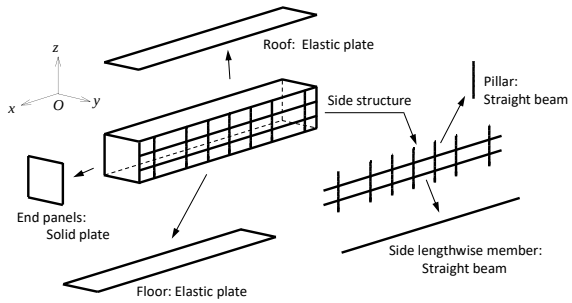

Figure 14. The three-dimensional analytical model for elastic vibrations of railway vehicle carbody as combination of plates and beams

of bending of an elastically supported beam, the counter measures are also studied by using such analysis model. Suzuki, et al. proposed to apply damping layer consist of viscoelastic and constraint layers [68]. In the study, the carbody was modelled as a partially layered beam to investigate the effect of damping layer, and it was found that the optimum length exists for the damping layer. The results were validated by running tests of an actual vehicle, and the damping layer was put into practical use of a commercial Shinkansen vehicle.

The idea to use underfloor equipment as dynamic vibration absorber (DVA) is also traditionally examined. Ishikawa and Sato [69] conducted a running test by applying elastically supported mass which imitated underfloor equipment and showed the reduction of carbody elastic vibration. However, there is no actual example to utilize under floor equipment as DVA in the trains for commercial passenger service in Japan. By the author's view, the one reason of this is that railway operating companies in Japan don't want to use equipment as moving mass; and the other reason is the difficulty to adjust the natural frequency of supported equipment to the target frequency of the carbody vibration. In addition, as shown in sub-section 4.1, more than one natural mode affect ride comfort in many cases. Recently, there are some trials to apply underfloor equipment to reduce multiple modes of carbody elastic vibration. Aida, et al. [70] proposed to support underfloor equipment with high-damping material having natural frequency less than that of the lowest carbody elastic vibration. By this treatment, they showed multi-modal vibration reduction can be realized without any frequency adjustment of DVA by the excitation tests for a 1:1 scale test vehicle on the roller rig. Looking into outside of Japan, Gong et al. [71] also studied to use several equipment underneath floor and on the roof to use DVAs for different elastic modes of vibration through numerical study using FE analysis.

As an interesting usage of DVA against elastic vibration of carbody bending mode, Tomioka and Takigami proposed to utilize the longitudinal motion of the bogie frames [62]. They derived the condition to tune the natural frequency of the longitudinal vibration of bogie frames to the target carbody bending frequency theoretically, and validated the formula through excitation test on the roller rig and running test on a commercial line of a Shinkansen. This formula is used in the bogie design for Shinkansen.

The studies on vibration reduction measure to consider the 3D deformation of carbody, Akiyama et al. [72] proposed to apply active mass dampers (AMDs) to reduce not only the bending mode but also the elastic mode with the diagonal distortion of carbody cross section. They conducted numerical analysis using their simple 3D vibration model (the Box-type model), roller rig test for 1:1 scale test vehicle, and also running test of a Shinkansen.

Structural design of carbody shells for railway vehicle is generally based on the concept of semi-monocoque structure, in which the outer thin panel of carbody shell plays main role on the strength and rigidity. Therefore, when improving carbody rigidity considering elastic vibration suppression, it needs modification of outer shell structure and there are many difficulty, especially for the existing vehicles. Takigami, et al. proposed to use non-structural members such as frames inside carbody [73, 74]. Their effort on this concept has been sophisticated by utilizing other lighter weight inner members such as handrails [75], and it is applied in the most recent commuter type vehicles as the interior roll-bar which intend to not only improving carbody rigidity but also crashworthiness against side impact.

4.4. Influence of passengers on the carbody vibrations

As the weight of vehicles reduce, the weight ratio of passengers to carbody increases; e.g. the weights of typical commuter vehicles in Japan are around 13 - 18 tonne in the case of trailer cars, while a full car load of passengers (approx. 160 passengers) weighs more than 9 tonne. If the passengers act as such a big mass loading on a vehicle, vibration characteristics of carbody shall be influenced greatly.

The effect of passengers on vehicle dynamics is usually taken into account as mass distributed on the floor. Designers design the carbody so that it can have higher natural frequencies (as far as possible, exceeding 8 Hz) under a full-capacity passenger load.

Kaneda et al. [76], however, reported that the change of natural frequencies was small in contrast with the relatively large reduction of vibration amplitude of the carbody in case passengers were boarding, as a result of excitation tests using a partial mock-up of a carbody. This suggest that on-board passengers act as damping elements upon the carbody elastic vibrations rather than additional mass.

Tomioka et al. studied the effect of passengers on the elastic vibrations using several types of actual vehicles [77, 78]. Figure 15(a) shows the acceleration PSD measured in a running test of a Shinkansen during 270 km/h for different numbers of passengers [77]. The peak observed around 10.5 Hz corresponds to the elastic vibration of carbody. It can be seen that the peak value reduces according to the increase of the number of passengers, whereas the change of peak frequency is very small. Figure 15(b) shows the comparison for different loadings; that is, for the loading cases with 51 passengers and 5100 kg of iron blocks on the floor. It is clear that the change of the peak around 10.5 Hz has different tendencies. From both figures, it has been found that passengers on the vehicles show the effect as not pure mass rather damping. Figure 16 shows the excitation test result for a commuter type vehicle on the roller rig [78]. Large vibration reductions are observed for at least two peaks around 7 Hz and 11 Hz.

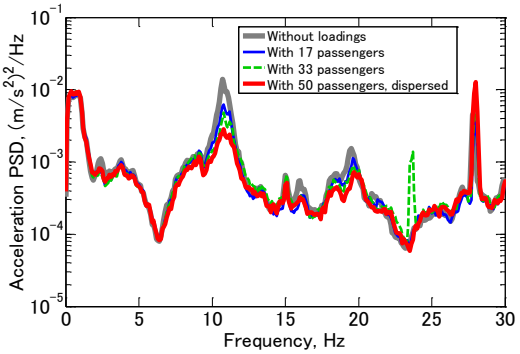

(a) Effect of the number of passengers.

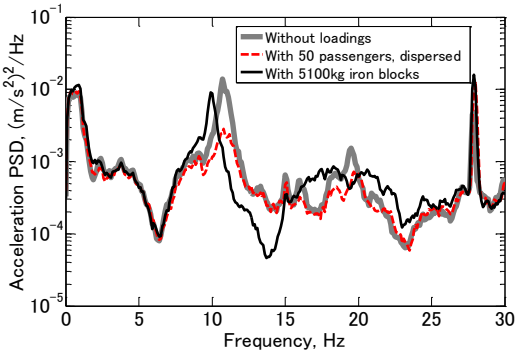

(b) Comparison of PSD loaded with 50 passengers and 5100 kg of iron blocks on the floor.

Figure 15. Acceleration PSDs of a Shinkansen measured during running at 270 km/h. (At longitudinal center, window side on the floor.)

The large and multi-modal vibration reduction effect by human body observed in actual vehicles suggests the possibilities to realize some new effective damping devises by mimicking the passengers' motion correctly. Some trials have been already conducted by the authors [70, 78-80].

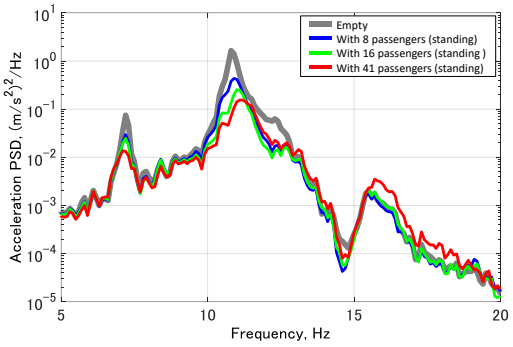

Figure 16. Acceleration PSDs of a commuter type vehicle measured by excitation test on the roller rig. (At longitudinal center, window side on the floor. All-axle simultaneous excitation,)

5. Conclusions

Engineering research subjects relating to the dynamics of railway vehicles have been surveyed in this paper. The focuses are particularly on the research works from Japan.

The researches concerning to the motion of wheelset; pantograph-catenary interaction; aerodynamic relating problems on the vehicle; and application of control techniques have been introduced firstly as the most distinctive subjects of railway vehicle dynamics.

The safety assessment and ride comfort evaluation have been dealt with, too. Those are important research topics on railway dynamics as public transportation system.

The subject concerning to carbody elastic vibration, which is important relating to ride comfort, has been described after that. The effect of passengers on the elastic vibration of carbody has been introduced as the interesting (and something surprising) topic.

Since this article assumes researchers outside the railway industry as the readers, the descriptions may be insufficient for the specialists in this field. For such readers, more detailed review is available by Miyamoto and Suda [81] about the research and development of advanced railway vehicle technologies in Japan.

The author thinks dynamics of railway vehicle is very interesting target of research, especially for the researchers in mechanical engineering. It is great pleasure for him if this survey can give some help or be an informative guide for researchers to take interests on railway vehicles.

References

[1] Wickens, A.H., Fundamentals of Rail Vehicle Dynamics, CRC Press, 2003.

[2] Iwnicki, S. (ed), Handbook of Railway Vehicle Dynamics, CRC Press, 2006.

[3] Klingel, Uber den Lauf der Eisenbahnwagen auf gerader Bahn, Organ fur die Fortschritte des Eisenbahnwesens in technischer Beziehung, Neue Folge, 20, 1883, pp.113-123.

[4] Matsudaira, T., Shimmy of Axle with a Pair of Wheels, Bulletin of the Railway Technical Laboratory Journal of railway engineering research, 9, 1952, pp. 16-26 [in Japanese].

[5] Matsudaira, T., Nosing of 2-axle Railway Cars and its Prevention: 1st Reports, Theory, Transactions of the Japan Society of Mechanical Engineers, 19, 1953, pp. 139-146 [in Japanese]. (DOI https://doi.org/ 10.1299/kikai1938.19.87_139)

[6] Matsudaira, T., Nosing of 2-axle Railway Cars and its Prevention: 2nd Report, Model Experiment, Transactions of the Japan Society of Mechanical Engineers, 19, 1953, pp. 146-153 [in Japanese]. (DOI https://doi.org/10.1299/kikai1938.19.87_146)

[7] Matsudaira, T., Nosing of 2-axle Railway Cars and its Prevention: 3rd Report, Application to Actual Cars, Transactions of the Japan Society of Mechanical Engineers, 19, 1953, pp. 154-157 [in Japanese]. (DOI https://doi.org/10.1299/kikai1938.19.87_154)

[8] Matsudaira, T., Hunting Problem of High-Speed Railway Vehicles with Special Reference to Bogie Design for the New Tokaido Line", Proceedings of the Institution of Mechanical Engineers Part 3F, 180, 1965, pp. 55-66.

[9] Suda, Y., High Speed Stability and Curving Performance of Longitudinally Unsymmetric Trucks with Semi-active Control, Vehicle System Dynamics, 23, 1994, pp. 29-52.

[10] Sato, E., Kobayashi, H., Tezuka, K., Okamoto, I., Kakinuma, H. and Tamaoki, T., Lateral Force during Curve Negotiation of Forced Steering Bogies, Quarterly Report of RTRI, 44, 2003, pp.8-14. (DOI https://doi.org/10.2219/rtriqr.44.8)

[11] Togami, Y.,Goto, R., Ogino, T., Shikata, K., Toide, T., Mizuno, M. and Shimokawa, Y., Development of the New Concept Steering Bogie, Journal of Mechanical Systems for Transportation and Logistics, 6, 2013, pp.124-132. (DOI https://doi.org/10.1299/ jmtl.6.124)

[12] Shimokawa, Y. and Mizuno, M., Development of the New Concept Steering Bogie, Nippon Steel & Sumitomo Metal Technical Report, 105, 2013, pp.41-47. (http://www.nssmc.com/en/tech/report/nssmc/pdf/ 105-08.pdf)

[13] Shibata, H., Problems on the Current Collection of an Electric Rolling Stock at High Speeds, Journal of the Society of Mechanical Engineers, 63, 1960, pp.1118-1128 [in Japanese].

[14] Manabe, K., Wave Motions and Vibrations in Railway Systems [in Japanese], Kotsu Shimbunsya, 2002.

[15] Aboshi, M. and Manabe, K., Analyses of Contact Force Fluctuation between Catenary and Pantograph, Quarterly Report of RTRI, 41, 2000, pp.182-187. (DOI https://doi.org/10.2219/rtriqr.41.182).

[16] Ikeda, M., The Contact Force between Pantograph and Contact Wire -An Estimation Method Using the Inversion Technique, Quarterly Report of RTRI, 41, 2004, pp.80-85. (DOI https://doi.org/10.2219/ rtriqr.45.80)

[17] Ikeda, M., Suzuki, M. and Yoshida, K. Study on Optimization of Panhead Shape Possessing Low Noise and Stable Aerodynamic Characteristics, Quarterly Report of RTRI, 47, 2006, pp.72-77. (DOI https://doi.org/10.2219/rtriqr.47.72)

[18] Koyama, T. and Aboshi, M., Revealing the generating mechanism of contact wire corrugation [in Japanese], Railway Research Review, 71-9, 2014, pp.8-11. (https://bunken.rtri.or.jp/PDF/cdroms1/0004/2014/0004006120.pdf)

[19] Manabe, K., Dynamic Analysis on the Generating Mechanism of Contact Wire Corrugation, Transactions of the Japan Society of Mechanical Engineers, 66, 2000, pp. 454-459 [in Japanese]. (DOI https://doi.org/10.1299/kikaic.66.454)

[20] Manabe, K., A hypothesis on a wavelength fixing mechanism of rail corrugation, Proceedings of the Institution of Mechanical Engineers Part F, 214, 2000, pp.21-26.

[21] Manabe, K., Verification of Wavelength-Fixing Mechanism for Rail Corrugation Caused by Multiple-Wheel Interaction, Quarterly Report of RTRI, 48, 2007, pp.164-169. (DOI https://doi.org/10.2219/rtriqr.48.164)

[22] Fujimoto, H., Miyamoto, M. and Shimamoto, Y., Lateral Vibration and its Decreasing Measure in the Tail Car of a Shinkansen (Decrease of Tail Car's Vibration with Yaw Damper between Cars), Transactions of the Japan Society of Mechanical Engineers Series C, 59, 1993, pp.1016-1022 [in Japanese]. (DOI https://doi.org/10.1299/kikaic.59.1016)

[23] Suzuki, M. Unsteady Aerodynamic Force Acting on High Speed Trains in Tunnel, Quarterly Report of RTRI, 42, 2001, pp.89-93. (DOI https://doi.org/10.2219/rtriqr.42.89)

[24] Suzuki, M., Ido, A., Sakuma, Y. and Kajiyama, H. Full-Scale Measurement and Numerical Simulation of Flow Around High-Speed Train in Tunnel, Journal of Mechanical Systems for Transportation and Logistics, 1, 2008, pp.281-292. (DOI https://doi.org/10.1299/jmtl.1.281)

[25] Suzuki, M., Nakade, K. and Ido, A. Countermeasures for Reducing Unsteady Aerodynamic Force Acting on High-Speed Train in Tunnel by Use of Modifications of Train Shapes, Journal of Mechanical Systems for Transportation and Logistics, 2, 2009, pp.1-12. (DOI https://doi.org/10.1299/jmtl.2.1)

[26] Sakuma, Y., Paidoussis, M. P., Price, S. and Suzuki, M. Aerodynamic Forces Acting on and Lateral Translational and Rotational Motions of Intermediate Cars Travelling in a Tunnel, Journal of System Design and Dynamics, 2, 2008, pp.240-250. (DOI https://doi.org/10.1299/ jsdd.2.240)

[27] Sakuma, Y., Suzuki, M., Ido, A. and Kajiyama, H. Measurement of Air Velocity and Pressure Distributions around High-Speed Trains on Board and on the Ground, Journal of Mechanical Systems for Transportation and Logistics, 3, 2010, pp.110-118. (DOI https://doi.org/ 10.1299/jmtl.3.110)

[28] Sasaki, K., Kamoshita, S. and Shimomura, T. Development and Field Results of Semi-Active Suspension High Speed Train. [in Japanese], RTRI report, 10, 1996, pp.25-30

[29] Oishi, T, Hayashi, T., Sasaki, K. and Arai, J. Development of Advanced Semi-Active Suspension System for Shinkansen Vehicles, Proceedings of the International Symposium on Speed-up and Service Technology for Railway and Maglev Systems 2003 (STECH2003), August 19-22.2003, Tokyo, Japan, pp.220-224.

[30] Sasaki, K., Toward More comfortable Shinkansen: Development of semi-active suspensions, Railway Research Review, 73-6, 2016, pp.20-23 [in Japanese]. (https://bunken.rtri.or.jp/PDF/cdroms1/0004/2016/ 0004006506.pdf)

[31] Goto, O. Development of Active Lateral Suspension for Railway Vehicle, Journal of The Society of Instrument and Control Engineers, 56, 2017, pp. 127-130 [in Japanese]. (DOI https://doi.org/ 10.11499/ sicejl.56.127)

[32] Sugahara, Y., Kazato, A., Koganei, R., Sampei, M. and Nakaura, S. Suppression of vertical bending and rigid-body-mode vibration in railway vehicle car body by primary and secondary suspension control: Results of simulations and running tests using Shinkansen vehicle, Proceedings of the Institution of Mechanical Engineers Part F, 223, 2009, pp.517-531.

[33] Sugahara, Y. Development of a Vibration Suppression System of Railway Vehicle Using Variable Vertical Dampers, Journal of The Society of Instrument and Control Engineers, 54, 2015, pp.668-671 [in Japanese]. (DOI https://doi.org/10.11499/sicejl.54.668)

[34] Okamoto, I., Speed-up in Curves, Journal of The Society of Instrument and Control Engineers, 32, 1993, pp.577-581 [in Japanese]. (DOI https://doi.org/10.11499/sicejl1962.32.7_577)

[35] Kobayashi, H. Okamoto, I. and Akiyama, Y. The Forced Steering Tilt Truck for Diesel Limited Express, Quarterly Report of RTRI, 41, 2000, pp.16-20. (DOI https://doi.org/10.2219/rtriqr.41.16)

[36] Suzuki, H., Shiroto, H., Tanaka, A., Tezuka, K. and Takai, H., Psychophysical Evaluation of Railway Vibrational Discomfort on Curved Sections, Quarterly Report of RTRI, 41, 2000, pp.106-111. (DOI https://doi.org/10.2219/rtriqr.41.106)

[37] Suzuki, H., Shiroto, H. and Tezuka, K., Effects of Low Frequency Vibration on Train Motion Sickness, Quarterly Report of RTRI, 46, 2005, pp.35-39. (DOI https://doi.org/10.2219/rtriqr.46.35)

[38] Enomoto, M., Kamoshita, S., Kamiyama, M., Sasaki, K., Hamada, T. and Kazato, A., Development of Tilt Control System Using Electro-Hydraulic Actuators, Quarterly Report of RTRI, 46, 2005, pp.219-224. (DOI https://doi.org/10.2219/rtriqr.46.219)

[39] Kamoshita, S., Sasaki, K., Kakinuma, H., Sato, I., Sato, Y. and Nakagaki,, S. A Control Method for Hybrid Tilting Systems using Tilting Beams and Air Spring Inclination, Quarterly Report of RTRI, 48, 2007, pp.1-7. (DOI https://doi.org/10.2219/rtriqr.48.1)

[40] Yamada, T. Air Spring Tilting Control System for Rolling Stock, Journal of The Society of Instrument and Control Engineers, 56, 2017, pp.123-126 [in Japanese]. (DOI https://doi.org/10.11499/sicejl.56.123)

[41] Ishida, H. et al., A New Continuous Measuring Method of Wheel/Rail Contact Forces, Quarterly Report of RTRI, 35, 1994, pp.105-111.

[42] Ishida, H., Matsuo, M., Tezuka, K. and Ueki, K., Method of Measuring Wheel and Rail Contact Forces and Derailment Quotients Continuously: Development of a Measuring Device, Transactions of the Japan Society of Mechanical Engineers Series C, 63, 1997, pp.3417-3423 [in Japanese]. (DOI https://doi.org/10.1299/ kikaic.63.3417)

[43] Accidental Investigation Commission, Report on the Train Derailment at Nakameguro Station on the Tokyo Metro Co. Hibiya Line, October 2000 [in Japanese].

[44] Ishida, H., Miyamoto, T., Maebashi, E., Doi, H., Iida, K. and Furukawa, A., Safety Assessment for Flange Climb Derailment of Trains Running at Low Speeds on Sharp Curves, Quarterly Report of RTRI, 47, 2006, pp.65-71. (DOI https://doi.org/10.2219/rtriqr.47.65)

[45] Kunieda, M., Theoretical Study on the Mechanics of Overturn of Railway Rolling stock, Railway Technical Research Report, 793, 1972, pp.1-15 [in Japanese].

[46] Hibino, Y. and Ishida, H. Static Analysis on Railway Vehicle Overturning under Crosswind, RTRI report, 17, 2003, pp.39-44 [in Japanese].

[47] Hibino, Y., Shimomura, T. and Tanifuji, K. Full-Scale Experiment on the Behavior of a Railway Vehicle being Subjected to Lateral Force, Journal of Mechanical Systems for Transportation and Logistics, 3, 2010, pp.35-43. (DOI https://doi.org/10.1299/jmtl.3.35)

[48] Miyamoto, T., Ishida, H. and Matsuo, M., Running Safety of Railway Vehicle as Earthquake Occurs, Quarterly Report of RTRI, 38, 1997, pp.117-122.

[49] Miyamoto, T., Ishida, H. and Matsuo, M., The Dynamic Behavior of Railway Vehicle during Earthquake : Vehicle Dynamics Simulation on Track Vibrating in Lateral & Vertical Directions, Transactions of the Japan Society of Mechanical Engineers Series C, 64, 1998, pp. 3928-3935 [in Japanese].
(DOI https://doi.org/10.1299/kikaic.64.3928)

[50] Miyamoto, T., Matsumoto, N., Sogabe, M., Shimomura, T., Nishiyama, Y. and Matsuo, M., Railway Vehicle Dynamic Behavior against Large-Amplitude Track Vibration —A Full-scale Experiment and Numerical Simulation, Quarterly Report of RTRI, 45, 2004, pp.111-115. (DOI https://doi.org/10.2219/rtriqr.45.111)

[51] International Organization for Standardization, ISO 2631-1: Mechanical vibration and shock -- Evaluation of human exposure to whole-body vibration -- Part 1: General requirement, 1997.

[52] Suzuki, H., Research trends on riding comfort evaluation in Japan, Proceedings of the Institution of Mechanical Engineers Part F, 212, 1998, pp.61-72.

[53] Japan Society of Mechanical Engineers (ed), Railway Vehicle Dynamics and Modeling, 2017 [in Japanese].

[54] Tomioka, T., Takigami, T. and Aida, K., Modal Analysis of Railway Vehicle Carbodies Using a Linear Prediction Model, Journal of System Design and Dynamics, 3, 2009, pp. 918-931.
(DOI https://doi.org/ 10.1299/jsdd.3.918)

[55] Tomioka, T., Takigami, T. and Aida, K., Modal Vibration Characteristics of Flexural Vibrations in Railway Vehicle Carbodies, Proceedings of the First International Conference on Railway Technology: Research, Development and Maintenance (Railways2012), April 18-20.2012, Las Palmas de Gran Canaria, Spain, Paper No. 33.

[56] Richard, J., Natural Frequencies of Bernoulli-Euler Beams Resting on Two Elastic Supports: Application to Railway Vehicles, Vehicle System Dynamics, 9, 1980, pp.309-326.

[57] Tanifuji, T., An Analysis of the Body-Bending Vibration of a Bogie Vehicle for an Evaluation of the Ride Quality with Deflated Airsprings, Proceedings of the Institution of Mechanical Engineers Part F, 205, 1991, pp.35-42.

[58] Suzuki, Y. and Akutsu, K., Theoretical Analysis of Flexural Vibration of Car Body, Quarterly Report of RTRI, 31, 1990, pp.42-48.

[59] Dumitriu, M., A new passive approach to reducing the carbody vertical bending vibration of railway vehicles, Vehicle System Dynamics, 55, 2017, pp.1787-1806.

[60] Gong, D., Zhou, J. and Sun, W., Passive control of railway vehicle car body flexural vibration by means of underframe dampers, Journal of Mechanical Science and Technology, 31, 2017, pp.555-564.

[61] Eickhoff, B. M., Evans, J. R. and Minnis, A. J., A Review of Modelling Method for Railway Vehicle Suspension Components, Vehicle System Dynamics, 24, 1995, pp.469-496.

[62] Tomioka, T. and Takigami, T., Reduction of bending vibration in railway vehicle carbodies using carbody–bogie dynamic interaction, Vehicle System Dynamics, 48 (Supplement), 2010, pp.467-486.

[63] Carlbom, P.F., Combining MBS with FEM for rail vehicle dynamics analysis, Multibody System Dynamics, 6, 2001, pp.291-300.

[64] Diana, G., Cheli, E., Andrea, C., Corradi, R. and Melzi, S., The development of a numerical model for railway vehicles comfort assessment through comparison with experimental measurements, Vehicle System Dynamics, 38, 2002, pp.165-183.

[65] Ribeiro, D., Calçada, R., Delgado, R., Brehm, M. and Zabel, V., Finite-element model calibration of a railway vehicle based on experimental modal parameters, Vehicle System Dynamics, 51, 2013, pp.821-856.

[66] Tomioka, T., Takigami, T. and Suzuki, Y., Numerical analysis of three-dimensional flexural vibration of railway vehicle car body, Vehicle System Dynamics, 44 (Supplement), 2006, pp. 272-285.

[67] Akiyama, Y., Tomioka, T., Suzuki, Y. and Takigami, T., Parameter Updating of Three-dimensional Vibration Model for Railway Vehicle Carbodies Using Measured Data, Proceedings of the 5th Asian Conference on Multibody Dynamics (ACMD2010), August 23-26. 2010, Kyoto, Japan, Paper No. 63816.

[68] Suzuki, Y., Akutsu, K., Maebashi, E., Sasakura, M. and Tomioka, T., Method for Flexural Vibration Damping of Rolling Stock Carbody, Quarterly Report of RTRI, 38, 1997, pp.123-128.

[69] Ishikawa, R. and Sato, Y., Decrease of vehicle body bending vibration by dynamic damper, Proceedings of the 68th JSME Spring Annual Meeting Vol. C, 1991, pp.531-533 [in Japanese].

[70] Aida, K., Tomioka, T., Takigami, T., Akiyama, Y. and Sato, H., Reduction of Carbody Flexural Vibration by the High-damping Elastic Support of Under-floor Equipment, Quarterly Report of RTRI, 56, 2015, pp.262-267. (DOI https://doi.org/10.2219/rtriqr.56.4_262)

[71] Gong, D., Zhou, J., Sun, W., Sun, Y. and Zhanghui, X., Method of multi-mode vibration control for the carbody of high-speed electric multiple unit trains, Journal of Sound and Vibration, 404, 2017, pp.94-111.

[72] Akiyama, Y., Tomioka, T. and Takigami, T., Development of Active Mass Dampers for Reducing Multi-modal Flexural Vibrations of Carbody, Quarterly Report of RTRI, 55, 2014, pp.1-6.
(DOI https://doi.org/10.2219/rtriqr.55.1)

[73] Takigami, T., Tomioka, T. and Aida, K., Improving the Rigidity of Railway Vehicle Carbodies Using Non-Structural Members, Quarterly Report of RTRI, 50, 2009, pp.63-69.
(DOI https://doi.org/10.2219/ rtriqr.50.63)

[74] Takigami, T., Tomioka, T. and Aida, K., Improving the Rigidity of Railway Vehicle Carbodies Using Inner Sub-Frames, Transactions of the Japan Society of Mechanical Engineers Series C, 76, 2010, pp.1115-1123 [in Japanese].
(DOI https://doi.org/10.1299/kikaic.76.1115)

[75] Imaoka, N., Improving the rigidity of Carbodies and Ride Comfort by Interior Roll-bar [in Japanese], J-TREC Technical Review, 2, 2013, pp.26-33. (https://www.j-trec.co.jp/company/070/02/jtr02.pdf)

[76] Kaneda, T., Kobayashi, H., Oda, M. and Akiyama, S., Study of human body effect to vibration of railway vehicle body, Proceedings of the 75th annual meetings of JSME Kansai-section No.004-1, March; 2000, pp.2.29-2.30 [in Japanese].

[77] Tomioka, T. and Takigami, T., Experimental and numerical study on the effect due to passengers on flexural vibrations in railway vehicle carbodies, Journal of Sound and Vibration, 343, 2015, pp.1-19.

[78] Tomioka, T., Takigami, T. and Aida, K., Experimental investigations on the damping effect due to passengers on flexural vibrations of railway vehicle carbody and basic studies on the mimicry of the effect with simple substitutions, Vehicle System Dynamics, 55, 2017, pp.995-1011.

[79] Tomioka, T., Tachikawa, S. and Akiyama, Y., Development of torus-shaped elastic body as a vibration absorber for flexural vibration in railway vehicle carbody and its experimental validation using

commuter-type vehicle, Mechanical Engineering Journal, 4, 2017, p.16-00467. (DOI https://doi.org/10.1299/mej.16-00467)

[80] Tomioka, T., Tachikawa, S., Akiyama, Y. and Aida, K., Reduction of flexural vibration of railway vehicle carbody by using elastic torus (Validation of vibration reduction effect using actual railway vehicle and numerical investigations on the vibration reduction mechanism), Transactions of the JSME, 83, 2017, p.16-00342 [in Japanese]. (DOI https://doi.org/10.1299/transjsme.16-00342)

[81] Miyamoto, M. and Suda, Y., Recent Research and Development on Advanced Technologies of High-Speed Railways in Japan, Vehicle System Dynamics, 40, 2003, pp.55-99.

EPI International Journal of Engineering
Volume 1, Number 2, August 2018, pp. 13-24
DOI: 10.25042/epi-ije.082018.02

*p*ISSN 2615-5109
*e*ISSN 2621-0541

History of Mitigating Rolling Contact Fatigue and Corrugation of Railway Rails in Japan - Review

Makoto Ishida[a,*]

[a]Railway Engineering Department, Railway Division, Nippon Koei Engineering Consultants. Email: ishida-mk@n-koei.jp

Abstract

Rail is the one of the most important materials to support and guide railway vehicles safely and smoothly. Since rail suffers from various interacting forces and environmental atmosphere, wear and fatigue pose large problems with wheel and rail. Hence, wear and fatigue of wheel and rail have been studied so far to keep running safety and some level of riding comfort of vehicle taking into account track maintenance cost in the world. In this review, the history of theory and practice of rail maintenance in Japanese railways is described focusing on rolling contact fatigue (RCF) corrugation of rails caused by dynamic rolling friction at wheel/rail interface. In particular, "squat" mainly callled in UK or "rail surface shelling" called in Japan which is one of typical fatigue phenomenon for steel wheel-on-rail system and rail corrugations caused by dynamic lateral friction and vertical loading at sharp curves and/or long wavelength of rail corrugation caused by longitudinal roll-slip or stick-slip excited by the resonance of unsprung mass of bogie vertical vibration supported by track stiffness. In addition, the practice of countermeasure for RCF defect of squat, preventive grinding, and countermeasure for top of low rail corrugation, top of low rail lubrication "Friction Moderating System" are described. Also, the possibility of preventing long wavelength of rail corrugation formed in tangential track in undersea tunnel (salty water) enviornment is described.

Keywords: Adhesive materials; preventive grinding, rail; rolling contact fatigue; rail corrugations; top of rail lubrication

1. Introduction

Rail is the one of the most important materials for rail way infrastructure to support and guide railway vehicles safely and smoothly. Vertical force and lateral force based on typically vehicle weight and dynamic behaviour such as vehicle negotiating curves interact between wheel and rail.

Also, traction force for driving and braking of vehicle interacts between wheel and rail longitudinally. In addition, thermal axial force acts on rail and longitudinal friction force interacts between rail and rail fastening system particularly under continuous welded rail (CWR). Since rail is suffered from such various interacting forces and environmental atmosphere, wear and fatigue pose large problems with wheel and rail. Hence, wear and fatigue of wheel and rail have been studied so far to keep running safety and some level of riding comfort of vehicle taking into account the economical aspect of track maintenance cost. However, the phenomena of wear and fatigue have been understood to obtain better solutions from the practical point of view but not enough from the best practice.

In this review, rolling contact fatigue (RCF) of rail which is one of typical fatigue phenomenon for steel wheel-on-steel rail system and rail corrugations caused by dynamic lateral friction and vertical loading at sharp curves and/or long wavelength of rail corrugation caused by longitudinal roll-slip or stick-slip excited by the resonance of vertical vibration of unsprung mass of bogie supported by track stiffness.

In addition, the practice of countermeasure for RCF defect of squat, preventive grinding, and countermeasure for top of low rail (inner rail of two rails of curved track along the axis of radius which is called as low rail due to cant, slope of lateral direction to cancel the centrifugal force caused by running at curved track, set along the curve of track, and high rail is outer rail which is the opposite rail against inner rail called as low rail) corrugation, top of low rail lubrication "Friction Moderating System" are described. Also, the possibility of preventing long wavelength of rail corrugation formed in tangential track in undersea, salty water, tunnel environment is described.

*Corresponding author. Tel.: +81-3-5276-2561
1-14-6 Kudonkita, Chiyodaku, Tokyo
102-8539, Japan

2. Rail RCF defects in Japanese Railways

2.1. Dark cracks generated in gentle curves

The Japanese history of RCF defects in rails is described mainly based on some findings and research achievements obtained so far by Railway Technical Research Institute (RTRI) and Japanese railway operators in Japan. Basically RCF defects must have been initiated just after steel wheel-on-steel rail system was developed. But the first comprehensive report on RCF defects in rails was written by a research project group in RTRI organized by Japanese National Railways (JNR) in 1952 [1].

At first some defects called “dark cracks” shown in Fig. 1 in those days were observed in gentle curves in San-yo line of JNR. Typical cracks were caused together with head checks as shown in Fig. 1. The naming of dark cracks is based on superficial feature that some part surrounding cracks look dark presumably due to slightly indented surface. Then such dark cracks posed so serious problem that a research project was established to study the mechanism of crack initiation following dark cracks. Those cracks were observed not only in curves but also in tangent tracks. Fig. 2 shows dark cracks take place in tangent tracks.

Shortly afterwards they came to be called shelling and/or rail surface shelling which is named to differentiate gauge corner shelling which is called as one of the typical fatigue defects of rail reported in heavy haul railways [2]. Also, after Hatfield accident [3], gauge corner cracks shown in Fig. 3 were focused on to understand their mechanism and establish some appropriate preventing and/or mitigating measures.

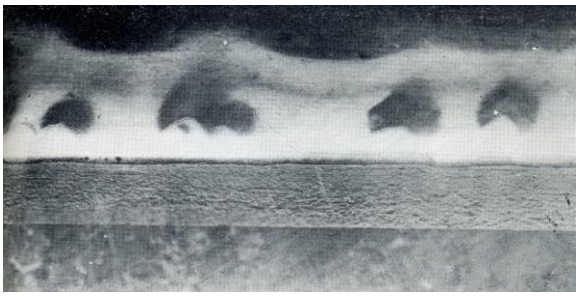

Figure 1. Dark cracks in gentle curves

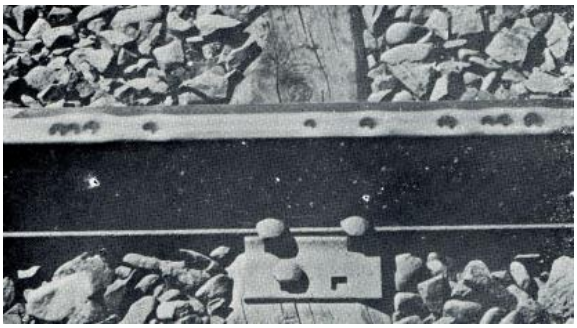

Figure 2. Dark cracks in tangent track

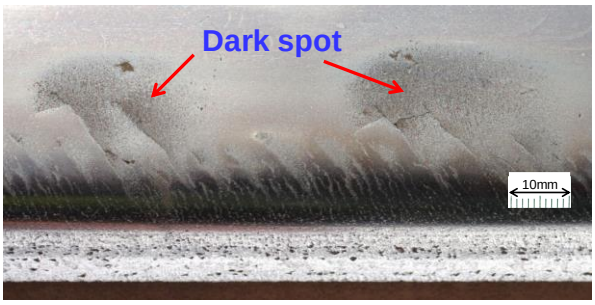

Figure 3. Gauge corner cracks

Considering some features of dark cracks reported in 60 years ago and gauge corner cracks bothering track maintenance engineers nowadays, those cracks look so similar each other not only superficially but also mechanically and metallurgically. Then the mechanism of initiation and propagation of those two cracks may be the same. In addition, gauge corner cracks are classified to rail surface shellings called in Japan or squats called mainly in UK shown in Fig. 4, which is commonly accepted in Japan.

But of course gauge corner cracks are usually caused under head checks generated at gauge corner. And gauge corner cracks are generated not just at gauge corner but slightly close to the centre of rail crown from the gauge corner. The influence of head checks on the initiation of gauge corners has not been clearly understood yet.

Also, gauge corner cracks do not necessarily occur at the location where head checks are observed. Head checks shown in Fig. 5 in the case of as-rolled rails and in Fig.6 in the case of head hardened rails are formed at almost all curves which mean, for example, at transition curves in the case of sharp curves and at circular curves in the case of gentle curves. In these figures, the crack spacing of as-rolled rails is larger than that of head hardened rails, the reason for which is not clearly understood.

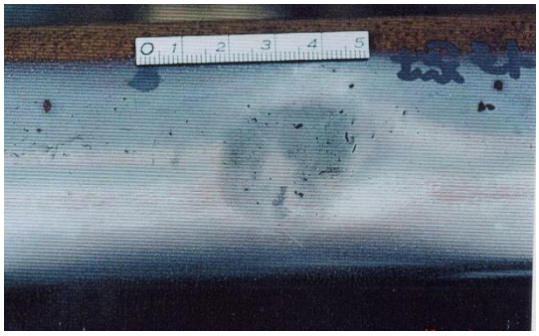

Figure 4. Typical RCF defect “Squat” called in UK and rail surface shelling called in Japan

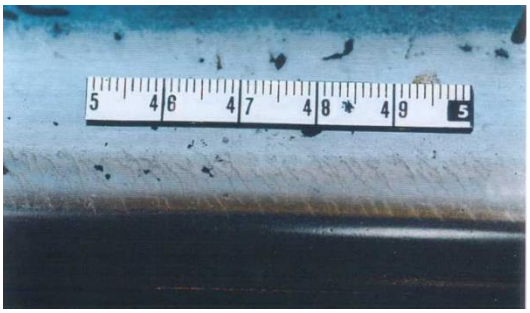

Figure 5. Head checks in as-rolled rail

From the different aspects, some curves whose radius is less than, for example, 800 m have potentiality of head check formation even if the radius of curvature is very small, because such sharp curves have their transition curves whose radius of curvature changes from small to large, up to tangent tracks, which means head checks can be generated at some location whose radius of curvature should be most suitable for head check generation.

Somehow, the project group studied a lot including laboratory simulation using a small scale rolling contact machine. In the study report written by the project group, dark cracks were likely to be caused at less wear places as a result and in addition water spray from steam locomotives to reduce wear must have had some impact on dark cracks initiation. After that, steam locomotives were changed to electric locomotives because of modernization of traction power, from steam to electricity.

Also, water spray was stopped since the steering performance of electric locomotives should have been improved. Fortunately the number of dark cracks initiation got less than before very much and the problem of dark cracks was settled down as a result.

2.2. Rail surface shellings generated in Japanese urban metro railways

In 1970s gauge corner cracks which were called as shellings at that time in Japan as mentioned above posed a large problem in underground railways in Tokyo. Similar to “dark cracks”, an investigation committee was established to understand the mechanism of such RCF defects [4, 5]. In the investigation report, less wear was newly pointed out similar to dark cracks and also the effect of lubrication on the initiation and propagation of RCF defects was pointed out. Then some appropriate amount of gauge face wear of rail to mitigate RCF defects was studied. As one of strategies, some head hardened rails were changed to as-rolled rails to increase wear for the purpose of mitigating RCF damage.

Figure 6. Head checks in head hardened rail

Figure 7 shows the variation of wear rate with the radius of curvature focusing on rail grade (AR: as-rolled rail, HT: heat treated rail = head hardened rail) and the initiation of RCF defects. Also, this figure shows the rough tendency of the initiation of RCF defects of both of as-rolled rails and head hardened rails based on wear rate. The both types of rail are suffered from RCF defects, such as squats and/or gauge corner cracks in the case of less wear. It is identified that the larger the radius of curvature is, the less wear rate is, which clearly suggests lateral force and/or steering force causes large wear. For example, considering two sections of Marunouchi line(AR), squats were generated in some sections of Marunouchi line(AR) of less wear rate than the other.

Focusing on Ginza line(HT) and two sections of Marunouchi line(HT), in the least wear rate section of three sections, squats were generated. Less wear is one of key functions for generating squats in both of as-rolled rail and heat treated (head hardened) rail.

2.3. First stage of rail surface shelling problem in Shinkansen

First stage of rail surface shelling problem in Tokaido Shinkansen which is the first Japanese high speed line opened in 1964 was raised. Since then most of the rail failures were related to rail welds. But the number of rail surface shellings had been increasing after about 10 years passed since starting its operation. Figure 8 shows the history of the number of rail failures in Tokaido Shinkansen.

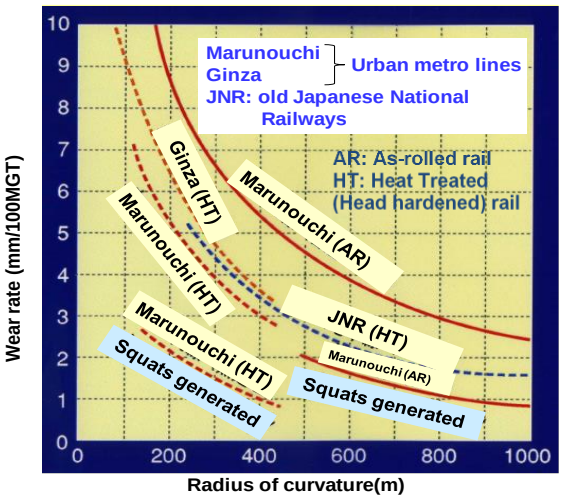

Figure 7. The variation of wear rate with the radius of curvature focusing on rail grade (AR: as-rolled rail, HT: heat treated rail = head hardened rail) and the initiation of RCF defects

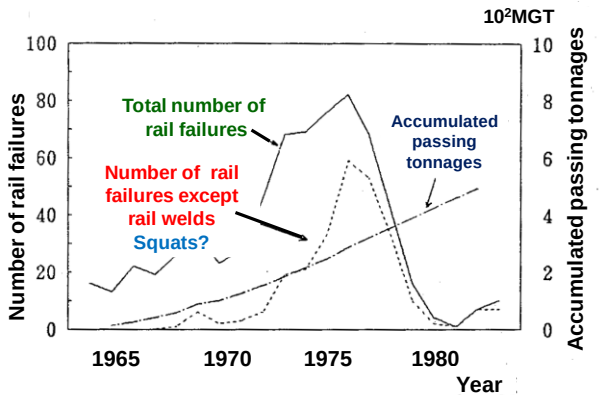

Figure 8. Transition of annual rail failures and accumulated passing tonnages in Tokaido Shinkansen (JIS50T rail)

In this figure, the number of rail failures located not at rail welds was increasing up to 1985. At that time rail surface shellings were not clearly identified by track maintenance people necessarily because the training for the track maintenance people was not enough to check the rail surface shellings, which means obtained data may have included unsuitable ones. But roughly speaking, the trend of changing the main factor of rail failures from rail welds to rail surface shellings can be identified. However fortunately again, the strategy of improving track structure in Shinkansen was implemented since 1977, which was exchanging JIS 50T rail to JIS 60 rail to reduce the damage of ballast track suffered from impact loads. Hence, the damaged rails of JIS 50T rail were naturally changed under such a strategy.

As a result, the problem of rail surface shellings was superficially settled down again. In a sense this process was very similar to the case of dark cracks, which means the mechanism of crack initiation was not clearly identified so that the effective strategy of mitigation was not obtained, but some strategies to improve other issues changed the situation of damaged rails and the problem of RCF defects was superficially settled down.

2.4. Second stage of rail surface shelling problems in Shinkansen

The second Shinkansen line, San-yo Shinkansen, started to operate in 1972. After about 10 years since starting operation, the accumulated passing tonnages reached to 150 to 200 (MGT: Million Gross Tons which is the unit of the number of passing axles multiplied by the weight of an axle to estimate track damage), so that the number of rail surface shellings was getting large. Also, the number of rail surface shellings was getting large in Tokaido Shinkansen after JIS 60 rail installation instead of JIS 50T rail similar to San-yo Shinkansen. Then the study group was newly established again in RTRI in 1985 [6].

It investigated the history of rail surface shellings and the findings related to RCF defects of rails obtained so far were summarized. So that new research programmes including a large twin disc machine for rolling contact fatigue experiments was started. After 10 to 15 years, preventive grinding method was established under the programme for the time being and basically taking into account Shinkansen wheel rail interface condition.

3. Mechanism of Crack Initiation, Propagation and Mitigation Method

3.1. Mechanism of crack initiation and propagation

The mechanism of crack initiation and propagation has been studied for a long time around the world. In particular, above-mentioned study has not been carried out enough to understand it even if many findings about some other tribological area are taken into account. Also, some important material behaviour and/or parameters such as crack tip stress condition including residual stress distribution have to be understood to develop this research area.

Considering such a status of research front, the author concentrated laboratory simulation using a large twin disc rolling contact machine taking into account the results of roughness contact stress analysis. However, both laboratory experiments and stress analysis for roughness contact have some limitations. Considering such limitation as limited test arrangements and analytical conditions, some appropriate test arrangements and analytical conditions were selected. Also, some findings were obtained from grinding tests and track site monitoring continued for 5 years from 1980 to 1985 in Tokaido Shinkansen. With regard to grinding frequency, every 100 MGT was not enough at least so that the grinding frequency should be expected to be less than 100 MGT, which was considered to decide experimental arrangements and analytical conditions. At that time, Shinkansen suffered from many squats caused mainly on the surface of as-rolled (not head hardened) rail installed in tangent tracks so that analytical conditions and experimental arrangements were discussed on the basis of as-rolled rail of JIS 60, tangent track, the running speed of 200 km/h and the average slip ratio of 0.01, for the time being.

Figure 9 shows the analytical conditions and its results with 2D roughness contact model constructed by Dr. Franklin and Prof. Kapoor under the collaboration between Sheffield Univ. and RTRI[7, 8]. In this figure, with regard to contact pressure between rail disc and wheel disc, roughness contact pressure is much larger than Herzian contact pressure. Also, with regard to Von Mises stress distribution, the maximum of Von Mises stress is located at the surface or very thin layer of the surface under roughness contact and no such a high stress takes place under Hertzian contact. Since this 2D analytical model is elastic and two dimensional, the analytical results don't have agreement with actual wheel-rail contact stress condition but suggest some important tendency of stress distribution to roughly understand the damage of rail material. From the analytical results, the damage of rail should be very large at very thin surface layer, which can lead to the effect of preventive grinding.

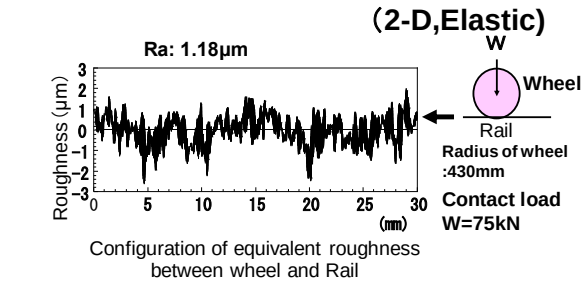

Configuration of equivalent roughness between wheel and Rail

(a) Analytical conditions

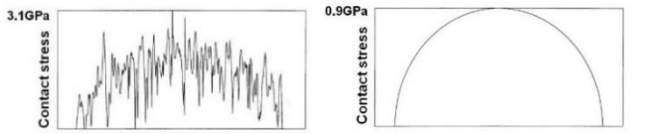

(b) Contact pressure distribution

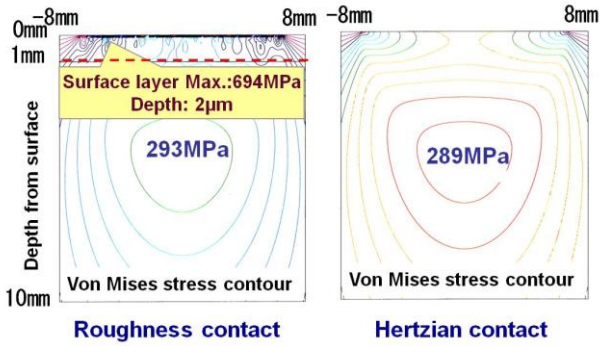

(c) Von Mises stress distribution in rail

Figure 9. The effect of roughness at wheel/rail contact interface on stress distribution

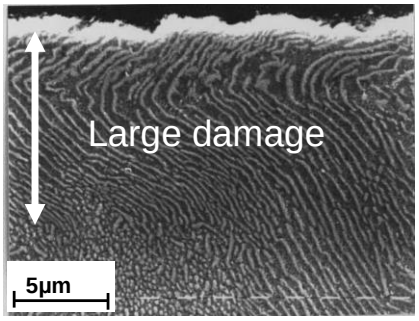

Figure 10. Plastic deformation at the contact surface layer of actual rail material

Figure 10 shows the plastic deformation at the surface of actual rail material. This figure roughly indicates the adequacy of the 2D analytical model and the possibility of RCF crack initiation at the very thin layer. Also, it suggests the possibility that effective grinding thickness should be more than 10 microns and less than 0.1mm of rail subsurface combining with analytical results of 2D roughness model. In addition, focusing on the slip plane of metallic crystal, it is identified that the direction of some specific slip planes is deformed to the same direction plastically under repeated loading [9]. Considering above-mentioned analytical and practical information, the grinding thickness was set to be the only variable parameter and other parameters were constant under the grinding frequency of 50MGT in the experiments using a large twin disc machine. Before grinding experiments, rolling fatigue experiments were carried out to investigate a certain suitable test arrangement for the test machine considering the difference of contact conditions between actual wheel/rail contact and wheel disc / rail disc contact for about more than 5 years [10].

3.2. Preventive grinding

After the rolling contact fatigue experiments, the experimental arrangements were decided and the grinding experiments with a key parameter of grinding thickness had been continued for more than 5 years.

Figure 11 shows the results of grinding experiments with the large twin disc machine [11]. In this figure, some regression curves were obtained to estimate the effect of grinding on RCF. Roughly speaking, 0.1mm of grinding thickness every 50 MGT has an appropriate effect of grinding to extend the service life of rail up to averagely 800MGT. The adequacy of this preventive grinding method, 0.1mm/every 50MGT was verified in the operation of Tokaido Shinkansen. Roughly speaking, all rails installed in the main line of Tokaido Shinkansen have been ground once a year, about 40 to 50 MGT of annual passing tonnages since 1993. Figure 12 shows the results of detecting rails in the monitoring section of Tokaido Shinkansen [7]. In this figure, the number of defects dramatically decreased since regular preventive grinding started in 1993.

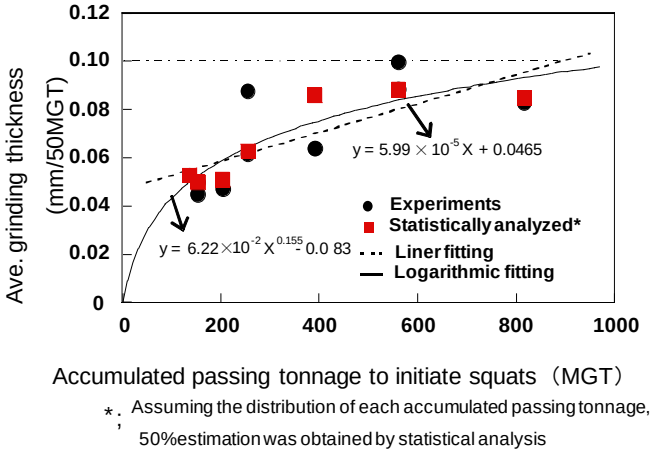

*, Assuming the distribution of each accumulated passing tonnage, 50%estimation was obtained by statistical analysis

Figure 11. The effect of preventive grinding on accumulated passing tonnages to initiate squats

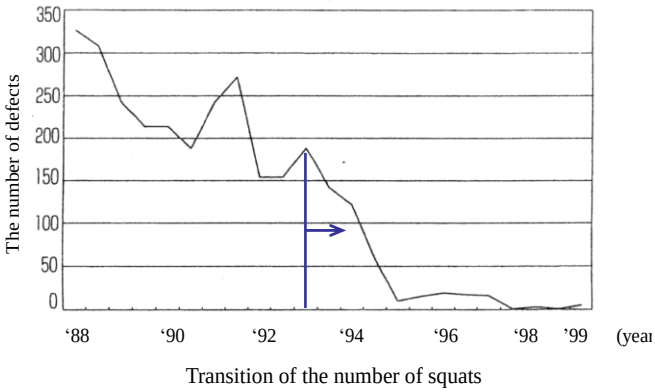

Figure 12. The effect of preventive grinding on mitigating the initiation of RCF defects (after 1993, whole main line of Tokaido was covered with grinding operation)

3.3. Balance between wear and RCF

In advance of describing the balance between wear and RCF, some interesting research activity and sophisticated achievements in this research area obtained by European and/or other railways than Japanese ones. Almost all railways must have suffered from wear and RCF and have long history of theoretical and practical approach to get the best solution to mitigate wear and RCF. In particular, just before Hatfield accident (Derailment and overturning of train accident caused by rail break due to RCF defects on 17th of Oct., 2000), comprehensive and fundamental research project, Integrated study of rolling CONtact fatigue (ICON) [12], was implemented as one of EU projects from 1997 to 2000 under the leadership of European Rail Research Institute (ERRI). A lot of very good achievements and findings were obtained, but unfortunately before such good deliverables had not been adopted yet, Hatfield accident took place in October, 2000. After the Hatfield accident, RCF was newly focused on to keep the running safety of vehicle. In addition, another EU project "INNOvative TRACK system (IINNOTRACK) [13]" was organised and coordinated by UIC which involved 36 partners from 11 European countries including international railway organisations as well as rail research specialised universities and representatives from rail operators, infrastructure managers and railway track industry suppliers.

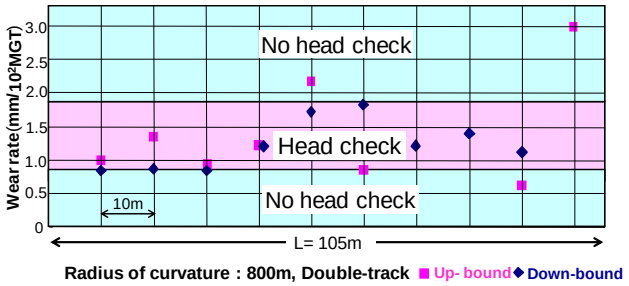

Figure 13. The concept of T-gamma model describing the balance between wear and RCF

After the Hatfield accident, the whole life rail model and T-gamma model were established [14, 15]. Figure 13 shows the concept of T-gamma model. This model is based on friction energy and material strength. According to friction energy, balance between wear and RCF can be evaluated, which is very helpful to select material level and strategy of lubrication and/or grinding. I hope the meaning of damage function should be clearer, for example, RCF function is the rate of crack propagation or plastic deformation and wear function is wear rate and so on. Then the next research subject will be expected to define the damage function.

Also, one of achievements obtained from INNOTRAK is that heat treated rail, head hardened rail, has great effect on mitigating crack propagation of head checks comparing with as-rolled rail. However, considering mitigating and/or preventing gauge corner cracks, heat treated rail may not be always effective in mitigating gauge corner cracks.

The relation between head checks and gauge corner cracks has not been clearly understood yet. As far as Japanese railways are concerned, gauge corner cracks are basically very close to squats, rail surface shellings called in Japan, so that grinding or wear is a key word to mitigate the initiation of gauge corner cracks [16].

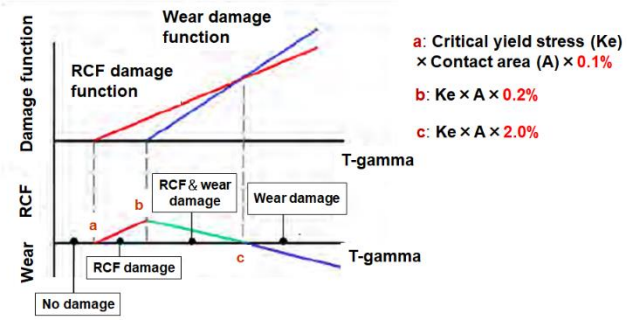

Figure 14. The relation between wear rate and head checks (Head Hardened rails)

Head checks can be generated by the balance between wear and fatigue, which means head checks must be one of RCF defects. Figure 14 shows some range of wear rate where head checks are likely to initiate even if the data are very limited. In the figure, very small amount of wear rate means damage is very less, too, middle range amount of wear rate means suitable balance between wear and RCF for head check initiation, and large amount of wear rate means fatigue damage is not accumulated and worn out.

Finally squat type RCF defects related to white etching layer must be described because this type of defects has been posing a large problem in Japanese conventional narrow gauge tracks [17].

Some reports have been already published in other railways [18, 19]. Figure 15 shows typical squat type RCF defects of white etching layer. Figure 16 shows microstructure of white etching layer.

The typical cause of forming white etching layer is friction heat generated by wheel sliding on rail. Some other causes, for example, large deformation, should surely have an effect on forming white etching layer.

Figure 15. Squat type of RCF defects related to white etching layer

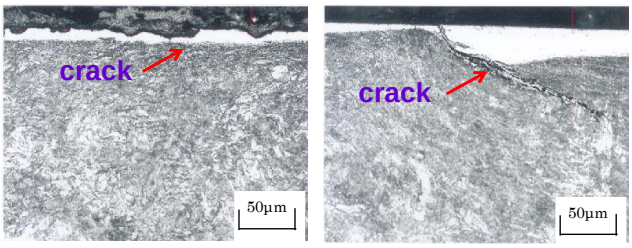

Figure 16. Micro-structure of white etching layer

From the experience of Japanese railways, driving force and/or braking force interacting between wheel and rail, sliding occurs because of less adhesion coefficient ("adhesion coefficient" is used in the field of Railway Engineering and "the maximum coefficient of traction" is generally used in the field of Tribology as the same meaning as adhesion coefficient) than needed potential of friction and heat is generated to change pearlite to martensite from metallurgical point of view. Since Shinkansen's train operation is well controlled to smooth driving and braking much better than narrow gauge conventional train system, almost no report on white etching layer observed in Shinkansen tracks. Considering the mechanism of white etching layer, martensite, formation, it is not easy to prevent wheel-rail sliding perfectly. Considering the current status of this type of defects, early detection is very important to prevent crack initiation from the martensite layer and to grind off fine cracks if already. Some detection system may be promising to mitigate this type of defects.

In addition, bainitic steel rail was developed to prevent squats, rail surface shellings, by modifying material structure [20]. Basically the concept of Japanese bainaitic steel rail is to prevent squat initiation based on the appropriate amount of wear, which means the wear resistance of bainitic steel is less than that of pearlitic steel but its hardness is larger than that of pearlitic steel to prevent large plastic deformation and/or to keep the configuration of rail for better running stability and ride comfort.

Finally considering the balance between wear and RCF, rail type and combination with wheel must be focused on because steel material, hardness and chemical composition and the interaction between rail and wheel have great influence on wear and RCF.

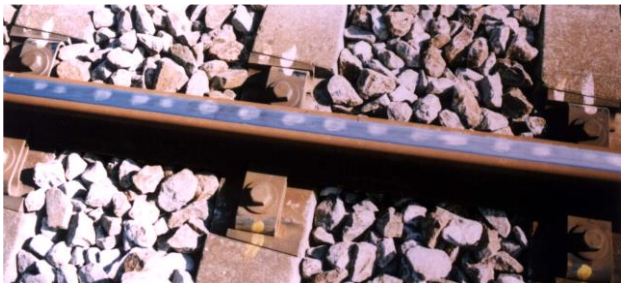

Figure 17. Typical short pitch corrugations formed on low rail surface

4. Rail Corrugation

4.1. Top of low rail corrugations in curved tracks

Short pitch corrugations on low rails shown in Fig. 17 pose acute problems of noise and track deterioration caused by vibrations excited by interacting between rail and wheel forces.

(1) Influential factors in causing corrugations

Tassily and Vincent developed a theoretical model of corrugations formed on low rails and high rails at curved tracks in Paris Rapid and Mass Transport Authority (RATP) [21]. They considered: quasi-static curving behaviour; dynamic interactions between the wheel-set and the track; field tests. The frequency ranges of corrugations studied were 50 to 80 Hz and 250 to 400 Hz. They showed the important relationship between transverse wear rate and roughness. They found two sensitive frequencies at about 60 Hz and 170 Hz.

The bogie, vehicle and track structures considered in their analysis are not the same as those used in Japan. But the two sensitive frequencies of 60 Hz and 170 Hz are very similar to high rail corrugations and low rail corrugations formed in Japanese railways. This means that the transverse wear rate may play an important role on the formation of corrugations. A question arose: which force, lateral creep force or longitudinal creep force, has more influence on the short pitch corrugations? If the lateral creep force is more influential, then dynamic behaviour of a leading axle of a bogie should be investigated rather than a trailing axle. Vehicle running tests and dynamic measurements at a track site were carried out to understand the effect of lateral force and lateral vibration of rail on the formation of corrugations [22].

Also the effect of lubrication on decreasing the lateral force and preventing corrugation formation were studied. Figure 18 shows Q/P (lateral force /vertical force) of low rail measured with strain gauges stuck at rail base flange for lateral force Q and at rail web for vertical force P during the vehicle running tests. In the figure, the Q/P of the leading axle was most significant and the effect of lubrication on reducing lateral forces was also significant. In addition, Figure 19 shows the first formation of corrugations on a new rail, which locates near the second tie from rail joint in the direction of vehicle running. It is not clearly understood that the coupled vibration between rail joint and wheel give rise

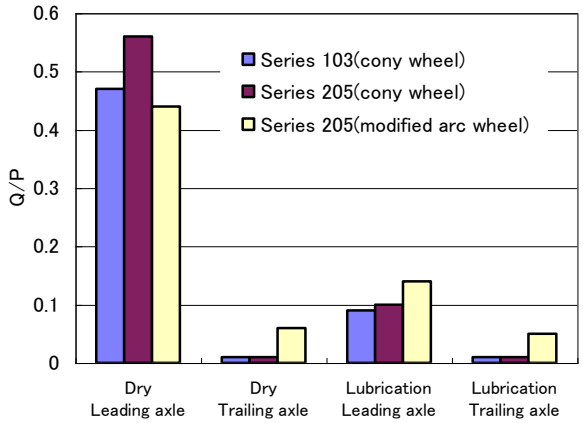

Figure 18. Q/P (lateral force /vertical force) of low rail measured at track site

to corrugations roughly near the second tie from the rail joint first, but almost the same phenomena were very often observed in investigations. It is surely identified that excitation at rail joint gives one of main opportunities of forming corrugations from the findings so far obtained.

Considering the above discussions, the investigation of longitudinal and lateral plastic flow on the surface of some corrugations was carried out [22]. There is little evidence of plastic flow in the longitudinal direction. Most of the plastic flow in Fig. 20 is in the lateral direction. Since plastic flow is greatly influenced by the friction force, plastic flow in the lateral direction indicates the importance of lateral creep forces. The direction of plastic flow (from gauge corner to field corner of the rail) corresponds with the direction of the lateral force on the rail applied by the wheel.

Field investigation shows that lateral creep force and / or longitudinal creep force, and the excitation at rail joints have a great influence on forming corrugations. Also, lateral creep force has greater influence on plastic flow on the surface of corrugations than longitudinal creep force. The excitation of vertical force between rail and wheel at rail joints causes the variation of friction force estimated from the coefficient of friction (COF) multiplied by a resultant of longitudinal and lateral creep forces between wheel and rail. Then, stick-slip phenomenon can be supposed to be induced between a resultant of mainly lateral creep force and longitudinal creep force, and the variation of friction force caused mainly by the vertical excitation at rail joints. This shows that the lateral creep force has a great influence on the formation of low rail corrugations. This may indicate that the behaviour of the leading axle of the bogie should play a more important role than that of the trailing axle.

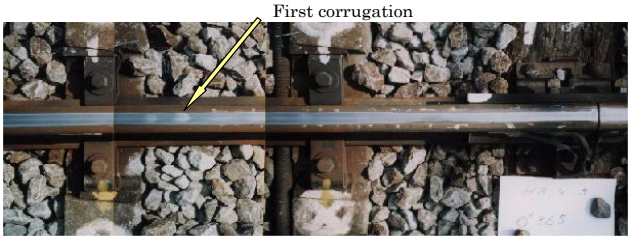

Figure 19. The first low rail corrugations formed on a new rail

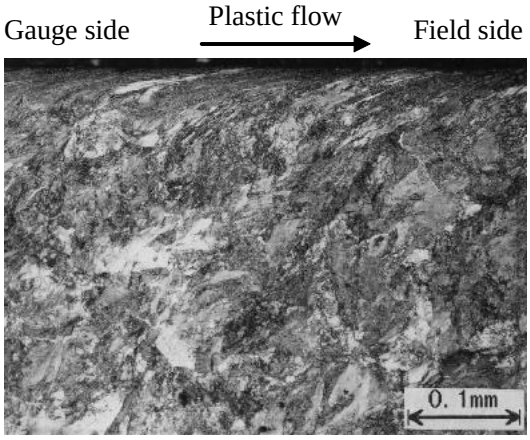

Figure 20. Microstructure of rail surface layer in lateral direction

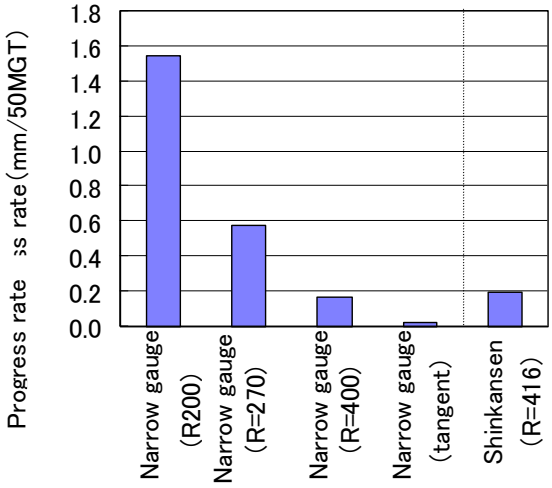

Figure 21. Variation of progress rate of the corrugations with the radius of curvature

Figure 21 shows the variation of progress rate of the corrugations with the radius of curvature. The progress rate is roughly inversely proportional to the radius of curvature. Considering that both lateral creep force caused by a leading axle and longitudinal creep force caused by a trailing axle increase together with the decrease of radius of curvatures, it is not clear which axle has more influence on the formation of corrugations. However, it is not contrary to the possibility of lateral forces influencing the development of corrugation.

(2) Causes of corrugations

Experimental investigations and microscopic observation indicate that

a) Lateral creep forces of a leading axle play an important role in low rail corrugations.
b) Rail joints can be the main trigger for exciting the fluctuation of Q/P (lateral force / vertical force).
c) The fluctuation of Q/P may lead to stick-slip between wheel and rail, and wear takes place to form corrugations.

The fluctuation of Q/P based on the vertical force P variation excited at rail joints and the resonance of rail tilting

vibration may be the main factors of formation of low rail corrugations, but this proposition cannot be experimentally proven because the fluctuation of Q/P cannot be directly measured *in situ* due to the too short interval of strain gauges installed at a rail which covers usually 200 mm long. Also, that of Q/P cannot be measured by strain gauges installed at a wheel because the signals whose frequencies more than 100 Hz are filtered due to the resonance of the wheel structure. To understand theoretically the mechanism of low rail corrugations, further study which considers dynamic vehicle / track interaction, curving performance of vehicle, and the lateral stiffness of track is required.

3) Lubrication

Lubrication between wheel and rail has been adopted to reduce (i) squeal, (ii) wheel flange vertical wear and (iii) rail gauge face wear. Lubrication is used to prevent low rail corrugations at sharp curves. To investigate the effect of lubrication on preventing corrugations, the normal lubricant was applied on the crown of low rails at a sharp curve with a radius of curvature of about 300 m. Investigations were carried out up to about 200 MGT and it was found that no corrugations formed [22]. It has been suggested that lubrication on the crown of low rails has significant effect on increasing safety against wheel flange climb derailment [23]. If the lateral creep force decreases due to lubrication, then the lateral force of high rail, usually called flange reaction, will decrease as well. This means that wheel flange vertical wear and rail gauge face wear should be reduced. On the other hand, lubrication of the rail crown has some risk of wheel sliding. Such significant advantages and risks need to be balanced by choosing a lubricant with an appropriate COF.

On the other hand, the mechanism of low rail corrugations is almost understood but its prediction model has not been established yet. Also, one of most effective solutions to prevent low rail corrugation in sharp curves is considered "friction modifier" which was developed focusing on preventing negative damping phenomenon in traction curve shown in Figure 22 and obtaining positive slope in sliding region of slip ratio [24].

A solid-type lubricant which was named as "friction moderator" to reduce lateral force and squealing noise excited by vehicle negotiating sharp curves was developed. Friction moderator consists of grains of coke whose raw material is artificial graphite crushed to a diameter of 0.2 mm and appropriately arranged about its graphitization, and

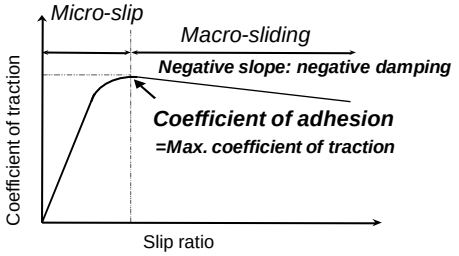

Figure 22. Typical characteristics of traction curve

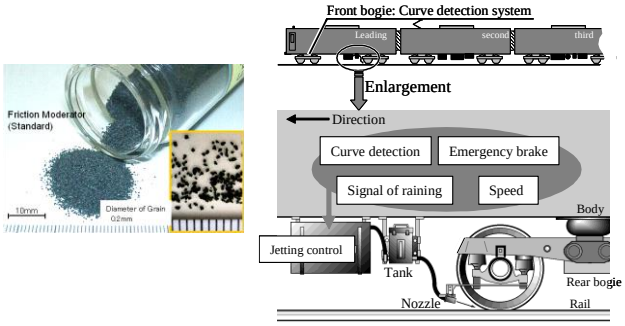

Figure 23. Friction Moderator and Friction Moderating System (on-board system)

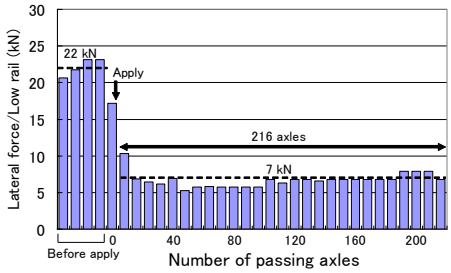

Figure 24. Effect of Friction Moderator (Lubricant) on decreasing lateral force

phenol resin which is adopted as coating for the grains of coke from the aspect of preventing them from catching fire and to aid braking (because phenol resin is used for composite brake shoes). Also, the jetting device was developed with a focus on the arrangement of the nozzle size and air pressure. Figure 23 shows friction moderator and its jetting system on board, which is called as Friction Moderating System (FRIMOS).

Figure 24 shows the lateral forces of the low-rail and high-rail as measured at the track site. In the figure, approximately 22 kN of lateral force on the low-rail before application of the friction moderator decreased to approximately 7 kN after application to the wheel/rail interface on the low-rail side using the jetting device of the FRIMOS that was installed on the test vehicle [25].

4.2 Long pitch corrugation in the tangent track under salty environmental tunnel

Figure 25 shows rail corrugations formed on slab track in the ascending slope of salty environmental tunnel, called Shin-Kammon Channel tunnel, of San-yo Shinkansen line [26]. Since they are causing noise and large interacting forces between wheels and rails, a lot of maintenance work such as frequent rail renewal and rail grinding have been spent to cope with those problems.

Figure 26 shows a typical photo of the waveforms and its phase lag of corrugations between left and right rails. In this figure, the wavelength is about 1.2m whose frequency calculated by running speed is about 70Hz which is almost the same as the resonance frequency of unsprung mass of vehicle supported by track stiffness. Also, there are two

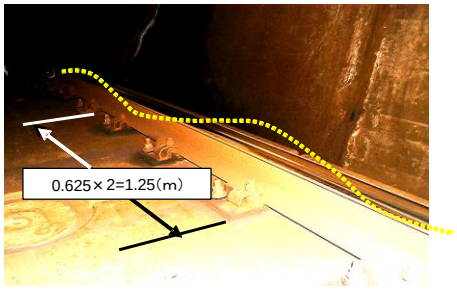

Figure 25. Rail corrugations formed in the ascending slope of Shin-Kammon Channel tunnel (salt water environmental tunnel)

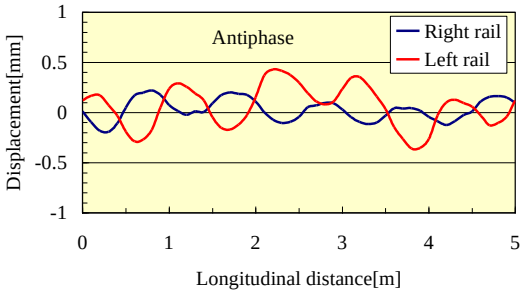

Figure 26. Typical example of the waveforms and its phase lag of rail corrugations

cases about the phase lag between the right rail and left rail corrugations. One is the same phase of both rails and the other is the phase lag of 180 degree between right rail and left rail. Considering those facts, the resonance of unspring mass of vehicle and the rolling frictional vibration of wheelset may have great influence on the mechanism of rail corrugations.

Figure 27 shows the location of rail corrugations observed in ascending slopes of the tunnel. In this figure, corrugations are generated only in ascending slopes not in descending slopes, and in almost tangent track, which suggests the corrugations may be caused by driving wheels not following wheels. According to the findings obtained from the Figs. 26 and 27, the possibility of the following mechanism of the corrugations can be considered.

The maximum traction force which is estimated by wheel load multiplied by adhesion coefficient called the maximum traction coefficient and is almost equal to kinetic friction coefficient in the case of normal dry condition, changes in proportion to wheel load variation. On the other hand, wheels drive on rails with some rolling inertia. Rolling inertia doesn't always follow the variation of maximum

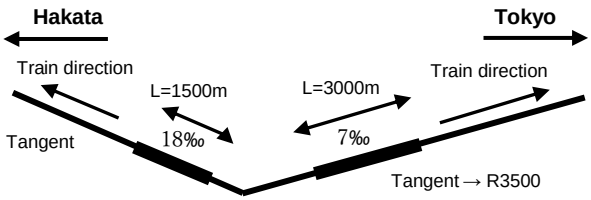

Figure 27. Location of rail corrugations observed in ascending slopes of Shin-Kammon Channel tunnel (upward-slop)

traction coefficient depending on the surface conditions of rail and wheel, which induce longitudinal roll-slip phenomenon along rails.

As a result, such a roll-slip phenomenon may cause rail corrugations. In fact, driving force can excess over the maximum traction force depending on wheel load variation and kinetic COF, and wheels can slip on rails very slightly.

To verify the above-mentioned mechanism of rail corrugations, it was desirable that the roll-slip phenomenon of wheel would be directly confirmed from the variation of wheel rotation, however, which was not easy at this moment because the precision of measuring rotational speed of axle was not enough to identify the phenomenon of about 70Hz. Then investigating the possibility of the roll-slip, the kinetic COF of rail was measured focusing on rust on the surface of rail due to the atmosphere in the tunnel under the sea to check the appropriately low COF which may induce roll-slip phenomenon.

(1) Plastic flow on corrugated rails

To confirm longitudinal roll-slip caused by wheel load variation, the longitudinal plastic flow of rail was investigated. Figure 28 shows longitudinal plastic flow on rail surface layer. In this figure longitudinal plastic flow is clearly observed. On the other hand, lateral plastic flow was not observed. This means such large traction force or driving force necessary for a vehicle to ascend a slope, may has a great influence on generating plastic flow and the possibility of roll-slip phenomenon to cause such corrugations.

(2) Influential factors on the maximum traction coefficient

Next, Figure 29 shows the surface condition of rail crown. In this figure, almost all area of running surface of rail look very rusty. This surface may suggest that COF measured by sliding probe system may not be evaluated properly because the shape and hardness of sliding probe

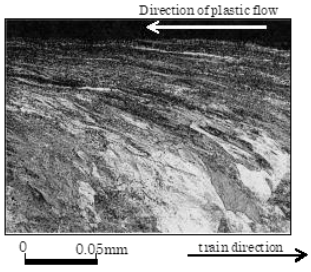

Figure 28. Microstructure of rail surface layer in longitudinal direction

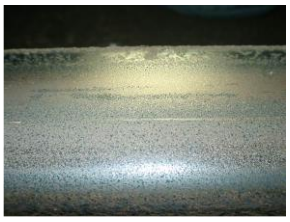

Figure 29. State of top surface of rail

should be checked from the aspect of suitability of contact interface between sliding probe of measuring apparatus. Accordingly, the measured COF may not be a parameter to evaluate the possibility of sliding. Considering such a situation, the surface substance or oxidized layer of rail crown was focused to investigate the possibility of roll-slip phenomenon.

At first Fourier transform infrared absorption spectroscopy was revised to analyse the surface of rail installed in track in situ but the analytical results were not clearly achieved. Then sample rails were put aside track in a salty environmental tunnel and a dry mountain tunnel which was selected as no corrugation condition to compare with the salty environmental tunnel. The sample rails were exposed in those two tunnels for 6 months to get rust enough for analysis. X-ray diffraction analysis was carried out to investigate the surface substances of sample rails.

Figure 30 shows the analytical results in comparison with the two tunnels. In this figure, some iron oxides and oxyhydroxides were identified, but β-FeOOH was found out only in the case of salty environmental tunnel. Since β-FeOOH is the material of low COF, the possibility of roll-slip phenomenon can be expected only in salty environmental tunnel. In this study, in situ analysis has not been successful yet, but laboratory analysis, particularly X-ray diffraction analysis, played a very important role to recognize the possibility of roll-slip phenomenon leading to the formation of corrugation.

(3) Formation mechanism of rail corrugations in salty environmental tunnel

Considering the above-investigated results, the factors of mechanism of rail corrugations are considered to be as follows:

(a) Large traction force is generated by driving wheels to climb up the ascending slopes of salty environmental tunnel
(b) Wheel load variation is excited at the irregularity of rail welds. The phase of one side wheel load variation is almost reverse to that of the other wheel.
(c) The maximum traction coefficient between wheel and rail is not large enough because of the small amount of β-FeOOH on the running surface of rail only in salty environmental tunnel.
(d) Roll-slip phenomenon may be induced based on the relationship between the driving force of wheel and the maximum traction force depending on wheel load variation excited at rail welds.
(e) Wheel load variation is excited more by the formation of corrugations and wear amount of corrugation is progressed by the wheel load variation.

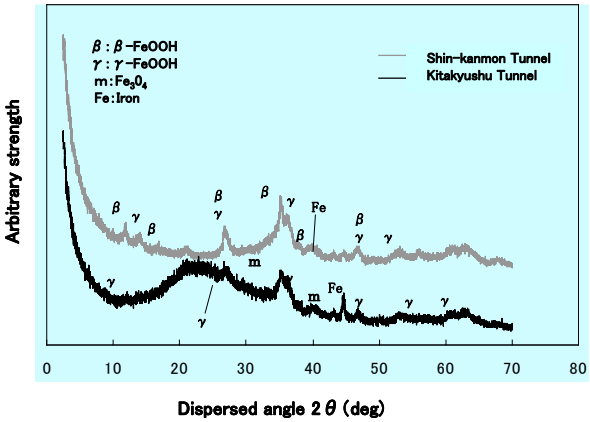

Figure 30. Results of X-ray diffraction analysis

Roughly speaking, rail corrugations described here are considered to form under the combination of decreasing the maximum traction coefficient appropriately up to not too small value and not enough value due to rust under the sea tunnel, the variation of the maximum traction force depending on wheel load variation excited at rail welds and the rolling inertia of driving wheels to climb up the ascending slopes in the tunnel.

5. Concluding Remarks

This review describes the history of rolling contact fatigue (RCF) defects of rails and two types of corrugations classified focusing on their wavelength and/or frequency formed in Japanese railways and their mitigation strategies from rail maintenance point of view. The concept of mitigation strategy for RCF defects is balance between wear and RCF. The effect of grinding is the same as that of wear. In fact, controlling wear amount is a key word to mitigate RCF defects with grinding and lubrication. Also, the concept of mitigation strategies for rail corrugations is controlling tribological conditions of wheel/rail interface, reducing lateral resistance (traction coefficient) and increasing longitudinal resistance (traction coefficient) to prevent stick/roll-slip at wheel/rail interface.

Finally, it should be better to control vehicle/track interaction focusing on the combination of vehicle/track dynamic interaction and wheel/rail tribology under the collaboration of vehicle engineers and track engineers who should be encouraged to improve vehicle/track maintenance strategies for advancing vehicle/track maintenance quality and cost reduction.

References

[1] Nakamura, R., Yamato, H. and Enomoto, S.: Synthetic report on rail dark crack, RTRI Report, No.379, 1963 [in Japanese].
[2] Gidelines to best practices for heavy haul railways operations-Infrastructure construction and Maintenance Issues, International Heavy Haul Associ., June, 2009, pp.3-9.
[3] Smith R.A.: Current Understanding of The Rolling Contact Fatigue Problem in Rails, Imperial College, London, Proceedings of ASIA TRIB 2006 KANAZAWA, JAPAN
[4] Kazamaki, T., et al: Rail shellings in Eidan underground, Tetsudo Senro (First half), 16-5, 1968, pp.27-31.
[5] Kazamaki, T., et al: Rail shellings in Eidan underground, Tetsudo Senro (Second half), 16-6, 1968, pp.35-39.
[6] T102 study group：Mitigation measures for rail shelling－1985 annual report－,RIRI report, A-87-81, 1987 [in Japanese].
[7] Ishida, M., Akama, M., Kashiwaya, K. and Kapoor, A.: The current status of theory and practice on rail integrity in Japanese railways-Rolling contact fatigue and corrugation, Fatigue & Fracture of Engineering Materials & Structures, 26, 2003, pp.909-919.

[8] Ishida, M. and Hua Chen, Franklin, F. : The effect of preventive grinding from the aspect of roughness contact, Journal of Japanese association of railway civil engineers, 38-2, 2000, pp.49-52 [in Japanese].
[9] Inoue, Y. : Mechanism of Shelling Initiation, Journal of Japan Railway Civil Engineering Association, Vol.32, 1994, pp.430-433 [in Japanese].
[10] Ishida, M. and Abe, N.: Experimental Study on Rolling Contact Fatigue from Aspect of Residual Stress, Wear 191, 1996, pp.65-71.
[11] Ishida, M., Abe, N. and Moto, T.: The effect of preventive grinding on rail surface shelling, Quarterly Report of RTRI, 39-3, 1998, pp.136-141.
[12] Modern Tribology Handbook, Volume Two, Editor-in-Chief of Bharat Bhushan, CRC press, Sep. 2000, p.1324.
[13] UIC : INNOTRACK, Innovative Track System, www.innotrack.eu, 2010.
[14] Burstow, M. C.: A model to predict and understand rolling contact fatigue in wheels and rails, Proc.of the 7th World Congress on Railway Research (WCRR 2006), Montreal, Canada, 2006.
[15] Dembosky, M., Doherty, A., Urban, C., Walker, R. and Gurule, S.: Management of rolling contact fatigue (RCF) in the UK system: a systems solution, Proc. of 7th World Congress on Railway Research (WCRR 2006), Montreal, Canada. 2006.
[16] Nakamura, T. & Kitahara, K. : Rail Grinding Tests to Control Rail Failures in Curved Tracks, Journal of Japan Railway Civil Engineering Association, Vol.51, No.3, 2013, pp.36-39 [in Japanese].
[17] Jin, Y., Ishida, M.: Analyses of White Etching Layer Generated on Rail Surface, RTRI report, 19-9, 2005, pp.17-22. [in Japanese].
[18] Grassie, SL: Squats and squat-type defects in rails: the understanding to date Proceedings of the Institution of Mechanical Engineers, Part F: Journal of Rail and Rapid Transit 226, 2012, pp.235-242.
[19] Schilke, M. and Persson, C.: White etching layers on the Stockholm local traffic network, Proc. of CM2012, Chengdu, China, 2012, pp.589-596.
[20] Satoh, Y., et al : Evaluation of Bainitic Steel Rail by Durability Tests in Revenue Line, RTRI Report, 22-4, 2008, pp.29-34 (in Japanese).
[21] Tassily, E. and Vincent, N., Rail corrugations: analytical model and field tests, Wear, 144 (1991), 163-178.
[22] Ishida, M. and Moto, T. and Takikawa, M., The Effect of Lateral Creepage Force on Rail Corrugations on Low Rail at Sharp Curves, Wear, 253(2002), 172-177.
[23] Ishida, M. and Nakahara, T., Derailment Accident in Hibiya Line and Tribology, Tribologist, 46(2001) No.7, pp46-53 [in Japanese].
[24] Eadie, D.T., Kalousek, J. and Chiddick, K.C., The Role of High positive Friction (HPF) Modifier in the Control of Short Pitch Corrugations and Related Phenomena, Wear, 253, 2002, pp.185-192.
[25] Ishida, M., Ban, T., and Fukagai, S. Friction Moderating System for Preventing Low Rail Corrugations in Sharp Curves, 8th International Conference on Contact Mechanics and Wear of Rail/Wheel Systems(CM2009), Firenze, Italy, September 15-18, 2009
[26] Ishida, M., Aoki, F., Sone, Y., Ban, T. and Shirouzu, K. (2005), Rail corrugations caused by low coefficient of friction in a submarine railway tunnel, Proc. of World Tribology Congress, Washington, DC, USA, 12-16 Sept., WTC2005-64346.

EPI International Journal of Engineering
Volume 1, Number 2, August 2018, pp. 25-29
DOI: 10.25042/epi-ije.082018.03

*p*ISSN 2615-5109
*e*ISSN 2621-0541

Approximating Bending Stiffness for Structural Optimization of Double-skin Hollowed Car Body Panels

Yoshiki Ohta[a,*]

[a]Department of Mechanical Engineering, Faculty of Engineering, Hokkaido University of Science. Email: ohta@hus.ac.jp

Abstract

This paper presents the evaluation of the approximate equivalent bending stiffness of double-skin hollowed car body panels. For this purpose, the equivalent bending stiffness of the rectangular panel is expressed first in the quadratic polynomial form with respect to the design parameters for structural optimization by using the Response Surface Method (RSM). Finite element formulation for bending problem of the panel is also formulated by using the ACM rectangular element, and then FE source code is developed by incorporating the equivalent stiffness obtained by the RSM. Finally, the numerical results obtained from the present FEA with the equivalent stiffness are compared with the ones by a commercial FE software, ANSYS, and then the applicability of the approximate equivalent stiffness is studied.

Keywords: Bending stiffness; double-skin hollowed extrusion; finite element analysis; response surface; structural optimization

1. Introduction

Aluminum alloy hollowed extrusions have been developed for a few decades, and many applications of the extrusions can be found not only in buildings and bridges but also in mechanical elements such as a railway car body and so on. In near futures it could be extensively applied to car body according to the light weightiness and the flexibility for structural optimization. Double-skin hollowed extrusions generally consist of two skins and inner ribs between the skins, and thus the topology optimization for the locations of the inner ribs and the size optimization for both of the skins and the inner ribs can be found for the design problem of the structures.

In the research for the aluminum hollowed extrusions, Kawasaki et al. [1] studied the structural FEM analysis on railway car bodies made of aluminum hollowed extrusions under uniformly distributed normal load, where the equivalent orthogonal anisotropic plate is employed through the selection of four main rigidities which describe principal deformation of car body. The FEM results calculated with orthogonal anisotropic plates are found to be in good agreement with the load test result. Kawasaki et al. also developed not only the energy absorber for crashworthy structure by using annealed aluminum hollowed extrusion [2], but also the friction stir welding (FSW) to manufacture railway car body made of aluminum hollowed extrusions [3].

Figure 1 shows an example of a railway car body made of aluminum hollowed extrusions [4]. In the structural analysis of the railway car body, whole car body is usually divided into many double-skin hollow panels, and finite element analysis is carried out for the panel. However the computational cost for numerical evaluations would not be small due to the complexity of the structure, and thus the costs would be greater due to many iterations of numerical calculation in optimization process for the numerical structural optimization. So if the double-skin panel could be replaced in numerical calculations by an orthogonal anisotropic plate with equivalent bending stiffness, the computational cost could be reduced greatly in actual structural optimization.

Figure 1. A railway car body made of aluminum hollowed extrusions [4]

*Corresponding author. Tel.: +81-11-688-2284
Maeda 7-15-4-1, Teine-ku, Sapporo
Hokkaido, Japan, 006-8585

This paper presents the evaluations of approximate equivalent bending stiffness for the structural optimization of double-skin hollowed rectangular panels. For this purpose, the equivalent bending stiffness of the panal is expressed first in the quadratic polynomial form with respect to the design parameters, which would be taken in the definition of the optimization problem at the next stage of this work; thickness of the whole plate, thickness ratios of a skin and an inner rib, and pitch ratio of the inner rib of double-skin hollowed extrusion. Experimental points for constructing the response surface [5, 6] of approximate equivalent bending stiffness is calculated by using the add-in software for Microsoft Excel® named RS-Maker [7]. Responses at each experimental point are calculated numerically for some simple problems such as 4-points bending problem and so on by using a commercial FE software, ANSYS. Finally, the response surfaces of the bending stiffness are determined from the responses by using the RS-Maker.

In the present paper, in order to study the applicability of the approximate equivalent bending stiffness determined, a finite element source code is also developed by introducing ACM's rectangular element and by incorporating the approximate bending stiffness obtained by the Response Surface Method, and finally numerical results obtained from the developed source code are compared with the numerical ones obtained by using ANSYS for the some numerical examples with different design parameter values.

2. Equivalent Stiffness of Double-Skin Hollowed Panel

Figure 2 shows the dimensions and coordinates of a double-skin hollowed rectangular panels. In the present study inner ribs are uniformly located in the *y*-direction as shown in the figure, and the widths of the plates, the pitch of an inner rib, the thickness of a skin and an inner rib and the whole thickness of the plate are denoted by *a*, *b*, *p*, *t* and *h*, respectively.

At the next stage of this work a structural optimization problem will be considered for the double-skin hollowed square panel (*a*=*b*), thus the whole thickness *h*, the pitch to the thickness *p/h* and the skin thickness to the whole thickness *t/h* are taken as design variables in the present problem. In the numerical examples, the design variables are discretized to select experimental points for response surfaces of approximate equivalent stiffness as shown in Table 1. The width of the plate *a* is also given such that the number of set of inner ribs is kept to be 14 in each numerical design.

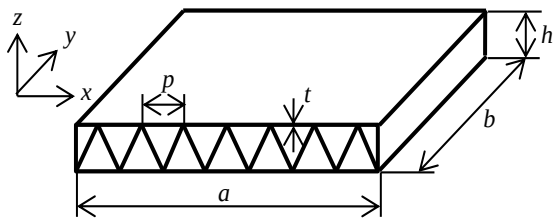

Figure 2. Dimensions and coordinates for a double-skin hollowed panel

Table 1. Discretized design variables for the double-skin panel

h [m]	*p/h*	*t/h*
0.02	0.8	0.06
0.03	1.2	0.07
0.04	1.6	0.08
0.05	2.0	0.09
0.06	2.4	0.10

For the double-skin hollowed rectangular panel, bending and twisting moments (M_x, M_y and M_{xy}) can be written by using bending and twisting curvatures (χ_x, χ_y and χ_{xy}) as

$$\begin{Bmatrix} M_x \\ M_y \\ M_{xy} \end{Bmatrix} = \begin{bmatrix} D_{11} & D_{12} & 0 \\ D_{21} & D_{22} & 0 \\ 0 & 0 & D_{66} \end{bmatrix} \begin{Bmatrix} \chi_x \\ \chi_y \\ \chi_{xy} \end{Bmatrix} \tag{1}$$

In the next section, the above stiffness (D_{11}, D_{12}, D_{21}, D_{22} and D_{66}) are tried to be expressed with respect to the design variables (*h*, *p/h* and *t/h*) by using Response Surface Methodology.

3. Construction of Response Surfaces for the Stiffness

In the present study, each response surface for the equivalent bending stiffness is expressed by using a quadratic polynomial as follows:

$$\begin{aligned} y(x_1, x_2, x_3) = {} & \beta_0 + \beta_1 x_1 + \beta_2 x_2 + \beta_3 x_3 \\ & + \beta_4 x_1^2 + \beta_5 x_2^2 + \beta_6 x_3^2 \\ & + \beta_1 x_1 x_2 + \beta_1 x_1 x_3 + \beta_1 x_2 x_3 \end{aligned} \tag{2}$$

where β_i are unknown coefficients of the response surface, and the response *y* and the variables x_i correspond to each equivalent bending stiffness D_{ij} and design variables mentioned in the previous section, respectively. It is known generally that more than twice number of experimental points is required as the number of unknown coefficients, so twenty experimental points are selected in the present study under the *D*-optimum criteria by using the add-in software for Microsoft Excel® named RS-Maker [7]. Table 2 shows the design variable values for twenty experimental points obtained numerically.

Table 2. Experimental points in RSM obtained by RS-Maker
($x_1 = h$, $x_2 = p/h$, $x_3 = t/h$)

x_1	x_2	x_3	x_1	x_2	x_3
0.02	0.8	0.06	0.04	2.4	0.06
0.02	0.8	0.08	0.04	2.4	0.10
0.02	0.8	0.10	0.06	0.8	0.06
0.02	1.6	0.06	0.06	0.8	0.08
0.02	1.6	0.10	0.06	0.8	0.10
0.02	2.4	0.06	0.06	1.6	0.06
0.02	2.4	0.08	0.06	1.6	0.10
0.02	2.4	0.10	0.06	2.4	0.06
0.04	0.8	0.06	0.06	2.4	0.08
0.04	1.6	0.08	0.06	2.4	0.10

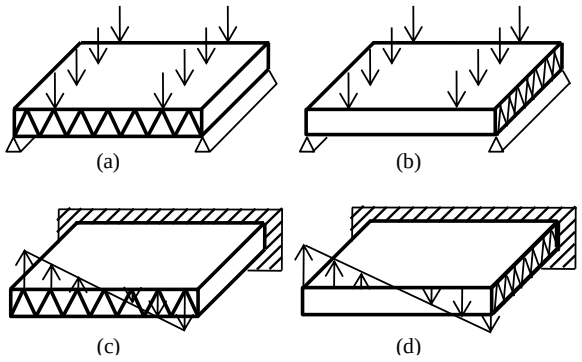

Figure 3. Numerical models employed for the evaluation of responses by using ANSYS

Table 3. Numerical conditions for finite element analysis

Software	ANSYS ED 9.0
Element type	SHELL 63
Young's moduls	72 GPa
Poisson's rotio	0.33

Next the response value for each experimental point, which corresponds to an equivalent stiffness value, is required in order to construct the response surfaces. In the present study, the responses are estimated from the numerical results obtained by using a commercial finite element software ANSYS for some simple bending and twisting problems shown in Fig. 3. Table 3 shows the numerical conditions for finite element analysis, the element-type employed in numerical calculations and material constants. After obtaining the responses for each experimental point by using ANSYS, each response surface is constructed for the bending stiffness by the RS-Maker.

Figure 4 shows the comparisons of stiffness values D_{11} at experimental points, which are obtained by finite element analysis with ANSYS and estimated by the response surface constructed, and Figure 5 corresponds to the case of the stiffness D_{22}. Table 4 also shows the coefficients of determination adjusted for degree of freedom. All of the coefficients are over 98%, and thus the response surfaces constructed in this study give good estimations for the equivalent bending stiffness.

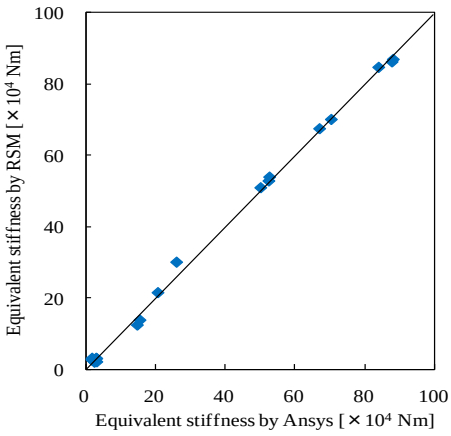

Figure 4. Comparisons of equivalent stiffness D_{11}

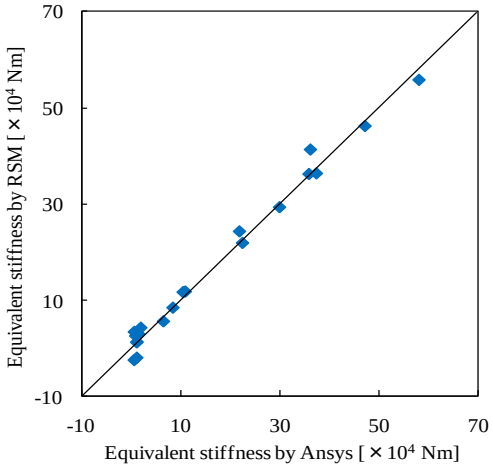

Figure 5. Comparisons of equivalent stiffness D_{22}

Table 4. Coefficients of determination adjusted for degrees of freedom

Stiffness	R^2
D11	0.997
D12	0.992
D21	0.983
D22	0.976
D66	0.97

4. Finite Element Analysis with Response Surfaces for Bending Problem

In the present study, the finite element source code with ACM rectangular bending element is developed by incorporating the response surfaces obtained in previous section. The applicability of the approximate bending stiffness estimated in this paper is then studied by comparing the present finite element solutions with the ANSYS's solutions where all of the skins and inner ribs are meshed for a simply bending problem of double-skin hollowed panels.

In the formulation of ACM rectangular bending element, coordinates, dimensions and nodal numbers are taken for the rectangular panel as shown in Figure 6. By using the nodal displacements $\{U\}$ and the nodal forces $\{F\}$, the governing equation is written as follows:

$$[K]\{U\} = \{F\} \tag{3}$$

where $[K]$ is the ACM stiffness matrix, and $[K]$ is calculated by

$$[K] = \int_{-B}^{B}\int_{-A}^{A}[B]^T [D][B]\,dXdY \tag{4}$$

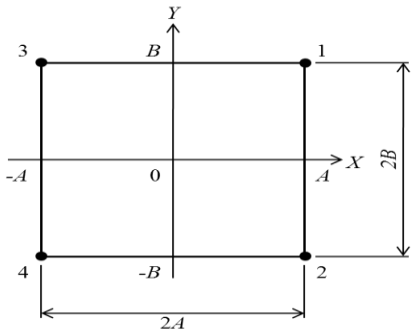

Figure 6. An ACM bending element

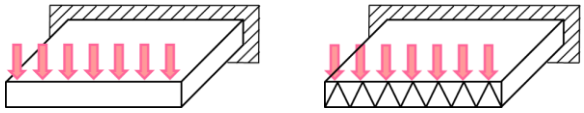

(a) Plate model by FEM code (b) Hollow extrusion model by ANSYS

Figure 7 Numerical examples

In the present study, the matrix [*D*] is calculated by using the response surfaces for equivalent bending stiffness constructed in the previous section, and matrix [*B*] is determined from the ACM formulations.

In numerical examples, a cantilevered panel is picked up, and uniformly distributed loads is considered as shown in Fig. 7.

Figure 8 shows the comparisons of the maximum deflections of the panel with different inner-rib thickness ratios, which is one of design variables in present problem, obtained by present FE source code and by the ANSYS. Figs. 9 and 10 also correspond to the results for the plate with different pitch ratios and inner-rib thicknesses, respectively. In each case, there are good agreements qualitatively except for some cases of small thickness values around between 0.02 and 0.03 in Fig. 10.

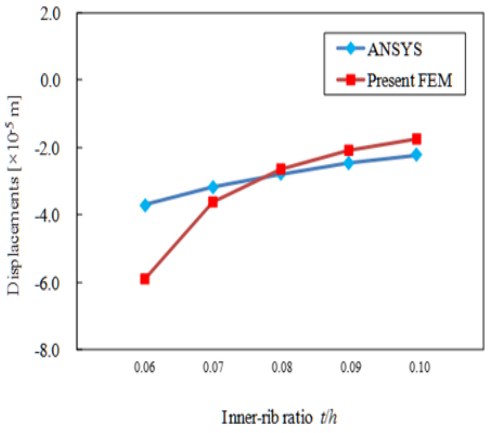

Figure 8. Evaluations of equivalent stiffness in the present study (*h*=0.04, *p*/*h*=1.6)

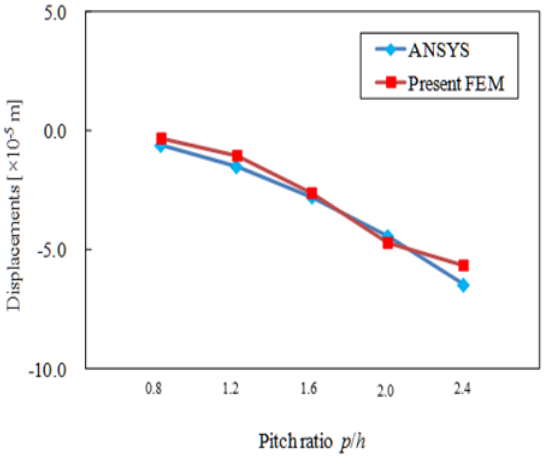

Figure 9. Evaluations of equivalent stiffness in the present study (*h*=0.04, *t*/*h*=0.08)

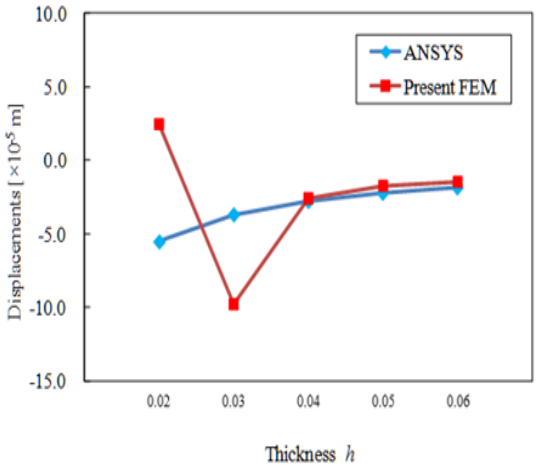

Figure 10. Evaluations of equivalent stiffness in the present study (*p*/*h*=1.6, *t*/*h*=0.08)

5. Conclusions

In the present paper, the response surfaces for the equivalent bending stiffness of a double-skin hollowed rectangular panel are first obtained with respect to parameters of dimensions of the plate by using Response Surface Methodology. In order to study the applicability of the approximate bending stiffness estimated, a finite element source code is developed by incorporating the approximate bending stiffness obtained, and then numerical results obtained by the source code developed are compared with the numerical ones obtained by using ANSYS. In the numerical examples there are good agreements qualitatively except for some exceptions, and it can be finally concluded that the present evaluation method for the equivalent bending stiffness of double-skin hollowed plates would be effective to reduce the computational cost in optimization calculations after some improving.

References

[1] Takeshi K., Sumio O., Kentarou M., Kazufumi Y., Tomomichi O., Ryouji I. and Shinichi H, Structural Analysis of Railway Car Body of Aluminium Hollow Extrusions [in Japanese], Transaction of JSME (Ser. A), 65-636, 1999, pp.1832-1838.

[2] Takeshi K., Takahisa Y., Hideshi O., Kentarou M. and Hideyuki N., Development of Energy Absorber Using Annealed Aluminium Hollow Extrusions for Railway Vehicles [in Japanese], Transaction of JSME (Ser. A), 70-697, 2004, pp.1341-1347.

[3] Takeshi K., Toshihisa Y., Yoshihiko I., Masakuni E. and Hideyuki N., Application of Friction Stir Welding to a Railway Car Body Made of Aluminium Hollow [in Japanese], Transaction of JSME (Ser. A), No. 71-701, 2005, pp.170-176.

[4] Takeshi H., Zusetu Shinkansen-Zenshi Vol.2 [in Japanese], Gakusyu-Kenkyu-sya, 2005.

[5] Raymond H. Myers and Douglas C. Montgomery, Response Surface Methodology Process and Product Optimization Using Designed Experiments, Wiley Series in Probability and Statistics, John Wiley & Sons. Inc., 1995.

[6] Douglas C. Montgomery, Design and Analysis of Experiments 4th edition, John Wiley & Sons. Inc., 1995.

[7] Akira T., RSMaker for Excel, http://www.todoroki-lab.net /ssoft/soft.html.

EPI International Journal of Engineering
Volume 1, Number 2, August 2018, pp. 30-34
DOI: 10.25042/epi-ije.082018.04

*p*ISSN 2615-5109
*e*ISSN 2621-0541

Vibration Analysis of Cracked Structures as a Roving Body Passes a Crack Using the Rayleigh-Ritz Method

Sinniah Ilanko[a], Yusuke Mochida[b]*, Julian De Los Rois[c]

[a]School of Engineering, The University of Waikato. Email:ilanko@waikato.ac.nz
[b]School of Engineering, The University of Waikato. Email:yusuke@waikato.ac.nz
[c]School of Engineering, The University of Waikato.

Abstract

The natural frequencies of a cracked plate with a roving mass were computed using the Rayleigh-Ritz Method for various sets of boundary condition. The obtained frequencies exhibit a sudden shift as a roving body crosses a crack. If the crack is only partial and continuity of translation is maintained, then the frequency shift occurs only when the body possesses a rotary inertia. If the crack is a complete one (through thickness) which permits differential translation to occur on either side of the crack, a particle having mass only (translatory inertia) is sufficient to cause a sudden shift. There is no need for a rotary inertia. This is potentially useful in detecting cracks in structures, as it is possible to track the changes in the natural frequencies of a structure as a test body such as a vehicle on a bridge moves and identify points where sudden frequency changes occur.

Keywords: Cracked plate; natural frequencies; rayleigh-ritz method; roving mass; vibration

1. Introduction

Identifying cracks through frequency measurements has been a subject of research for decades [1-14], but it still remains a challenge due to two main reasons. The frequency changes due to cracks are usually very small and the inverse problem of identifying cracks is further complicated by the fact that the frequencies depend on both the number, severity and locations of cracks. However, recent work [15] shows that in a beam, a roving body that has a rotary inertia causes a sudden shift in frequencies as it passes a crack.

In this paper, this phenomena is investigated for a plate with a roving body. Vibration analysis of plates with cracks also attract many researchers for decades [16-22]. We show that the frequencies of a plate with a crack will change abruptly as a mass attached to the plate is moved from one side of the crack to the other. This is potentially useful in detecting cracks in structures, as it is possible to track the changes in the natural frequencies of a structure as a test body such as a vehicle on a bridge, moves and identify points where sudden frequency changes occur. These would then correspond to potential crack locations irrespective of the number and severity of the cracks. To identify a crack and its location all that is needed is an observation of a sudden change in the natural frequencies. The location of the roving body then corresponds to a crack location. This sudden shift in frequency occurs in all modes with the exception of certain cases where the crack is at the nodal line and the use of a cumulative frequency shift parameter also helps to address the difficulty due to frequency changes being too small.

*Corresponding author. Tel.: +64-7-837-9380
Waikato, 0800 New Zealand

2. Method

The Rayleigh-Ritz Method is used to find the natural frequencies of rectangular plates with cracks and a roving body (Fig. 1). The type of crack considered here is that there is a discontinuity in flexural rotation but the translation is continuous such as those considered in beams [15]. The differential rotation is related to the bending moment at the crack and a rotational spring stiffness representing the effective stiffness of the joint. In plates, the crack can also go through the full thickness and in this case, both translation and rotation are discontinuous.

The plate is also subject to a roving body, that is, a body whose location is changed to track any change in the frequencies but the body has no velocity relative to the plate. The Rayleigh-Ritz Method is then applied to calculate the natural frequencies of the plate and the results are then plotted against the location of the roving body. The crack is

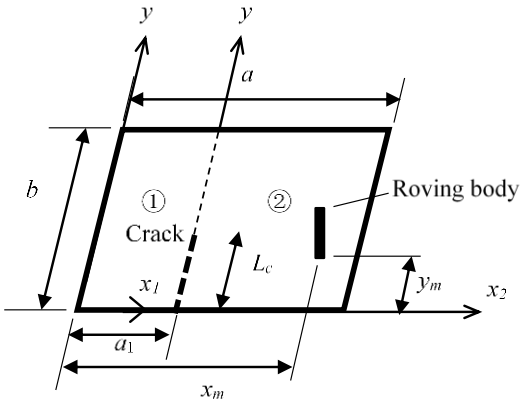

Figure 1. A cracked plate with a roving body

introduced as follows: The plate is formed by assembling two rectangular plates and the coupling between the two plates is enforced through distributed penalty stiffness that control the relative translations and rotations between the two components. A length along which a crack is present is subject to zero or low penalty stiffness but elsewhere along the joint sufficiently high penalty stiffness is applied. To represent a complete (through thickness) crack both translational and rotational penalty stiffness are set to zero while for flexural cracks similar to those in beams, the translational stiffness is set to a high value but rotational stiffness is set to a smaller value. Suitable magnitude of penalty stiffness is determined by using positive and negative stiffness values [23] which help to ensure that any error due to violation of the continuity is kept within the required accuracy.

The plate was subdivided into two rectangular segments (Segment 1 and 2) that have the separate coordinates (x_1, y) and (x_2, y), and for each segment the admissible functions in x, y directions consisted of a constant, a linear function, a quadratic function and a cosine series [24]. The out-plane displacement plate of a segment of a completely free plate, W_k (k = 1 or 2) can be defined by the following equations.

$$w_k\left(x_k, y, t\right) = W_k\left(x_k, y\right) \sin \omega t \tag{1}$$

with

$$W_k\left(x_k, y\right) = \sum_{i=1}^{N}\sum_{j=1}^{N} G_{ij}\phi_i\left(x_k\right)\phi_j\left(y\right) \tag{2}$$

and

$$\phi_i\left(x_k\right) = \left(\frac{x_k}{a_k}\right)^{i-1} \qquad \text{for } i = 1, 2 \text{ and } 3$$

$$\phi_i\left(x_k\right) = \cos\left(\frac{\left(i-3\right)\pi x_k}{a_k}\right) \qquad \text{for } i \geq 4$$

where ω is the circular frequency and t is time. $G_{i,j}$ are undetermined weighting coefficients. The above equations are substituted into the strain energy expression, V_k and kinetic energy expression, T_k given by Eqs. (3) and (4) respectively.

$$Vk = \frac{1}{2}D\int_0^{a_k}\int_0^{b}\left[\left(\frac{\partial^2 W_k}{\partial x^2}\right)^2 + \left(\frac{\partial^2 W_k}{\partial y^2}\right)^2 + 2\nu\frac{\partial^2 W_k}{\partial x^2}\frac{\partial^2 W_k}{\partial y^2} + 2\left(1-\nu\right)\left(\frac{\partial^2 W_k}{\partial x \partial y}\right)^2\right] + dx_k d_y \tag{3}$$

and

$$T_k = \frac{\omega^2 \rho h}{2}\int_0^{a_k}\int_0^{b} {W_k}^2 dx_k dy \tag{4}$$

where,

$$D = \frac{Eh^3}{12\left(1-\nu^2\right)}$$

Here, D is the plate rigidity, E is Young's modulus, ν is Poisson's ratio, ρ is the density of the material and h is the thickness of the plate.

The two segments were joined together by translational and rotational springs. For the length of the crack the rotational stiffness was of low magnitude for partial flexural cracks but for full cracks the stiffness values were set to zero. Elsewhere very high stiffness values of the order 10^6 times that of the typical plate stiffness was used to enforce continuity. The strain energy due to the springs between the plate segments are given by Eqs. (5) and (6)

$$V_t = \frac{1}{2}\int_0^{b} k_t\left(W_2\left(0, y\right) - W_1\left(a_1, y\right)\right)^2 dy \tag{5}$$

$$V_r = \frac{1}{2}\int_0^{b} k_r\left(W_2^{'}\left(0, y\right) - W_1^{'}\left(a_1, y\right)\right)^2 dy \tag{6}$$

where k_t and k_r are translational and rotational spring constants of artificial springs attached between the two segments respectively.

The translational and rotational kinetic energy of the roving mass are given by Eqs. (7) and (8) respectively.

$$T_t = \frac{1}{2}M_m\left(W_k\left(x_m, y_m\right)\right)^2 \qquad (k = 1 \text{ or } 2) \tag{7}$$

$$T_r = \frac{1}{2}I_m\left(W_k^{'}\left(x_m, y_m\right)\right)^2 \qquad (k = 1 \text{ or } 2) \tag{8}$$

By attaching translational and rotational springs along the plate edges, any typical set of boundary conditions can be incorporated with the penalty method [25]. The strain energy due to attached springs along the plate edges, V_e is given by Eq. (9).

$$\begin{aligned} V_e = {} & \frac{1}{2}\int_0^{b} K_t\left\{W_1\left(0, y\right)^2 + W_2\left(a_2, y\right)^2\right\} dy \\ & + \sum_{k=1,2}\frac{1}{2}\int_0^{a_k} K_t\left\{W_k\left(x_k, 0\right)^2 + W_k\left(x_k, b\right)^2\right\} dx_k \\ & + \frac{1}{2}\int_0^{b} K_r\left\{W_1^{'}\left(0, y\right)^2 + W_2^{'}\left(a_2, y\right)^2\right\} dy \\ & + \sum_{k=1,2}\frac{1}{2}\int_0^{a_k} Kr\left\{W_k^{'}\left(x_k, 0\right)^2 + W_k^{'}\left(x_k, b\right)^2\right\} dx_k \end{aligned} \tag{9}$$

where, $a_2 = a - a_1$, and K_t is translational spring constant and K_r is rotational spring constant of the attached spring on the edges.

Equations (10) and (11) give the total strain and kinetic energy.

$$V_{total} = V_1 + V_2 + V_t + V_r + V_e \quad (10)$$
$$T_{total} = T_1 + T_2 + T_t + T_r$$

The stiffness matrix and mass matrix used in the Rayleigh – Ritz analysis are derived from the total strain and kinetic energy equations.

3. Results and Discussion

The natural frequencies of a rectangular plate with a crack running parallel to one edge were computed using the Rayleigh-Ritz Method. The results were generated for various sets of boundary conditions with a partial flexural crack at a_1=0.4a running the full width of the plate (L_c=b) for the non-zero natural frequency. When the mass is exactly at the location of the crack, (i.e. x_m/a = 0.4) the natural frequencies were calculated for two cases, one is where the mass is on the edge of Segment 1 and the other is where it is on Segment 2. Roving body had a mass of 5% of the plate mass. For the rotary inertia a radius of gyration of 0.1a was used.

A convergence study was carried out for a completely free square plate with a crack that located at a_1 = 0.4a. Table 1 shows frequency parameters against the order of polynomial in Eq. (2). It shows that the results for first three bending modes are converged in four significant figures by the order of polynomial of 10 × 10.

Figure 2 shows the variation of a non-dimensional first frequency parameter $\Omega = \omega a^2(\rho h/D)^{0.5}$ for a completely free square plate against the location (x_m/a) of a roving body with (continuous line) and without (dotted line) rotary inertia, for y_m = 0.3b. With the roving mass having rotary inertia, it can be seen that there is a sudden change in the frequency parameter when the roving mass passes the crack.

Table 1. Convergence of frequency parameters for a completely free square plate with a crack (a_1 = 0.4a)

Mode	Order of polynomial (i × j)					
	5x5	6x6	7x7	8x8	9x9	10x10
1	12.23	12.23	12.23	12.23	12.23	12.23
2	13.50	13.44	13.44	13.43	13.43	13.43
3	21.71	21.71	21.70	21.70	21.70	21.70

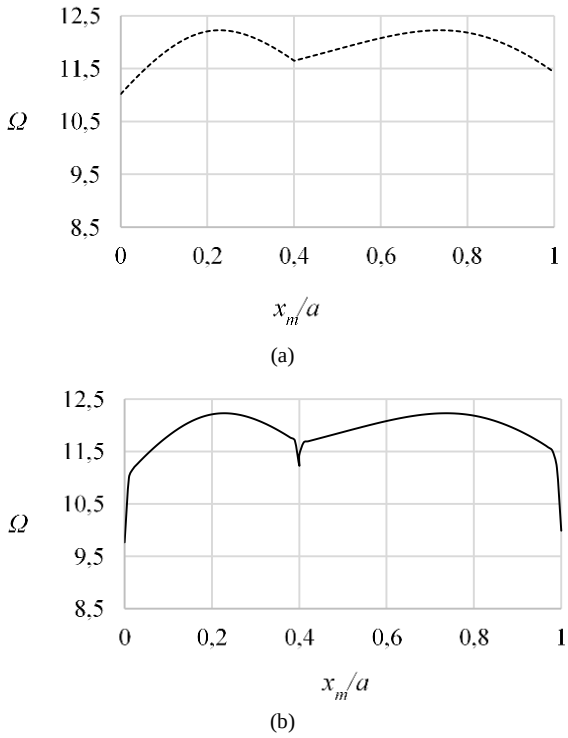

Figure 2. The frequency parameter against the location of the roving mass for a completely free square plate (a) without rotary inertia, (b) with rotary inertia.

Figures 3 and 4 show the first frequency parameter computed including the rotary inertia for simply supported and clamped square plates respectively. Those results were obtained using the penalty method with Eq. (9). It can also be seen that there is a sudden change in the frequency parameter when the roving mass passes the crack.

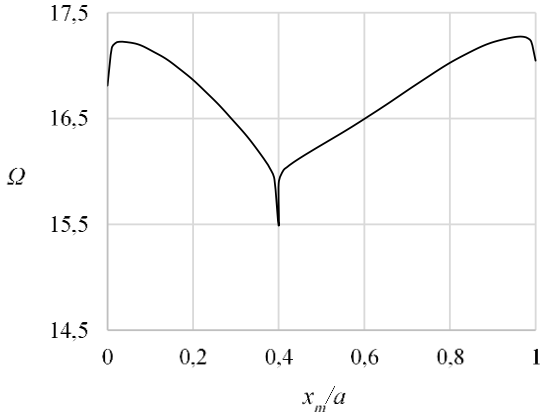

Figure 3. The frequency parameter against the location of the roving mass for a simply supported square plate.

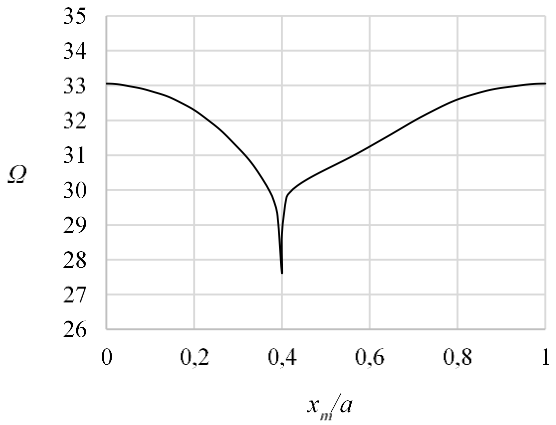

Figure 4. The frequency parameter against the location of the roving mass for a clamped square plate.

For the case of the clamped plate (Fig. 4), there is no effect of the roving mass when it is on the plate edges, (i.e. x_m/a = 0 and 1) since there is no translation and rotation on the clamped edge. However, this is not the case for completely free and simply supported plates. The effect of the roving mass when it is on the edges of these plates are observed in Figs. 2 and 3.

Figure 5 shows the first frequency parameter for a cantilever plate where the crack is perpendicular to the clamped edge. An abrupt change in the frequency is observed however, the change is smaller than those of the simply supported and clamped plates.

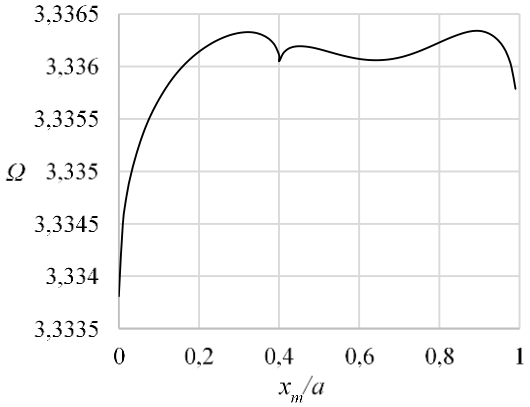

Figure 5. The frequency parameter against the location of the roving mass for a cantilever square plate.

4. Conclusions

The natural frequencies of a thin square plate under various boundary conditions with a crack parallel to an edge were computed using the Rayleigh-Ritz Method. The computed frequencies exhibit a sudden shift as a roving body crosses a crack. If the crack is only partial and continuity of translation is maintained, then the frequency shift occurs only when the body possesses a rotary inertia, as has been observed in beams. If the crack is a complete one (through thickness) which permits differential translation to occur on either side of the crack, a particle having mass only (translatory inertia) is sufficient to cause a sudden shift. There is no need for a rotary inertia. Future work would be to study the effect of cracks that are not parallel to an edge, and non-straight cracks. The body used in this study was assumed to possess mass and rotary inertia at a point. The effect of a body of small but finite dimensions also would be investigated.

References

[1] M. M. Alamdari, T. Rakotoarivelo, and N. L. D. Khoa, A spectral-based clustering for structural health monitoring of the Sydney Harbour Bridge, Mechanical Systems and Signal Processing, 2017;87;384-400.

[2] J.-C. Golinval, Damage Detection in Structures Based on Principal Component Analysis of Forced Harmonic Responses, Procedia Engineering, 2017.

[3] M. Silva, A. Santos, E. Figueiredo, R. Santos, C. Sales, and J. C. Costa, A novel unsupervised approach based on a genetic algorithm for structural damage detection in bridges, Engineering Applications of Artificial Intelligence, 2016;52;168-180.

[4] Z. Tan, D. Thambiratnam, T. Chan, and H. A. Razak, Detecting damage in steel beams using modal strain energy based damage index and Artificial Neural Network, Engineering Failure Analysis, 2017;57;253-262.

[5] Y. Yang and S. Nagarajaiah, Blind identification of damage in time-varying systems using independent component analysis with wavelet transform, mechanical systems and signal processing, 2014;47;3-20, 20.

[6] A. C. Altunışık, F. Y. Okur, and V. Kahya, Modal parameter identification and vibration based damage detection of a multiple cracked cantilever beam, Engineering Failure Analysis, 2017:79;154-170.

[7] M. Reda Taha, A. Noureldin, J. Lucero, and T. Baca, Wavelet transform for structural health monitoring: a compendium of uses and features, Structural Health Monitoring, 2006;5;267-295.

[8] H. Hao and Y. Xia, Vibration-based damage detection of structures by genetic algorithm, Journal of computing in civil engineering, 2002;16;222-229.

[9] M. Stache, M. Guettler, and S. Marburg, A precise non-destructive damage identification technique of long and slender structures based on modal data, Journal of Sound and Vibration, 2016;365;89-101.

[10] M. S. Hossain, Z. C. Ong, Z. Ismail, S. Noroozi, and S. Y. Khoo, Artificial neural networks for vibration based inverse parametric identifications: A review, Applied Soft Computing, 2017;52;203-219.

[11] D. A. Tibaduiza, L. E. Mujica, J. Rodellar, and A. Güemes, Structural damage detection using principal component analysis and damage indices, Journal of Intelligent Material Systems and Structures, 2016;27;233-248.

[12] S. Caddemi and I. Caliò, Exact closed-form solution for the vibration modes of the Euler–Bernoulli beam with multiple open cracks, Journal of Sound and Vibration, 2009;327;473-489.

[13] N. Khiem and L. Toan, A novel method for crack detection in beam-like structures by measurements of natural frequencies, Journal of Sound and Vibration, 2014;333;4084-4103.

[14] C. Bilello, L. A. Bergman, and D. Kuchma, Experimental investigation of a small-scale bridge model under a moving mass, Journal of Structural Engineering, 2004;130;799-804.

[15] Cannizzaro, F, De Los Rios, J, Caddemi, S. Caliò, I, Ilanko, S. On the use of a roving body with rotary inertia to locate cracks in beams, Journal of Sound and vibration 2018;425:275-30.

[16] Shashank Soni, N. K. Jain, and P. V. Joshi, "Vibration analysis of partially cracked plate submerged in fluid", J. of Sound and Vibration, Volume 412, pp 28-57, 2018.

[17] C. S. Huang, and Y. J. Lin, "Fourier series solutions for vibrations of a rectangular plate with a straight through crack", Applied Mathematical Modelling, 2016;40;10389-10403

[18] P. V. Joshi, N. K. Jain, and G. D. Ramtekkar, Analytical modeling for vibration analysis of thin rectangular orthotropic/functionally graded plates with an internal crack, Journal of Sound and Vibration, 2015; 344; 377-398.

[19] Tanmoy Bose, and A. R. Mohanty, Vibration analysis of a rectangular thin isotropic plate with a part-through surface crack of arbitrary orientation and position, Journal of Sound and Vibration, 2013;332;7123-7141.
[20] C. Huang and A. Leissa, "Vibration analysis of rectangular plates with side cracks via the Ritz method," Journal of Sound and Vibration, 2009;323;974-988.
[21] Yan Wang, and Zhong-min Wang, Transverse vibration of viscoelastic rectangular plate with linearly varying thickness and multiple cracks, Journal of Sound and Vibration, 2008;318;1005-1023.
[22] Guan-Yuan Wu, and Yan-Shin Shih, Dynamic instability of rectangular plate with an edge crack, Computers & Structures, 2005:84:1-10.
[23] L. Monterrubio, The use of eigenpenalty parameters in structural stability analysis. Proc Inst Mech Eng C: J Mech Eng Sci 2012;226:861–70.
[24] L. E. Monterrubio, S. Ilanko, Proof of convergence for a set of admissible functions for the Rayleigh–Ritz analysis of beams and plates and shells of rectangular planform. Computers & Structures, 2014;147:236-243
[25] S. Ilanko, L. E. Monterrubio, The Rayleigh-Ritz Method for Structural Analysis. London: ISTE Ltd; 2014.

.

EPI International Journal of Engineering
Volume 1, Number 2, August 2018, pp. 35-39
DOI: 10.25042/epi-ije.082018.05

*p*ISSN 2615-5109
*e*ISSN 2621-0541

Effect of Moment of Inertia of Attached Mass on Natural Frequencies of Cantilevered Symmetrically Laminated Plates

Kenji Hosokawa[a,*]

[a]Department of Mechanical Engineering, Chubu University. Email: hosokawa@isc.chubu.ac.jp

Abstract

Since composite materials such as laminated composite plates have high specific strength and high structural efficiency, they have been used in many structural applications. It is therefore very important to make clear the vibration characteristics of the laminated plates for the design and the structural analysis. Especially, the vibration characteristics of the laminated plates with attached mass are essential. However, we cannot find the theoretical or experimental approaches for the free vibration of laminated plates with attached mass. In the present study, the experimental and numerical approaches are applied to the free vibration of cantilevered symmetrically laminated plates with attached mass. First, by applying the experimental modal analysis technique to the cantilevered symmetrically laminated plates with attached mass, the natural frequencies and mode shapes of the plates are obtained. Next, the natural frequencies and mode shapes of the cantilevered symmetrically laminated plates with attached mass are calculated by Finite Element Method (FEM). Finally, from the experimental and numerical results, the effect of the moment of inertia of the attached mass to the natural frequencies and mode shapes of the cantilevered symmetrically laminated plates are clarified.

Keywords: Composite material; experimental modal analysis; FEM; free vibration; vibration of continuous system

1. Introduction

Since aerospace structures require the high specific strength and high specific modulus, many composite materials such as carbon fiber reinforced plastics (CFRP) have been used. Also, in many engineering applications, the substructures may be added to the laminated composite plates. For example, the problem of plates with attached masses relates to the design of electronic systems. These attachments affect the vibration characteristics of the laminated composite plates.

Many studies on the free vibrations of a thin isotropic plate with attached mass have been reported in the literature [1-6]. However, studies on the free vibrations of laminated plate with attached mass are limited. Using the Hamilton's principle by means of a double Fourier series, the free vibration of a simply supported laminated composite plate with distributed patch mass is solved by Alibeigloo *et al*. [7]. Malekzadeh *et al*. analyzed the free vibration of the rectangular composite plate with distributed attached mass by using the standard Galerkin procedure [8]. As mentioned above, one can find a few published researches on a numerical analysis of the free vibration of the laminated composite plate with attached mass. However, only few reports can be found on an experimental analysis of the free vibration of the laminated composite plate with attached mass.

In the present study, the experimental and numerical approaches are applied to the cantilevered symmetrically laminated plates with attached mass. First, by applying the experimental modal analysis technique to the cantilevered symmetrically laminated plates with attached mass, the natural frequencies and mode shapes of the plates are obtained. Next, the natural frequencies and mode shapes of the cantilevered symmetrically laminated plates with attached mass are calculated by Finite Element Method (FEM). Finally, from the experimental and numerical results, the effect of the moment of inertia of attached mass to the natural frequencies and mode shapes of the cantilevered symmetrically laminated plates are studied

2. CFRP Laminated Plates

The symmetrically laminated square and trapezoidal plates were used. Each layer material, that is lamina, is reinforced by carbon fibers. This fiber's tensile elastic modulus is 230GPa. The matrix is an epoxy resin ($130°$C cure). The fiber volume fraction is 55%. The laminae of the

*Corresponding author. Tel.: +81-568-51-9345
1200 Matsumoto-cho
Kasugai, Aichi, Japan, 487-8501

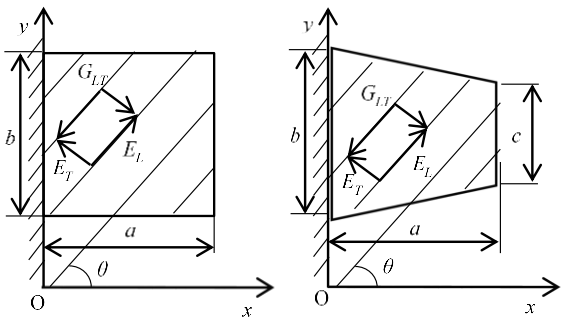

(a) Square plate (b) Trapezoidal plate

Figure 1. Lamina of cantilevered plate

Table 1. Material properties of lamina

E_L (GPa)	E_T (GPa)	G_{LT} (GPa)	ν_{LT}
97.6	6.26	5.18	0.33

square and trapezoidal plates are made of the same layer material and the both plates were made under the same curing condition. As shown in Fig. 1, the plate configuration of the square plate is as follows: a = 0.2 m, b=0.2 m. The stacking sequence of the square plate is $[-\theta/+\theta/+\theta/-\theta]$, fiber orientation angle $\theta = 60°$ and the plate thickness h is 1.6×10^{-3} m. And, the plate configuration of trapezoidal plate is as follows: a = 0.2 m, b = 0.2 m, c=0.1m. The stacking sequence of the trapezoidal plate is $[-\theta/+\theta/+\theta/-\theta]$, fiber orientation angle $\theta = 30°$ and the plate thickness h is 1.6×10^{-3} m. The density of the both laminated plates is 1535 kg/m^3. The measured material properties of the lamina are listed in Table 1. Table 1 shows the moduli of elasticity E_L, E_T in the direction of the parallel and normal to the fiber, respectively, shear modulus G_{LT}, and Poisson's ratios ν_{LT} of each layer (See Fig. 1).

3. Attached Mass

In this study, three different shapes of attached mass were used. The shape of the attached mass is shown in Fig. 2. The dimensions of masses are presented by Table 2. The bottom part is the hexagon nut (M5; JIS). The mass of these attached masses is the same by 21g. Also, the moment of inertia of these masses are shown in Table 3. The attached mass was bonded to the plate by epoxy based adhesive.

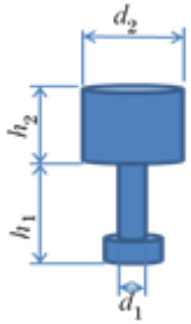

Figure 2. Shape of attached mass

Table 2. Dimensions of attached masses

Attached mass	d_1 (mm)	h_1 (mm)	h_2 (mm)	d_2 (mm)
K	4	8	15	14.42
L	4	12	15	14.27
M	4	12	15	14.12

Table 3. Moment inertia of attached masses

Attached mass	Moment of inertia (kgm^2)
K	5.24×10^{-6}
L	7.81×10^{-6}
M	1.09×10^{-5}

4. Experimental and Numerical Approaches

Experimental and numerical studies were carried out for the cantilevered symmetrically laminated square and trapezoidal plates with the attached mass. In the numerical studies, Finite Element Method was used. And, LS-DYNA was applied to this free vibration problem.

4.1. Experimental modal Analysis

To satisfy the boundary conditions, the plates were clamped by using a rigid clamping fixture as shown in Fig. 3. As shown in Fig. 3, to measure the transfer function (accelerance), an accelerometer was attached to one reference point and then all reference points were impacted by an impulse force hammer. The mass of the accelerometer is 2.12g. Also, as shown in Figure 4, except for the clamped edge, the reference point on the square plate is 42 and the reference point on the trapezoidal plate is 36. In Figure 4, the notation ⭘ represents the location of attached mass, and × represents the location of the attached accelerometer. From the obtained transfer function, the natural frequencies and mode shapes of the plates were estimated by applying the experimental modal analysis technique.

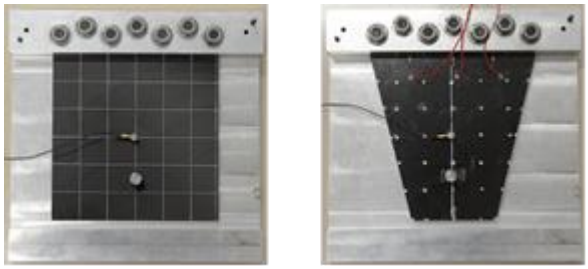

(a) square plate (b) trapezoidal plate

Figure 3. Clamping fixture of cantilevered plate

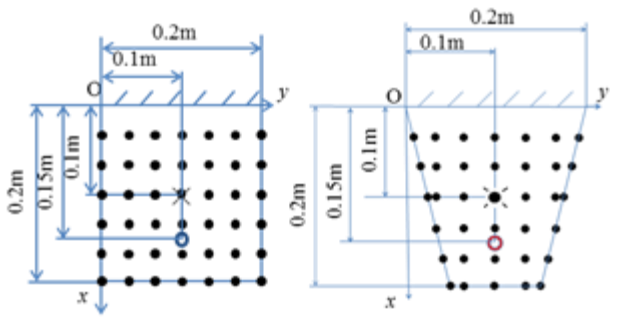

(a) square plate (b) trapezoidal plate

Figure 4. Reference points of laminated plate

Table 4. Material properties of lamina

E_V (GPa)	E_{TV} (GPa)	G_{VL} (GPa)	ν_{TV}	ν_{VL}
6.26	2.41	5.18	0.33	0.02

4.2. Finite Element Method (FEM)

The computations were carried out using the FEM eigenvalue program with solid elements. Each layer is divided into 3600 elements. Therefore, each plate is divided into 14400 elements. In the numerical calculations, the mass of the accelerometer was considered. Also, the material properties shown in Table 1 were used. Furthermore, to apply the FEM (LS-DYNA), the material properties in the plate thickness direction (V axis) are need. Therefore, the other parameters shown in Table 4 were estimated in reference to literature [9].

4.3. Comparison of experimental and numerical results

Figure 5 shows the natural frequencies and mode shapes of the cantilevered laminated square plate without attached mass. And, Figure 6 shows the natural frequencies and mode shapes of the cantilevered laminated trapezoidal plate without attached mass. In these figures, the upper edge of the plate is a clamped edge, the notation × represents the location of the attached accelerometer. From these figures, one can see that the difference between experimental and numerical natural frequencies is about 3.6% at the most. Also, it follows that one can find good agreement between experimental and numerical mode shapes.

Modal order	1st	2nd	3rd	4th	5th	6th
Numerical mode shape	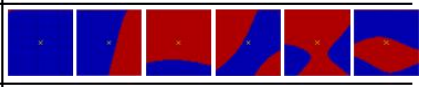					
Numerical natural frequency (Hz)	17.72	69.95	109.0	206.7	272.7	348.5
Experimental mode shape	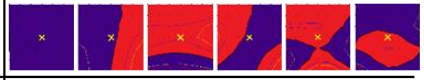					
Experimental natural frequency (Hz)	17.15	71.53	105.4	213.5	272.8	351.8
Error(%)	3.3	-2.2	3.4	-3.2	-0.04	-0.94

Figure 5. Experimental and analytical results of FRP laminated square plate without attached mass

Modal order	1st	2nd	3rd	4th	5th	6th
Numerical mode shape	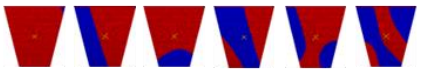					
Numerical natural frequency (Hz)	43.35	134.6	241.5	337.2	423.0	589.6
Experimental mode shape						
Experimental natural frequency (Hz)	43.42	136.5	241.3	347.9	427.8	611.7
Error(%)	-0.16	-1.4	0.08	-3.1	-1.1	-3.6

Figure 6. Experimental and analytical results of FRP laminated trapezoidal plate without attached mass

5. Effect of Moment of Inertia of Attached Mass

Figures 7 to Figure 9 show the natural frequencies and mode shapes of the laminated square plate with attached mass. Also, Figure 10 to Figure 12 show the natural frequencies and mode shapes of the laminated trapezoidal plate with attached mass. In these figures, the upper edge of the plate is a clamped edge, the notation ● represents the location of attached mass, and × represents the location of the attached accelerometer. From the numerical and experimental results, the similar results were obtained. The natural frequency of the plates with attached mass is smaller than that of the plates without attached mass. With the increase of the moment of inertia of the attached mass, the natural frequency of the plate is decreasing. Also, the lower mode shapes do not change with the increase of the moment of inertia of the attached mass.

Modal order	1st	2nd	3rd	4th	5th	6th
Numerical mode shape	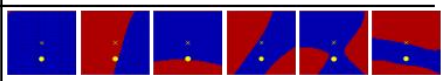					
Numerical natural frequency (Hz)	15.03	68.55	104.7	190.8	268.4	299.7
Experimental mode shape	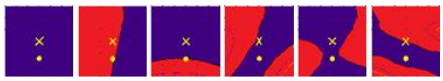					
Experimental natural frequency (Hz)	14.85	71.30	102.1	198.2	264.0	299.3
Error(%)	1.2	-3.9	2.5	-3.7	1.7	0.13

Figure 7. Experimental and analytical results of FRP laminated square plate with attached mass (K)

Modal order	1st	2nd	3rd	4th	5th	6th
Numerical mode shape	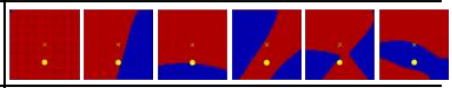					
Numerical natural frequency (Hz)	15.00	68.00	102.5	190.8	265.1	293.4
Experimental mode shape	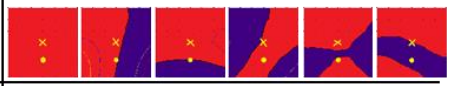					
Experimental natural frequency (Hz)	14.83	70.19	99.89	198.0	262.4	293.9
Error(%)	1.1	-3.1	2.6	-3.6	1.0	-0.17

Figure 8. Experimental and analytical results of FRP laminated square plate with attached mass (L)

Modal order	1st	2nd	3rd	4th	5th	6th
Numerical mode shape	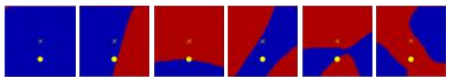					
Numerical natural frequency (Hz)	14.98	67.37	100.1	190.8	257.1	285.0
Experimental mode shape	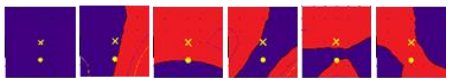					
Experimental natural frequency (Hz)	14.70	69.35	97.12	197.9	243.3	284.1
Error(%)	1.9	-2.9	3.1	-3.6	5.7	0.32

Figure 9. Experimental and analytical results of FRP laminated square plate with attached mass (M)

Modal order	1st	2nd	3rd	4th	5th	6th
Numerical mode shape						
Numerical natural frequency (Hz)	33.87	125.0	226.6	296.6	382.3	454.9
Experimental mode shape	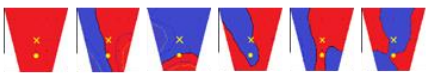					
Experimental natural frequency (Hz)	34.11	126.8	224.9	305.4	392.0	450.5
Error(%)	-0.70	-1.4	0.76	-2.9	-2.5	1.0

Figure 10. Experimental and analytical results of FRP laminated trapezoidal plate with attached mass (K)

Modal order	1st	2nd	3rd	4th	5th	6th
Numerical mode shape	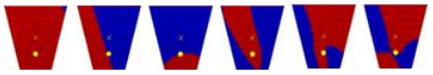					
Numerical natural frequency (Hz)	34.19	119.8	221.9	292.4	347.1	436.1
Experimental mode shape	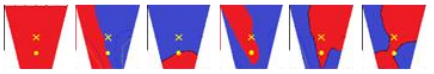					
Experimental natural frequency (Hz)	33.91	121.6	216.4	297.9	343.8	424.0
Error(%)	0.83	-1.5	2.5	-1.8	1.0	2.9

Figure 11. Experimental and analytical results of FRP laminated trapezoidal plate with attached mass (L)

Modal order	1st	2nd	3rd	4th	5th	6th
Numerical mode shape	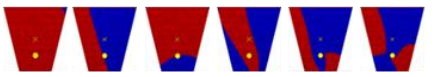					
Numerical natural frequency (Hz)	33.55	114.5	209.5	288.7	316.0	420.6
Experimental mode shape	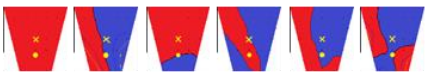					
Experimental natural frequency (Hz)	33.82	116.9	207.4	290.8	319.7	408.4
Error(%)	-0.80	-2.1	1.0	-0.72	-1.2	3.0

Figure 12. Experimental and analytical results of FRP laminated trapezoidal plate with attached mass (M)

6. Conclusions

The experimental and numerical approaches were applied to the free vibration of cantilevered symmetrically laminated plates with and without the attached mass. First, by applying the experimental modal analysis technique to the cantilevered symmetrically laminated plates with and without the attached mass, the natural frequencies and mode shapes of the plates were obtained. Next, the natural frequencies and mode shapes of the cantilevered symmetrically laminated plates with and without the attached mass were calculated by Finite Element Method (FEM).

From the all experimental and numerical results, one can see that the difference between experimental and numerical natural frequencies is about 5.7% at the most. Also, it follows that one can find good agreement between all experimental and numerical mode shapes. Accordingly, one can see good agreement between experimental and numerical results.

From the experimental and numerical results, it follows that: (1) the natural frequency of the plates with attached mass is smaller than that of the plates without attached mass, (2) the fundamental natural frequency of the plates is hardly influenced by the difference in the moment of inertia of the attached mass, (3) with the increase of the moment of inertia of the attached mass, the natural frequency of the plate is decreasing, (4) the higher mode shapes of the plates change with the increase of the moment of inertia of the attached mass. Therefore, not considering the shape of attached mass and considering the attached mass as the concentrated load, it is a problem to analyze the free vibration of the laminated plate with attached mass.

Acknowledgements

The author would like to convey a great appreciation to Mr. Nakagawa and Mr. Nakamura for assisting this research.

References

[1] R. E. Rossi and P. A. A. Laura, Symmetric and Antisymmetric Normal Modes of a Cantilever Rectangular Plate: Effect of Poisson's Ratio and a Concentrated Mass, Journal of Sound and Vibration, Volume 195(1), 1996, p. 142-148.

[2] K. H. Low, G. B. Chai, T. M. Lim, and S. C. Sue, Comparison of experimental and theoretical frequencies foe rectangular plates with various boundary conditions and added masses, International Journal of Mechanical Sciences Volume 40(11), 1998, pp.1119-1131.

[3] O. Kompaz and S. Telli, Free Vibration of a Rectangular Plate Carrying Distributed Mass, Journal of Sound Vibration, Volume 251(1), 2002, pp.39-57.

[4] W. O. Wong, The Effect of Distributed Mass Loading on PlateVibration Behavior, Journal of Sound and Vibration, Volume 252(3), 2002, pp.577-583.

[5] M. Amabili, M. Pellegrini, F. Righi, and F. Vinci, Effect of concentrated masses with rotary inertia on vibrations of rectangular plate, Journal of Sound and Vibration, Volume 295(1), 2006, pp.1-12.

[6] S. D. Yu, Free and forced flexural vibration analysis of cantilever plates with attached point mass, Journal of Sound and Vibration, Volume 321(1-2), 2009, pp.270-285.

[7] A. Alibeigloo, M. Shakeri and M. R. Kari, Free Vibration Analysis of Antisymmetric Laminated Rectangular Plates with Distributed Patch Mass Using Third-order Shear Deformation Theory, Ocean Engineering, Volume 35(2), 2007, pp.183-190.

[8] K. Malekzadeh, S. Tafazoli, and S.M.R. Khalili, Free Vibrations of Thick Rectangular Composite Plate with Uniformly Distributed Attached Mass Including Stiffness Effect, Journal of Composite Materials, Volume 44(24), 2010, pp.2897-2918.

[9] Y. Narita, Y. Ohta, and S. Morika, The Three Dimensional Vibration Analysis of Symmetrically Laminated, Cross-ply Thick Rectangular Plates, Proceedings of Japan-U.S. CCM-VII, Kyoto, 1995, pp.617-623.

EPI International Journal of Engineering
Volume 1, Number 2, August 2018, pp. 40-46
DOI: 10.25042/epi-ije.082018.06

*p*ISSN 2615-5109
*e*ISSN 2621-0541

Experimental Study on Thermal Performance of Loop Heat Pipe with Flat-Rectangular Evaporator Under Gravity Assisted Condition

Phuoc Hien Huynh[a,*], Kyaw Zin Htoo[b], Keishi Kariya[c], Akio Miyara[d,e]

[a]Graduate school of Science and Engineering, Saga University. Email: hphien@hcmut.edu.vn
[b]Graduate school of Science and Engineering, Saga University. Email: kyawzinhtoo@gmail.com
[c]Department of Mechanical Engineering, Saga University. Email: kariya@me.saga-u.ac.jp
[d]Department of Mechanical Engineering, Saga University. Email: miyara@me.saga-u.ac.jp
[e]International Institute for Carbon-Neutral Energy Research, Kyushu University

Abstract

In company with extreme developments of electronic devices, there are some unavoidable challenges to the conventional cooling methods such as high heat dissipation, limitation of cooling space, reliable operation as well as saving energy consumption. Therefore, the necessity of studying on new or how to improve the existing technologies is undoubted. Among various methodologies, the loop heat pipe (LHP) whose operation principle base on phase changing process, can be considered as one of the potential solutions of modern electronics cooling. This paper introduces the experimental investigation on the thermal performance of a flat-rectangular evaporator LHP with sintered stainless-steel wick when functioning under gravity assisted condition. Working fluid of this LHP was water. The present LHP could maintain stable operation in the range of heating power from 50 W to 520 W and keep the temperature on the heater's top surface at 85^{o}C, commonly recommended as the limitation temperature of electronics, when heating power reaches value 350 W (129.6 kW/m^2). Besides, when turning the heater off, it took about 15 minutes for the LHP to cool the heating block from 102^{o}C to 37^{o}C. In addition, an assumption of the boiling heat transfer is introduced in this paper to explain the performance of evaporator at different heat flux conditions of the experiment.

Keywords: Boiling heat transfer; electronics cooling; gravity assisted condition; loop heat pipe; phase change

1. Introduction

In recent decades, the rapid developments in telecommunication and information technology led to the dramatic changes in the data center industry. One of the most changes is the gain of generated heat power and heat flux because of the increment of the components installed on one chip. While in the 1960s, there were about one thousand elements functioning on one chip, it is predicted that this number can reach 20 billion for the 1-cm^2 size chip 2020 [1]. It limits the utilization the present cooling methods such as air cooling or 1-phase cooling because of low cooling capacity. In addition, the existent of various new social networks, cloud computing technologies, the number of data centers increases years after years. For examples, it was recorded that in the United States, the number of data centers increased from 432 to 2094 units during the period 1998-2010 [2]. As a result, there is the increased demand for electricity energy to operate these systems. Also mentioned in [2], in 2010 electrical energy consumed by data centers took 1.3% of total global using, and annual increment was predicted as high as 15 to 20%. However, around 33% of them was used by the mechanical equipment functioning inside the thermal management systems or become useless energy [3]. In consequence, requirements of an effective modern cooling methodology are not only keeping the electronics operating stably under the safety temperature but also making them friendly with the environment by reduced electricity energy consumption.

From the above points, loop heat pipe (LHP), a novel catalog of the heat pipe, can be one of the potential candidates. In comparison with a normal heat pipe, LHP can transfer heat with the lower thermal resistance through the further distance because the liquid and vapor lines are separated together and there is no wick or capillary structure requested on the whole length of the liquid line, so reducing the total pressure drop along the loop [4]. The working fluid

*Corresponding author. Tel.: +81-80-6439-8809
Saga, Japan, 840-0027

is circulated between evaporator and condenser by capillary forced or gravity force, so there is no work input to operate the pump or compressor as in the case of other two-phase cooling methods. It means that the both of electricity consumption and operating cost can be reduced while the lifespan and reliable operation become higher due to the reduction of mechanical components. When applied in the fields such as cooling the processors of the high-performance computers or data centers on earth, it is possible to arrange the position of the condenser to be higher than evaporator; as the result, heat transfer capacity of LHP can be increased significantly more than in the case of horizontal or anti-gravity operating condition.

Therefore, studying on the LHP operating under gravity assisted condition or loop thermosyphon has taken attention from different research groups. Ji Li et al. [5] conducted an experiment to investigate the startup and stable operation of LHP with a square-flat evaporator and grooved-sintered copper wick. From the measuring and observation results, they proposed two modes, boiling trigger mode and evaporation trigger mode to explain the different startup behavior of LHP for different heat loads. To more understand the effect of inventory on LHP performance, the research group of J. Xu et al. [6] made the flat cooper LHP with evaporator's cover made from polycarbonate. They made the conclusion that large inventory can prevent heat leak through the wick body but cause high-frequency temperature oscillation during startup as well as during operation period. One of the most recent studies was conducted by G. Zhou et al that focused on the two-phase flow characteristics of LHP with flat evaporator [7]. Their observation and measuring results show that boiling incipience depends slightly on the heat loads and nucleate boiling as well as thin film evaporation are the two-main heat transfer mechanisms inside their evaporator. Moreover, there are other studies on the wickless LHP or loop thermosyphon. Most of these studies try to modify the evaporator or change the working fluid to improve cooling capacity. A. Suzuki et al [8] introduced a LHP that applies the JEST (Jet Explosion Stream Technology) technology to enhance the heat transfer in the evaporator. In the studies conducted by C. Kondou et al [9] and H. He et al. [10], the heat transfer in the evaporator can be enhanced if the wettability characteristics of the boiling surface is modified appropriately. Indicated in [9], the super-hydrophilic surface could enhance the evaporator heat transfer when working fluid is volatile fluids such as R134a, R1234ze(Z), R1234ze(E). However, in the cases that working fluid is water, a mixed-wettability surface is suggested to eliminate the negative effect due to the boiling of water under sub-atmosphere pressure [10].

Although there are numerous studies on loop thermosyphon or LHP operating with the favorable gravitational condition, it still requires more research to simplify the structure of LHP, particularly evaporator to make the LHP become the commercialization state as normal heat pipe. In this study, a copper LHP with sintered stainless-steel wick was manufactured and investigated its thermal performance during startup, stable operational period as well as cooling performance under zero – heating power when functioning under gravity assisted condition. The different design of the present evaporator is the crossing groove or fin array was machined on the inner surface of the evaporator as shown in Fig. 1. This design can avoid machining the grooves on the wick surface that can damage or change the surface characteristics of the wick. Besides, it also guarantees the sufficient space for evaporation as well as paths for vapor flow out easily, so prevent vapor forming inside the wick. The evaporator cover is made of polycarbonate to observe the state of compensation chamber; therefore, water is selected as working fluid because of low operational pressure. Our experimental result indicate that this simple design of evaporator can satisfy the heat power generated from the future electronic device. Moreover, in this study, we assumed a theory of boiling heat transfer to explain the various performance of the evaporator with different heat flux values.

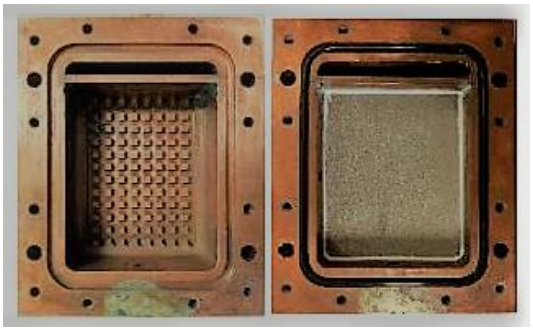

Figure 1. The evaporator without and with the stainless-steel wick

2. Experimental Setup and Data Reduction

2.1. Experimental setup

The schematic diagram of the experiment is described in Fig. 2. The evaporator was heated by four cartridge heaters that were inserted to the copper heating block. The magnitude of heating power was adjusted by the YAMABISHI MVS-520 Volt-slider and monitored on the YOKOGAWA WT230 digital power meter. On the other hand, the condenser was cooled by water whose inlet temperature and mass flow rate were set at 27.5 °C and 27 kg/h respectively by the ADVANTEC LV–400 constant temperature circulator device. However, for determining the accurate value of heat flow rate from heating block to evaporator, the temperatures on the top surface of heating block as well as the bottom surface of evaporator, three 0.5 mm-diameter thermocouples T_1, T_2, T_3 were attached into the heating block and another 1 mm-diameter T_4 was inserted into evaporator base body as shown in Fig. 3. Between the heating block and evaporator there was a thin layer of thermal conductivity grease that eliminates the thermal contact resistance. In addition, for understanding the state of circulation inside the LHP, four thermocouples including T_{eo}, T_{ci}, T_{co} and T_{cci} were inserted directly to path of the LHP at different locations such as outlet of evaporator, inlet of condenser, outlet of condenser, and inlet of

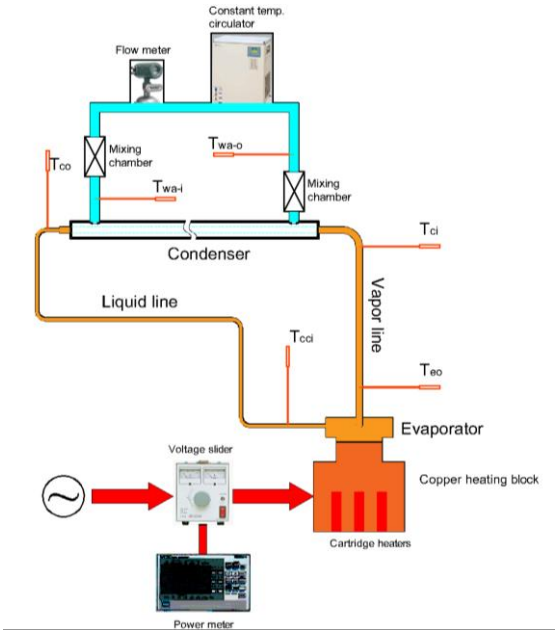

Figure 2. Schematic diagram of experiment

Table 1. Main parameters of LHP

Heating block	
Material	Copper
Mass, kg	4.36
Evaporator body	
Material	Copper
Length, mm	80
Width, mm	70
Height, mm	24.5
Active area, mm^2	60 x 45
Fin geometry	
Cross area, mm^2	2 x 2
Height, mm	1.5
Fin pitch, mm	4
Wick structure [11]	
Material	Stainless steel
Opening, μm	63
Void ratio, %	36 – 48
Bulk volume, mm^3	50 x 41 x 5
Vapor line	
OD/ID, mm	6.35/4.35
Length, mm	800
Condenser line	
OD/ID, mm	6.35/4.35
Length, mm	600
Liquid line	
OD/ID, mm	3.2/1.7
Length, mm	1300
Working fluid	Water

Table 2. Uncertainty values

	Uncertainty
T_1, T_2, T_3	±0.06ºC
T_4	±0.07ºC
T_{eo},	±0.06ºC
T_{ci},	±0.06ºC
T_{co}, T_{cci}	±0.1ºC
$T_{wa\text{-}i}$,	±0.1ºC
$T_{wa\text{-}o}$	±0.06ºC
T_a	±0.16ºC
Mass flow meter	0.18% of reading

compensation chamber respectively. In addition, heat released from condenser could be estimated by mass flow rate and different temperature of cooling water between inlet and outlet by MASSMAX MMM7150K flowmeters and two thermocouples $T_{wa\text{-}i}$ and $T_{wa\text{-}o}$. Table 1 lists the main specifications of the LHP, and the uncertainty of measurement devices are shown in Table 2.

2.2. Data reduction

Heat flux q and heat flow rate Q flowing from the heating block to the evaporator

$$q = k\frac{T_1 - T_2}{\delta_1} = k\frac{T_2 - T_3}{\delta_1} = k\frac{T_1 - T_3}{2\delta_1} \quad (1)$$

$$Q = qA \quad (2)$$

Temperature on the top surface of heating block T_{s1} and bottom surface of evaporator T_{s2}

$$T_{s1} = T_1 - 3\frac{q\delta_1}{k} = T_2 - 2\frac{q\delta_1}{k} = T_3 - \frac{q\delta_1}{k} \quad (3)$$

$$T_{s2} = T_4 + \frac{q\delta_2}{k} \quad (4)$$

Total thermal resistance R_t, evaporator thermal resistance R_e, condenser thermal resistance R_c and contact thermal resistance R_{ct}.

$$R_t = \frac{T_{s1} - T_{wa-i}}{qA} \quad (5)$$

$$R_e = \frac{T_{s2} - T_{eo}}{qA} \quad (6)$$

$$R_c = \frac{T_{ci} - T_{wa-i}}{Q_c} \quad (7)$$

With Q_c is heat released at condenser

$$Q_c = m_{wa}c_p(T_{wa-o} - T_{wa-i}) \quad (8)$$

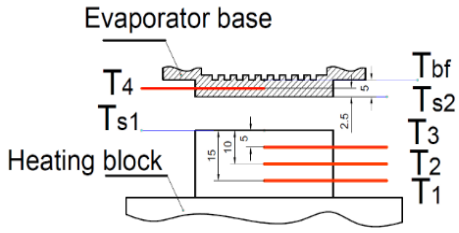

Figure 3. Temperature gradient measurement

$$R_{ct} = \frac{T_{s1} - T_{s2}}{qA} \quad (9)$$

Evaporator heat transfer coefficient h_e

$$h_e = \frac{q}{T_{bf} - T_{eo}} \quad (10)$$

In the Eq. 10, T_{eo} is considered as saturated temperature inside evaporator. As being described in Fig. 3, T_{bf} is the temperature at the base of the fin which can be estimated by the following equation

$$T_{bf} = T_4 - \frac{q\delta_2}{k} \quad (11)$$

3. Results and Discussion

During the experiment, the heating power was adjusted in the range from 50 W to 520 W. The upper limitation is the maximum capacity of the Volt-slider. The performance of the loop heat pipe could be considered as stable characteristic if the temperatures T_1, T_2, T_3, T_4 could maintain stably more than 30 minutes.

3.1. Startup characteristics of the LHP

Figures 4, 5, and 6 demonstrate the change of temperature inside the heater T_1, outlet of evaporator T_{eo}, inlet of condenser T_{ci}, outlet of condenser T_{co} and inlet of compensation chamber T_{cci} during the startup of this LHP under different heating powers such as 50 W, 135 W and 270 W, respectively. The startup period could be divided into two stages. The first stage is the beginning of evaporation or value of T_{eo} starting to increase while the ending of the second stage is indicated by the sudden increase of T_{ci} as well as a slight raise of T_{co} and T_{ci}. It means that the hot vapor from evaporator entered the condenser, condensed into liquid, then returned the compensation chamber or the circulation happened totally. Generally, the time for the LHP to startup reduced from 12 mins to 2.5 mins when heating power increased from 50 W to 270 W. In addition, at the end of startup period, there was the presence of temperature overshoot of T_{eo}. Its magnitude also reduced with the increase of heating power. Moreover, in the cases of 125 W and 270 W, T_{eo} increases suddenly in the second stage of startup while it increased slowly at heating power of 50 W. This phenomenon indicates that under low heating power condition, the grooves and lower part of vapor line of the LHP was flooded with liquid phase that prevented the vapor from flowing out the evaporator to enter the condenser. This is also the reason that caused the temperature overshoot happens. When the heating power increased, the combination of high evaporation rate and reduction of the liquid phase in the vapor line made the duration of second stage and magnitude of temperature overshoot reduce significantly; consequently, the LHP could startup faster.

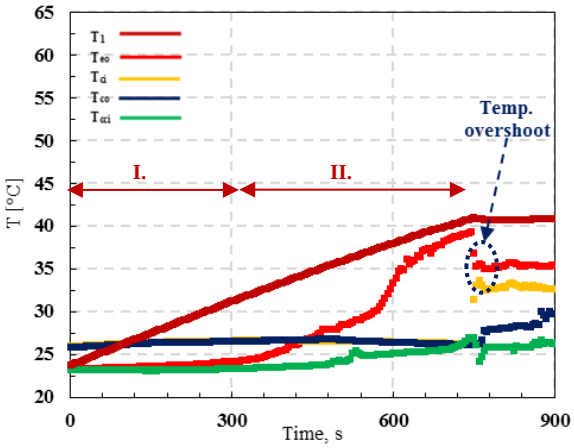

Figure 4. Startup of LHP when heating power was 50W

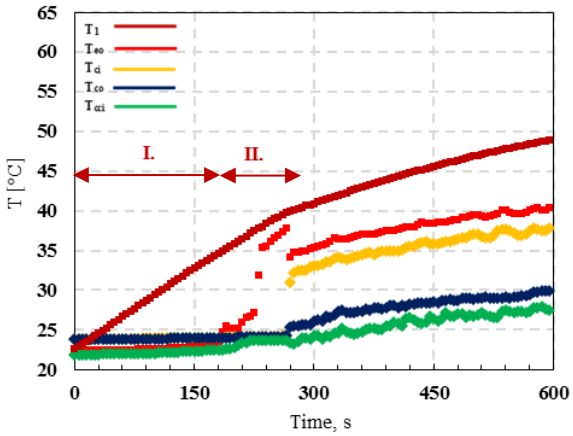

Figure 5. Startup of LHP when heating power was 125 W

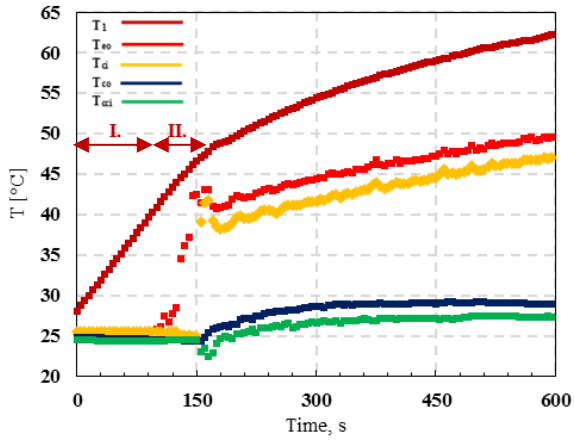

Figure 6. Startup of LHP when heating power was 270 W

3.2. Change of operating temperatures with the heat load

Figure 7 demonstrates the dependence of temperatures on the heating block's top surface T_{s1}, outlet of evaporator T_{eo}, inlet of condenser T_{ci}, outlet of condenser T_{co} and inlet of compensation chamber T_{cci} on the heating power Q. Firstly, during the whole range of Q, the relation of T_{s1}, T_{eo} with heating power is nearly linear. At every certain heat load, T_{eo} and T_{ci} existed almost at the same values while T_{co} and T_{cci} were nearly equal together. This result confirms the stable circulation of working fluid existing inside the loop. The difference between T_{eo} and T_{ci} became smaller with the increase of the heating power. It can be explained because the high heating power made the pressure inside the evaporator increase, so the slope of saturation line (dP/dT) would be higher or the difference in saturation temperature because of pressure drop becomes smaller. In this experiment, T_{s1} can be regarded as the electronics temperature which is commonly recommended to be lower than 85°C for the reliable and effective operating condition [2]. The present LHP could satisfy this condition until the heating power reaches the value 350 W. In addition, the stable increasing of T_{s1} in the range of heating power from 50 W to 520 W indicated that there was no sign of dry-out existing inside the evaporator in this experiment.

3.3. Change of thermal resistances with heating power

Figure 8 shows the relations between total thermal resistance R_t, evaporator thermal resistance R_e, condenser thermal resistance R_c and contact thermal resistance R_{ct} with the heating power.

In general, both of total thermal resistance R_t and evaporator resistance R_e decreased when the heating power increased; however, they reduced significantly when heating power increased from 50 W to 150 W. Under low heating power operational condition, it could be difficult for boiling to happen, so heat leakage through the wick body to the compensation chamber became significant. This kind of heat leakage could prevent the circulation or cause the total thermal resistance became higher. Consequently, the minimum value of R_t and R_c were 0.149 K/W and 0.0036 K/W respectively when heating power had value 520 W. On the other hand, condenser thermal resistance reduced to the minimum value when heating power was around 160 W, then raised up slightly. By observing the state of compensation chamber, this result could be explained based upon the liquid distribution inside the LHP. The higher heating power was supplied to LHP, the less liquid presented inside compensation chamber or there was more liquid phase inside the condenser; as a result, performance of condenser slightly reduces. In this experiment, the thermal contact resistance R_{ct} had the average value 0.07 K/W and changed between 0.005 K/W to 0.01 K/W. The next section explains detailly about the performance of evaporator under various heat flux condition.

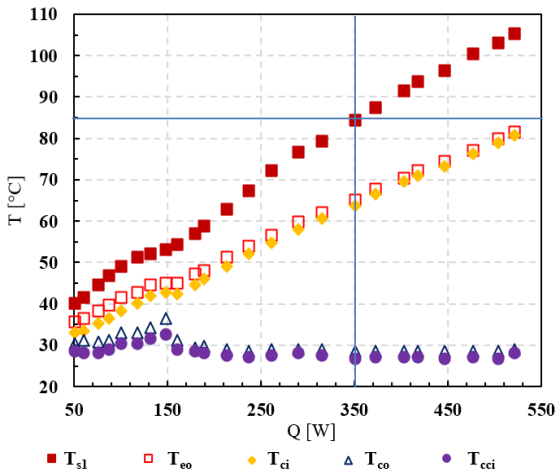

Figure 7. Changing of temperatures at different positions in experiment on heating power

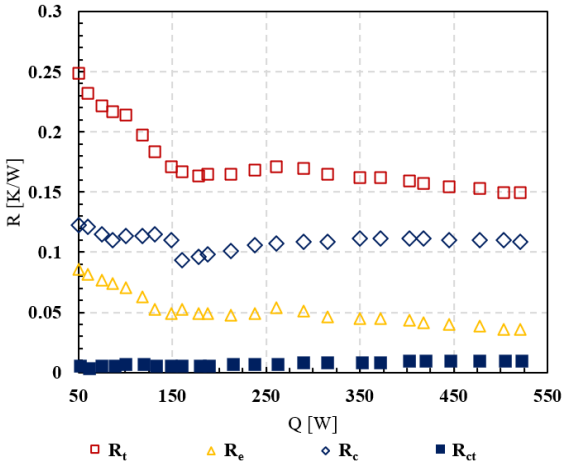

Figure 8. Changing of different thermal resistances on heating power

3.4. Evaporator heat transfer coefficient h_e and the assumption about boiling heat transfer phenomenon inside evaporator

Figure 9 demonstrates the change of evaporator heat transfer coefficient h_e with heat flux, and Figure 10 does the change of heat flux with super heat degree. To evaluate the performance of this evaporator with the bare surface, the experiment results were compared with calculational results that is estimated by Rohsenow correlation whose obtained results can be in error by ±30% for superheat degree for a given heat flow rate [12]. In general, both of experimental and calculational results almost increased with the increase of heat flux. However, while the calculational results raised up nearly linearly with the flux, the changing of experiment results was different with various heat flux ranges. Firstly, when heat flux is smaller than 50 kW/m^2, the relation between h_e and heat flux was almost linear. In the range of heat flux from 50 kW/m^2 to 100 kW/m^2, the values of h_e was almost constant or changed slightly. Continuing increasing heat flux made the relation become linear again. In addition, the experimental results were only higher than calculational results when heat flux is lower than 100 kW/m^2.

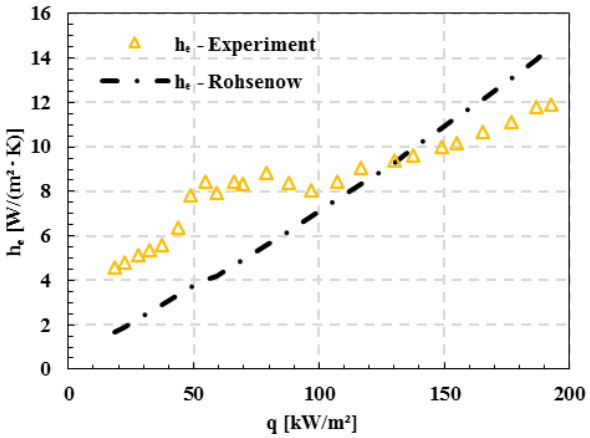

Figure 9. Relation between heat flux and evaporator heat transfer coefficient determined from experiment and Rohsenow correlation

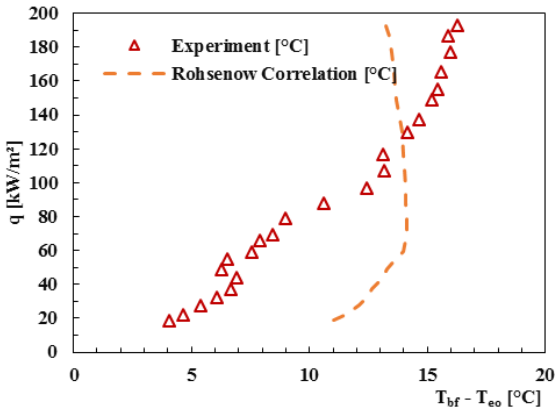

Figure 10. Relation between heat flux and superheat degree determined from experiment and Rohsenow correlation

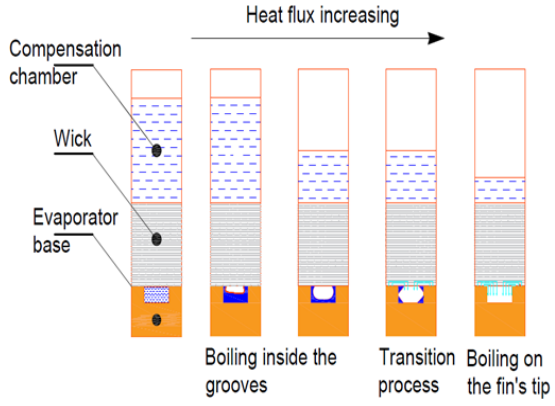

Figure 11. Assumption about boiling phenomenon under different heat flux

To explain the about results, an assumption about boiling heat transfer described in Fig. 11 was supposed in this study. Under low heat flux condition, the combination between small evaporation rate and more liquid existing inside evaporator or the liquid flooding the vapor grooves that made vapor flow out evaporator difficultly. This was also the reason which causes the heat leakage as well as total resistance R_t to be larger in this situation. When increasing heat load, the liquid existing at the vapor grooves became less, the liquid-vapor interface area become larger that helped vapor escape evaporator more easily. On the other hand, when compared with the results from Rohsenow correlation, the experimental results had the higher values. It could be explained because the array of fins on the inner surface of evaporator increased the heat transfer area from the solid base to the liquid; as a result, enhanced the heat transfer coefficient under this situation. When heat flux was more than 50 kW/m^2, less liquid existing inside the grooves caused the liquid-vapor interface surface insufficient with heat input; therefore, a fraction of heat input would serve for boiling inside the grooves, the rest fraction must transfer through the fins to make boiling happen on contact surface between the fins and wick body, but this boiling now was not too active. It explains why within this range of heat flux, h_e was almost constant with heat flux. Keeping on increasing heat flux more than 100 kW/m^2, nucleate boiling would happen efficiently on the fin's tip surface; hence, heat transfer coefficient h_e increased proportionally with heat flux again. On the contrary, within this range of heat flux, the results obtained from Rohsenow correlation became higher than experiment. From the above assumption, when heat flux was higher than 100 kW/m^2, the boiling happens almost on the tip surface of the fins. It means that the height of the fins might cause the evaporator thermal resistance increase.

Besides, the change of boiling from inside the grooves to on the contact surface tip of the fins also reduces the area for boiling. Two above explanations could be the reasons why the evaporator heat transfer coefficient determined from experiment had the lower values than from correlation in the range of heat flux being larger than 100 kW/m^2. In summary, under small heat flux, the liquid-vapor interface presents inside vapor grooves and expands its area with heat flux value. Keeping heat flux increasing can clear all liquid inside vapor grooves and cause the liquid-vapor interface to move to the contact surface between wick and evaporator body. The above results also show that it is necessary to conduct the study on finding the optimal size of the fin to improve the performance of the evaporator when functioning under high heat flux situation.

3.5. Cooling performance under no heating power condition

This experiment was carried out after the stable operation of LHP. Figure 12 demonstrates the change of temperature T_1, T_{eo}, T_{ci}, T_{co}, T_{cci} after turning heaters off. It took about 15 minutes to reduce the T_1 from 102 °C to 37 °C, then value of T_1 almost constant. The cooling rate reduced with time. During the first five minutes, the average cooling rate was around 8.12 °C/min and decreased to 3.83 °C/min during the next five minutes and finally was 1.15°C/min. When T_1 had value 37.6 °C, T_{ci} dropped suddenly far from T_{eo} or the circulation stopped. T_{eo} did not reduce, that indicates the evaporation still happened, but the heat released from heater was not strong enough to maintain the circulation.

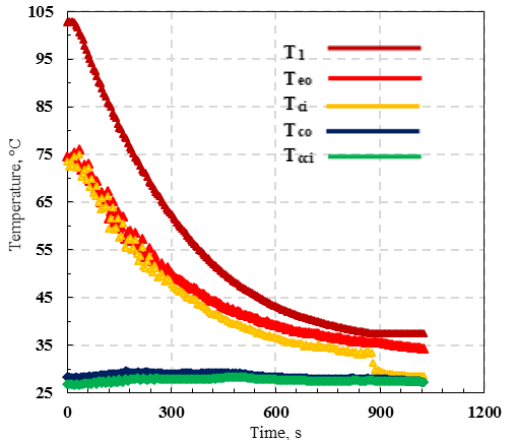

Figure 12. The cooling performance of the present loop heat pipe when heaters were turn off

4. Conclusion

In this study, a LHP with flat-rectangular evaporator was manufactured and investigated performance under gravity assisted condition in the range of heating power from 50 W to 520 W. The time for the present LHP to startup reduced from 12 mins to 2.5 mins when heating power increased from 50 W to 270 W. The flooding situation at the vapor line could be the reason that caused the startup to be longer and the appearance of temperature overshoot at the end of startup under low heating power condition.

The present LHP could maintain temperature on top surface of the heating block below 85 °C, which is the commonly suggested limitation value for the safe and effective operation, when heating power was smaller than 350 W. Besides, it kept the stable operational performance on the whole range of heating power without the sign of dry-out inside evaporator.

In general, both of total thermal resistance R_t and thermal resistance of evaporator R_e became smaller with the increase of heating power. Consequently, R_t and R_e had the minimum values 0.149 K/W and 0.0036 K/W respectively when heating power was at 520 W. The thermal contact resistance R_{ct} had maximum value 0.01 K/W.

In addition, an assumption of boiling heat transfer was introduced in this study for explaining the change of the evaporator heat transfer coefficient of the present LHP with heat flux. At small heat flux, the liquid-vapor interface formed inside vapor grooves and gains its surface area with heat flux. When heat flux had value more than 100 kW/m^2, it presented at the contact surface between fin and wick body. Evaporator heat transfer coefficient h_e was almost constant with heat flux during transition process, where heat flux is from 50 kW/m^2 to 100 kW/m^2.

With the 4.36-kg copper heating block, under no heating power condition, it took about 15 minutes to reduce the temperature T_1 inside the heating block from 102 °C to 37 °C with the max cooling rate that was 8.12 °C/min in the first five minutes of cooling period.

Nomenclature

A	:	area of the top surafce of the heating block, m^2
c_p	:	specific heat of cooling water, J/(kgK)
h_e	:	evaporator heat transfer coefficient, kW/(m^{2}K)
ID/OD	:	pipe inner, outer diameter, mm
k	:	copper thermal conductivity, W/(m·K)
m_{wa}	:	cooling water mass flow rate, kg/s
q	:	heat flux, kW/m^2
Q	:	heat load, W
Q_c	:	heat released from condenser, W
R_t,	:	total thermal resistance, K/W
R_e,	:	evaporator thermal resistance, K/W
R_c,	:	condenser thermal resistance, K/W
R_{ct}	:	thermal contact resistance, K/W
T_1 *to* T_3	:	heater temperature, °C
T_4	:	evaporator base temperature, °C
T_a	:	room temperature, °C
T_{bf}	:	temperature at the base of fin, °C
T_{ci}	:	temperature at condenser inlet, °C
T_{co}	:	temperature at condenser outlet, °C
T_{cci}	:	temperature at compensation chamber inlet, °C
T_{eo}	:	temperature at evaporator outlet, °C
T_{s1}	:	temperature at heater surface, °C
T_{s2}	:	temperature at evaporator bottom surface, °C
$T_{wa\text{-}i}$	:	temperature of cooling water at inlet position, °C
$T_{wa\text{-}o}$	:	temperature of cooling water at outlet position, °C
δ_1	:	distance between the thermocouples inside heating block
δ_2	:	distance between the thermocouple T_4 and the bottom surface of evaporator

References

[1] S. M. Sohel Murshed and C. A. Nieto de Castro, A critical review of traditional and emerging techniques and fluids for electronics cooling, Renew. Sustain. Energy Rev. 2017, 78, pp.821–833.

[2] K. Ebrahimi, G. F. Jones, and A. S. Fleischer, A review of data center cooling technology , operating conditions and the corresponding low-grade waste heat recovery opportunities, Renew. Sustain. Energy Rev.2014 , pp.622–638.

[3] A. C. Kheirabadi and D. Groulx, Cooling of server electronics: A design review of existing technology, Appl. Therm. Eng. 2016, 105, pp. 622–638.

[4] Y. F. Maydanik, Loop heat pipes, Appl. Therm. Eng. 2005, 25, pp. 635–657

[5] J. Li, D. Wang, and G. P. Peterson, Experimental studies on a high performance compact loop heat pipe with a square flat evaporator, Appl. Therm. Eng. 2010, 30, pp.741–752.

[6] J. Xu, Z. Wang, H. Xu, and L. Zhang, Experimental research on the heat performance of a flat copper-water loop heat pipe with different inventories, Exp. Therm. Fluid Sci. 2017, 84, pp.110–119.

[7] G. Zhou and J. Li, Two-phase flow characteristics of a high performance loop heat pipe with flat evaporator under gravity, Intl. Journal of Heat and Mass Transfer 2018, 117, pp.1063–1074.

[8] A. Suzuki, K. Sato, Y. Koito, and T. Tomimura, Prototype Experiment on Cooling Performance of a JEST-type Loop Heat Pipe, 4th World Conf. Appl. Sci. Eng. Technol. 2015, pp.24–27.

[9] C. Kondou, S. Umemoto, S. Koyama, Y. Mitooka, Improving the heat dissipation performance of a looped thermosyphon using low-GWP volatile fluids R1234ze(Z) and R1234ze(E) with a super-hydrophilic boiling surface, Appl. Therm. Eng. 2017, 118, pp.147–158.

[10] H. He, K. Furusato, M. Yamada, B. Shen, and S. Hidaka, Efficiency enhancement of a loop thermosyphon on a mixed-wettability evaporator surface, Appl. Therm. Eng. 2017, 123, pp.1245–1254.

[11] SMC Coporation, Sintered metal element (EB/ES Series), pp.103–118.

[12] A. J. G. Yunus A. Cengel, Heat and Mass Transfer: Fundamental & Application, 5th ed. Mc Graw Hill, 2014, p.602.

EPI International Journal of Engineering
Volume 1, Number 2, August 2018, pp. 47-50
DOI: 10.25042/epi-ije.082018.07

*p*ISSN 2615-5109
*e*ISSN 2621-0541

Temperature Control of Soft Drinks on Vehicle with Portable Storage Thermoelectric Cooler

Basri[a], Mustofa[b*], Daud Patabang[c], Yuli Asmi Rahman[d], Wahyu Haryadi Piarah[e]

[a]Department of Mechanical Engineering, Engineering Faculty, Tadulako University, Palu. Email: basri@untad.ac.id
[b]Department of Mechanical Engineering, Engineering Faculty, Tadulako University, Palu. Email: mustofauntad@gmail.com
[c]Department of Mechanical Engineering, Engineering Faculty, Tadulako University, Palu. Email: daudpatabang@gmail.com
[d]Department of Electrical Engineering, Engineering Faculty, Tadulako University, Palu. Email: yuliasmi.rahman81@gmail.com
[e]Department of Mechanical Engineering, Engineering Faculty, Hasanuddin University, Gowa. Email: wahyuhpiarah@unhas.ac.id

Abstract

This study aims to design a control system with fuzzy logic on a system of cooling the storage of soft drinks with thermoelectric coolers. This storage can be carried in a vehicle using a DC electric power from a photovoltaic solar cell mounted on the roof of the car. Under certain conditions the energy source of cigarette lighter in a car can replace the solar cells. The test results show that a temperature of 15°C can be reached within 30 minutes with fuzzy control, while without fuzzy control the time needed in 63 minutes, 30 minutes longer.

Keywords: *Fuzzy TEC; Peltier effect; POTECO; photovoltaic-on roof; soft drinks*

1. Introduction

The generation of thermoelectric technology (TE) has developed rapidly in the past decade because of its ability to convert thermal into electrical energy. Likewise, solar cell technology is often combined with a thermolectric either as a cooling solar cell or as a source of electrical energy in parallel with PV. Recent researches involving thermoelectric as an electric energy generator or thermoelectric with photovoltaic can be refer to [1-7].

In contrast, TE applications as coolants that utilize DC electric current sources are also intensively studied. Several related papers such as on [8, 9] and that combines TE as a coolant and a power plant at the same time [10]. The working principle can be seen in Fig. 1, where TE as a TEC cooler and as an electric energy generator is TEG.

The problem in the TEC application is temperature control that is in accordance with the wishes. Control systems in TEC applications are still rarely done. Therefore, this study will display temperature control schemes using fuzzy logic compared with no fuzzy programs as preservatives or soft drinks coolers on portable boxes. Temperature control is very useful that suits the needs of cooled objects. The thermoelectric phenomenon as a cooler

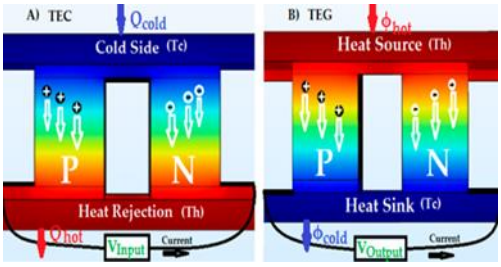

Figure 1. working principle of; (A) Thermoelectric Cooler; (B) Thermoelectric Generator [10]

is known as the Peltier effect [11]. The use of buck converter with fuzzy-PID control from DC motor energy sources has been displayed by Jumiyatun and Mustofa [12]. This control characteristic can be applied to this TEC paper research.

2. Portable Storage of Soft Drinks on Vehicle

The need for drivers and passengers on vehicles will treat fresh and cold drinks throughout the trip cannot be ignored. Therefore, it needs the storage cooler by utilizing the Peltier effect of the thermoelectric cooler (TEC) that utilize a DC electric current supply from photovoltaic solar cells that can be placed on the vehicle roof. Besides that, if soft drink needs are still needed until the night during the trip, the DC source can be obtained from the cigarette lighter plug on the car. The model of this cooler storage is abbreviated

* Corresponding author. Tel.: +62-813-4107-4257
Palu, Indonesia, 94118

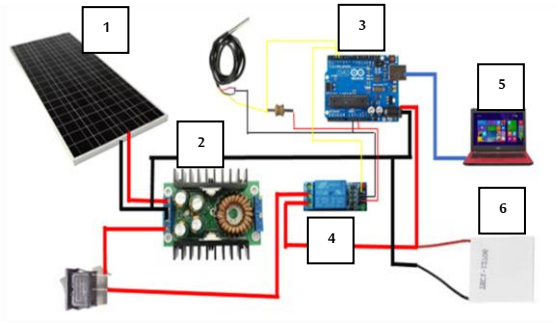

Figure 2. Experimental set-up; (1) PV; (2) Converter step-up step-down; (3) Arduino; (4) Relay 12 V; (5) LCD; (6) TEC

POTECO (Portable Storage Thermoelectric Cooler) as explained as follows.

3. Experimental Set-up

The design of this test can be seen in the scheme of Fig. 2 and block diagram in Fig. 3 which places polycrystalline solar cell as DC power energy sources. From Fig. 2, PV produces voltage with an average of 19 Volt. This voltage goes to the buck boost converter with an output setting of 12 Volt. This output is the source for TEC and Arduino. Relay is connected between 12 Volt and TEC voltage output which will disconnect/connect depending on the control commands of Fuzzy Logic contained in Arduino. The LCD functions to display temperature. The polycrystalline PV solar cell is Solartech with a capacity of 85 Wp, a buck converter circuit step up-step down, a thermoelectric TEC 12706 for cooling soft drinks in the storage, a relay, and then Arduino as controller. The control method used is fuzzy logic to make the temperature constant at 15° C.

4. Results and Discussion

To verify the POTECO scheme above, the cooler has been created as shown in Fig. 4(a) by placing the TEC module on the side wall of the container. Cold side of the module is inside the container of the refrigerator and hot side is in contact with the

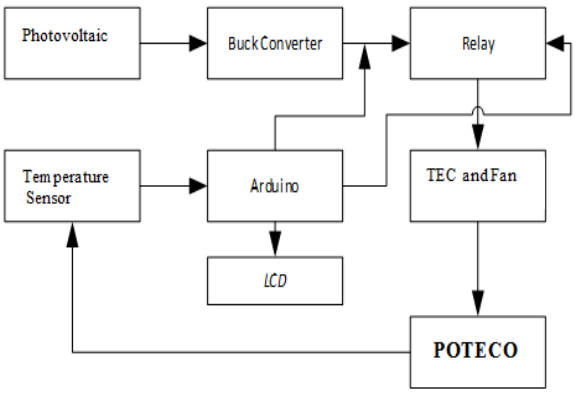

Figure 3. Block diagram of POTECO

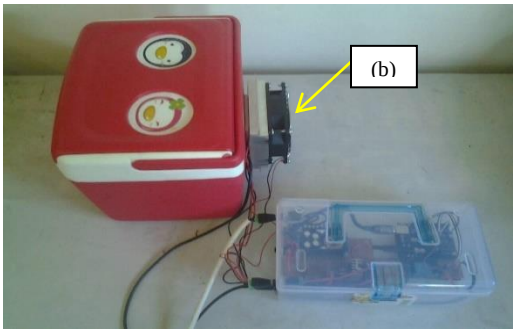

(a)

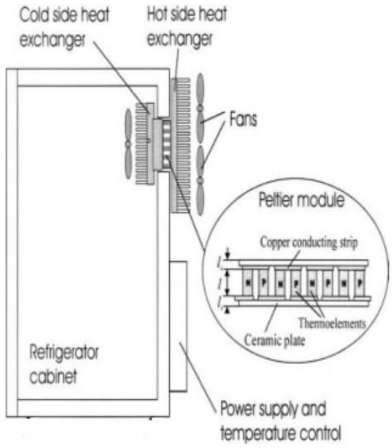

(b)

Figure 4. POTECO (a) and the TEC module detail (b) [13]

Table 1. Temperature vs Time of POTECO

TEMPERATURE (°C)	TIME (MINUTES)
27.44	0
27	0.6
26	0.7
25	1.5
24	2
23	2.53
22	3.2
21	4.1
20	5.3
19	7.2
18	8.4
17	10.46
16	16.7
15	26.2
14	55.1
13.88	**63.37**

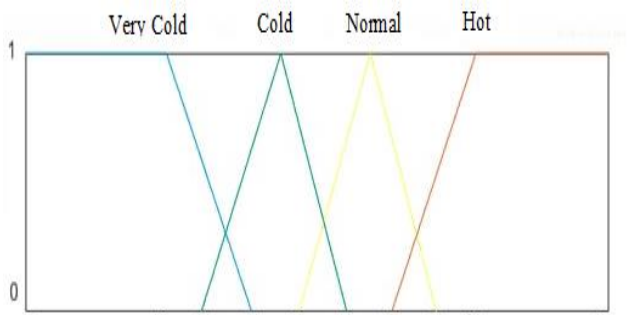

Figure 5. Fuzzy rule of POTECO

surrounding air in the vehicle cabin. Heat will be removed from hot side with help of Aluminum heat sink. Heat sink is connected on the hot side of the module. Min and Rowe [13] also put the TEC module like that as depicted in Fig. 4(b).

From the test results showed that the storage temperature reached 13.88°C in 63.37 minutes as the data in Table 1. This figure was obtained without system control.

4.1. Fuzzy controls

Fuzzy rules are simply made as shown in Figure 5. Furthermore, this fuzzy rule can be referred to [14].

The above rule means that:

1. If temperature **Very Cold** (<= 15), relay OFF 30 seconds
2. If temperature **Cold** (14 – 17), relay OFF 20 seconds
3. If temperature **Normal** (16 – 19), relay OFF 10 seconds
4. If temperature **Hot** (>= 18), Then relay ON

Or in the form of computer program:

```
if (temperaturenow <= 15) { relay off = 30 seconds}
else if (14 < temperaturenow && temperaturenow <= 17) { relay off = 20 seconds}
else if (16 <temperaturenow && temperaturenow <= 19) { relay off = 10 seconds}
else if (18 <= temperaturenow) {relay on}
```

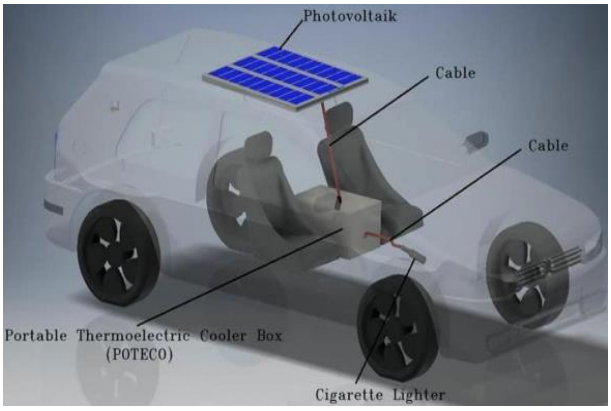

Figure 6. Work scheme of POTECO on vehicle

The results show that a temperature of 14.94°C is achieved in just 30 minutes, approximately 30 minutes faster than without fuzzy control. This number is also 13 hours faster than the time achieved by Aziz et al. [9] in the same TEC module, storage dimensions are almost the same as digital control methods. Furthermore, the POTECO storage if placed in the car cabin will look like in Figure 6 positioned between the driver and accompanying passengers in front.

5. Conclusion

In this experiment it was found that the fuzzy control design works well and is faster in reaching the cold side of the TEC temperature as early set-up. This possibility is caused by a source of DC electrical energy as the TEC input produces a large amount of power at 85 Wp. Further work is needed to assess the performance of cooling systems with variations in series and parallel TEC modules and the stability of the system for long periods of time. Furthermore, the cigarette lighter performance of the car needs to be tested as a DC power source.

Acknowledgements

Thank you to Aria Nurul Haq, a student of Electrical Engineering at Tadulako University who has contributed greatly to the experiment and design of its fuzzy control.

References

[1] N. Watjanatepin and P. Somboonkij, "The Design and Development of Photovoltaic Electrical Generating System Experimental Set," pp. 120–123, 2010.

[2] P. Li, L. Cai, P. Zhai, X. Tang, Q. Zhang, and M. Niino, "Design of a concentration solar thermoelectric generator," *J. Electron. Mater.*, vol. 39, no. 9, pp. 1522–1530, 2010.

[3] G. Min, "Thermoelectric module design under a given thermal input: Theory and example," *J. Electron. Mater.*, vol. 42, no. 7, pp. 2239–2242, 2013.

[4] P. Cheng, "The design of solar temperature difference power generation device," no. Isss, pp. 458–461, 2015.

[5] Mustofa, Basri, and Y. A. Rahman, "Experimental investigation from different focal length of Fresnel lens on thermoelectric generators performance," in *IOP Conf. Series: Earth and Environmental Science 175 (2018) 012004*, 2018.

[6] Mustofa, Z. Djafar, W. H. Piarah, and Syafaruddin, "A New Hybrid of Photovoltaic-thermoelectric Generator with Hot Mirror as Spectrum Splitter," *J. Phys. Sci.*, vol. 29, pp. 63–75, 2018.

[7] F. J. Willars-Rodriguez, E. A. Chavez-Urbiola, P. Vorobiev, and Y. V Vorobiev, "Investigation of solar hybrid system with concentrating Fresnel lens , photovoltaic and thermoelectric generators," *Int. J. Energy Res.*, 2016.

[8] D. K. Chavhan and S. D. Mahajan, "Testing and Validation of Thermoelectric Coolers," *Int. J. Eng. Res. Appl.*, vol. 5, no. 8, pp. 5–9, 2015.

[9] R. Aziz, M. Tanwirul, S. Sunanto, and K. Karsid, "Sistem Kontrol Suhu Penyimpan Buah-Sayur Pada Mesin Pendingin," *J. Teknol. Terap.*, vol. 3, no. September, pp. 32–36, 2017.

[10] K. Teffah, Y. Zhang, and X. Mou, "Modeling and Experimentation of New Thermoelectric Cooler–Thermoelectric Generator Module," *Energies, MDPI*, vol. 1, no. 1, 2018.

[11] H. Najafi and K. A. Woodbury, "Optimization of a cooling system based on Peltier effect for photovoltaic cells," *Sol. Energy*, vol. 91, pp. 152–160, 2013.

[12] J. Jumiyatun and M. Mustofa, "Controlling DC-DC Buck Converter Using Fuzzy- PID with DC motor load," in *IOP Conf. Series: Earth and Environmental Science 156 (2018) 012003*, 2018.

[13] G. Min and D. M. Rowe, "APPLIED thermoelectric domestic-refrigerators," vol. 83, pp. 133–152, 2006.

[14] G. Feng, "Introduction to Fuzzy Logic Control," Vol. 20102151, No. October, pp. 1–12, 2010.

EPI International Journal of Engineering
Volume 1, Number 2, August 2018, pp. 51-58
DOI: 10.25042/epi-ije.082018.08

*p*ISSN 2615-5109
*e*ISSN 2621-0541

Heat Utilization of Incinerator Chimneys as Mini Power Generator Based on Thermoelectric

Usman Syamsuddin[a], Zulkifli Djafar[b], Thomas Tjandinegara[c], Zuryati Djafar[d], Wahyu Hariyadi Piarah[e]

[a]Department of Mechanical Engineering, Hasanuddin University. Email:usmansyamsuddin69@gmail.com
[b]Department of Mechanical Engineering, Hasanuddin University. Email:zulkiflidjafar@unhas.ac.id
[c]Department of Mechanical Engineering, Hasanuddin University. Email:thomastjandinegara@unhas.ac.id
[d]Department of Mechanical Engineering, Hasanuddin University. Email:zuryatidjafar@unhas.ac.id
[e]Department of Mechanical Engineering, Hasanuddin University. Email:wahyupiarah@unhas.ac.id

Abstract

The thermoelectric generator (TEG) has long been used to produce electrical energy. When a temperature difference occurs between two semi-conductor materials on TEG, this thermoelectric element will produce a voltage difference and flow an electric current known as the 'Seebeck effect'. This research was conducted to determine the potential of electrical energy from the TEG module as an alternative energy source by utilizing chimney heat from an incinerator for household non-organic waste. Tests are carried out with a variation of 1, 2 and 3 m chimney height with solid waste treatment without compaction and compaction. The test results show that with 12 TEG modules arranged in series electricity can produce an output voltage with a maximum temperature difference of each ΔV 3.31 Volt ; ΔT 15.0 °C (1 m), ΔV 3.92 Volt; ΔT 17.8 °C (2 m), ΔV 4.84 Volt ; ΔT 22.0 °C (3 m) while the compaction of each value ΔV 6.34 Volt ; ΔT 29.2 °C (1 m), ΔV 7.69 Volt ; ΔT 35.2 °C (2 m), ΔV 9.09 Volt ; ΔT 41.5 °C (3 m). The potential power that can be produced is as big as 3.22 W (1 m); 4.56 W (2 m); 6.88 W (3 m) while the compaction of waste is equal to each value 11.80 W (1 m); 17.36 W (2 m); 24.25 W (3 m). The addition of chimney height variation resulted in an increase in the hot side temperature (Th), cold side (Tc) and temperature difference (ΔT) so that heat energy and power energy increased.

Keywords: Electrical energy; heat transfer; incinerator; seebeck effect; thermoelectric generator

1. Introduction

Energy cannot be separated from human life in carrying out their daily activities. The need for energy is increasing along with the development of technology. However, not all energy sources used can be renewed so that one day the energy source will run out, such as fossil energy. Fossil energy is energy derived from fossil resources such as coal and petroleum that occur due to fossil stockpiling for millions of years. Fossil energy sources can run out at any time if it is used continuously and ironically, fossil energy is the most widely used [1].

Development of alternative energy such as wind energy, solar cell, OTEC (Ocean Thermal Energy Conversion), geothermal energy, river flow, waste and other sources of plant origin such as jatropha and biogas energy need attention the serious ones from government, industry, universities and society. In addition to the development of alternative energy, attention to saving energy or conserving energy needs to get the same attention because saving energy or increasing the thermal efficiency of an energy system can extend the depletion of fossil fuel supplies [2].

The thermoelectric generator (TEG) is a power plant based on the Seebeck effect, which was first discovered in 1821 by Thomas Johann Seebeck. The working principle of the Seebeck effects that works on a thermoelectric generator system are: if two metal materials (generally semi conductors) are connected in an environment with different temperatures, the material will flow electric current or electromotive force. If this effect is applied to an incinerator with a waste heat temperature that has an interval of 200-1500 ^{o}C, the temperature difference between the two can be used to obtain an electromotive force [3].

*Corresponding author. Tel.: +62 853-422-724-69
Faculty of Engineering Hasanuddin University
South Sulawesi, Indonesia, 90245

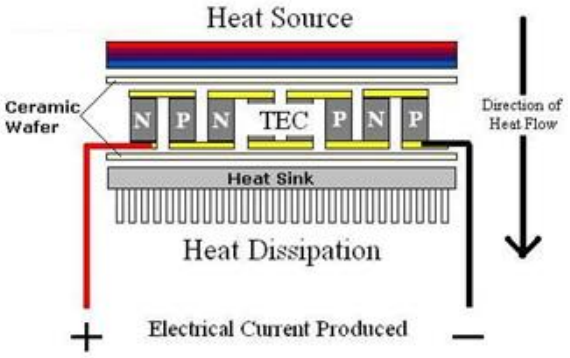

Figure 1. Thermoelectric power generation structure [4]

Figure 1 shows the structure of a Thermoelectric Generator (TEG) which consists of an array of n-type elements (material with an excess of electrons) and p-type (material with a lack of electrons). Heat to enter on one side and is discharged from the other side, producing a voltage that passes through the thermoelectric connection. The amount of voltage produced is proportional to the temperature gradient.

In a that developed a thermoelectric based battery charger. The system developed produces a maximum power of 7.99 Watts. The study uses heat source of heat dissipation from the walls of traditional furnaces. This thermoelectric generator has also been developed for application of laptops. The plant uses heat generated from butane gas. The power produced is around 13.35 Watt [4]. Another study that developed and tested a thermoelectric plant in a traditional fire furnace in Lebanon using free convection on the thermoelectric side which produced a power of 4.2 Watt [5].

There are several advantages of using a thermoelectric generator (TEG) as a means of converting heat of electricity, including safe for the environment, simple, small, very light, noiseless and does not require maintenance because there are no moving parts. Besides its advantages, low efficiency is still a major drawback of TEG. However, because the energy source to activate this technology is obtained from free heat sources available, the low efficiency problem is not the main barrier factor of its application. In addition, several steps to increase efficiency can be obtained by optimizing its components, improving manufacturing quality and better design and the development of materials used [6].

The efficiency value of the thermoelectric module can be increased by the way the heat is dissipated on the cold side of the module, such as the use of heatsink, fan, water jacket or simply by giving the ambient temperature above the cold side of the module to maintain the temperature difference in the heat side. Use of heat sinks to help increase heat release on the cold side, thereby increasing the efficiency of the module. The power generation potential for a single thermoelectric module will vary depending on size, construction and temperature differences. The greater temperature difference between the hot side and the cold side of the module will produce greater voltage and current. Thermoelectric modules can also be connected together in series or parallel like a battery to produce the desired voltage or electric current. Each module is able to produce an average voltage of 1-2 V DC and even up to 5 V DC depending on variations in temperature difference, but generally one thermoelectric module produces 1.5-2 V DC [7].

2. Experimental Methods

The design of the equipment used is presented in Figure 2 below. A holder made of thin rectangular aluminum plates as a place to place the TEG module and mounted on an incinerator chimney that functions to use heat to generate electricity, in this case voltage difference. In this test, a single module is used with 3 variations on chimney height 1, 2 and 3 meters. A single module uses 12 TEGs that is spread in a series with an electric series circuit (Fig. 3). The cool heatsink and fan are installed above the TEG module which serves to remove heat of the cold side so that the temperature difference can be maximized.

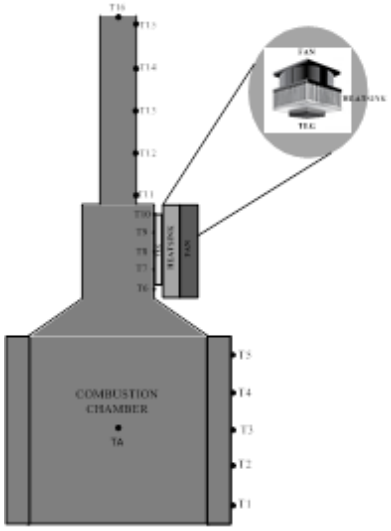

Figure 2. Test equipment design

Information:

- Fire temperature measurement point (TA)
- Lower body temperature measurement point (T1 to T5)
- Upper body temperature measurement point (T6 to T10)
- Chimney temperature measurement point (T11 to T15)
- Exhaust gas temperature measurement point (T16)

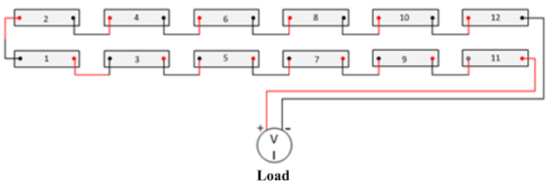

Figure 3. Single series electric module circuit (12 TEG)

The output voltage of the TEG module is measured using a multimeter after a while getting heat flow from the aluminum plate. Measurement of hot side temperature (Th), cold side (Tc) and voltage (ΔV) of the TEG module is carried out with an interval of 3 minutes for 60 minutes. The data obtained is then recorded in the observation table.

In analyzing the performance of the thermoelectric module, the Seebeck coefficient that describes the voltage (electromotive force) arises because the temperature difference becomes very important. The Seebeck coefficient can be expressed by the following equation [8, 9]:

$$\alpha = \frac{\Delta V}{(T_h - T_c)} \quad (1)$$

Where:

ΔV = Voltage difference (V)
α = Seebeck coefficient between two semiconductor materials, P and N (V/°C)
T_h = Temperature of the thermocouples on hot side (°C)
T_c = Temperature of the thermocouples on hot side (°C)

While the generated electric current is given by the following equation [10]:

$$I = \frac{\alpha\ \Delta T}{R_i + R_L} = \frac{\alpha\ \Delta T}{R_i + R_L} \quad (2)$$

Where:

I = Electric current flowing in the circuit (A)
R_i = Internal load of the thermoelectric generator module (Ω)
R_L = External load (Ω)
ΔT = Th – Tc (°C)

The rate of heat transfer (Q_h) coming from the heat source of temperature (T_h) to the cold surface at a temperature (T_c) is as follows [6]:

$$Q_h = (\alpha\ I\ T_h) + K(T_h - T_c) \quad (3)$$

where K is the thermal conductance of the module element (W/M °C). The output power (P) which generated to counter the outside loads [6] and the efficiency (η) of thermoelectric generator is as follows [8]

$$P = I^2 R_L \quad (4)$$

$$\eta = \frac{P}{Q_h} \quad (5)$$

3. Result and Discussion

3.1. *Without compaction waste of 1 m chimney*

Figure 4 shows the history of average hot side temperature (Th *avg*), average cold sides temperature (Tc *avg*) and average temperature difference (dT *avg*) to the time, t (minute) which increases over time and reaches the peak in the 9th minute. Furthermore, it decreased continuously until it approached the ambient temperature in the 60th minute. The biggest value of each is; Th avg is 76.0 °C, Tc *avg* is 61.0 °C and dT *avg* is 15.0 °C. The picture above shows that the temperature has increased from the combustion processed until the peak conditions where the burning waste has reached the maximum amount. Furthermore, the temperature decreases continuously until the garbage burn out.

Figure 5 shows the relationship between voltage difference (dV) and temperature difference (dT). The temperature range that can be achieved is 15.0 °C which corresponds to the voltage difference is 3.31 V. This shows that the Seebeck coefficient value of this process is still relatively small at 0.22 V/°C because the TEG module used is of low quality (home industrial production).

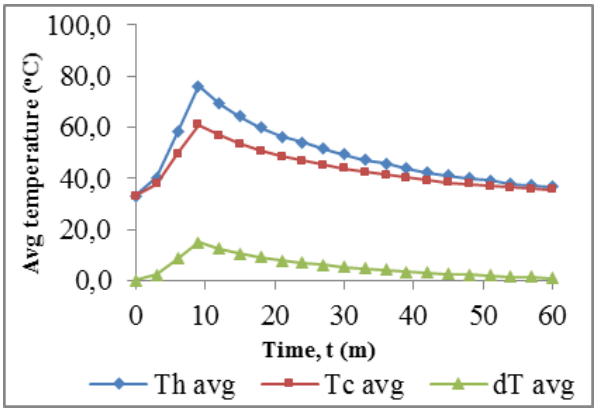

Figure 4. History of average hot side temperature (Th avg), average cold side temperature (Tc avg) and average temperature difference (dT avg) at 1 m chimney height

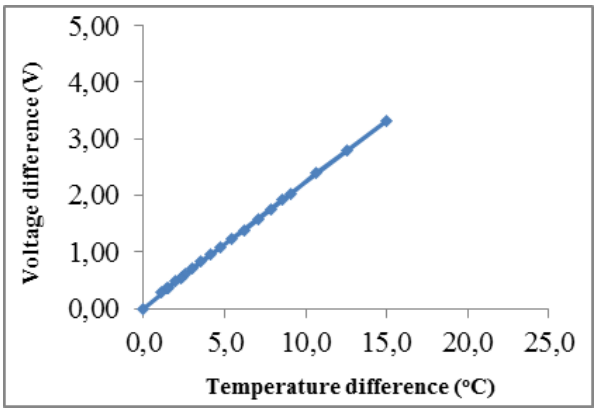

Figure 5. Relationship between voltage difference (dV) to temperature difference (dT) at 1 m chimney height

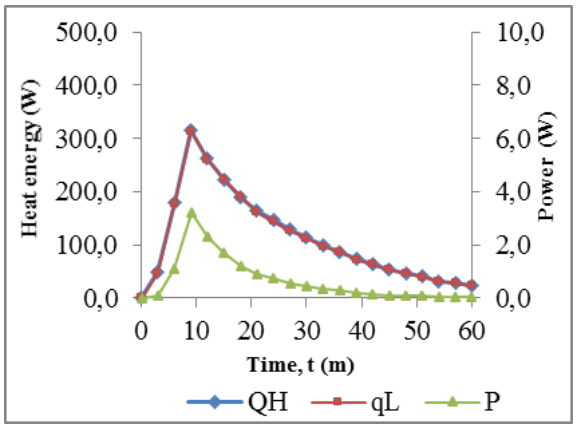

Figure 6. Comparison of power (P), heat energy absorbed (QH), heat loss energy (qL) to time, t (m) at 1 m chimney height

Figure 6 shows the ratio of power (P), absorbed heat energy (QH) and the heat loss energy (qL) to the time that increased until the 9th minute then decreased continuously until it approached the surrounding temperature in the 60th minute. absorbed by 315.60 W is converted to a power of 3.22 W and the rest is released into the surrounding environment. This result is for conditions without compaction of waste with a 1 m chimney height.

3.2. Compaction waste of 1 m chimney

Figure 7 shows the history of average hot side temperature (Th avg), average cold sides temperature (Tc avg) and average temperature difference (dT avg) to time, t (m) which increased with time and peaked at 6th, then it decreased continuously until it approached the surrounding temperature at 60th. The biggest value of each was; Th avg is 113.4 °C, Tc avg is 84.4 °C and dT avg is 29.0 °C. The temperature experienced a significant increase when compared to conditions without compaction of waste because the conditions of compaction of the waste combustion process is faster so that the temperature also increases on the hot side, on the cold side and temperature difference.

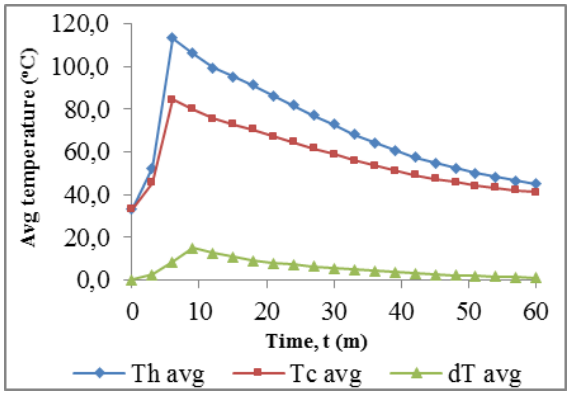

Figure 7. History of average hot side temperature (Th avg), average cold side temperature (Tc avg) and average temperature difference (dT avg) at 1 m chimney height

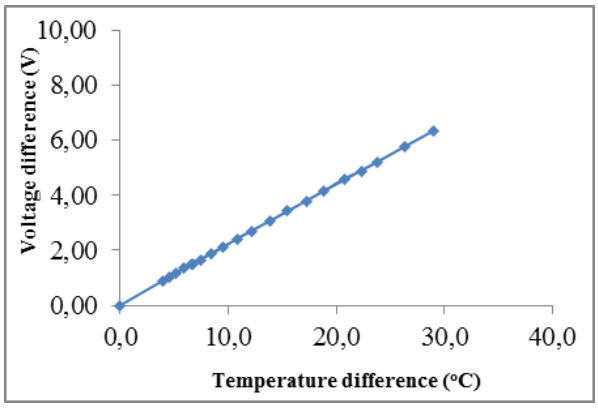

Figure 8. Relationship between voltage difference (dV) to temperature difference (dT) at 1 m chimney height

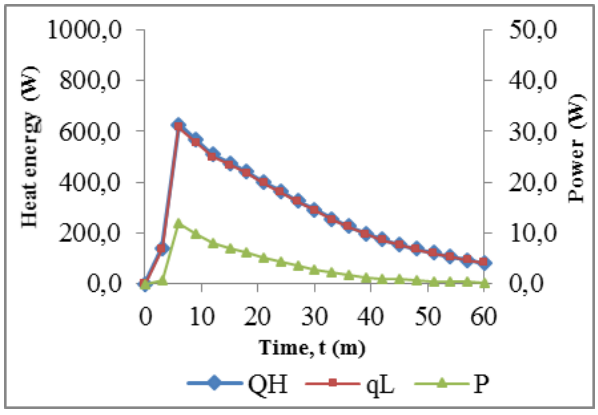

Figure 9. Comparison of power (P), heat energy absorbed (QH), heat loss energy (qL) to time, t (m) at 1 m chimney height

Figure 8 shows the relationship between voltage difference (dV) and temperature difference (dT). The temperature difference that can be achieved is 29.0 °C which corresponds to the voltage difference is 6.34 V. Seebeck coefficient in this process of 0.18 V/°C as in the previous case.

Figure 9 shows the comparison of power (P), absorbed heat energy (QH) and the heat loss energy (qL) against the time that increased until the 6th minute then decreased continuously until it approached the surrounding temperature in the 60th minute. absorbed by 625.11 W is converted into power of 11.80 W and the rest is released into the surrounding environment. This result is for compaction conditions with 1 m chimney height.

3.3. Without Compaction waste of 2 m chimney

Figure 10 shows the history of average hot side temperature (Th avg), average cold sides temperature (Tc avg) and average temperature difference (dT avg) to time, t (m) which increased with time and peaked at 9th, then it decreased continuously until it approached the surrounding temperature at 60th. The biggest value of each was; Th avg of 83.6 °C, Tc avg of 65.7 °C and dT avg of 17.9 °C. The temperature experienced a significant increase when compared to conditions without compaction of waste

because the condition of compaction of the waste combustion process is faster so the temperature also increases on the hot side, cold side and temperature difference. The addition of 2 m chimney height variations also has a significant effect due to the increase in cross-sectional area so that it affects the increase in temperature.

Figure 11 shows the relationship between voltage difference (dV) and temperature difference (dT). The temperature difference that can be achieved is 17.9 °C which corresponds to the voltage difference is 3.94 V. Seebeck coefficient in this process of 0.22 V/°C

Figure 12 shows the comparison of power (P), absorbed heat energy (QH) and the heat loss energy (qL) against the time that increased until the 9th minute then decreased continuously until it approached the surrounding temperature in the 60th minute. absorbed by 378.14 W is converted to a power of 4.56 W and the rest is released to the surrounding environment. This result is for conditions without compaction of waste with 2 m chimney height.

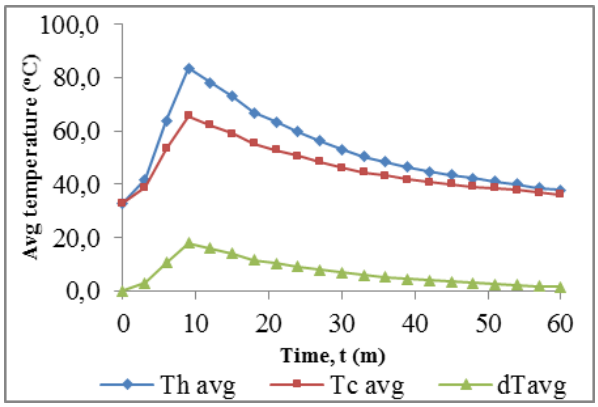

Figure 10. History of average hot side temperature (Th avg), average cold side temperature (Tc avg) and average temperature difference (dT avg) at 2 m chimney height

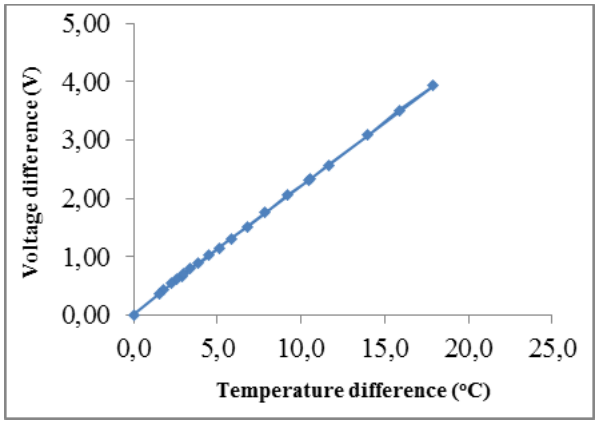

Figure 11. Relationship between voltage difference (dV) to temperature difference (dT) at 2 m chimney height

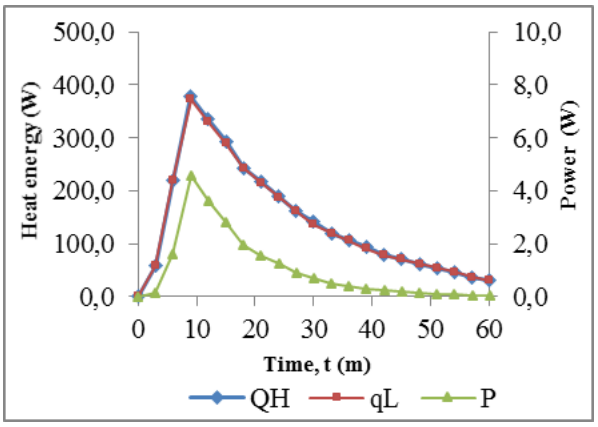

Figure 12. Comparison of power (P), heat energy absorbed (QH), heat loss energy (qL) to time, t (m) at 2 m chimney height

3.4. Compaction waste of 2 m chimney

Figure 13 shows the history of average hot side temperature (Th avg), average cold sides temperature (Tc avg) and average temperature difference (dT avg) to time, t (m) which increased with time and peaked at 6th, then it decreased continuously until it approached the surrounding temperature at 60th. The biggest value of each was; Th avg is 129.8 °C, Tc avg is 94.6 °C and dT avg is 35.2 °C. The addition of 2 m chimney height variations resulted in an increase in the voltage difference resulting from the increase in temperature difference due to the increase in chimney crosses section area.

Figure 14 shows the relationship between voltage difference (dV) and temperature difference (dT). The temperature difference that can be achieved is 35.2 °C which corresponds to the voltage difference is 7.69 V. Seebeck coefficient in this process of 0.22 V/°C.

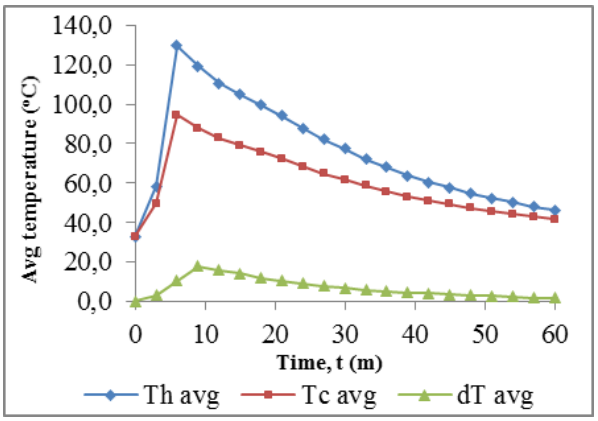

Figure 13. History of average hot side temperature (Th avg), average cold side temperature (Tc avg) and average temperature difference (dT avg) at 2 m chimney height

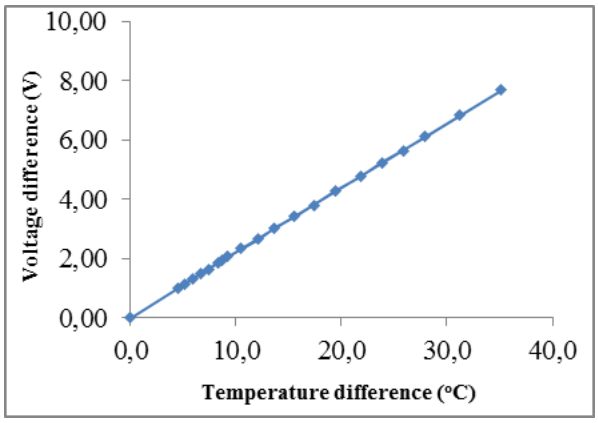

Figure 14. Relationship between voltage difference (dV) to temperature difference (dT) at 2 m chimney height

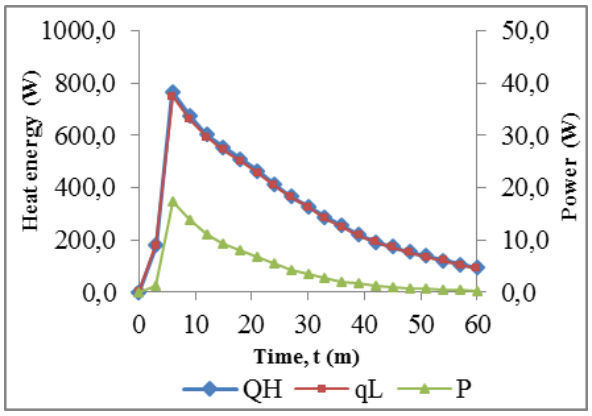

Figure 15. Comparison of power (P), heat energy absorbed (QH), heat loss energy (qL) to time, t (m) at 2 m chimney height

Figure 15 shows the comparison of power (P), absorbed heat energy (QH) and the heat loss energy (qL) to the time that increased until the 6th minute then decreased continuously until it approached the surrounding temperature in the 60th minute. absorbed by 765.45 W is converted to a power of 17.36 W and the rest is released into the surrounding environment. This result is for conditions without compaction of waste with 2 m chimney height.

3.5. Without Compaction waste of 3 m chimney

Figure 16 shows the history of average hot side temperature (Th avg), average cold sides temperature (Tc avg) and average temperature difference (dT avg) to time, t (m) which increased with time and peaked at 9th, then it decreased continuously until it approached the surrounding temperature at 60th. The biggest value of each was; Th avg is 94.7 °C, Tc avg is 72.7 °C dan dT avg is 22.0 °C. The addition of 3 m chimney height variations resulted in an increase in the voltage difference resulting from the increase in temperature difference due to the increase in chimney crosses section area.

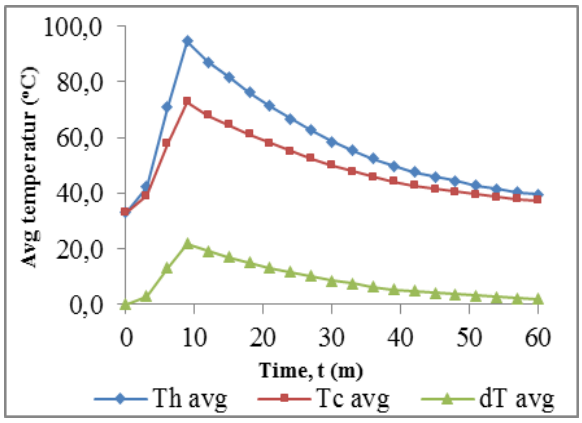

Figure 16. History of average hot side temperature (Th avg), average cold side temperature (Tc avg) and average temperature difference (dT avg) at 3 m chimney height

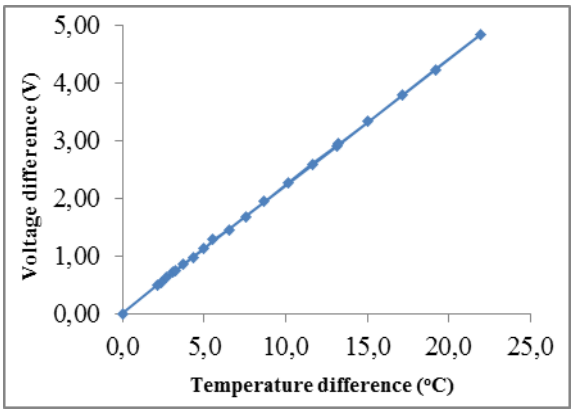

Figure 17. Relationship between voltage difference (dV) to temperature difference (dT) at 3 m chimney height

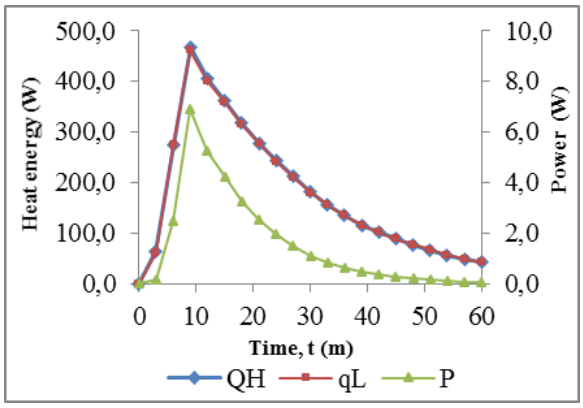

Figure 18. Comparison of power (P), heat energy absorbed (QH), heat loss energy (qL) to time, t (m) at 3 m chimney height

Figure 17 shows the relationship between voltage difference (dV) and temperature difference (dT). The temperature difference that can be achieved is 22.0 °C which corresponds to the voltage difference is 4.84 V. Seebeck coefficient in this process of 0.22 V/°C.

Figure 18 shows the comparison of power (P), absorbed heat energy (QH) and the heat loss energy (qL) to the time that increased until the 9th minute then decreased

continuously until it approached the surrounding temperature in the 60th minute. absorbed by 467.95 W converted to a power of 6.88 W and the rest is released to the surrounding environment. This result is for conditions without garbage compaction with a 3 m chimney height.

3.6. Compaction waste of 3 m chimney

Figure 19 shows the history of average hot side temperature (Th avg), average cold sides temperature (Tc avg) and average temperature difference (dT avg) to time, t (m) which increased with time and peaked at 6th, then it decreased continuously until it approached the surrounding temperature at 60th. The biggest value of each was; Th avg is 146.5 °C, Tc avg is 105.0 °C and dT avg is 41.5 °C. The addition of 3 m chimney height variations resulted in an increase in voltage difference resulting from the increase in temperature difference due to the increase in the chimney crosses section area.

Figure 20 shows the relationship between voltage difference (dV) and temperature difference (dT). The temperature difference that can be achieved is 41.5 °C which corresponds to the voltage difference is 9.09 V. Seebeck coefficient in this process of 0.22 V/°C.

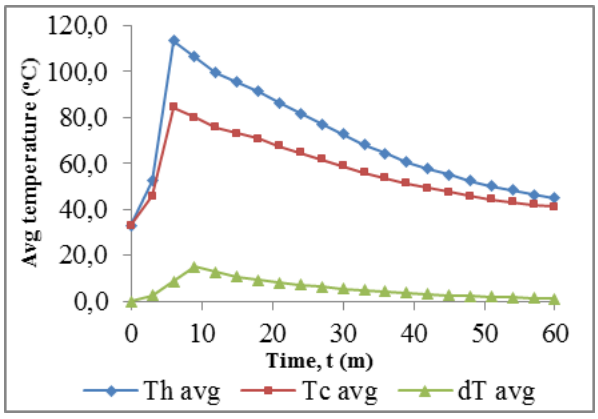

Figure 19. History of average hot side temperature (Th avg), average cold side temperature (Tc avg) and average temperature difference (dT avg) at 3 m chimney height.

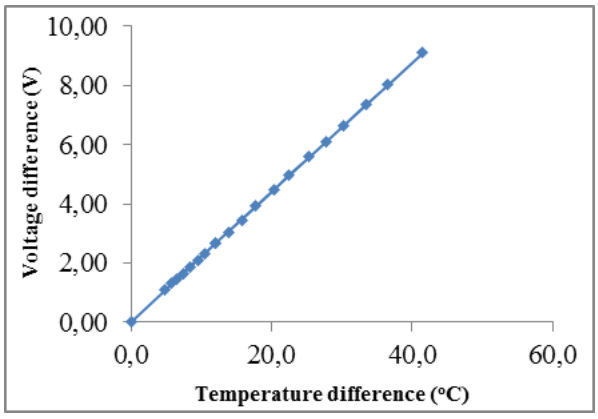

Figure 20. Relationship between voltage difference (dV) to temperature difference (dT) at 3 m chimney height

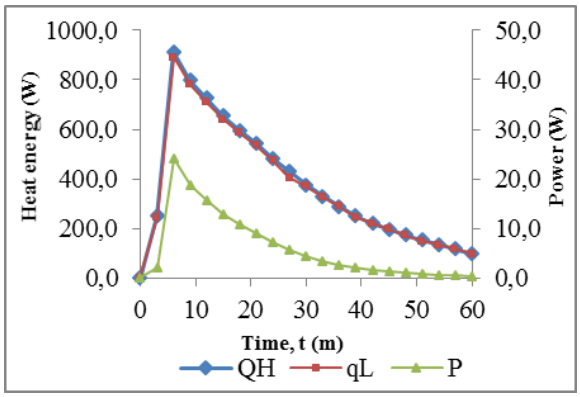

Figure 21. Comparison of power (P), heat energy absorbed (QH), heat loss energy (qL) to time, t (m) at 3 m chimney height

Figure 21 shows the ratio of power (P), absorbed heat energy (QH) and the heat energy released (qL) to the time that increased until the 6th minute then decreased continuously until it approached the surrounding temperature in the 60th minute. absorbed by 913.70 W is converted into power of 24.25 W and the rest is released into the surrounding environment. This result is for compaction conditions with 3 m chimney height.

4. Conclusion

The test results to indicate that the resulting voltage difference increases from the addition of chimney height with or without compaction of waste because it has not reached optimum height. The temperature difference also increases with each value of ΔV 3.31 Volt; ΔT 15.0 °C (1 m), ΔV 3.92 Volt; ΔT 17.8 °C (2 m), ΔV 4.84 Volt; ΔT 22.0 °C (3 m) while the compaction of each value ΔV 6.34 Volt; ΔT 29.2 °C (1 m), ΔV 7.69 Volt; ΔT 35.2 °C (2 m), ΔV 9.09 Volt; ΔT 41.5 °C (3 m). The potential power that can be produced is as big as 3.22 W (1 m), 4.56 W (2 m), 6.88 W (3 m) while the compaction of waste is equal to each value 11.80 W (1 m), 17.36 W (2 m), 24.25 W (3 m). The addition of chimney height variation resulted in an increase in the heat sides temperature (Th), cold side (Tc) and temperature difference (dT) so that heat and power energy increased.

References

[1] Kementerian Energi dan Sumber Daya Mineral, "National Energy management strategies in ensuring availability of Energy Security," 2010.

[2] http://www.alpensteel.com/article/121-107--bio-gas-energy/2367--develovement-of-alternative-energy-from-biogas. Accessed on 07 February 2017.

[3] G. Min, D.M. Roe, Handbook of Thermoelectrics, Peltier devices as generator, CRC Press LLC, Florida, p. 479, 1994.

[4] J. Eakburanawat, I. Boonyaroonate, "Development of a thermoelectric battery-charger with microcontroller-based maximum power point tracking technique" J. Appl. Energy, 83/7, 687-704. 2006.

[5] Rida Y. Nuwayhid, Alan Shihadeh, Nesreen Ghaddar, "Development and Testing of a Domestic Woodstove Thermoelectric Generator with Natural Convection Cooling", J. Energy Conversion and Management, Volume 46, Issues 9-10, 1631-1643.

[6] Nandy Putra, Raldi Artono Koetoer, M. Adhitrya, Ardian Roekettino, and Bayu Trianto., "The Potential Power Generation Thermoelectric for Hybrid Vehicles", J. Makara Teknologi. Vol. 13. No. 2., 53-58, 2009.

[7] Ismail, B.I., Ahmed, W.H., *Thermoelectric Power Generation Using Waste-Heat Energy as an Alternative Green Technology*, Recent Patents on Electricals Engineering, Vol. 2, p. 27-39, 2009.

EPI International Journal of Engineering
Volume 1, Number 2, August 2018, pp. 59-64
DOI: 10.25042/epi-ije.082018.09

*p*ISSN 2615-5109
*e*ISSN 2621-0541

Design and Hydrodynamic Model Test of Mini Submarine Propeller with High Efficiency and Low Cavitation

Mahendra Indiaryanto[a,*], Mohammad Ridwan Utina[b], Nurwidhi Asrowibowo[c], Siti Sadiah[d]

[a]Balai Teknologi Hidrodinamika, BPPT. Email: mahendra.indiaryanto@bppt.go.id
[b]Balai Teknologi Hidrodinamika, BPPT. Email: muhamad.ridwan@bppt.go.id
[c]Pusat Teknologi Rekayasa Industri Maritim, BPPT. Email: nurwidhi.asrowibowo@bppt.go.id
[d]Balai Teknologi Hidrodinamika, BPPT. Email: siti.sadiah@bppt.go.id

Abstract

Design and development of propellers for submarines are in some ways different from propellers for surface vessels. The most important demand is low acoustic signature and propeller efficiency. The design for the propulsor for submarine is a specialist task of a later stage of design. The propulsive efficiency has essentially three parts in the traditional method of approach. The first and major part is the efficiency of the propeller itself as a device which may develop to overcome the resistance to motion the vessel. The aim of this research is to design a mini submarine propeller and obtain high efficiency and low cavitation. To reach this aim, model tests were performed both in Towing Tank and Cavitation Tunnel. From the propeller model tests, the result shows a good efficiency and low cavitation.

Keywords: Cavitation; efficiency; propeller; submarine

1. Introduction

In designing a mini-submarine propeller, there are some important things that need to be taken into consideration, namely the model results on a mini-submarine, whether obtained through model testing, as well as by means of numerical computation using CFD program.

In contrast to surface ships, in the propeller design process, submarine needs to consider the efficiency of the propeller as well as the cavitation [1]. Unlike surface ships, submarines, in addition to considering propeller efficiency, also need to pay attention to signature of acoustic aspects which may come from cavitation.

The thrust produced by the propeller is needed to move forward the submarine in certain speed. The relationship between propeller thurst resistance can be translated into the following equation:

$$T = \frac{R_T}{(1-t)} \tag{1}$$

where T is the thrust of propeller, R_T is the resistance of mini submarine and t is the thrust deduction factor of mini submarine [2]. Assuming the value of thrust deduction factor is 0:17 which refers to published studies on the relationship between the ship's hull with propeller submarine.

Basically, model testing to measure drag on mini-submarines can be performed in Towing Tank [3] or in Wind tunnel (Fig. 1). The following is an example of ship model testing performed in towing tank and Wind Tunnel.

The result is almost the same as the difference in the density of the fluid acting on each testing facility

$$R_T = \frac{1}{2}\rho V^2 A_{frontal} C_D \tag{2}$$

Figure 1. Model test of submarine in wind tunnel and towing tank (IHL)

*Coresponding author. Tel.: +62-85655617011
Jl. Hidrodinamika, Kompleks ITS, Sukolilo
Surabaya 60111

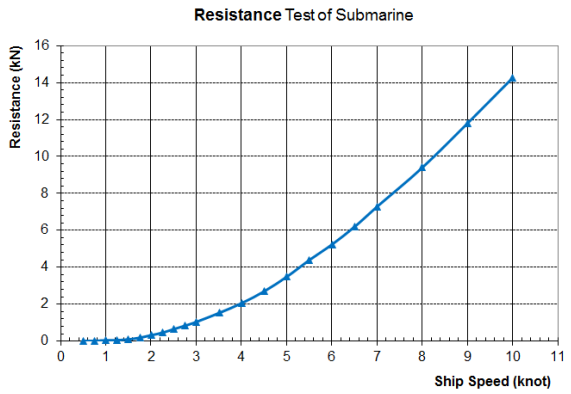

Figure 2. Resistance model test result of submarine model in towing tank [2]

where R_T is the resistance of mini submarine, ρ is the density of water, V is the velocity mini submarine, A is the frontal area of mini submarine and C_D is the coefficient drag [4].

In Indonesian Hydrodynamic Laboratory (IHL), a package of resistance model test of mini submarine has been performed in Towing Tank [3]. The model submarine is tested at submerge mode, submarine model was tested at depth of 2 m. The results from model test in Fig. 2 are as follows:

The data from resistance test is very useful in designing propeller to obtain an optimum efficiency according to its purpose during operational.

Propeller design with low cavitation levels is absolutely necessary for submarine. This propeller cavitation can cause noise. Propeller cavitation may occur in the propeller tip area, the root area of the propeller and the vortex on the hub propeller.

Based on literature studies, to reduce cavitation in the propeller tip area required a good skew form on the propeller blade.

2. Theory and Methodology

The use of open-source programs such as *Open Prop V.2.4.6* that run with MATLAB, can be entered multiple input data such as vessel speed, rpm, diameter, and thrust to get initial design propeller. For planning Thrust price is determined using Eq. (1).

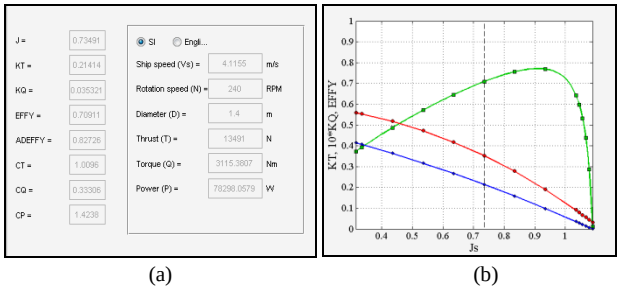

(a) (b)

Figure 3. Computational analysis using Matlab (a) Input, (b) Diagram K_T K_Q J

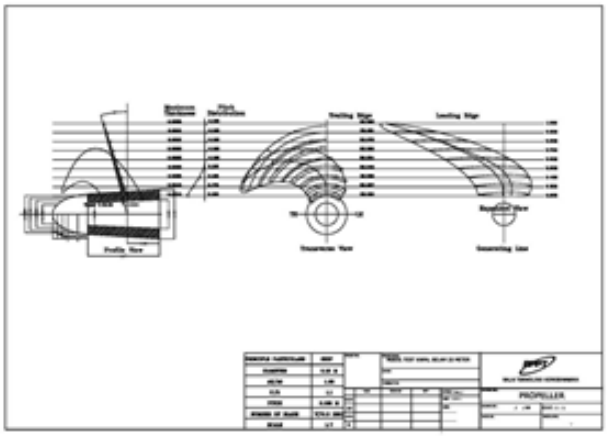

(a)

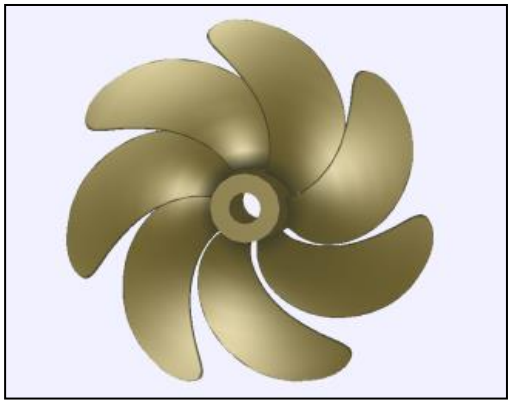

(b)

Figure 4. (a) 2D, (b) 3D propeller design with 7 blades

In this research a lifting line theory and Matlab program were used in designing submarine propeller in order to get the outline and thickness of the blade. By running Matlab program, some results are obtained as presented in Fig. 3. From the initial analysis, the design of blade is a type of blade symmetrical, so still need few changes with the addition of skew outline propeller on the propeller tip to reduce the level of cavitation that occurs at the end of the propeller blade. The final design result is shown in Figs. 4a (2D design propeller) and 4b (3D design propeller).

In Figure 4(a), is a design model submarine in the form of two-dimensional, used as working drawings in making a mini-submarine propeller model. Whereas in Fig. 4(b) is a three-dimensional visual in solid form, this image is used as a basic drawing for further numerical analysis program Computer Fluid Dynamic (CFD).

A few changes in outline of propeller drawing with the addition of a model propeller blade skew on the CFD analysis is required. This addition of skew at the blade propeller efficiency will decline and the rising value of the Coefficient Advance (J). But the effect is not too significant to the prediction of the initial design of the propeller. Besides being used for numerical analysis of a 3D image can serve as a visual tool. So, it can be used as a validation of the physical form in propeller model manufacture that will be carried out.

2.1. Propeller efficiency

The basic aim of this research is to determine how much the efficiency of the designed propeller. To determine the efficiency of the propeller can be done by open water test along with a test dummy models in cavitation tunnel facility. The open water test using an Open Water Propeller Apparatus which is available in IHL. Through this testing, the amount of thrust and torque propeller models can be measured by varying the speed of the propeller models when tested. so we get the values of thrust (*T*) and torque (*Q*) and can be calculated thrust coefficient and torque coefficient K_T K_Q based advanced coefficient (J). K_T, K_Q, by following equations

$$K_T = \frac{T_{prop}}{\rho n^2 D^2} \tag{3}$$

$$K_Q = \frac{Q_{prop}}{\rho n^2 D^3} \tag{4}$$

$$J = \frac{V_a}{nD} \tag{5}$$

Where K_T is the coefficient thrust of propeller, K_Q is the coefficient torque of propeller T_{prop} is the thrust of propeller, Q_{prop} is the torque of propeller, ρ is the density of water, *n* is the rotation of propeller, Va is the advance velocity of mini submarine, *J is* the advance coefficient of mini submarine and *D* is the Diameter propeller [2]. While the efficiency of propeller can be represented by the following equation:

$$\eta_0 = \frac{J}{2\tau}\frac{K_T}{K_Q} \tag{6}$$

where η is the efficiency of propeller [2].

2.2. Cavitation

To observed the cavitation phenomenon on the propeller, a testing in the cavitation tunnel is important. The propeller noise consists of four components which is cavitation noise, blade singing noise, blade noise and turbulence noise rate. Cavitation noise is the largest component of the propeller noise, especially on ships moving at high speed. Singing noise caused by vibrations that arise as a result of the curvature blade propeller. The amount of noise frequency is dependent on the magnitude of vibration frequencies [5].

The tests carried out in the Towing Tank and Cavitation Tunnel in Indonesia Hydrodynamics Laboratory, which aims to determine the results of the performance of the design of a propeller that has been determined through CFD calculations. The research methodology can be presented as follows

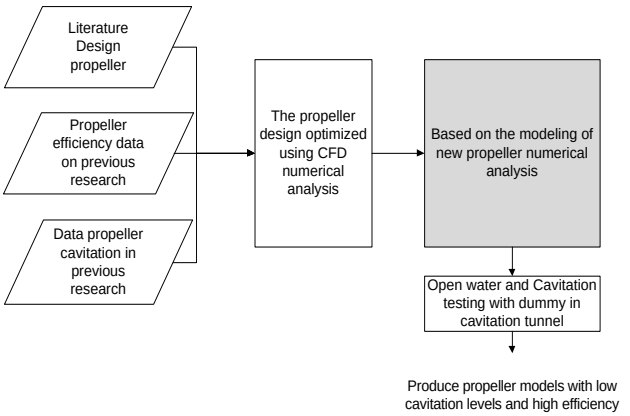

Figure 5. Research flow chart

Step of research as in Figure 5 can be explained as follows:

- Collecting data design, efficiency and propeller cavitation, both from the literature study and previous research
- Recalculating data using Matlab to obtain numerical simulation initial performance of the model propeller that we will create, which of the results obtained following the model as a primary measure
    - Propeller Diameter Model = 0.20 m
    - P/D = 0.816
    - Ae/Ao = 0.880
    - Total Blade = 7 blade
    - Scale = 1:7
- Performing numerical simulation (CFD) to create a 3D design in the form of solid propeller. This calculation should be done due to changing outline of design models by adding skew propeller on propeller blade about 54º, as well as provide an overview of the characteristics of the propeller during design step.
- Making the model propeller according propeller drawings 4a. Based on these images can be created for table offset and table measurements that will be used to manufacture a model propeller with 7 blades.
- Testing the model propeller in Cavitation Tunnel by adding a dummy model of submarine as well as variations in pressure on the fluid to determine the cavitation occurs when the propeller operated at the specified depth.

Dynamometer measuring instrument consists of a motor, the holder of the measuring instrument, measuring instrument holder as well as a model propeller shaft. Where the measuring instrument function is to determine the amount of the value of thrust in units (*Newton*) and in units Torque (*Newton meter*). The output of this measure was to determine the efficiency of a propeller taking into account the magnitude of the coefficients and coefficients Torque Thrust. Cavitation Tunnel test performed at IHL.

3. Result and Discussion

3.1. Numerical simulation results

The use of 3D solid program needed to obtain images in the form of 3-dimensional propeller, so it can be used on meshing as shown in Fig. 6(a). Meshing the propeller models aims to break the measuring object into an infinite element, making it easier for a computer to calculate the shape of the element finite. This is needed to get the results of numerical simulations in the form of Computer Fluid Dynamic (CFD) .

CFD simulation for this propeller using ANSYS. where in the previous study the comparison between the numerical method (CFD) and the test differed between 10% -20% [6]. After the meshing process both propeller and fluid models that operate around the propeller, CFD can be done running the program with steps that run the program as well as the time of testing the open water tests in Cavitation Tunnel.

From the results of numerical simulations using CFD then obtained value Thrust and torque at any speed propeller models. Equations (3) and (4) are used to obtain the propeller thrust and torque coefficients. Furthermore, in Eq. (6) is used to get the propeller efficiency. From the results of these calculations can be shown in Table 1, with maximum efficiency rates of 0689 where it is comparable with the price coefficients thrust and coefficients torque respectively are 0.257 and 0.436 [3].

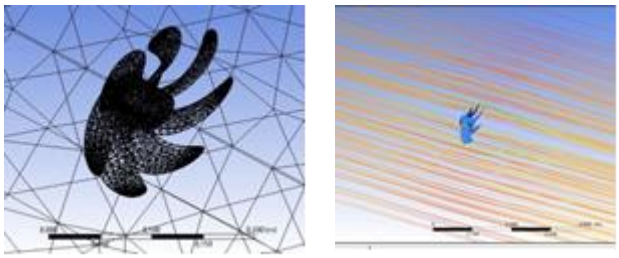

(a) Meshing (b) Running Propeller

Figure 6. Meshing and numerical analysis

Table 1. Result of numeric simulation

J	Thrust (n)	Torque (Nm)	KT	10KQ	η
0.184	71.602	2.194	0.400	0.612	0.191
0.276	69.707	2.142	0.389	0.598	0.286
0.367	65.888	2.062	0.368	0.575	0.374
0.459	60.065	1.942	0.335	0.542	0.453
0.551	55.148	1.841	0.308	0.514	0.526
0.643	50.692	1.684	0.283	0.470	0.616
0.735	46.020	1.563	0.257	0.436	0.689
0.827	36.086	1.510	0.201	0.421	0.629
0.919	26.771	1.456	0.149	0.406	0.538
1.011	20.751	1.345	0.116	0.375	0.497
1.102	15.828	1.235	0.088	0.345	0.450

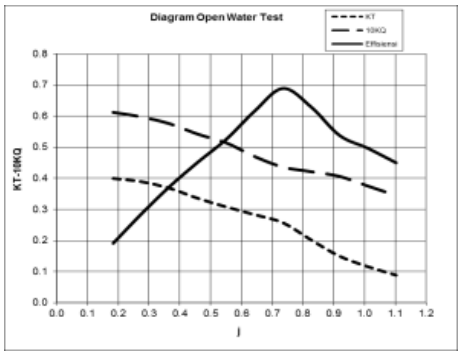

Figure 7. Result numerical simulation

So that the results of this testing are known that the propeller can work efficient on value J 0.735. Based on data from Table 1, the characteristics of the propeller can be known, but it cannot make the excuse that the propeller numerical simulation represents the actual condition of the propeller.

Tests carried out on propeller revolution per second (Rps) remain with the provision of carriage speed variation between 0.194 m/s to 1.750 m/s, where the model speed used by the scale factor 1:7.

Based on the results in Table 1 it can be presented in diagrams of propeller performance, whereas in Fig. 7 the results of numerical simulation of propeller design.

3.2. Model test results

The phenomenon of cavitation to consider in designing a submarine propeller after propeller models known characteristics of the test results open water test. Because cavitation generated from a submarine propeller can cause noise on the submarine. Noise that is too large will result in easily detectable presence of submarines by the enemy. Therefore, propeller submarine good are those that have a low cavitation.

On testing in cavitation tunnel remeasured performance mini-submarine propeller models at each pressure, the pressure variation at 1 bar and 1.5 bar. Where the provision of the pressure on the propeller models assuming real condition mini submarine at a depth of operational areas.

Table 2. Test results in Cavitation Tunnel at the pressure of 1.0 bar

J	Thrust (n)	Torque (Nm)	KT	10KQ	η	Cavitation
0.167	66.6	1.93	0.374	0.542	0.183	Lc
0.347	59.4	1.79	0.33	0.502	0.363	Lc
0.402	56.4	1.71	0.315	0.483	0.416	Lc
0.475	53.3	1.69	0.297	0.477	0.470	Lc
0.562	47.8	1.56	0.267	0.44	0.542	Lc
0.626	43.7	1.44	0.244	0.406	0.598	Lc
0.736	37.8	1.31	0.210	0.370	0.665	Lc
0.841	32.5	1.23	0.181	0.347	0.697	Lc
0.908	28.2	1.13	0.155	0.319	0.705	Lc
0.998	22.4	1.01	0.124	0.287	0.685	Lc
1.101	14.1	0.85	0.077	0.240	0.559	Lc

*Lc = Low Cavitation

Based on the Table 2, testing by giving pressure 1.0 bar can be seen that maximum efficiency occurs at a value 0.705. When compared with the value of the maximum efficiency of numerical simulations, the asset is increased both the value of the advance coefficient (*J*) and the efficiency of the propeller itself. due to the dummy models installed in front of the model propeller causing propeller flow into *Va* (advance velocity) is increasingly directed towards the propeller, that increase the efficiency and value of the advance coefficient (J), along with the rising value of *Va*, is directly proportional to the value of *J*, while the value of *J* is directly proportional to the efficiency of the propeller.

It can be concluded that the propeller has been designed based numerical approach and validated by hydrodynamic phisical model testing. In the present study propeller suitable for use in the form of mini-submarine hull model of 22 m. That applies to the testing of propeller models with the addition of 1.5 bar pressure, in which the additional pressure also affects its advance velocity *(V_a)*, because the pressure acting on the larger propeller at a depth of operational, resulting in a small value of V_a in line with Euler equations. A number of results from testing in Cavitation Tunnel at a pressure of 1.5 bar shown in Table 3.

Table 3. Test results in cavitation tunnel at the pressure of 1.5 bar

J	Thrust (N)	Torque (Nm)	KT	10KQ	η	Cavitation
0.220	70.525	2.138	0.395	0.559	0.231	Lc
0.334	66.821	2.064	0.372	0.58	0.341	Lc
0.379	63.027	1.975	0.351	0.555	0.381	Lc
0.504	57.213	1.881	0.318	0.529	0.482	Lc
0.579	52.256	1.738	0.29	0.489	0.547	Lc
0.666	47.160	1.628	0.261	0.457	0.606	Lc
0.738	43.460	1.525	0.241	0.429	0.660	Lc
0.833	36.894	1.360	0.204	0.382	0.707	Lc
0.922	33.169	1.317	0.183	0.371	0.726	Lc
1.013	27.510	1.204	0.151	0.338	0.721	Lc
1.095	20.613	1.035	0.112	0.291	0.673	Lc

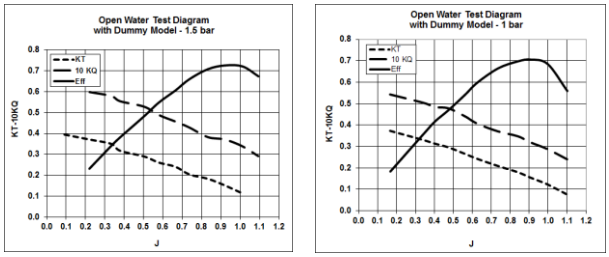

(a) Test 1 bar (b) Test 1.5 bar

Figure 8. Test results in cavitation tunnel with a pressure of 1 bar and 1.5 bar

Testing in Cavitation Tunnel at a pressure of 1.0 bar and 1.5 bar pressure increases both the efficiency and value of the value of the advance coefficient (*J*). But the increase is not significant, this can be seen from the value *J* in 0.922

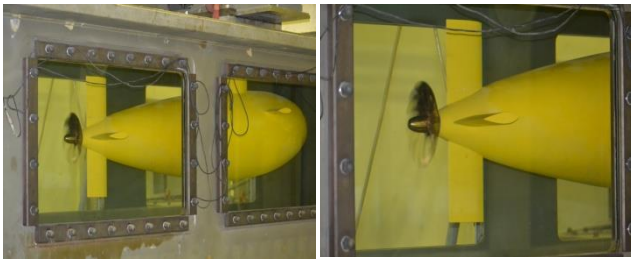

Figure 9. Photos in cavitation tunnel testing

with efficiency 0.726 at 1.5 bar. In other words, if the mini-submarine propeller 22 meters operated at a depth of approximately 100 meters then the propeller efficiency will be slightly increased thus saving consumption battery use on submarines that are connected to an electric motor. So that the propeller on a comparison of the characteristics of the test with a pressure of 1 bar and 1.5 bar can be seen in Fig. 8.

In terms of the characteristics of the cavitation test results in both diagrams are relatively similar and both have a low cavitation levels, so the noise that is expected to arise as a result of propeller cavitation occurs is very low.

Giving difference of pressure on testing in cavitation tunnel is aimed to know propeller characteristic if operated at surface condition and when operational in water depth based on test results in cavitation tunnels. The efficiency of propellers produced a good result 0.7, but seen from the propeller thrust is still less when compared with the curve of the test results of miniature submarine resistance at 8 knots.

Therefore, for further research can change the pitch propeller to get a suitable thrust at a speed of 8 knots

4. Conclusion

Maximum Efficiency in the range of 0.6 numerical, while addition of a dummy model of the cavitation tunnel testing is able to add to the efficiency of the range 0.7, difference 0.1 at maximum efficiency. Little cavitation occurs on the propeller, this is evidenced by cavitation test at a pressure of 1 bar and 1.5 bar at the operational round, so this propeller is very suitable for use in models of mini-submarines 22 m , due to an increase after testing efficiency by using dummy models. This propeller is suitable for submerge mode operational, due to a slight increase in efficiency.

Reference

[1] Paul A, Kappel, J. J., Spangenburg E., (2009), Aspects of Propeller Development of Submarine, International Symposium of Marine Propulsor, Trondheim, Norway, June.

[2] Lewis Edward V, Editor (1988), Principles of Naval Architecture Second Revision, Published by The Society of Naval Architecture and Marine Engineers. 601 Pavonia Avenue, Jersey City.

[3] Erwandi, (2010), Report of Resistance Model Test of 22 M Submarine.

[4] Renilson, M. (2015), Submarine Hydrodynamics, Launceston, TAS, Australia.

[5] Carlton, J, (2007), Marine Propellers and Propulsion, 2nd ed. Oxford, UK (Butterworth- Heinemann).

[6] Mahendra I. (2014), Propeller Design Optimization for a Mini submarine, The 9th International Conference on Marine Technology. MARTEC, Surabaya, Indonesia.
[7] Epps, (2010) OpenProp v2.4 Theory Document.
[8] Kuiper, G (1992), The Wageningen Propeller Series, MARIN Publication 92-001.
[9] Clarke GE (1988) The Choice of propulsor design for an underwater weapon. In: UDT conference, London 26-28 Oct 1988.

EPI International Journal of Engineering
Volume 1, Number 2, August 2018, pp. 65-69
DOI: 10.25042/epi-ije.082018.10

*p*ISSN 2615-5109
*e*ISSN 2621-0541

Maneuver Control System for Collision Avoidance Based on Experimental Study

Kusnindar Priohutomo[a]*, Agus Achmad Masroeri[b], Chandra Permana[c]

[a]Indonesian Hydrodynamics Laboratory, Agency for the Assessment and Application of Technology (BPPT). Email: kusnindar.priohutomo@gmail.com
[b]Departement of Ship Design Engineering, Institut Teknologi Sepuluh Nopember (ITS). Email: aamasroeri@its.ac.id
[c]Indonesian Hydrodynamics Laboratory, Agency for The Assessment and Application of Technology (BPPT).

Abstract

Autopilot mode in the ship navigation system is intended to assist the work of the captain in controlling the ship, but the autopilot mode still has some disadvantages such as in the case of maneuvers to avoid collisions. Many studies on design of anti-collision design. But almost all use a numerical approach. In this paper will be discussed the design of maneuver controls that will be used on the ship model to avoid the ship from the collision. Where within the control system there are several sensors, including ultrasonic sensors, gyro sensors and Qualysis cameras. From ship model testing conducted, the design of maneuver control proved able to avoid the ship from the occurrence of collisions. Minimum distance of ship and obstacle at 250 m distance is 34.17 m, at a distance of 200 m is 13.46 m while at a distance of 150 m is 13.36 m.

Keywords: Collision avoidance; fast patrol boat; microcontroller; model test; system control

1. Introduction

The mode of autopilot in the cruise world becomes an important discussion as it helps the seafarers in making it easier to sail the ship. But in autopilot mode itself still has weakness among others in use to avoid collision.

Avoiding collisions is an important issue in transportation systems. The purpose of collision avoidance maneuvers is that ships avoid the risk of collisions and determine actions to avoid or reduce collisions [1].

Much research on the design of controls maneuver to avoid collisions on ships with various methods. Methods ever used among others is manual calculation method, fuzzy logic method and image processing method. Each method has different advantages and disadventages. Some studies releted to avoid ship collisions include reference [2]. The object used in this study is USV (unmanned surface vehicle) in the form of unmanned ships that work automatically according to the program designed. To support the working system USV required several types of sensors such as cameras. The camera works to record the image in front of the ship for further processing by the computer by using the image processing method of HSV Filter, to identify the object and use Fuzzy Logic to determine the angle of the turning of the ship while avoiding the object. From this research, it can be concluded that the ship succeeded in avoiding obstruction objects in all scenarios, to identify the object distance using image processing, the optimal angle of object readings is 750 to 1050 with the average of object coordinate readout error of 0.868 px and the mean error the object's reading angle is 7.450 ˚/cm [3].

Based on research that has done, the conclusion as follows has been done a design of fuzzy logic controller to control the bow and the speed for this type of MT Brotojoyo Tanker which capable of keeping the trajectory in the Port of Tanjung Perak, Surabaya. In the test without disturbance occurs the maximum error of 35.09 meters and a minimum error of 0.9 meters, while in testing with disturbance macimum error value of 35.59 meters and a a minimum errror of 0.84 meters. Fuzzy logic system has been designed can increase the efficiency of time sailing 38 minutes [4].

The fuzzy logic control system used is the Sugeno method with nine fuzzy rules. The value of fuzzy output using the weight average method. The control system is designed using a GPS module to determine the position and compass sensor to determine the direction. The conclusion of this research is the design of control system using fuzzy logic controller can control the ship to track the path well. The ship can move at a speed of 0.28 m/s and the rudder

*Coresponding author. Tel.: +62315948060
Jl. Hidrodinamika, Kompleks ITS, Sukolilo
Surabaya 60112

speed is 5.639 m/s. The compass sensor used has an error of 0.089 %. While the GPS module has an average error error of 6.449 meters. The average time it takes is 3.625 seconds.

From several literatures, it is done by using ship model scale test method in the basin of maneuver testing. For the purposes of testing it is necessary to design the proper maneuver control so that the ship can avoid the collision. The use of microcontroller and some sensors such as ultrasonic sensors to detect the distance of the ship with obstacles, gyro sensors to know the movement of ship yaw, servo rudder to know the movement of ship rudder and Qualysis camera to know the trajectory between the ship and obstacles

2. Experiment Method

The research methodology was developed to produce a technically good maneuver control design, in which the steps in the methodology can be described as follows:

2.1. Main dimension

First determine the main dimension of the ship which is an important factor in ship designing. The ship model used follows Fast Patrol Boat, where the main dimension between real scale and model scale to be used in research can be seen in Table 1.

2.2. Collision avoidance control system equipment

2.2.1. Arduino Mega 2560

Arduino Mega 2560 is a microcontroller board based on Atmega 328. This board has 54 digital input/output pins (14 pins can be used as PWM output), 16 analog inputs. 16 MKz crystal oscillator, USB connection, power jack, ICSP header and reset button, as shown in Fig. 1.

Figure 1. Microcontroller Arduino Mega 2560

Table 1. Main dimension.

No	Symbol	Rate Scale	Model Scale
1	LOA	90 m	1.27 m
2	LWL	86.45 m	1.22 m
3	Breadth	13 m	0.185 m
4	Draught	3.6 m	0.051 m
5	Displacement	1700 ton	4.66 kg
6	LCB	0.54% LPP	
7	Service Speed	18 knot	1.1 m/s
8	Top Speed	28 knot	1.71 m/s
9	Propeller	3.3 m	0.047 m

2.2.2. Ultrasonic sensor

The ultrasonic sensor used is a non-contact distance measuring module shown in Fig. 2. To trigger and read the measurement data requires only 1 pin microcontroller. In addition provided 12C communication interface.

Figure 2. Ultrasonic sensor

2.2.3. IMU sensor

The inertial measurements unit (IMU) is shown in Fig. 3 as an inertial component used to guide a system commonly used in ground vehicles, marine vehicles, and control rockets. The IMU sensor works by sensing a movement, and the directional displacement using a combination of accelerometer sensor is used to determine the acceleration of gravity, gyroscopes are used to determine angular acceleration and the magnetometer sensor is used for heading or determining the direction of the wind and is used as a reference to the yaw axis.

Figure 3. IMU sensor GY-521

2.2.4. Radio Telemetry

Radio telemetry shown in. Fig. 4 is a hardware that serves to transmit data using wirelesscommunication system.

Figure 4. Radio Telemetry 433 Mhz

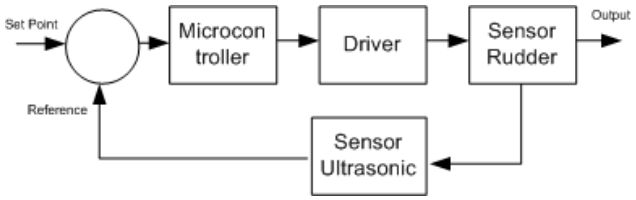

Figure 5. Ultrasonic sensor block diagram [5]

2.3. Design of control system

2.3.1. Ultrasonic sensor design model test

In the ultrasonic sensor book manual of Elecfreaks [5], the design of ultrasonic sensors serves to know and measure the distance of the model with a obstacle.

In the design of ultrasonic sensors, block diagram in Fig. 5 and wire communication in Fig. 6 are used by connecting Vcc, Gnd, Echo and trigger pins.

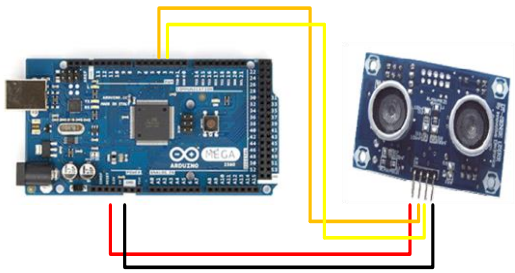

Figure 6. Design of ultrasonic sensor

To avoid the ship from collision, the ultrasonic sensor is set as listed in Table 2.

Table 2. Ultrasonic sensor setting

No	Distance of the Collision (m)	Sensor Setting (m)
1	250	285
2	200	235
3	150	185

2.3.2. IMU sensor design model test

According to the manual book of IMU Sensor [6], the design of gyro sensor serves to know and measure changes in heading angle yaw model of the ship.

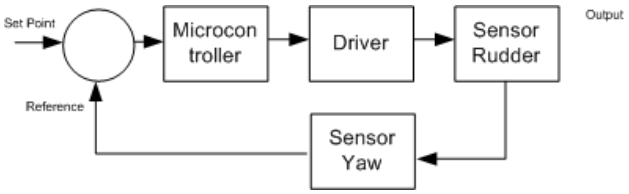

Figure 7. IMU sensor block diagram

The design of the gyro sensor uses block diagram in Fig. 7 and i2c serial data communication by connecting Vcc, Gnd, SDA, SCl and INT, as illustrated in Fig. 8.

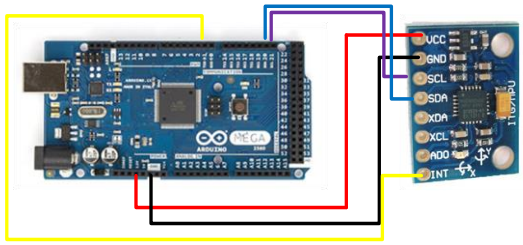

Figure 8. Design of IMU sensor

2.3.3. Servo rudder design model test

The design of servo rudder in Fig. 9 serves to know and measure the angle change rudder model ship. The design of servo rudder using PWM (Pulse Width Modulation) method. With PWM method can be generated servo movement is quite accurate with the desired resolution.

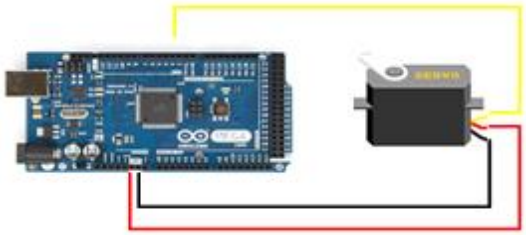

Figure 9. Design of servo rudder

2.3.4. Radio telemetry design model test

In the Advanced Telemetry System manual book [7], telemetry radio design on the test model in Fig. 10 serves to transmit raw data information changes yaw model ship to the system ground station with realtime.

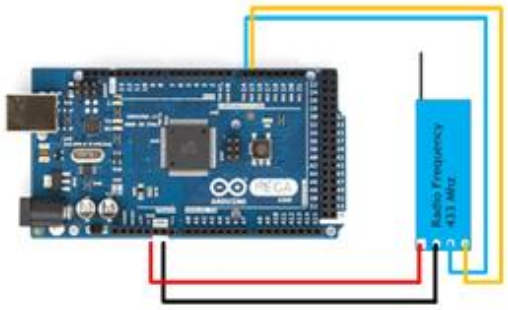

Figure 10. Design of radio telemetry

2.4. Trajectory model measurement system

Measurement of trajectory model movement during the test was performed using QTM (Qualisty Track Manager) equipment. QTM is a software designed using Qualisys camera model, the camera is used as a medium of fast and precise data collection. This system allows users to record data in real time both in 2D, 3D and 6DOF with fast

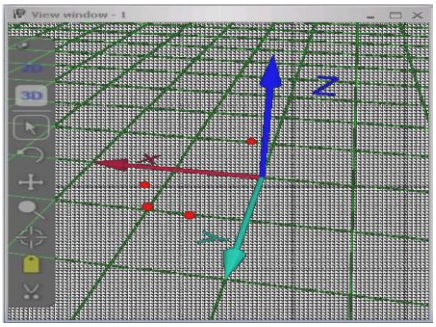

Figure 11. QTM

response time [8]. QTM can also identify marker automatically either passive or active marker, easy in addition of camera if necessary expansion of area object that is recorded. Figure 11 shows the coordinate system on the display.

At the time of capture measurement implemented software will immediately record marker movement (if no setting delay) and can be displayed preview of measurement with preview button. For the sampling rate of the measurement itself can be adjusted from the capture period. The results of the QTM calibration can be seen in Fig. 12. Where the red dot is the marker of the ship that has been installed the Qualisys marker, whereas the x, y and z axis each represent the axis present in the test basin.

2.5. Scenario testing

The test scenario in this study follows the pattern of COLREG 72. COLREG 72 has arranged scenarios to avoid collisions in accordance with the position of the ship, including head-on position, crossing position and overtaking (the ship behind will precede the ship in front). Of the three scenarios according to COLREG 72 which will be used in this research is the head-on scenario (ship facing). Where the two ships will do the steering wheel (rudder) to the starboard (right). So the ship can avoid the collision.

In this study the speed of the ship is made constant at 10 knots. While the speed of the ship obstacle at 2 knots. Model test conducted at Manauvering Ocean Basin (MOB) where basin test fasilities belongs Indonesian Hydrodynamics Laboratory - BPPT Surabaya, in calm water condition (non disturbance).

Variations that are done is the distance of the ship with the obstacle (the distance of the collision) that is 250 meters, 200 meters and 150 meters. Tests on each variation of the distance of the ship against the obstruction are done as much as 3x in order to be taken on average.

3. Results Analysis and Discussion

3.1. Ship and obstacle trajectory

From the test results by using Qualysis camera, the ship trajectory graphic (*x* axis, *y*-axis) at 250 m, 200 m and 150 m.

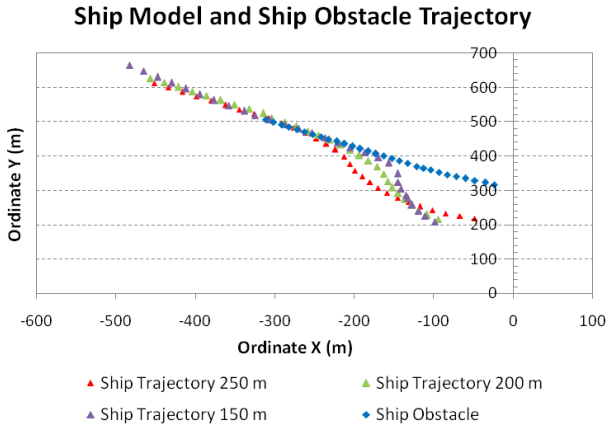

Figure 12. Ship and obstacle at distance of collision 250 m, 200 m and 150 m

3.2. Distance from ship to obstacle

From the trajectory of the ship and the obstacle in Fig. 12, we can find the distance between the two points of the ship's trajectory point (*x*-axis, *y*-axis) and the point of the obstacle (*x*-axis, *y*-axis). The *z*-axis on the ship and the obstacle is not counted because during the test the ship moves on the axis of the 2D axis is the X and Y axis. The formula for finding two points is as follows:

$$\text{Distance} = \sqrt{difference\ x^2 + difference\ y^2} \quad (1)$$

$$= \sqrt{(x_2 - x_1)^2 + (y_2 - y_1)^2} \quad (2)$$

Where:

x_1 = Value X Obstacle
x_2 = Value X Ship
y_1 = Value Y Obstacle
y_2 = Value Y Ship

From Eq. 2, we can calculate the distance between the two points that is *x*-axis, *y*-axis of the ship's trajectory and *x*-axis, *y*-axis obstacle at 250 m, 200 m and 150 m. The results shown in Fig. 13.

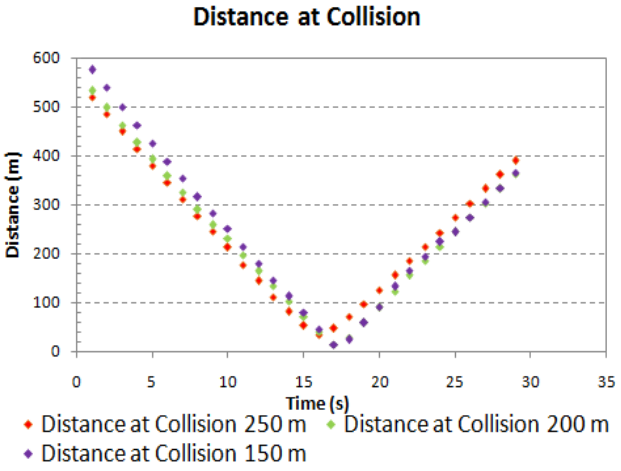

Figure 13. Distance from ship and obstacle at distance of collision 250 m, 200 m and 150 m

4. Conclusion

From the results of measurement and analysis of test results it can be taken a conclusion. Based on the experimental results it is found that the design of maneuver controls installed in the model of fast patrol boats during the test, may prevent the ship from occurring collisions.

Ships at 10 knots can avoid collisions at 250 m, 200 m and 150 m in non-disturbance conditions. The closest distance between the ship and the obstac le at a distance of 250 m is 34.17 m at T = 16 seconds, at a distance of 200 m is 13.46 m at T = 17 seconds and at a distance of 150 m is 13.36 m at time T = 17. This distance is obtained when the ship is adjacent or side by side with obstacles.

References

[1] L. P. Perera, J. P. Carvalho, and C. . Guedes Soares, "Autonomous Guidance and Navigation Based On The COLREGs Rules and Regulations of Collision Avoidance.," *Adv. Sh. Des. Pollut. Prev.*, no. 1999, pp. 205–216, 2010.

[2] M. Iqbal, R. Nugraha,"Design Boat Control System for Collision Avoidance," *e-Proceeding Universitas Telkom*, vol. 4, no. 2, pp. 1426–1433, 2017.

[3] A. S. Aisjah, A. A. Masroeri, M. A. Efendi, E. B. Djatmiko, W. D. Ariyawan, and F. A. Iskandarianto, "Fuzzy Control for Optimizing Ship Tracking in Karang Jamuang – Tanjung Perak," *The Journal for Technology and Science*, vol. 23, no. 4, pp. 118–125, 2012.

[4] M. Ridwan, A. S. Aisjah, "Prototype Design of Control Systems Tracker Tracks on Unmanned Vessel Using Fuzzy Logic," J*urnal Teknik. Elektro* ,no. 1, pp. 1–8. 2014.

[5] E. Freaks, "HC-SR04 User Guide," *Elec. Freaks*, pp. 1–6, 2011.

[6] Studuino, "Studuino Gyroscope." *Environment and Software*, pp. 1-15, 2012.

[7] Ats, "Advanced Telemetry Systems - *Manual Tracking*," pp. 1–5, 2009.

[8] A. Fallis, "Qualisis pdf," *J. Chem. Inf. Model.*, vol. 53, no. 9, pp. 1689–1699, 2013.

[9] IMO, "COLREGS - International Regulations for Preventing Collisions at Sea," *Conv. Int. Regul. Prev. Collisions Sea, 1972*, pp. 1–74, 1972.

EPI International Journal of Engineering
Volume 1, Number 2, August 2018, pp. 70-73
DOI: 10.25042/epi-ije.082018.11

*p*ISSN 2615-5109
*e*ISSN 2621-0541

In Use of Permeable Groin for Reducing Longshore Sediment Transport at Tanjung Bayang Beach of South Sulawesi

Hasdinar Umar[a,*], Sabaruddin Rahman[b], Chairul Paotonan[c], Ahmad Yasir Baeda[d]

[a] Department of Coastal Engineering/Laboratory of Coastal Engineering, Faculty of Engineering, Universitas Hasanuddin. Email: hasdinar.umar@gmail.com
[b] Department of Coastal Engineering/Laboratory of Coastal Engineering, Faculty of Engineering, Universitas Hasanuddin. Email: sabarahman5@gmail.com
[c] Department of Coastal Engineering/Laboratory of Coastal Engineering, Faculty of Engineering, Universitas Hasanuddin. Email: paotonan_ch@yahoo.com
[d] Department of Coastal Engineering/Laboratory of Coastal Engineering, Faculty of Engineering, Universitas Hasanuddin. Email: baedayasir@gmail.com

Abstract

Breaking wave near beaches is the main force to generate longshore currents, which moved the sediment at surrounding area. Due to its negative outcome, which are erosion and sedimentation, the need of longshore sediment transport analysis become very important. One of the tools for solving that problem is by using coastal protection structure such as permeable groin. Permeable groin may reduce the rate of longshore sediment transport respectively by changing the level of permeability of the groin itself. The objective of this research was to obtain analytical results of the longshore sediment transport reduction analysis by using permeable groins at Tanjung Bayang Beach of South Sulawesi. Reduction of sediment transport along the beach was analyzed by calculating reduction coefficient, which is the ratio between the longshore current before and after hitting the permeable groins. The result showed that with 40% of permeability, the groin can reduce longshore sediment transport at Tanjung Bayang Beach for almost 50%; from 341.37×10^3 m^3/year to 170.68×10^3 m^3/year.

Keywords: Permeable groin; reduction; sediment transport

1. Introduction

Erosion and sedimentation solemnly occurred on some beaches in Indonesia. For example, the erosion occurred in the beach of Teluk Segara Bengkulu City due to crib from the old port of Bengkulu [1]. The crib blocked the longshore sediment transport to the east. Junarsa [2] stated that the erosion occurred in Pantai Pasaruan Serang occurred due to the sediment transport. Umar [3] analyzed the longshore sediment transport at Glagah Beach, Central Java was 343,32,103 m^3/year (west direction). If permeable groins were used with density of piles groin (*p*) 40% then it could reduce the longshore sediment transport up to 166.36.103 m^3/year. Reduction of longshore sediment transport can be determined using the parameter of reduction coefficient [3]. Groin was effectively as sediment traps in the longshore direction and coastal stability buildings at Teluk Penyu Beach. The pattern of coastal line change of Teluk Penyu Beach for 5 years (2014 - 2019) has accretion but tends to be stable with the same value of equal accretion and erosion that was equal to 421 m^2 and 408.56 m^2 [4]. Suswanto [5] determined the critical points of erosion and arranged concept of erosion prevention which considered as a few alternatives of cost protection structure such as groin, breakwater and also recommendations needed to treat Teluk Penyu Beach comprehensively. The cross-shore sediment transport was dominant to the west and longshore sediment transport was to the south. It caused in Akkarena Beach having significant erosion, especially in the area around the estuary [6].

Problems that occured in Tanjung Bayang Beach were the large sedimentation in the upstream of the Jeneberang estuary then emptied at Tanjung Bayang Beach. To overcome the problem, the use of permeable groin as a controller of the longshore sediment transport, was proposed. This paper will discuss and analyze the reduction process of longshore sediment transport by using permeable groin at Tanjung Bayang Beach, South Sulawesi.

*Corresponding author. Tel.: +62-811-416-5078
Jalan Poros Malino km. 6, Bontomarannu
Gowa, Indonesia, 92171

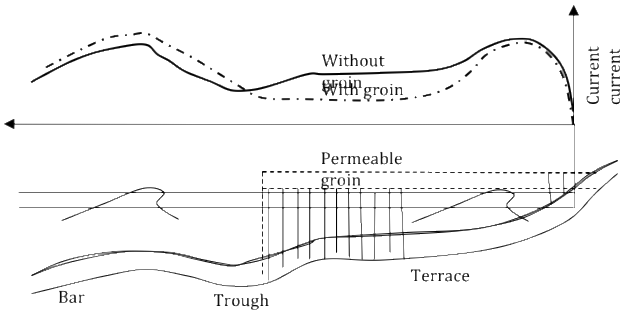

Figure 1. Beach profile after groin piles and alteration of longshore current [7]

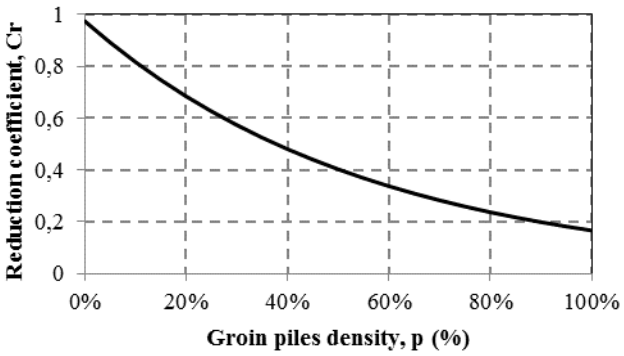

Figure 2. Relation between reduction coefficients (Cr) with density of groin (p)

2. Permeable Groin

The permeable groin has a split structure so that the longshore current can passed through the structure and the sediment can still be transported to the other side. The longshore currents and longshore sediment transport, which flowed through the permeable groins can be controlled by the gap density of the permeable groin structure itself. The widely used permeable groin was a piles groin, one of which was in Raudkivi [7] that examined the use of groin piles on the coast of Baltic Sea. Permeable groin used to reduce the longshore currents and longshore sediment transport but can still provide sediment supply to the other side of groin, which also called down drift groin. The longshore current reduction that occurs after the groin piles can be seen in Fig. 1.

3. Longshore Sediment Transport

The resulting movement of beach sediment along the coast is referred to as littoral transport or longshore sediment transport. In engineering application, the longshore sediment transport rate as the volume transport rate Q_l having units such as m^3/day or m^3/year. The equation of longshore sediment transport as a function of longshore current can be written as follows [8].

$$Q_l = K \frac{\rho \sqrt{g/\gamma b}}{16(\rho_s - \rho)(1-n)} H_b^{2.5} \sin\ \alpha_b \cos\ \alpha_b \qquad (1)$$

with Q_l is longshore sediment transport (m^3/year), K is empiric coefficient which affected by diameter of sediment grains (D_{50}), $K = 1.4e^{-2.5D_{50}}$, ρ is specific gravity of water/sea water (kg/m^3), ρ_s is specific gravity of sediment (kg/m^3), n is porosity of sediment (n = 0.4), H_b is breaking wave height (m), α_b is breaking wave angle (^{o}).

Longshore sediment transport is of particular importance inthat the transport can either be interrupted by the construction of jetties or groin (structure which block all or a portion of the longshore sediment transport), or can be captured by inlets and submarine canyons. If the beach uses the structure of permeable groin, then longshore sediment transport rate would be reduced, so the longshore sediment transport rate after the permeable groin can be written as follows [3]

$$Q_l = C_r K \frac{\rho \sqrt{g/\gamma b}}{16(\rho_s - \rho)(1-n)} H_b^{2.5} \sin\ \alpha_b \cos\ \alpha_b \qquad (2)$$

with C_r is reduction coefficient, where the value of the reduction coefficient parameter depends on the density parameter of the groin piles.

4. Reduction of Longshore Sediment Transport

If the value of the average velocity of the longshore current after the permeable groin can be determined, the coefficient parameter of the longshore current velocity reduction (C_r) can also be determined; which is the ratio between longshore current velocity after the instalment of permeable groin with longshore current velocity without any groin [3].

$$Cr = \frac{\langle v \rangle\, groin}{\langle v \rangle\, without\ groin} = \frac{1}{1 + \dfrac{C_d\, phr}{1.3 C_f\, d_t}} \qquad (3)$$

Equation (3) shows that the parameters of groin piles density affect the magnitude of the longshore current reduction coefficient. If it was illustrated the relationship between the reduction coefficient and the groin piles density, it shows that the greater percentage value of the groin piles density (the gap between the groins was getting denser), the smaller reduction coefficient will be (as in Fig. 2).

5. Case Study of Tanjung Bayang Beach

Tanjung Bayang Beach was located in the mouth of the Jeneberang river which was one of the major rivers in South Sulawesi that flows from Mount Bawakaraeng to Makassar strait and empties into the sea [9].

Table 1. Wave data

Year	Hs(m)	Ts(s)	Dir(deg.)
2007	1.8	7.18	265.26
2008	1.13	5.64	275.92
2009	1.08	5.59	273.62
2010	0.85	5.48	279.43
2011	2.45	7.57	267.11
2012	1.36	6.18	270.14
2013	2.01	7.71	280.15
2014	0.83	6.25	269.37
2015	0.64	7.07	272.96

Table 2. Wave data based on return period

Return period (year)	Hs (m)	Ts (s)
2	1.24	6.29
5	1.94	7.88
10	2.41	8.78
25	3.00	9.80
50	3.44	10.49
100	3.88	11.13

The wave data used in the analysis are the result of wind data analysis in Makassar waters from 2007 to 2015, as shown in Table 1.

Based on the wave data for the above years it could be said that the expected wave was equaled or exceeded once in a given year period, which was a wave with a return period that showed in Table 2.

Based on the wave data then the calculation of longshore sediment transport can use the dominant direction of the wave from West, as shown in Fig. 3.

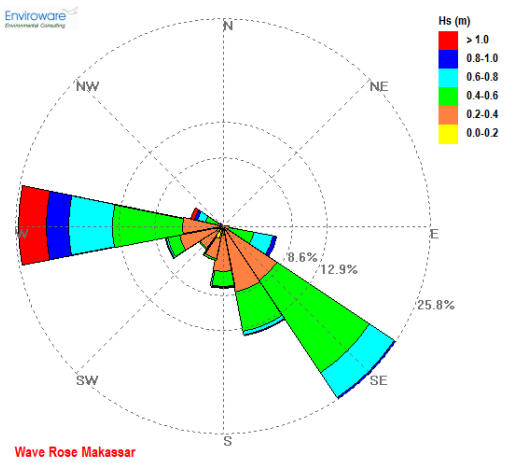

Figure 3. Wave rose of Tanjung Bayang beach

The image of the coastline position toward the wave direction is shown in Fig. 4. The calculation results wave analysis of Tanjung Bayang Beach is shown in Table 3.

Table 3. Wave parameter of Tanjung Bayang Beach

Direction	Return period	H_o (m)	H_b (m)	α_b (°)
West $\alpha = 45^o$	2	1.24	1.21	4.44
	5	1.94	1.89	4.42
	10	2.41	2.35	4.43
	25	3.00	2.93	4.42
	50	3.44	3.36	4.43
	100	3.88	3.79	4.43

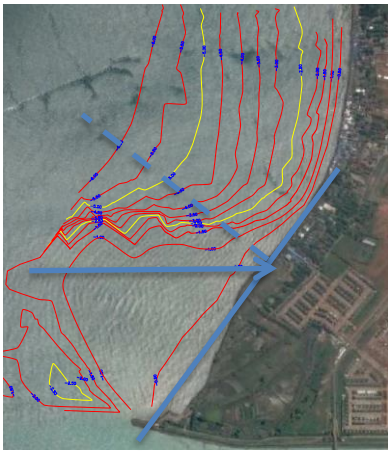

Figure 4. Location of study [10]

Table 4. Longshore sediment transport of Tanjung Bayang beach

Dir	Return period	$Q_{without\ groin}$ (10^3 m^3/year)	$Q_{groin\ permeable}$ (10^3 m^3/year)			
			10%	20%	30%	40%
West $\alpha = 45^o$	2	341.37	273.1	238.96	204.82	170.68
	5	1041.86	833.5	729.3	625.12	520.93
	10	1793.2	1435	1255.2	1075.9	896.59
	25	3097.63	2478	2168.3	1858.6	1548.8
	50	4364.74	3492	3055.3	2618.8	2182.4
	100	5908.41	4727	4135.9	3545	2954.2

While the calculation results of longshore sediment transport at Tanjung Bayang beach before and after there are permeable groin is shown on Table 4. Table 4 showed that with 10% permeability, the groin can reduce the longshore sediment transport up to 80%; with 20% permeability can reduced up to 70% and so on until it can reach 50% reduction at 40% permeability. Raudkivi [6] said that with 50% reduction, beach stability can still be maintained in general. Table 3 also showed that from return period of 2 years until 100 years, if the groin can be maintaining its permeability at 40% and no big changes in structure nor changing climate of surroundings area, then the reduction of longshore sediment transport can also be maintained at approximately 50% respectively.

6. Conclusion

Based on the characteristics of Tanjung Bayang beach and the result analysis of longshore sediment transport reduction, it could be concluded that longshore sediment transport at Tanjung Bayang beach was 341,37.10^3 m^3/year

eastward (due to wave from the west) without the installment of permeable groin. But by using 40% of permeability or groin density, the longshore sedimentation transport at Tanjung Bayang beach can be reduced up to $170.68x10^3$ m^3/year.

Acknowledgements

The authors would like to thank to LP2M Unhas for the grant of Maritime Indonesia Specific Continent (BMIS) 2017 and Coastal Engineering Laboratory, Coastal Engineering Department, Universitas Hasanuddin.

References

[1] Kesumajaya, (2005), Study of coastal erosion and sedimentation Teluk Segara District, Bengkulu City, Magister Tesis, ITB, Bandung.

[2] Junarsa. Dedi, (2006), Study of erosion and solving system at Pasauran Beach, Kabupaten Serang, Propinsi Banten, Magister Thesis ITB, Bandung.

[3] Umar, Hasdinar, (2016), Reduction of Longshore Sediment Transport, Enjiniring Journal, Fakultas Teknik Unhas, ISSN 1411-6243, Vol 20 No. 2, November 2016; page 82.

[4] Yustian. Aulia,and Nugroho, Denny, (2016), Groin Effectiveness Study on The Changes of Coastal Line at Teluk Penyu Beach, Cilacap, Oseanografi Journal, Vol 5, No. 3, 2016, page 406-414.

[5] Suswanto, B, (2017), Study of Coast Protection Structure in Teluk Penyu Beach as Supporting at The Waterfront City Concept in Tobali City South Bangka Regency, Master Theses, ITB, 2017.

[6] Munandar. F.A and Baeda. A.Y, (2014), Study of Sediment Transport at Akkarena Beach, Widyaiswara Network Journal, First Edition No. 1, Jan-Mar 2014.

[7] Raudkivi, (1996), Permeable Pile Groins, Journal of Waterway, Port, and Coastal Engineering, ASCE, 122 (6), pp 267-272.

[8] USACE, (2002), Coastal Engineering Manual, Washington, D.C.

[9] Langkoke, (2011), Coastal Morphodynamic and Prospect of Vegetation Distribution by Backshore Sediment: Estuary Jeneberang Makassar, Doctoral Dissertation.

[10] Anonim, (2012), Tanjung Bayang, Google earth, accessible year 2012.

EPI International Journal of Engineering
Volume 1, Number 2, August 2018, pp. 74-80
DOI: 10.25042/epi-ije.082018.12

*p*ISSN 2615-5109
*e*ISSN 2621-0541

Study on Longitudinal Ship Strength Caused by the Placement of Beams and Girders on Upper Deck Side

Andi Ardianti[a,*], Andi Mursid Nugraha[b], Ganding Sitepu[c], Hamzah[d], Ade Khantari[e], Suandar Baso[f]

[a]Departement of Naval Architecture, Engineering Faculty, Hasanuddin University. Email: aardianti@gmail.com
[b]Departement of Naval Architecture, Engineering Faculty, Hasanuddin University. Email: andi.mursid08@gmail.com
[c]Departement of Naval Architecture, Engineering Faculty, Hasanuddin University. Email: g.sitepu@unhas.ac.id
[d]Departement of Naval Architecture, Engineering Faculty, Hasanuddin University. Email: anca_naval99@yahoo.com
[e]Departement of Naval Architecture, Engineering Faculty, Hasanuddin University. Email: ade.khantari@gmail.com
[f]Departement of Naval Architecture, Engineering Faculty, Hasanuddin University. Email: andar_baso@yahoo.co.id

Abstract

The location of the beam and the deck girder of the ship can be effect on it is strength especially for the longitudinal strength due to the vertical wave bending moment. The objective of this study is to know the structural response of the ship due to vertical bending moment load on hogging and sagging conditions. The analysis is carried out by using Finite Element Method so-called ANSYS™. The results shows that the stress occurring on the ship model with deck beam above the deck plate is larger than the ship model with deck beam under the deck plate. When the load with the variated of 0.2 x moment of vertical moment load, there is an increase of stress that occurs both on the deck area about 12% while on the bottom area about 0.98%. This study also conducted a stress comparison by using analysis methods with analytical methods. The results show that by the Stress differences that occur in the structure with the longitudinal deck beam and deck girder above are 14.1% on the deck and 7.1 on the bottom. Whereas in the structure with deck longitudinal deck eam and deck girder under there is a difference of 5.7% on the deck area and 3.5% in the bottom area of the ship. The stress that occur in both models have a difference that is not too far away and still under the permisible stress by the classification society so that both can be applied to the construction of a tanker.

Keywords: Deck beam; deck girder; longitudinal strength; stress; tanker

1. Introduction

Technical feasibility is one of important aspect in order to build a ship. Technical aspects that must be considered are the strength of ship construction. Ship construction will be good if it is able to withstand the load acting on it. The load type that works on the ships structure consist of internal load and external load. Internal loads are caused by loading on the ship and external loads caused by ocean waves and the position of the ship against the waves themselves and also the wind. While the benchmark that can guarantee the strength of the ship's structure is the stress (stress) experienced by the construction on the ships structure.

To ensure the feasibility of ships structure, regulations on ship construction planning have been issued by the classification bureau in various countries. Ships designed according to class regulations are expected to be able to withstand the load that works while the ship is operating. The thing that needs to be considered in the planning is the continuous distribution of stress flow. The position of ship construction must be avoided by misalignment so that the load distribution is maintained

The ships structure is also efficiently designed to maximize the loading function of the ship. One method of efficiently ship is the installation of deck beams and girders above deck plates on tankers. By using this method, cargo tank will be completely clean on all sides.

The deck beams and deck girder that installed above deck plates may affect the behavior of deck structures in hogging and sagging conditions. Thus, it is important to analyze the impact of deck beams and deck girders placement above deck plates behavior and also the vertical bending moments. For this reason, this study conducted to analize the structure stress due by differences the deck beam and deck girders locations on tankers where the first condition is the deck beam and deck girders installed above the deck plate (Model 1). The second condition is deck beam and deck girders installed under the deck plate (Model 2).

*Corresponding author. Tel.: +62 812 8785620
Jl. Malino, Borongloe, Bontomarannu, Kabupaten Gowa, Sulawesi Selatan 921119

2. Literature Review

2.1. Tanker

Tanker is a type of ship that carry large amounts of flammable oil. As a result, it should build differently from other ships [1]. The requirements that shoud be considered to design a tanker are:

- The stability of tanker is strongly influenced by the effect of free surface of the fluid in the tank
- The cleaning of the oil that settles around the tank makes a lot of pressure on the structural elements of the tanker.
- The surface change of the liquid that is loaded due to temperature expansion and cargo contraction that requires the installation of an expansion trunk in the cargo tank.
- The process of loading and unloading is faster so that it uses less time at the port (not more than one day at a time).
- Tankers implement a one-way traffic system where the vessel is always empty on one route so that it requires sufficient ballast systems.
- Fire risk must be considered and a special ventilation system is applied to allow to release gas, all of task must be resistant to oil.
- Oil can have a very corrosive effect on the hull constructions

2.2. Tanker construction

According to the Lloyd's Register (LR), generally a ship requires full longitudinal framing if the length of the ship exceeds 150 m [2]. Tankers with longitudinal construction have longitudinal bottom frames and longitudinal decks through the tank room. In some cases of tankers, decks beam was installed on top of the deck plates to maximize the ship's loading function and so that the loading tank was completely clean on all sides.

2.3. Loads on the ships hull

According to Rasyid [3], loads that work on ship structures can be grouped into four types, namely:

- Static load,
- Low frequency dynamic loads
- High frequency dynamic loads
- Collition loads

According to Shama [4], the load of hull girder can be categorized as follows:

1. Bending moment
2. Shear load
3. Torsional load
4. Local load

Still water bending moments accounts for an important part of the shear force and bending moment on most ships, wave-induced effects must be added.

The main components of the bending moment of the ships beam are:

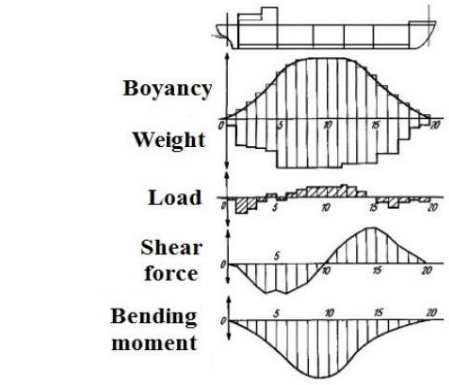

(a)

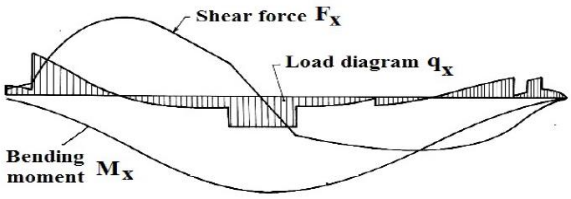

(b)

Figure 1. (a) Load Distributions, Shear Force, and Bending Moments. (b) Combined of Load Distribution, Shear Force, and Bending Moments [4]

a. Still water bending moments
b. Wave bending moments
c. Dynamic bending moments (whipping, slamming, springing)

The bending moment is caused by the load acting on the center of a structure, it is causing the structure to curve.

- Still water bending moments

The bending moment load in still water and the shear force is obtained from the buoyancy distribution (water pressure point) and the weight along the lengthwise construction of the ship as shown in Fig. 1a. Figure 1b shows the combination graph of load distribution, shear force, and bending moment.

- Wave bending moment

This moment is caused by wave conditions such as hogging and sagging conditions. In hogging conditions, the ship get a tensile strenght on the bottom and pressure on the deck. In contrast to sagging conditions. For more details, see Fig. 2.

According to BKI Vol. II [5], the moment caused by wave may be determined by using Eq. 1 below:

$$M_{WV} = L_2 \cdot B \cdot c_0 \cdot c_1 \cdot c_L \cdot c_m \,(\text{KN.m}) \qquad (1)$$

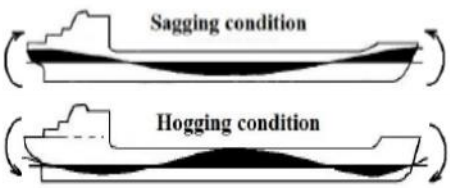

Figure 2. Sagging and Hogging Conditions [4]

where,
L : Ships length (m)
C_0 : Wave Coefficient, as follow;

$= \left[\frac{L}{25}+4\right]C_{RW}$ for L < 90 m

$= \left[10,75-\left(\frac{300-L}{100}\right)^{1,5}\right]C_{RW}$ for 90 m ≤ L ≥ 300 m

$= 10,75 \cdot C_{RW}$ for L > 300 m

C_{RW} : service range coefficient
= 1,00 for unlimited service range
= 0,90 for service range P
= 0,75 for service range L
= 0,60 for service range T

C_1 : sagging/hogging condition as follow
C_{1h} = 0,19. Cb for hogging condition
C_{1s} = -0.11(Cb+0,7) for sagging condition

$C_L = \sqrt{\frac{L}{90}}$ for L < 90 m

= 1,0 for L > 90 m

Cm : distribution factor, see Fig. 3

C_{MH} : hogging condition

$= 2.5 \cdot \frac{X}{L}$ for $\frac{X}{L} < 0.4$

= 1.0 for $0.4 \le \frac{X}{L} \le 0.65$

$= \frac{1-\frac{X}{L}}{0.35}$ for $\frac{X}{L} < 0.65$

C_{MS} : sagging conditon

$= Cv\ 2.5 \cdot \frac{X}{L}$ for $\frac{X}{L} < 0.4$

$= Cv$ for $0.4 \le \frac{X}{L} \le 0.65 \cdot Cv$

$= Cv \cdot \frac{\frac{X}{L}-0.65 \cdot Cv}{1-Cv}$ for $\frac{X}{L} < 0.65 \cdot Cv$

C_v : influence with regard to speed v_0 of the vessel

$= \sqrt[3]{\frac{v_0}{1.4 \cdot \sqrt{L}}} \ge 1.0$ for $1.4 \cdot \sqrt{L} \ge 14$

= 1.0 for damaged condition

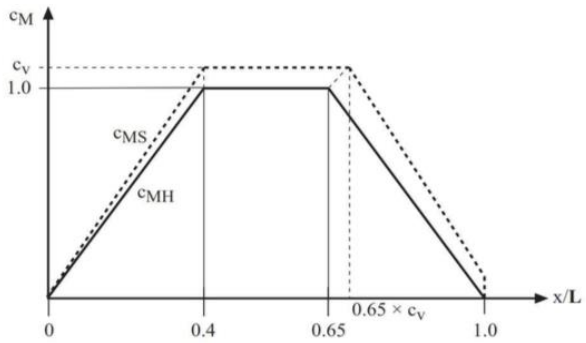

Figure 3. Distribution factor c_M and influrnce factor C_v [5]

2.4. Stress and strain

Stress is defined as the amount of force acting per unit area. There are two types of stress: normal stress and shear stress. Normal stress (σ) is normal force or axial force per unit area [6]. Mathematically, it is formulated as follows:

$$\sigma = \frac{F}{A} \quad (2)$$

where:
σ = stress (N/mm^2)
F = force or load (N)
A = face area (mm^2)

Strain is expressed as the increase of length per unit length. Hooke's law states that within certain limits, the stress on a material is directly proportional to the strain. Strain can be written as:

$$\varepsilon = \frac{\Delta L}{L} \quad (3)$$

where:
ε = strain (N/mm^2)
ΔL = total of length increase (mm)
L = initial lenght (mm)

Stress is static amounts, it is a measure for pressure on structural materials. On the other hand, strains are kinematic amounts; it measures structural deformation. However, deformation depends on the load acting on the structure. Therefore, the stress and strain are not independent. The physical relationship that links this number is called constitutive law. This describes the behavior of structures material under load. It depends on the material and can only be obtained with the help of experiments [7].

One of the most important experiments to find the relationship between stress and strain is the tension or compression test. Here, small specimens of material are placed into the test machine and are elongated or shortened. The force F applied by the machine to the specimen can be read at the engine speed; That causes normal stress $\sigma = F / A$. The change of Δl from the length of the specimen can be obtained and strain can be measured by using $\varepsilon = \Delta l / l$.

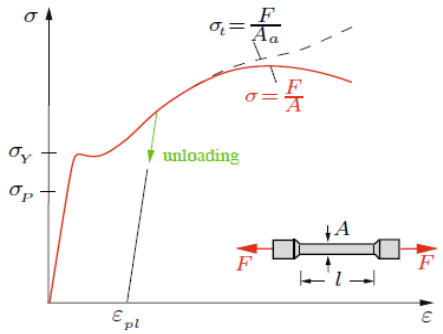

Figure 4. Stress – Strain Curve [7]

The graph of the relationship between stress and strain is shown schematically (not scaled) for the steel specimen in Fig. 4. This graph is called a stress-strain diagram. The graph show that for small values of strain, the relationship is linear (straight line) and the stress is proportional to the strain. This behavior applies until the stress reaches the proportional limit σP. If the stress exceeds the proportional limit, the strain begins to increase faster and the slope of the curve decreases. This continues until the stress reaches the yield stress σY. From this point, the stress-strain diagram show that strain increases at constant stress. Note that many materials do not show clear results points. At the end of the slope the curve increases again which indicates that the material can maintain additional load. This phenomenon is called strain hardening.

2.5. Permissible stress

Permit stress is the stress that causes a construction to experience a large deflection, where the deflection is the limit of a construction that still safe to overcoming the load that occurring or working on it. If the permit stress of the construction concerned is smaller than the maximum stress that occurs, then the construction is not safe.

Based on BKI rules, the normal strength of the steel hull structure is that the hull steel structure has a yield point of REH = 235 N/m^2 and tensile strength Rm = 400 - 520 N/m^2.

The stress acting on the structure can be evaluated by using the value of the permit stress issued by the classification bureau which is 150/k [N/mm^2]. If the working stress that occurs in the conditions of loading the vertical bending moment exceeds the permit stress, the structure or object of the research in an unsafe condition and if the working stress value is less than the value of the permit stress, the structure is in safe condition or meets the rules standards.

2.6. Finite Element Method

Finite Element Method is a numerical method used to solve technical and mathematical problems of a physical phenomenon. The types of physical and mathematical problems that can be solved by finite element methods are structural and non-structural analysis. The type of structural analysis problem includes stress analysis, buckling and vibration analysis. The type of non-structures analysis include heat and mass transfer, fluid mechanics, and the potential distribution of electricity and magneticity [8].

By using Finite Element method, all the complexity of the problem, such as various forms, boundary conditions and loads are maintained but the solutions obtained are estimates number. This is because of its diversity and flexibility as an analytical tool. Quick improvements in computer hardware technology and reduced computer costs have driven this method, because computers are a basic need for the application of this method. A number of popular brand element analysis packages are now commercially available to simplify a complex structure analysis [9]. Some popular packages are STAAD-PRO, GT-STRUDEL, NASTRAN, NISA and ANSYS.

3. Research Methodology

3.1. Tankers data

The models on this study is a tanker with longitudinal framing length less than 150 m, and also the construction of deck beams is above the deck plate. For this reason, this research was conducted to determine the effect of laying the beam against the longitudinal strength of the ship. The data needed for this research is the main dimentions of the tanker, as follow:

Ships Type	:	6500 LT DWT OIL TANKER	
LOA	:	108	meter
B	:	19.2	meter
H	:	9.3	meter
T	:	6	meter

Type of plate material based on ABS [10] are:

Grade	:	A	(ABS Rules)
Tensile Strength	:	550	(N/mm^2)
Yield Point	:	235	(N/mm^2)
Temperature	:	20	(°C)
Young's modulus	:	2,06 x 105 (N/mm^2)	
Poisson ratio	:	0,3	

3.2. Structure modeling

Modeling is done by using ANSYS^{TM} software, the modeling started from defining the element type, installing constraints, loading and analyzing results. The steps in modeling the structure of the load space are:

- Structural modeling, tanker structure is modeled in two ways, installing the deck beams and deck girders above deck plates and installing the beams and deck supports under deck plates. The modeled part of the tanker's construction is frame 85 - 90 with distance 650 mm.
- The element type that used is the shell element type 63. The shell element type is selected because it is suitable for plate modeling and has six degrees of freedom for each node.
- Meshing, meshing size and quality is very important to obtain a good result, but the smaller the meshing value, the computer device used must have high specifications. In this study, the meshing size used was 100 mm in quad mapped form.
- Installation of constraints and the boundary conditions applied to the finite element model is dependent on the type of load increase process that used. The boundary conditions in this study are all end points of the aft part model are given a full constraint. There is no loading at the reference point aft. At the end of the model section fwd at the reference point of the neutral axis, given the bending moment then all points at the end of the fwd are rigid full link constraints to the neutral axis reference point. The taking of the boundary conditions in this calculation is the pinch pedestal on one side and the simple support on the other side.
- Loading, in this analysis use the vertical bending moment in hogging and sagging conditions with reference to BKI rules.

- Settlement, in general, there are two types of solutions, namely static analysis and dynamic analysis. In this analysis static analysis was carried out. Completion is carried out on the model in the form of elements according to the loading and conditions of the boundary conditions given to the model. This process is called running. At this stage finite element software runs the analysis process of the model that has been harmonized in element form until given certain boundary and load conditions.

3.3. Loading variations

Loading variations conducted to get the tendency of the tanker's structural response to any changes in load. In this study, the maximum vertical bending moment load is 4.59 x 1011 N/mm^2 in hogging conditions and -4.43 x 1011 N/mm^2 in sagging conditions, the reference load is assumed to be 100% load. The load will decrease every multiple of 0.2 x Total vertical bending moment (Mt) in hogging and sagging conditions.

4. Numerical Result

After the analysis process, the stress values that occur in each model were obtained. Figure 5 shows the example of the results of deck construction analysis by using software ANSYS. The input data is listed in Table 1.

Table 1. Value of Vertical bending moment variation

Load Variation	Vertical Bending Moment	
	Hogging Condition	Sagging Condition
0	0	0
0.2 x Mt	9.18E+10	-8.86E+10
0.4 x Mt	1.84E+11	-1.77E+11
0.6 x Mt	2.75E+11	-2.66E+11
0.8 x Mt	3.67E+11	-3.55E+11
Mt	4.59E+11	-4.43E+11

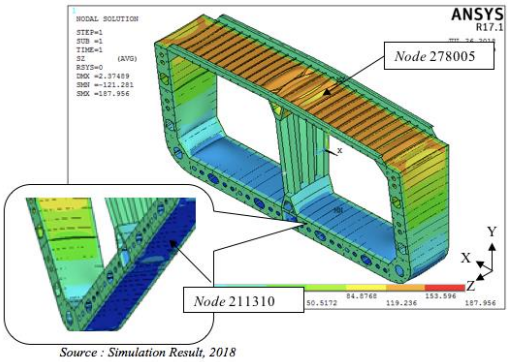

(a) Model 1

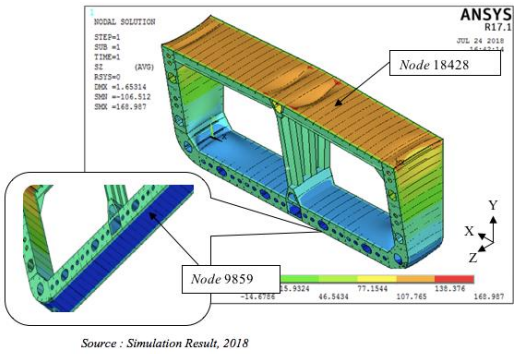

(b) Model 2

Figure 5. Behavior of stress distribution in hogging conditions with beams and deck supports above deck plate. (a) Model 1, tankers construction with deck beam and deck girder installed above the deck plate. (b) Model 2, tankers construction with deck beam and deck girder installed under the deck plate

From the results of the analysis, it will be reviewed about the maximum stress of the deck area and the bottom area of each model under hongging conditions and sagging conditions. Analysis is carried out at maximum stress because this voltage is considered to be the most influential in determining whether the structure meets the requirements or not.

Tabel 2. Stress that occurs during Hogging conditions

Load Variation	*Moment Hogging* (Nmm)	Model 1		Model 2	
		Stresses on deck (N/mm^2)	Stresses on Bottom (N/mm^2)	Stresses on deck (N/mm^2)	Stresses on Bottom (N/mm^2)
0	0,00E+00	0	0	0	0
0,2 x Mt	9.18E+10	27.576	-16.466	24.035	-16.301
0,4 x Mt	1.84E+11	55.27	-33.003	48.174	-32.674
0,6 x Mt	2.75E+11	82.608	-49.325	72.00	-48.833
0,8 x Mt	3.67E+11	110.24	-65.827	96.087	-65.17
Mt	4.59E+11	137.88	-82.328	120.17	-81.507

Table 3. Stress that occurs during Sagging Conditions

Load Variation	*Moment Hogging* (Nmm)	Model 1		Model 2	
		Stresses on deck (N/mm^2)	Stresses on Bottom (N/mm^2)	Stresses on deck (N/mm^2)	Stresses on Bottom (N/mm^2)
0	0,00E+00	0	0	0	0
0,2 x Mt	-8. 86 E+10	-26.615	15.892	-23.197	15.733
0,4 x Mt	-1.77 E+11	-53.17	31.748	-46.342	31.431
0,6 x Mt	-2.66 E+11	-79.905	47.711	-69.643	47.235
0,8 x Mt	-3.55 E+11	-106.64	63.674	-92.945	63.039
Mt	-4.43 E+11	-133.07	79.458	-115.99	78.666

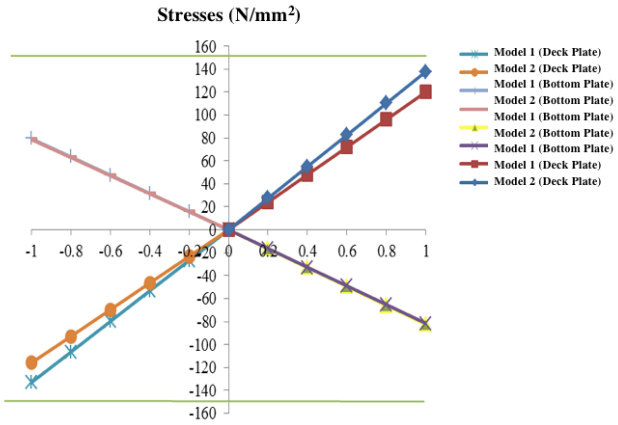

Figure 6. The relationship curve between the increase of the vertical bending moment and the working stress

According to Tables 2 and 3, it is known that the stress that occurs due to the vertical bending moment in the tankers constructin with deck beam and deck girder installed above the deck plate is greater than the stress that occurs in the tanker's construction with deck beam and deck girder installed under the deck plate both in hogging and sagging conditions. In hogging conditions, the difference stress that occurs on the deck area is 12.8% and the stress that occur on bottom area is 0.98%. Whereas in sagging conditions, the stress difference that occurs in tankers construction with deck beam and deck girder intalled above deck plates comared with deck beam and deck girder installed under deck plates is 12.82% on deck area and 0.996% on bottom area. However, this stresses value are still below of the stress allowed by the BKI so the structure is concluded safe. Besides that, the stresses difference between the two structural models is not too much different.

The comparison of stresses that occur on the models with deck beam and deck girder construction lay on above deck plate and the models with beams and deck girder construction under the deck plate was show in Fig. 6.

Based on Table 4, the stress difference between FEA and Analytic on the deck area is 14.1% while on the bottom area is 7%.

Table 4. Comparison of the stresses generated by using the FEA and analytic methods in Hogging condition for Model 1

Moment Hogging (Nmm)	Deck Plate			Bottom Plate		
	FEA (N/mm^2)	Analytic (N/mm^2)	Difference (%)	FEA (N/mm^2)	Analytic (N/mm^2)	Difference (%)
0,00E+00	0	0.00	0	0	0.00	0
9.18E+10	27.576	23.69	14.11	-16.466	-17.64	7.12
1.84E+11	55.27	47.37	14.29	-33.003	-35.28	6.89
2.75E+11	82.608	71.06	13.98	-49.325	-52.91	7.28
3.67E+11	110.24	94.74	14.06	-65.827	-70.55	7.18
4.59E+11	137.88	118.43	14.11	-82.328	-88.19	7.12

Table 5. Comparison of the stresses generated by using the FEA and analytic methods in Sagging condition for Model 1

Moment Hogging (Nmm)	Deck Plate			Bottom Plate		
	FEA (N/mm^2)	Analytic (N/mm^2)	Difference (%)	FEA (N/mm^2)	Analytic (N/mm^2)	Difference (%)
0,00E+00	0	0.00	0	0	0.00	0
-8. 86 E+10	-26.615	-22.87	14.09	15.892	17.03	7.15
-1.77 E+11	-53.17	-45.73	13.99	31.748	34.06	7.27
-2.66 E+11	-79.905	-68.60	14.15	47.711	51.08	7.07
-3.55 E+11	-106.64	-91.46	14.23	63.674	68.11	6.97
-4.43 E+11	-133.07	-114.33	14.08	79.458	85.14	7.15

Table 5 shows that the averaged stress difference on deck areas and bottom area analysis by using FEA and Analytical method about 14.1% on deck areas while in the bottom area was 7.1%.

In addition to using ANSYS™ Software in this study, analytic calculations were performed to compare the results obtained in the FEA method. Comparison of stresses that occur between these two methods can be seen in Table 4 and Table 5. The result comparisons result for models with deck beam and deck girder construction installed above deck plate was show in Table 6 and the result for models with deck beam and deck girder installed under the deck plate was show in Table 7.

Table 7 shows that the stresses difference between FEA and Analytical on deck plate stress is 5.6% while on the bottom plate is 3.5%. Table 6 shows that the stress difference between FEA and Analytic on deck plate is 5.7% while on the bottom plate is 3.55%.

Table 6. Comparison of the stresses generated by using the FEA and analytic methods in Hogging condition for Model 2

Moment Hogging (Nmm)	Deck Plate			Bottom Plate		
	FEA (N/mm^2)	Analytic (N/mm^2)	Difference (%)	FEA (N/mm^2)	Analytic (N/mm^2)	Difference (%)
0,00E+00	0	0.00	0	0	0.00	3.56
9.18E+10	24.04	22.74	5.70	-16.301	-16.88	3.33
1.84E+11	48.17	45.48	5.93	-31.674	-33.76	3.71
2.75E+11	72.00	68.22	5.54	-48.833	-50.64	3.61
3.67E+11	96.09	90.96	5.64	-65.17	-67.53	3.56
4.59E+11	120.17	113.70	5.69	-81.507	-84.41	3.56

Table 7. Comparison of the stresses generated by using the FEA and analytic methods in Sagging condition for Model 2.

Moment Hogging (Nmm)	Deck Plate			Bottom Plate		
	FEA (N/mm^2)	Analytic (N/mm^2)	Difference (%)	FEA (N/mm^2)	Analytic (N/mm^2)	Difference (%)
0,00E+00	0	0.00	0	0	0.00	3.56
-8. 86 E+10	-23.197	-21.95	5.67	15.733	16.30	3.58
-1.77 E+11	-46.342	-43.90	5.55	31.431	32.59	3.70
-2.66 E+11	-69.643	-65.86	5.75	47.235	48.89	3.51
-3.55 E+11	-92.945	-87.81	5.85	63.039	65.19	3.41
-4.43 E+11	-115.99	-109.76	5.68	78.666	81.48	3.58

5. Conclusions

This research conducted by using ANSYS 17.1 software and analysis by using Finite Element Method. Based on the result from this research can be concluded as below:

- The deck beam and deck girder position give effect to the magnitude of the cross-section modulus. By installing the deck beam and deck girder above the deck plate, it will increase the location of the center of gravity of the ship's structure by 2.3%. Changes in the location of the center of gravity (Neutral Axis) will have an impact on the change in inertia moment of the cross section.
- The maximum stress that occurs in construction with deck beams and deck girder installing above deck plates is greater than the construction of ships with deck beams and deck girders under deck plates. In other words, the construction of a ship with deck reinforcement installing under the deck plate is better than the construction of a ship with a deck reinforcement that installing above the deck plate, although it is not significant.
- In both conditions, the stresses difference that occurs in both models construction are 12.84% on the deck plate and 0.98% on the bottom plate.
- Stress difference using Finite Element Analysys (FEA) method and analytical method in hogging conditions are 14.1% on deck plates and 7.1% on bottom plate. Whereas in sagging conditions the stress difference is 5.6% on the deck plate and 3.5% on the bottom plate

References

[1] Barabanov, N. 1972. Structural Design of Sea-Going Ships. Translated by: Oleg Sapunov. Peace Publisher. Moscow.
[2] Eyres, D.J. 2001. Ship Construction fifth edition. Butterworth Heinneman. London.
[3] Rasyid, Daniel Muhammad. 2000. Strength of Ship Structure. Pradnya Paramita. Jakarta. [in Bahasa Indonesia]
[4] Shama, Mohamed. 2013. Buckling of Ship Structures. Alexandria University, Egypt.
[5] Biro Klasifikasi Indonesia. 2014. Rules for the Clasification And Construction Seagoing Steel Ship, Volume II. BKI. Jakarta.
[6] Patnaik, Surya N. and Dale A. Hopkins. 2004. Strength of Materials. Elsevier. Amsterdam.
[7] Gross, Dietmar. 2011. Engineering Mechanics 2 “Mechanics of Materials”. Springer. London.
[8] Susatio, Yerri. 2004. Basics of Finite Element Method. Andi. Yogyakarta. [in Bahasa Indonesia].
[9] Bhavikatti, S.S. 2005. Finite Element Analysis. New age International Publisher. New Delhi.
[10] ABS. 2013. Rules for Requirement Materials and Welding, USA.

EPI International Journal of Engineering
Volume 1, Number 2, August 2018, pp. 81-86
DOI: 10.25042/epi-ije.082018.13

*p*ISSN 2615-5109
*e*ISSN 2621-0541

Improved Performance of Silicon Rubber Insulation with Coal Fly Ash Micro Filler

Tajuddin Waris[a,*], Yoshinobu Murakami[b], Naohiro Hozumi[c], Tomohiro Kawashima[d], Salama Manjang[e], Ikhlas Kitta[f]

[a]Department of Electrical and Electronic Information, Toyohashi University of Technology. Email: t17922@edu.tut.ac.jp
[b]Department of Electrical and Electronic Information, Toyohashi University of Technology. Email: murakami@ee.tut.ac.jp
[c]Department of Electrical and Electronic Information, Toyohashi University of Technology. Email: hozumi@ee.tut.ac.jp
[d]Department of Electrical and Electronic Information, Toyohashi University of Technology. Email: kawashima@ee.tut.ac.jp
[e]Department of Electrical Engineering, Hasanuddin University. Email: salamamanjang@unhas.ac.id
[f]Department of Electrical Engineering, Hasanuddin University. Email: ikhlaskitta@gmail.com

Abstract

This paper presents the effect of coal fly ash micro filler (CFA) on the electrical properties of silicon rubber insulation. The observed electrical properties are volume resistance, surface resistance, flash over inception voltage dependence on CFA filler loading and temperature. The type of silicon used is room temperature vulcanized (RTV) 683 and the filler concentrations of the matrix are 0,10.20,30,40 per-hundred gram of resin (phr). The test results show that the surface resistance increased significantly with the increasing of CFA loading filler. The increasing of volume resistance is nonlinear; the volume resistance tends to decrease when the CFA loading filler exceeds 20 phr. Flashover inception voltage increase with the increasing of CFA filler loading, but decrease with the temperature increase.

Keywords: coal fly ash; flashover; resistance; silicon rubber

1. Introduction

Today, polymeric insulators probably the most efficient solution for outdoor insulator due to some advantages such as ultralow conductivity, excellent hydrophobicity, high flashover voltage, easy maintenance, and processing at low cost. The polymeric insulators are incredibly suitable for applications in the transmission and distribution sector. It has an impressive spectrum of electrical, physical, mechanical and chemical properties [1].

Compared to other polymeric materials, silicones exhibit very good long lasting hydrophobicity. Insulating components made of silicone rubber compounds still repel water after many years in application. Silicone elastomers are particularly resistant to UV radiation, even harsh weather conditions, as found in coastal regions. In addition, Silicones have high electrical resistivity, low dielectric loss factor, extremely elastic, low flammability and temperature stability [2-3].

The polymer can not perform satisfactorily in numerous application in pure form (unfilled). Therefore, the application of filler on polymer insulation is required to improve mechanical and electrical properties and to reduce unit the cost of insulation. Currently, the popular filler used are SiO_2, Al_2O_3 and MgO in nano and micro size [3-5].

They have been reported as good filler from the viewpoint of electrical properties. However, their price is still very high hence the unit price of insulation increase.

CFA is the waste by-product from coal steam power. Its vast majority of chemical content are SiO_2, Al_2O_3, and Fe_2O_3. Also, its price is very cheap even almost free and available abundantly. Those reasons make coal fly ash could be applied as a filler on silicon rubber insulation [6].

Up to now, the application of coal fly ash as a filler mostly on material construction and ceramic industry [7].

2. Material and Experimental Method

2.1. Silicon rubber

Silicone or Polysiloxanes rubber is an elastomer compose of silicon, carbon, hydrogen, and oxygen. It is widely applied as material insulation on electrical power system particularly in a high voltage transmission line to substitute porcelain insulation. Silicon rubber has superiority properties over porcelain insulator. The most outstanding property of silicone rubber is excellent dielectric

*Corresponding author. Tel.: +81-80-2290-8979
Machi Hata Cho- Aza Morita 49, Sakou Jutaku 1-17
Toyuhashi Shi, Japan, 441-8101

properties, low relative permittivity, low dielectric loss, high stretch ability and excellent hydrophobicity.

Silicone rubber offers excellent resistance to extreme temperatures, being able to apply from −100 to 300 °C. Some other properties such as elongation, creep, cyclic, flexing, tear strength, thermal conductivity, high compression, fire resistance and high tensile. Therefore, it is suitable for the application at high polluted and when retention of initial shape and mechanical strength are requirements under heavy thermal stress or sub-zero temperatures. In addition, it has a carbon-to-carbon backbone which can leave it susceptible ozone, heat and other aging factors that silicone rubber can withstand well. By which silicone rubber one of the elastomers of choice in extreme environment application [8].

Silicon differs from other polymers. Its backbones consist of cycling Si-O-Si units. Unlike many other polymers that contain carbon backbones. Silicon has a very large angle and bond length compared to other polymers such as polyethylene. Hence, It can move farther and change formation easily yielding a flexible material. In addition, it also tends to be chemically inert, due to the strength of the silicon-oxygen bond [9].

There some kinds of silicon rubber such as high temperature vulcanize silicon rubber (HTV-SiR), room temperature vulcanizing silicon rubber (RTV-SiR) and liquid silicon rubber. In this study, silicon rubber used is RTV 683, supplied by PT. Metapel.

2.2. Coal Fly Ash (CFA)

The characteristic of CFA mostly depends on the coal quality and combustion process. The quality of coal fly ash has been reported in [10]. Those reports show the characteristic from many sources of CFA which involves chemical content, size, microstructure and electrical resistance.

The CFA used in this research is provided by local cement industry, PT. Semen Tonasa (Persero). The Classification CFA ash used is F class according to ASTM C612.

The image of a microstructure of coal fly ash used in this study obtained from Scanning Electron Microscope (SEM) is presented in Fig. 1. It shows that the particle of CFA is irregular shape and size.

CFA is a composite material which consists of some chemical substance as presented in Table 1. The chemical contents of CFA used have been examined by using XRF (X- Ray Fluorescence).

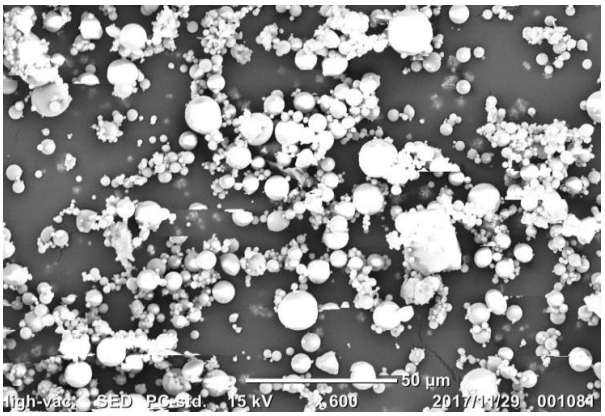

Figure 1. SEM images of coal fly ash (CFA)

Table 1. The Chemical contents of CFA

Chemical	Percentage
SiO_2	40.16
Fe_2O_3	20.22
Al_2O_3	19.48
CaO	8.35
K_2O	1.75
TiO_2	1.30
BaO	0.19
SrO	0.12
ZrO_2	0.06
Others	8.0

Table 1 highlights that vast majority contents of CFA are Si_2O_3, Fe_2O_3 and Al_2O_3. Those chemicals have been used as filler in composite material both on epoxy and silicon rubber in form of nano-filler or micro-filler. Their applications have proven to improve the electrical and mechanical properties of composite insulation material. Their effectiveness as a filler was determined by some factors, such as: particles size, filler loading and dispersion [3-5].

The particle size distribution of CFA has been examined by using Shimadu SALD-2300 (wing SALD II Version 3.32). Its particle size distribution is presented in Table 2. It shows that the particle size is irregular, the vast majority of CFA particle size is equal or less than 20 µm.

Table 2. Range of particle size distribution of Coal Fly Ash

Range of Particle Size (µm)	Percentage (%)
$20 \geq x$	55.14
$40 \geq x > 20$	29.54
$60 \geq x > 40$	8.47
$80 \geq x > 60$	3.95
$x > 80$	2.90

In this research different mass concentration of CFA was added as a filler into RTV Silicon rubber as a matrix. The impact of the coal fly concentration on electrical properties of silicon rubber composite would be studied.

2.3. Sample preparation

The silicon rubber room temperature vulcanize namely RTV 683 is applied as host matrix without any pre-treatment. While coal fly ash as a filler. The silicon rubber is supplied by PT. Metapel and the coal fly ash is provided by PT. Semen Tonasa (Persero).

To investigate the effect of filler concentration on the electrical properties of silicon rubber, the samples are grouped according to the phr filler loading 0,10,20,30,40 phr respectively. Sample with filler 0 phr means sample without filler and investigates as references. The hardener is also applied to fasten the vulcanizing process. Material sample is vulcanized in room temperature 28 °C, humidity 75%.

The sample preparation consists of some steps as as presented in Fig. 2.

The material sample that consists of silicon rubber, hardener and CFA are weighed using a digital scale with accuracy up to 0.01 gram. Silicon rubber and CFA with the specific amount ratio (phr) were mixed and mechanically blended for 30 minutes at room temperature to well dispersion. The next step is vacuuming or degassing process to remove air bubble trapped (void) in the mixture. The vacuum pressure applied is 650 mmHg for 25 minutes. Then, the mixture was molded into a circular molding pot with dimension 200 mm and 3 mm in diameter and thickness respectively. The vulcanizing time is about 2 hours at room temperature, and humidity is about 30 °C and 80% respectively. The samples were released from molding case after 3 hours. Finally, the samples put into the oven for 12 hours at 85 C for drying. Samples produced by the above process are shown in Fig. 3.

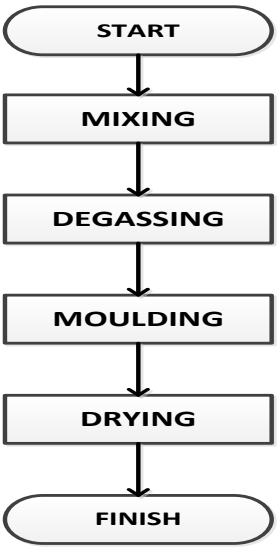

Figure 2. Sample preparation flowchart

Figure 3. Sample of silicon rubber with coal fly ash filler

2.4. Experimental method

The electrical properties of silicon rubber with CFA filler investigated in this study consists of surface resistance, volume resistance, surface flashover and dependence of surface flashover over ambient

2.4.1. Surface resistance

The surface resistance of samples is measured according to ASTM standard D257. Experimental setup for surface resistance is depicted in Fig. 4.

Sample dimension was adjusted according to the size of the electrode system, 100 mm x 40 mm 3 mm. The number of samples per group is 5 sample. The sample was placed on electrode system after its surface wiping with ethanol and to improve the surface contact between the electrode and the sample; the constant weight was put on the sample.

The volume conduction current of a sample was measured for 300 seconds under 1.5 kV, DC. The surface resistivity was calculated by the following equation:

$$\rho_s = \frac{V \cdot W}{I_s \cdot d} \quad (1)$$

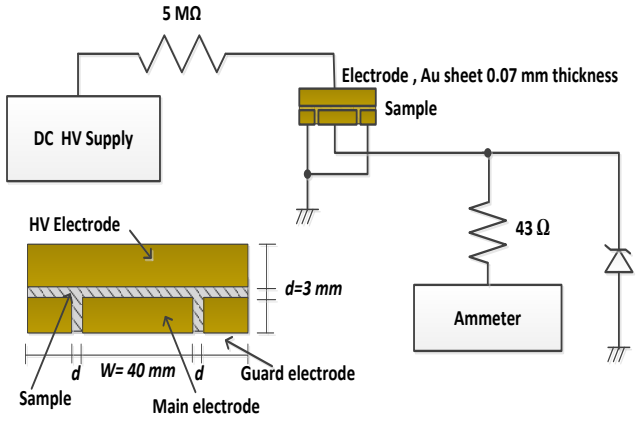

Figure 4. Surface conduction current measurement system

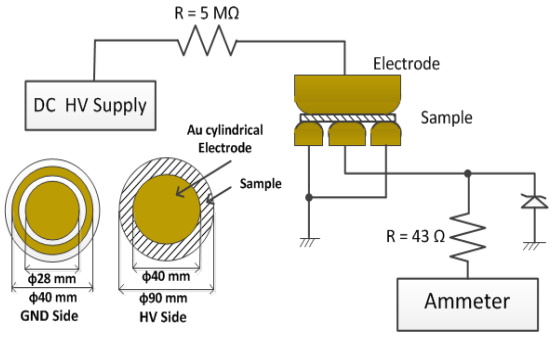

Figure 5. Volume conduction current measurement system

Where W is the width of the main electrode and d the distance between electrodes. V is the applied voltage and I_s is the average value of the surface conduction current after the first 60 seconds due to the transient current in this time range.

2.4.2. *Volume resistivity*

Volume resistance of samples are measured according to ASTM standard D257. Experimental set up is presented in Fig. 5. The sample was placed between HV electrode and the main electrode. To improve the contact between electrode and sample and to prevent disposition of sample, the pressure on the sample is controlled by adjusting the screw of the electrode system. HV supply is 1.5 kV, DC. Volume conduction current is measured for 300 seconds.

The volume resistivity was calculated by the following equation:

$$\rho_v = \frac{V \cdot S}{I_v \cdot d_v} \tag{2}$$

S is the surface area of the main electrode and d_v is the distance between HV electrode and main electrodes. V is the applied voltage and I_v the average value of the volume conduction current. As like on surface conduction current measurement, volume conduction current during transition time is also neglected.

2.4. *Flashover inception voltage*

Dry power frequency external flashover has been determined by averaging five flashover voltage measurements, according to IEC 60060-1. Fig. 6 shows measurement system for flashover inception voltage test.

The electrode system is a copper tape with thickness 75 µm in semicircular configuration with the diameter of 30 mm, and the gap between electrode is 25 mm. The sample prepared is Silicon rubber with different loading CFA filler. Sample dimension is 40 mm x 15 mm x 5 mm. Before testing, samples are wiped with ethanol to eliminate contaminant on the sample surface.

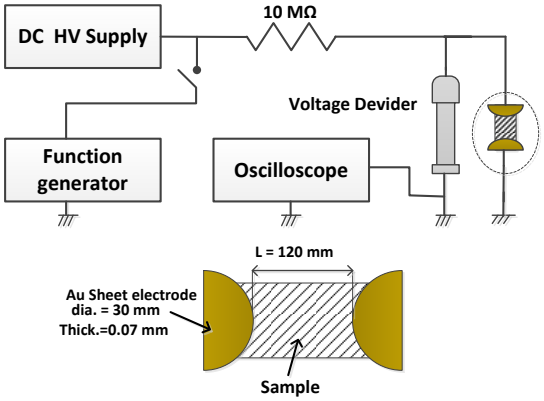

Figure 6. Flashover inception voltage experimental set up

The sample tested put into the oven. The oven temperature is adjusted to a specific temperature to simulate the ambient condition. During the test, the temperature and humidity are maintained constant. To determine the effect of temperature on FOIV of silicon rubber with CFA filler, the testing is carried at some specific temperature 25,40,60,80 °C respectively. In this case, only a group sample with 30 phr is tested. Humidity during the testing is 58 %.

The FOIV has been obtained by increasing the voltage linearly to flashover with increasing rate 1.0 kV/second. The DC ramp voltage is applied until the flashover on the surface of the sample occurs. The occurrence of flashover is monitored using an oscilloscope, and FOIV value is recorded.

3. Results and Discussion

3.1. *Volume resistivity*

The volume resistivity of silicon rubber with different CFA filler loading is presented in Fig. 7. Five valid measurement data was obtained so the accurate volume resistivity data could be calculated.

. The values presented in Fig. 7 are the average value from five measurements. It is revealed that, with the addition of CFA filler loading, the significant increase of volume resistivity is observed, but when CFA filler loading

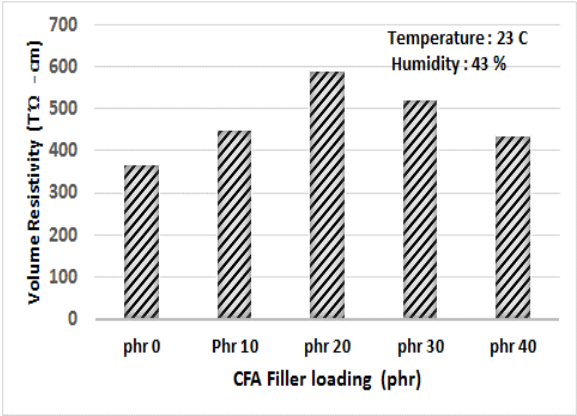

Figure 7. Volume resistivity of Silicon Rubber with different CFA filler loading

reaches higher than 20 phr, the volume resistivity decline. The decreasing of volume resistivity after 20 phr due to semi-conducted materials content of CFA such as Fe2O3, at high filler loading internal distance between filler particles become smaller leads to the formation of resistance bridge as a consequence the volume resistance of composite tends to decrease

3.2. Surface resistance

Surface resistance of silicon rubber with different CFA filler loading is presented in Fig. 8. It can be seen that the surface resistance increases with increasing filler concentration. Based on the nature of electric current, when the voltage applied to the surface, current does not flow on the surface only but also inflow in the material. Therefore, the sample thickness also determined the surface resistivity. Also, the surface contaminant, temperature, and humidity affect the surface resistivity of the tested material.

The increasing of surface resistivity could be caused by some factors, such as mineral content of CFA like and are high resistance in nature. The electrical strength on the surface of the material during the testing change the property of semi-conductive mineral contained on CFA filler. The polarization of the material surface due to a high electric field may increase the surface resistivity; the longer material surface is exposed to electrical field the more surface resistivity increase.

3.3. Flashover Inception Voltage.

The average values of flashover inception voltage (FOIV) of silicon rubber with different CFA filler loading is presented in Fig. 9.

It can be seen from the Fig. 9, flashover inception voltage increase with the increasing of CFA filler loading. The flashover inception voltage is determined by some factors such as electrical properties, physical structure and environmental parameter on the material surface [11]. In this case, the increasing of flashover inception voltage mainly is determined by the surface resistance of silicon rubber. The higher surface resistance, the higher flashover inception voltage.

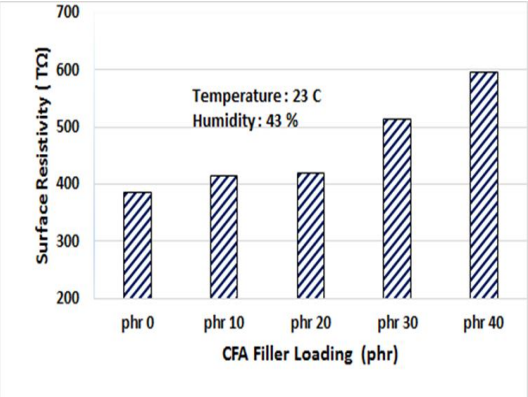

Figure 8. Surface resistivity of Silicon Rubber with different CFA filler loading.

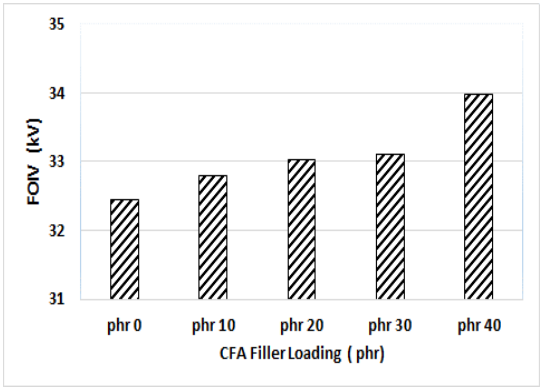

Figure 9. The effect of CFA filler loading on flashover inception voltage of Silicon Rubber

As depicted in Fig. 8, the surface resistivity increase with the increasing of CFA filler loading. Therefore, the increasing flashover inception voltage as presented in Fig. 9 directly correlated with the increase of surface resistance.

It is assumed that the surface charge is generated from the HV electrode and move toward the counter electrode [12]. The surface charge movement change by the surface resistivity of the sample. In case of high surface resistivity of the sample, the surface charge hardly moves to approach the counter electrode. Therefore, the inception voltage increase with the increase of surface resistivity of the material composite.

The effect of temperature on FOIV of silicon rubber with CFA filler is depicted in Fig. 10. It shows that as the temperature increase the VOIV also increase. Surface resistance is one of the factor affecting flashover. Since insulation resistance tends to decrease with the increasing temperature. FOIV of the silicon rubber insulation have a temperature dependence in the temperature range over 40 °C, but it is nearly constant in the temperature range under 40 °C.

In this study, the application of CFA filler on silicon rubber has shown improvement electric insulating property. Hence it has a good prospect in application in insulation material. However, further study has to be carried out for some other dielectric properties such as: hydrophobicity, permittivity, dielectric loss, and breakdown strength.

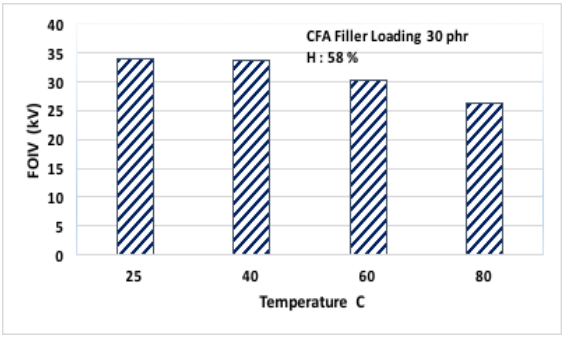

Figure 10. Dependence of FOIV of Silicon Rubber with CFA on temperature.

4. Conclusions

This study, the effect of CFA as a filler on electrical properties of silicon rubber was investigated. The effects of CFA filler loading can be summarized as follow:

1) The increasing of CFA loading filler increase the volume resistivity of composite silicon rubber significantly. But when CFA filler loading reaches higher than 20 phr, the volume resistivity tens to decline.
2) The loading of CFA effectively improve the surface resistivity of Silicon rubber composite, and CFA loading filler exceed 20 phr has a better improvement.
3) Obtained results show that flashover inception voltage increase with the increasing of CFA filler loading. In this case, the increasing of flashover inception voltage mainly is determined by the surface resistance of silicon rubber. The surface resistivity decrease with the increase of temperature yields the decline of flashover inception voltage (FOIV).

Acknowledgement

The first author would like to thanks to Project for Capacity Building in Engineering, Science and. Technology (C-BEST), Hasanuddin University for doctoral scholarship at Toyohashi University of Technology.

References

[1] Kyriako Siderakis, Demosthenes Agoris, Stanslaw M. Gubanski. Salt Fog Evaluation of RTV SIR Coating WithDifferent Fillers. IEEE Transaction on Power Delivery, Vol. 23 No. 4, October 2008, pp. 2270 – 2277.

[2] B.X.Du. Hydrophobicity Evaluation of Silicone Rubber Insulator Using DC Discharge Induced Acoustic Wave. IEEE Trans. On Dielectric and Electrical Insulation, October 2013, pp.1836 – 1844.

[3] M. Ehsani, H. Borsi, E. Gockenbah, J. Morshedian, G.R. Bakhshadendeh. An investigation of dynamic, thermal, and electrical of housing materials for outdoor polymeric insulators. European Polymer Journal 40 (2004) pp. 2495-2503.

[4] Z. Li, K. Okamoto, Y. Oki and T. Tanaka. Effect of Nano Filler Addition on Partial Discaharge resistance and dielectric breakdown strength of Micro – Al_2O_3/Epoxy Composite. IEEE Transaction Dielectr. Electr. Insulation Vol.17, pp. 653-661, 2010.

[5] Z. Li, K. Okamoto, Y. Oki and T. Tanaka. The Role of Nano and Micro Particles on on Partial Discharge and Breakdown Strength in Epoxy composite. IEEE Trans. Dielectr. Electr. Insulation, Vol. 18, pp. 678-681.

[6] I. Kitta, S. Manjang, W. Tjaronge, R. Irmawaty. Performance Study of Silicone Rubber Polymer was Filled Fly Ash as Insulator Material on High Voltage Transmission Tower, International Journal of Innovative Research in Advanced Engineering (IJIRAE), ISSN: 2349-2763, Issue 01, Volume 3, January, pp. 120-124, 2016.

[7] Shixin Zeng, Jialai Wang. Characterization of mechanical and electric properties of geopolymers synthesized using four locally available fly ashes. Elsevier Construction and Building Material 121 (2016) pp. 386 -399.

[8] Shin-Etsu. Characteristic Properties of Silicone Rubber Compounds. http://www.silicone.jp/e/catalog/pdf/rubber_e.pdf.

[9] Anjum Saleem, Lars Frormamn, Alexander Soever. Fabrication of Entrinsically Conductive Silicon Rubbers with High Elasticity and Analysis of Their Mechanical and Electrical Characteristics. Polymer 2010, ISSN 2073-4360.

[10] Avinash Candra. Some Investigation on Fly Ash Resistivity Generated in India Power Plants. 11th International Conference on Electrostatic Precipitation, 2010.

[11] S. Venkataraman, R. S. Gorur and A. P. Mishra. Impact of Weathering on Flashover Performance of Nonceramic Insulators. IEEE Transactions on Dielectrics and Electrical Insulation, Vol. 15, No. 4, August 2008, pp. 1073-1080.

[12] H. Tanaka, T. Kawashima, Y. Murakami, M. Nagao. Flashover Characteristics of Silicon Rubber Surface Influenced by Surface Charge. Annual Report Conference on Electrical Insulation and Dielectric Phenomena, 2015.

EPI International Journal of Engineering
Volume 1, Number 2, August 2018, pp. 87-93
DOI: 10.25042/epi-ije.082018.14

*p*ISSN 2615-5109
*e*ISSN 2621-0541

Earthquake Damages and Disaster Prevention of Aboveground Storage Tanks

Shoichi Yoshida[a,*]

[a]High Pressure Institute of Japan, Tokyo, Japan. Email:k3syoshidas@tea.odn.ne.jp

Abstract

Severe damages in aboveground storage tanks (AST) have been often experienced due to earthquakes in Japan. In this paper, earthquake damages of ASTs which occurred for the last several decades are reviewed. These are damages in the 1964 Niigata Earthquake, the 1978 Miyagi Earthquake, the 1983 Sea of Japan Earthquake, the 1995 Kobe Earthquake, the 2003 Hokkaido Earthquake and the 2011 Great East Japan Earthquake. The damages of ASTs can be classified into 3 types in accordance with the characteristics of earthquake. These are the impulsive motion due to a high frequency earthquake, the sloshing motion due to a low frequency earthquake and the tsunami attack. In the impulsive motion, buckling of sidewall plates and uplift of sidewall-to-bottom joints occurred. In the sloshing motion, sinking of floating roofs into liquid and buckling of sidewall-to-roof joints occurred. In the tsunami attack, ASTs moved and overturned to leak oil.

Keywords: Aboveground storage tank; disaster prevention; earthquake damage; impulsive motion; sloshing

1. Introduction

Aboveground storage tanks (hereafter, it is abbreviated as AST) are cylindrical and a welded steel structure. They are used to store crude oil, petroleum products, chemical products, etc. in oil refineries, chemical plants, thermal power plants, stockpiling bases and tank terminals. Severe damages in ASTs have been often experienced due to earthquakes in Japan. In this paper, earthquake damages of ASTs which occurred for the last several decades are reviewed. These are damages in the 1964 Niigata Earthquake, the 1978 Miyagi Earthquake, the 1983 Sea of Japan Earthquake, the 1995 Kobe Earthquake, the 2003 Hokkaido Earthquake and the 2011 Great East Japan Earthquake in Japan. Finally, the disaster prevention of ASTs is considered based on these damages.

2. AST and Earthquake

ASTs are a welded structure and they are made of carbon steel plates. A typical AST is shown in Fig. 1. An AST is classified into three types as illustrated in Fig. 2, a fixed roof tank, an external floating roof tank and an internal floating roof tank. The external floating roof tank is used in large diameter tanks to store crude oil, naphtha, etc. The fixed roof tank and the internal floating roof tank are used in small diameter tanks to store petroleum and petrochemical products.

Figure 1. Aboveground storage tank (AST)

Table 1 presents the number of ASTs in Japan as of March 2017. This table includes ASTs for oil storage only, and excludes water storage tanks which are used in nuclear power plants, food plants, agricultural facilities, etc. ASTs in table 1 are used in oil refineries, chemical plants, thermal power plants, stockpiling bases and tank terminals.

ASTs in Japan is not damaged by all the earthquakes. They have suffered damages in massive earthquakes which occurred at approximately 10 years interval. The epicenters of the massive earthquakes in which ASTs were damaged are shown in Fig. 3. Damages and failures of ASTs in these earthquakes are described in this paper.

*Corresponding author. Tel.: +81-3-3516-2270
4-7-1, Nihonbashi Honcho, Chuou-ku
Tokyo, Japan, 103-0023

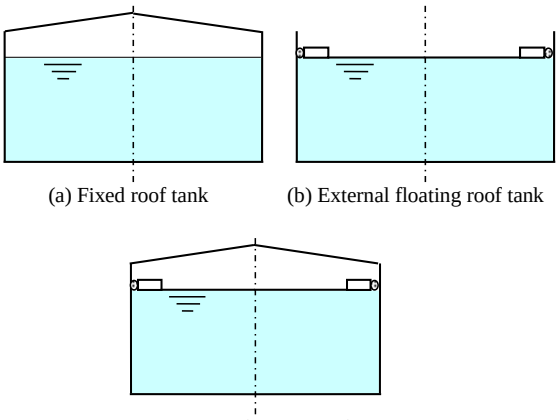

(a) Fixed roof tank (b) External floating roof tank

(c) Internal floating roof tank

Figure 2. AST types

Table 1. The number of ASTs for oil storage in Japan

Capacity range	AST quantity
1,000 m^3 or less	53,464
1,000 m^3 to 5,000 m^3	3,585
5,000 m^3 to 10,000 m^3	1,520
10,000 m^3 to 50,000 m^3	1,353
50,000 m^3 to 100,000 m^3	430
100,000 m^3 or more	448
Total	60,800

As of March 31, 2017

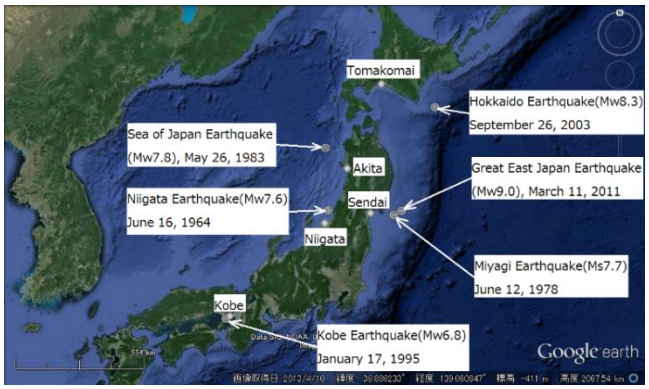

Figure 3. Epicenters of massive earthquakes in Japan

3. Failure Patterns of AST in Earthquake

3.1. High frequency earthquake and low frequency earthquake

Damages of ASTs in earthquakes can be classified into 3 types in accordance with the the characteristics of earthquake. These are the impulsive motion due to a high frequency earthquake, the sloshing motion due to a low frequency earthquake and the tsunami attack. In the high frequency earthquake, a vibration occurs in sidewall plates as shown in Fig. 4(a), and it is referred to as an "impulsive motion". The natural period of the impulsive motion in an AST is between 0.1 s and 0.5 s. If a tank is large, the natural period becomes long. It is about 0.1 s in a 1,000 m^3 tank and about 0.5 s in a 100,000 m^3 tank. In the low frequency earthquake, a vibration occurs in the liquid surface as shown in Fig. 4(b), and it is referred to as a "sloshing motion". The natural period of the sloshing motion in an AST is between 3 s and 15 s. It is 10 s or more in a 100,000 m^3 tank.

If the predominant period of the earthquake wave is between 0.1 s and 0.5 s which is the high frequency earthquake, the impulsive motion occurs in ASTs. If the predominant period of the earthquake wave is between 3 s and 15 s which is the low frequency earthquake, the sloshing motion occurs. The earthquake waves may contain both the high frequency and the low frequency component. In some cases, the impulsive motion and the sloshing motion occurred simultaneously.

In the high frequency earthquake, an amplitude of the earthquake motion rapidly decreases with increasing a distance from an epicenter. On the other hand, it slowly decreases in the low frequency earthquake. The low frequency earthquake mainly consists of surface waves which are the Rayleigh wave and the Love wave. It can occur at a location where is far from an epicenter. Although there were no damages in buildings, civil engineering structures and industrial facilities at that location, ASTs had been only damaged by the sloshing.

3.2. Failures of ASTs due to high frequency earthquake

Most of the ASTs are unanchored and rest freely on flexible foundations. When an unanchored tank is subjected to lateral load induced by the high frequency earthquake, an overturning moment is developed at a base of the tank sidewall. The tank will rock in response to this overturning moment. As a result, a sidewall-to-bottom joint of the tank contacts and compresses the foundation strongly on one side, and lifts off from the foundation on the other side, as shown in Fig. 5.

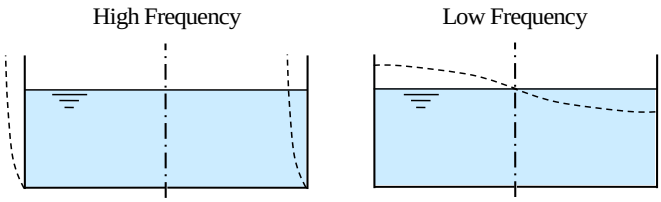

(a) Impulsive motion (b) Sloshing motion

Figure 4. Vibration modes of AST in an earthquake

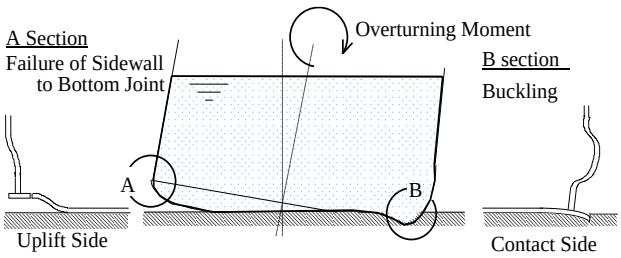

Figure 5. Rocking motion due to high frequency earthquake

On the contact side, buckling of the sidewalls may occur due to excessive vertical compressive force. This buckling is characterized by a "diamond-shape buckle" or an "elephant foot bulge". On the other hand, the uplifting causes large plastic strain at a toe of the sidewall-to-bottom fillet weld, and this leads to a catastrophic failure of ASTs.

3.3. Failures of ASTs due to low frequency earthquake

The sloshing in an AST may occurs due to the low frequency earthquake. When the sloshing wave reaches to roof plates in the fixed roof tank, the sidewall-to-roof joint is subjected to internal pressure as shown in Fig. 6. This pressure causes circumferential compression force in this joint, and the bifurcation buckling with a high circumferential wave number may occur. The sidewall-to-roof joint is usually designed to be weak from the viewpoint of the frangible roof joint. When an overpressurization occurs due to an ignition of flammable vapors existing inside tank, the sidewall-to-roof joint is expected to fail before failure occurs in the sidewall-to-bottom joint. This is a design concept of the frangible roof joint.

The floating roofs are used in many large ASTs to reduce evaporation. It may deform during the sloshing due to the low frequency earthquake (Fig. 7), and it may cause rupture. When the floating roof loses its buoyancy, it will sink into oil. The floating roof tank was considered to be safer than the fixed roof tank, because only a seal fire might occur and a full surface fire as shown in Fig. 8 could not occur. However, when the floating roof sinks, the full surface fire possibly occurs. The full surface fire will be extinguished when oil burns out in a large AST. It will take several days.

3.4. Failures of ASTs due to tsunami

When a small AST is empty or low oil level, it moves by tsunami. In the moving process, AST may float on tsunami and may overturn to cause rupture and leakage of oil. If it does not move, the sidewall may buckle due to external tsunami pressure. In a large AST, it is hard to move by tsunami.

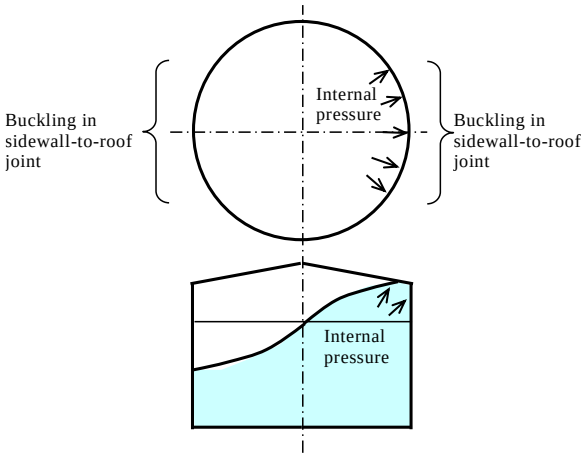

Figure 6. Buckling mechanism of a sidewall-to-roof joint in a fixed roof tank due to low frequency earthquake

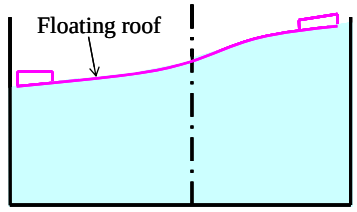

Figure 7. Sloshing of floating roof tanks due to low frequency earthquake

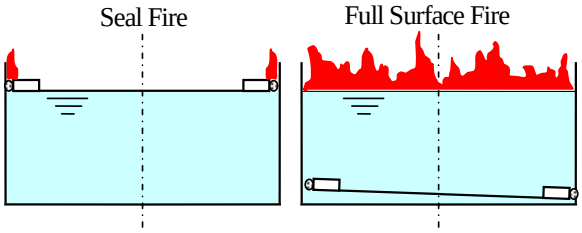

Figure 8. Fire in floating roof tanks

4. 1964 Niigata Earthquake

The 1964 Niigata Earthquake occurred on June 16, 1964 with a moment magnitude 7.6. The epicenter was located on the continental shelf off the northwest coast of Honshu Island about 50 km north of Niigata as shown in Fig. 3. 26 people lost their lives, 1,940 residential houses were completely destroyed, and 6,640 residential houses were severely damaged.

Full surface fires of 12 ASTs occurred at a refinery of Showa Oil, Inc. in Niigata due to the 1964 Niigata Earthquake. The fires lasted two weeks. The cause of the fires was considered the soil liquefaction at first. The low frequency earthquake was not recognized at that time. The cause was concluded to be the sloshing due to the low frequency earthquake later. Two large external floating roof tanks with nominal capacity 45,000 m^3 were included into the burned tanks. The fires were extinguished when oil burned out.

All floating roofs have an annular space between a sidewall and a floating roof to permit smooth travel of the roof within the tank. A rim seal is used to seal the annular space. A mechanical shoe seal came into collision with the sidewall due to this sloshing in the earthquake. An ignition of flammable vapors occurred. The mechanical shoe seal was the cause of the tank fire. A foam-filled fabric seal is currently used instead of the mechanical shoe seal to prevent an ignition inside the tanks in Japan.

It was not clear whether the floating roofs sank before the fire occurred. The fires finally became a full surface fire in several floating roof tanks and they spread to other tanks.

It was the 1968 Tokachi Oki Earthquake that the low frequency earthquake has been recognized for the first time. This earthquake occurred on May 16, 1968, and its moment magnitude was 8.3. The ground motion wave was recorded in Hachinohe, northern city of Honshu Island, and it included a low frequency component. No major damages of ASTs occurred in the 1968 Tokachi Oki Earthquake.

5. 1978 Miyagi Earthquake

The 1978 Miyagi Earthquake (the 1978 Miyagi-Ken Oki Earthquake) occurred on June 12, 1978 with a surface wave magnitude 7.7. The epicenter was located off the northeast coast of Honshu Island about 100 km east of Sendai as shown in Fig. 3. It caused 28 deaths and 1,325 injures. Approximately 4,400 residential houses were completely destroyed, and 86,000 residential houses were partially destroyed in City of Sendai.

A refinery of Tohoku Oil, Inc. was located near Sendai. An uplifting occurred at the sidewall-to-bottom joints in three large fixed roof tanks due to the high frequency earthquake in this refinery. Two of them had the same size and stored heavy fuel oil. Their diameter was 43.6 m, the height was 21.9 m, the nominal capacity was 31,500 m^3, the sidewall thickness of the lowest course was 19 mm and the annular plate thickness was 9 mm. The other tank stored diesel oil and the diameter was 37.8 m, the height was 21.9 m, the nominal capacity was 23,700 m^3, the sidewall thickness of the lowest course was 16 mm and the annular plate thickness was 8 mm.

The uplifting caused large plastic strain in the sidewall-to-bottom fillet weld. The fracture started at the toe of the fillet weld, and it led to catastrophic tank failure. The three tanks lost their contents which then spilled over a dike, inundated much of the refinery area and spilled into the port. Black area in Fig. 9 shows the spilled oil. Fortunately, no fire broke out.

6. 1983 Sea of Japan Earthquake

The 1983 Sea of Japan Earthquake (the 1983 Nihonkai Chubu Earthquake) occurred on May 26, 1983 with a moment magnitude 7.8. The epicenter was located off the northwest coast of Honshu Island in the Sea of Japan about 120 km northwest of Akita as shown in Fig. 3. 104 people lost their lives. 100 of them were the victims of tsunami, which struck communities along the coast. The tsunami warning was issued 14 minutes after the earthquake, but many parts of the nearby coast were struck before any action could be taken.

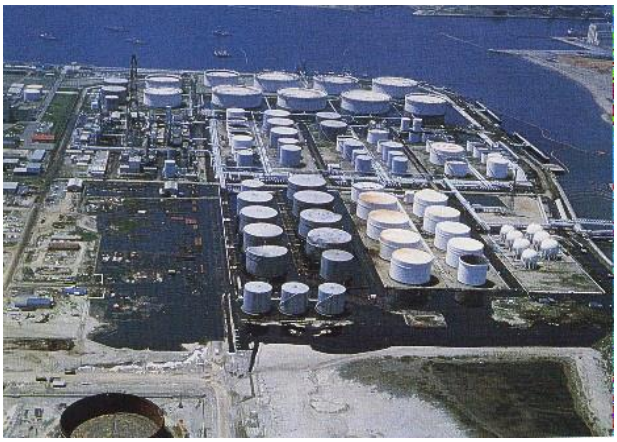

Figure 9. Spilled oil inundated a refinery area in Sendai at the 1978 Miyagi Earthquake (Courtesy of Kahoku Simpo Publishing Co.)

A seal fire broke out in a 35,000 m^3 external floating roof tank with crude oil storage at a thermal power plant of Tohoku Electric Power Company in Akita, and it was extinguished 2 hours later. A projection which was welded at a peripheral upper part of the double-deck floating roof had collided with a sidewall due to the sloshing, and the collision generated sparks. The diameter was 50 m and the height was 20 m in this AST.

Two external single-deck floating roofs of large ASTs ruptured due to the sloshing and oil spilled on the roof in Niigata. Niigata is located 220 km south of Akita. These floating roofs did not sink and no fire broke out.

7. 1995 Kobe Earthquake

The 1995 Kobe Earthquake occurred on January 17, 1995 with a moment magnitude 6.8. The epicenter was the Nojima Fault on the northern end of Awaji Island, 20 km away from Kobe as shown in Fig. 3. 6,434 people lost their lives, and approximately 44,000 people were injured.

The high Frequency earthquake was predominant in Kobe, because the epicenter was near. The buckling of sidewalls in small ASTs occurred due to the rocking motion in Kobe. Figure 10 shows the diamond-shape buckle, and Figure 11 shows the elephant foot bulge of the sidewall in ASTs. The soil liquefaction also occurred everywhere in Kobe. Small ASTs were inclined by the soil liquefaction as shown in Fig. 12. Although a leak occurred in a water storage tank and many resident houses were burned, no oil leak and no fire occurred in ASTs.

Figure 10. Diamond-shape buckle of a sidewall in a small AST in Kobe at the 1995 Kobe Earthquake (Courtesy of National Research Institute of Fire and Disaster, Japan)

Figure 11. Elephant foot bulge of a sidewall in a small AST in Kobe at the 1995 Kobe Earthquake (Courtesy of National Research Institute of Fire and Disaster, Japan)

Figure 12. Inclination of small ASTs due to the soil liquefaction in Kobe at the 1995 Kobe Earthquake (Courtesy of National Research Institute of Fire and Disaster, Japan)

8. 2003 Hokkaido Earthquake

The 2003 Hokkaido Earthquake (the 2003 Tokachi Oki Earthquake) occurred on September 26, 2003 with a moment magnitude 8.3. The epicenter was located about 60 km offshore of Hokkaido Island as shown in Fig. 3. Tsunami attacked to two persons who were fishing on a river, one person was dead and the other was missing.

A refinery of Idemitsu Kosan Co., Ltd. is located in Tomakomai, 220 km northwest of the epicenter. A seal fire of an external single-deck floating roof tank with 30,000 m^3 crude oil storage broke out immediately after the earthquake, and was extinguished 7 hours later. The diameter was 42.7 m, the height was 24.4 m in this AST.

In this tank, crude oil spilled over the floating roof by the sloshing, and it evaporated. The cause of the ignition was presumed a collision of the apparatus at the upper sidewall with the floating roof, or a fall of the gauger's platform which installed at a top of sidewall to the floating roof. The floating roof did not sink in this AST.

There was another external single-deck floating roof tank with 30,000 m^3 naphtha storage near the crude oil tank at the same site. The tank size was the same as the crude oil tank. The floating roof was ruptured due to the sloshing, and it sank into oil completely one day after the earthquake. A full surface fire broke out in this tank two days after the earthquake, and continued 44 hours [1]. The fire was extinguished when naphtha burned out. The cause of ignition was unknown. Both Figure 13 and Figure 14 show this full surface fire.

Figure 13. Full surface fire in a 30,000m^3 naphtha storage tank in Tomakomai at the 2003 Hokkaido Earthquake (Courtesy of National Research Institute of Fire and Disaster, Japan)

Figure 14. Aerial photo of full surface fire in a 30,000m^3 naphtha storage tank in Tomakomai at the 2003 Hokkaido Earthquake (Courtesy of National Research Institute of Fire and Disaster, Japan)

Other 6 ASTs had experienced sinking failures of single-deck floating roofs in this refinery. The pontoons and the deck plates were ruptured, and the floating roofs lost buoyancy due to the sloshing. The roofs sank into oil slowly taking several days. Figure 15 and Figure 16 show the sunken floating roof of an AST with 100,000 m^3 crude oil storage. These photos were taken several months after the earthquake when the oil was drained from the floating roof and the tank was cleaned. The large deformation and failure of the floating roof is presumed to be caused during the sinking process. This roof remained afloat without collapse for 1.5 days after the earthquake according to aerial photos.

Though floating roofs had been designed under the load of rain water, snow and buoyancy, the earthquake sloshing had not been taken into consideration. This full surface fire and the sinking failures led to an establishment of the seismic design method of floating roofs. The regulation for

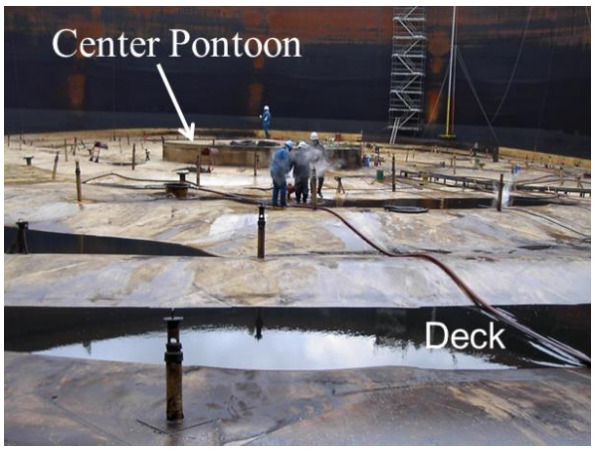

Figure 15. Deck plate of a sunk single-deck floating roof of a 100,000 m^3 crude oil storage tank at the 2003 Hokkaido Earthquake

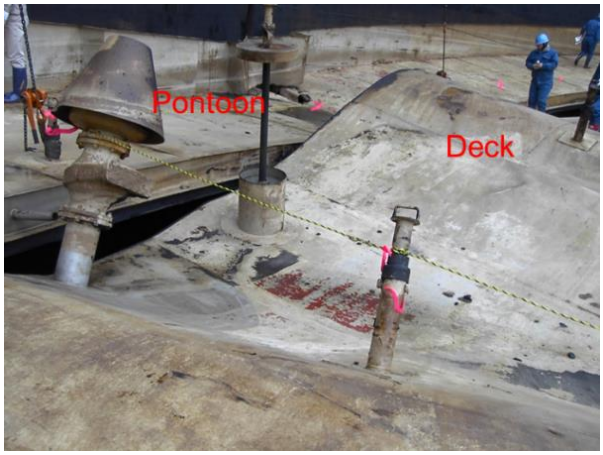

Figure 16. Deck plate and pontoon of a sunk single-deck floating roof of a 100,000 m^3 crude oil storage tank at the 2003 Hokkaido Earthquake

a floating roof design was issued on January 14, 2005 by the Fire Service Law of Japan [2].

9. 2011 Great East Japan Earthquake

The 2011 Great East Japan Earthquake occurred on March 11, 2011 with a moment magnitude 9.0. The epicenter was off the northeast coast of Honshu Island as shown in Fig. 3. It was the most powerful earthquake ever to have hit Japan, and it was the fourth most powerful earthquake in the world since 1900. Powerful tsunami attacked to the northeast coast, and it caused nuclear power plant incidents in Fukushima. 15,883 people lost their lives, 2,640 people were missing and 6,150 people injured in this earthquake.

There are many fishing ports along the coastline of northeast Honshu Island. Several small ASTs were installed at the fishing ports. The ASTs had stored the fuel for fishing boats. Tsunami moved the tanks and overturned them. Some of them sank to sea. Leaked oil from ASTs made massive fire. Figure 17 shows an AST moved to higher ground and overturned by the tsunami.

Figure 17. AST moved to higher ground and overturned by the tsunami at the 2011 Great East Japan Earthquake (Courtesy of National Research Institute of Fire and Disaster, Japan)

An external single-deck floating roof in Kawasaki near Tokyo sank to oil due to the sloshing. Several aluminum internal floating roofs also sank in Sakata, northwest coast of Honshu Island. Fortunately, no fire broke out in these ASTs. Except for the overturning accidents of ASTs by tsunami and the sinking accidents of floating roofs mentioned above, there were few accidents in ASTs in this earthquake.

A spherical LPG storage tank at a refinery of Cosmo Oil Co., Ltd. in Chiba near Tokyo was being used for a hydrostatic test during this earthquake. The hydrostatic load was twice larger than usual load, and it was collapsed by the earthquake. This tank destroyed an adjoining LPG tank when it collapsed, and gas leaked. As a result, a massive fire broke out.

10. Disaster Prevention of ASTs

10.1. High frequency earthquake

The uplift of sidewall-to-bottom joint due to high frequency earthquake easily occurs in large AST, resulting in extremely large plastic strains at the toe of fillet weld. If this part is broken, it will become a catastrophic oil spill and the risk of fire will increase. In the disaster prevention measures, it is important to perform the safety management of ATS, that is the internal inspection on corrosion of bottom plate and defects of weld at proper interval.

10.2. Low frequency earthquake

In the low frequency earthquake, the maximum liquid height is important to set so that the sloshing wave does not reach the upper limit of the sidewall to prevent both the overflow of content and the buckling of sidewall-to-roof joint. However, it is very difficult to determine the

reasonable design sloshing height, and often sloshing that exceeds the assumption is occurring.

The floating roof is installed to prevent emission of hydrocarbon vapors to the atmosphere. It is not a pressure resistant member. Even if the floating roof sinks, oil does not leak outside the tank, but a full surface fire may occur. It is not practical to make the floating roof stiff in strength as the pressure resistant member. Floating roofs designed with current concept can be damaged by sloshing due to low frequency earthquake.

It is important that the floating roof does not sink in order to prevent the full surface fire of AST. If a full surface fire breaks out, it will be extinguished when oil burns out a few days later and air pollution will occur while burning. In recent years, unsinkable floating roof which is made of FRP has been developed as shown in Fig. 18. In addition, it is also important to develop a foam extinguishing agent that extinguishes in a short time when the full surface fire occurs.

10.3. Tsunami

From the Great East Japan Earthquake, countermeasures against tsunami in ASTs also became an important issue. It is not realistic to make individual ASTs resistant to tsunamis. If possible, it is desirable to transfer ASTs to a high place not subject to the tsunami or a place far from the coast. However, when it cannot be done, it is necessary to think in the framework of disaster prevention measures for the entire local area or the AST base.

Figure 18. Unsinkable FRP floating roof (Courtesy of HMT Inc.)

11. Conclusion

Earthquake damages of ASTs which occurred for the last several decades in Japan are reviewed. These are damages in the 1964 Niigata Earthquake, the 1978 Miyagi Earthquake, the 1983 Sea of Japan Earthquake, the 1995 Kobe Earthquake, the 2003 Hokkaido Earthquake, the 2011 Great East Japan Earthquake.

A massive earthquake with an epicenter at Nankai Trough off the south coast of Honshu Island is due in not-too-distant future. In this earthquake, ASTs in the industrial area in Tokyo, Osaka, and Nagoya are expected to suffer damage. There is an urgent need for disaster prevention and mitigation of ASTs for these earthquakes.

References

[1] Hazardous Materials & Safety Technique Association, Report on Damages of Oil Storage Tanks in Kushiro and Tomakomai, Safety & Tomorrow, No.95, 2004, pp.23-39 [in Japanese].

[2] Hazardous Materials & Safety Techniques Association, Report of the Committee on Screening Criterion of Floating Roofs of Oil Storage Tanks, Safety & Tomorrow, No.99, 2005, pp.66-79 [in Japanese].

EPI International Journal of Engineering
Volume 1, Number 2, August 2018, pp. 94-99
DOI: 10.25042/epi-ije.082018.15

*p*ISSN 2615-5109
*e*ISSN 2621-0541

Model Test Ultimate Bearing Capacity of Bakau Piles Foundation on Soft Soil Deposit

Muhammad Yunus[a,*]

[a]Department of Civil Engineering, Polytechnic State of Fakfak. Email: muhammadyunus@polinef.id

Abstract

The pile foundation is one of the deep foundation types commonly used to support building loads when hard soil layers are deeply located. To determine the ultimate bearing capacity of a pile foundation of the load test results, there are several methods commonly used to interpretation test results such as Davisson method, Mazurkiewich method, Chin method, Buttler Hoy method and De Beer method. The aim of this study was to determine the characteristics of soft soil and bakau piles used in the study and to analyze the size of the bearing capacity ultimate of pile foundation that is modeled on a small scale in the laboratory. From the test results of material characteristics of the soil used is organic clay type with medium plasticity with specific gravity 2.75, liquid limit, *LL* = 50.36% and plasticity index, *PI* = 13.2%. While the results of testing the characteristics of bakau piles obtained average water content of 21.58%, tensile strength of 18.51 MPa, compressive strength of parallel fiber 23.75 MPa and perpendicular fiber 14.10 MPa, bending strength 106.22 MPa, and strong split 29.91 MPa. From the result of loading test of the foundation model in the laboratory, it is found that the ultimate bearing capacity of the model without foundation is 41.00 kN with the ultimate settlement of 14.00 mm, the model of the 20 cm long bakau piles foundation is 52.00 kN with the ultimate settlement of 13.00 mm, the foundation model a 30 cm long bakau piles foundation of 54.00 kN with a 10.00 mm ultimate settlement, a 40 cm long bakau piles foundation model of 56.00 kN with an ultimate settlement of 8.50 mm.

Keywords: Bakau piles; bearing capacity; loading test; piles foundation

1. Introduction

As a result of development especially building of public works infrastructure sector, so the need of land for development will also continue to grow. In large cities to meet these needs inevitably the development must be done on very soft soil and sometimes even to reclaim the beach. Soft clay and very soft clay have properties such as tend to be very compressible, low shear strength, low permeability, and have low bearing capacity. It is these qualities that become the main problem of planners if they will build a structure on it.

To overcome the existing problems, the planners usually use the stake for the construction of the foundation. The use of piles is commonly used to overcome the impossibility of using shallow foundations and overcome land subsidence. The use of piles is commonly used to overcome the impossibility of using shallow foundations and overcome land subsidence. In addition other reasons for the use of piles are the easy workmanship, the inventory in many plants, and the formulation of carrying capacity can be estimated by the existing formulas.

Judging from the way to support the load, the pile foundation is divided into 2 (two) kinds [1].

1. End bearing pile, is a pile whose support capacity is more determined by the pole end resistance.
2. Friction pile, is a pile whose capacity is determined friction resistance between the pole side and the surrounding ground.

Indonesian is one of the countries that has tropical climate and has a vast forest area, so that Indonesia is a country that is very rich in wood materials both types and quantities and can be utilized as pile foundation material. The commonly used wooden pile foundation generally has a diameter of 10-25 cm, while for cerucuk wood piles are widely used in Indonesian to increase the soft soil bearing capacity of 8-15 cm in diameter and 4 meters in length.

Many advantages derived from the use of wood piles, among others [2]:

1. Pile is relatively light so easy to transport.
2. Tensile strength so that at the time in the lift for erection does not cause difficulties as in the pile of concrete precast.
3. Easy to cut if wooden pole can not enter again into the ground.
4. Wooden piling is more suitable for friction pile than end bearing pile because the pressure is relatively small.

In addition to the above advantages, there are some shortcomings of the use of wooden piles, among others [2]:

*Corresponding author. Tel.: +62-811-4212-748
Jalan TPA Imam Bonjol Atas Air Merah, Kelurahan Wagom Fakfak, Papua Barat, Indonesia, 98611

1. Since this pile must always be located under the lowest groundwater level for long lasting, so if the groundwater is the lowest it is located very deep, it will increase the cost for excavation.
2. Wooden piles are of relatively small lifespan compared to concrete or steel piles, especially in areas where the water level is often up and down.
3. At the time of erection on the rocky ground (gravel) the end of the wood pile can be shaped in the form of a broom or can also tip the pole is crushed, if the wooden pole is less straight then at the time of placement will cause deviations against the direction that has been specified.
4. Wooden piles are not resistant to aggressive objects and fungi that cause decay.

2. Literature Review

a. Ultimate bearing capacity

Ultimate bearing capacity can be defined as the smallest pressure that can cause shear failure on the supporting ground just below and around the foundation. There are three types of failure that have been identified and described in relation to the bearing capacity of the soil with reference to Fig. 1 [3].

1. *General shear failure*. This failure will occur when pressure is raised to achieve the initial plastic equilibrium conditions on the ground around the sides of the foundation and then gradually spread down and out. Finally, the ultimit plastic state of balance will form along the ground above the failure plane. The ground surface on both sides of the field that receives the load is lifted. The way this collapse occurs on low-compressed soil is tight or rigid soil.
2. *Local shear failure*. There is considerable compression in the soil beneath the burdened plane and the plastic equilibrium state is formed only in part of the soil alone. The failure surface does not reach the surface, and there is little ground lifting. Local shear failure usually occurs on highly compressible soil and is marked by a relatively large decline, and the fact that ultimit support capacity can not be defined.
3. *Punching shear failure.* Occurs if there is compression under the plane that accepts the load accompanied by the vertical shift around it. This failure is characterized by a relatively large decline, and an undefined ultimate bearing capacity.

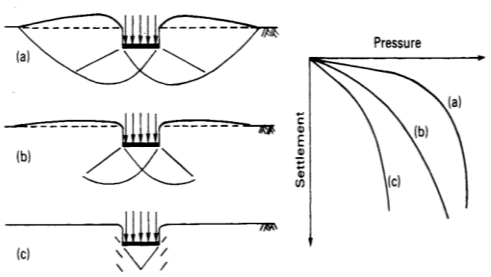

Figure 1. Types of failure, (a) general shear failure, (b) local shear failure, (c) punching shear failure [3]

b. Soil settlement

Settlement on the soil is inseparable from the incompressibility of the soil. On coarse grained soils and pores filled with water when receiving the load will decrease immediately. This happens because the water in the pore will be faster out through the crack of coarse grained soil. While on fine-grained soil and pores filled with water, the decrease that occurs due to the load will be slower than coarse grained soil. This happens because water will be difficult to pass through the smaller pore. In the field of geotechnical engineering, this settlement is differentiated in the following types [4].

1. Immediate Settlement
2. Primary Consolidation Settlement
3. Seconday Consolidation Settlement

c. Pile loading test

In principle, this pile loading procedure is performed by providing a vertical load placed over the head of the pile, then the magnitude of the vertical deformation occurring is measured using a dial mounted on the pile. The deformation that occurs consists of elastic and plastic deformation. The elastic deformation is a deformation caused by the elastic shortening of the pole and the ground, whereas plastic deformation is a deformation caused by the collapse of the supporting ground on the tip or around the pile. If the relationship between the deformation and the load is represented in the curve it will be seen that the graph will consist of 3 (three) parts as shown in Fig. 2 [5].

3. Research Methodology

3.1. Soil characteristic test

Testing of soil characteristics carried out in the laboratory among others, water content test, volume weight, specific gravity, Atterberg limits, sieve analysis, hydrometer test, compaction, unconfined compression strength and direct shear test.

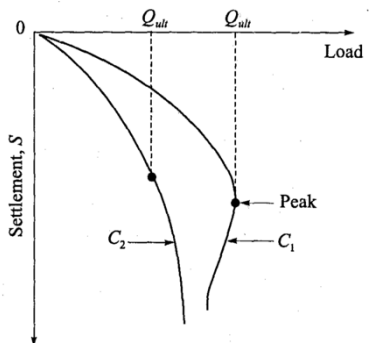

Figure 2. Load vs settlement [5]

3.2. Bakau pile characteristic test

Testing of wood characteristics carried out in the laboratory, among others, testing the moisture content, flexural strength, tensile strength, compressive strength and strength of split. For each test, wood samples were prepared for 3 (three) samples. From the results of testing the characteristics of bakau can be classified strong grade of bakau wood used in this study.

3.3. Preparation of foundation model in laboratory

The modeling of the foundation in the laboratory consists of 4 (four) variation model, model without reinforcement of pile foundation, model with reinforcement of pile foundation with pole length 20 cm, 30 cm and 40 cm.

- Soil model without reinforcement of pile foundation

Soft clay that has been tested its characteristics inserted into the drum with a diameter of 60 cm and height 60 cm. Then compacted perlayer with a thickness of 10 cm perlayernya to a height of 50 cm with a density of 80% of the maximum density obtained from standard compaction tests that have been carried out in the laboratory. After that put plate loading test with diameter plate size of 30 cm and plate thickness of 1.5 cm as seen in Fig. 3.

Attach dial gauge 3 (three) pieces, above the plate bearing test of 1 piece to read the settlement and 2 (two) pieces each in addition to the plate loading test to read the deformation that occurs. The burden on the foundation model is done by using hydraulic jack until the failure occurs while the dial gauge reading is done according to the amount of load given until the collapse occurs on the ground.

- Soil model with pile foundation length 20, 30, 40 cm

Subsequently the soil model in the drum was dismantled and the clay that has been tested its characteristic was inserted into the drum and then compacted the perlayer with a thickness of 10 cm perlayer to a height of 50 cm with a density level of 80% of the maximum density obtained from the standard compaction test that has been carried out in the laboratory.

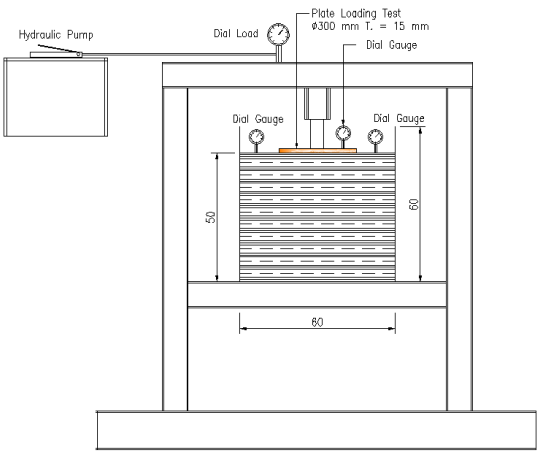

Figure 3. Model without of pile foundation

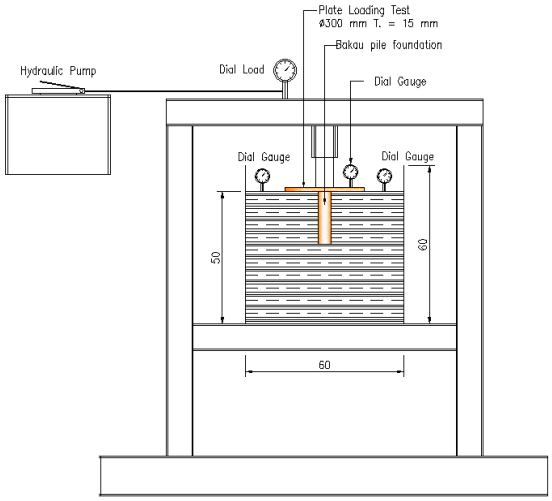

Figure 4. Model pile foundation

After that pile wooden mast with wood diameter about 3-5 cm which will be used as a single pole foundation with size of pole length which is 20 cm, 30 cm and 40 cm as in Fig. 2. Then put plate bearing test with diameter plate size 30 cm and 1.5 cm thick plate above the mast pole that has been fixed as seen in Fig. 4.

Attach dial gauge 3 (three) pieces, above the plate bearing test of 1 piece to read the settlement and 2 (two) pieces each in addition to the plate loading test to read the deformation that occurs. The burden on the foundation model is done by using hydraulic jack until the failure occurs while the dial gauge reading is done according to the amount of load given until the collapse occurs on the ground.

4. Result and Discussion

4.1. Testing results of soil characteristics

From the results of soil characteristics test obtained data in Table 1.

Table 1. Testing results of soil characteristics

Types of testing	Unit	Result
Water content	%	36.00
Spesific gravity	-	2.75
Atterberg Limit		
a. Liquid Limit (LL)	%	50.36
b. Plastic Limit (PL)	%	37.23
c. Plasticity Index (PI)	%	13.12
d. Shrinkage Limit (SL)	%	29.86
Grain of Soil		
a. Soil grained coarse	%	45.90
b. Soil grained fine	%	54.10
Soil Classification		
a. USCS Method	-	MH & OH
b. AASHTO Method	-	A-7-5
Unconfined compression test (q_u)	kg/cm	0.72
Compaction		
a. Water content optimum (w_{opt})	%	41.75
b. Weight volume dry (γ_{dry})	gr/cm^3	1.22
Direct shear		
a. Cohesion(c)	kg/cm^2	0.104
b. Internal friction angle (ϕ)	^{0}	17.32

Table 2. Testing results bakau wood characteristics

Types of testing	Unit	Result
Moisture content	%	21.580
Tensile strength	MPa	18.515
Modulus of elasticity tensile strength	MPa	690.423
Compressive strength parallel fiber	MPa	23.757
Modulus of elasticity parallel fiber	MPa	964.596
Compressive strength perpendicular fiber	MPa	14.710
Modulus of elasticity perpendicular fiber	MPa	591.230
Bending strength	MPa	106.224
Strong split	MPa	29.910

4.2. Testing results of bakau wood characteristics

From the test results of bakau material characteristics obtained data in Table 2.

While from the results of X-Ray Diffraction testing can be known mineral composition contained in bakau wood as shown in Fig. 5. The results of testing the composition of bakau wood materials showed that the wood-forming minerals are Silicate (SiO2), Aluminum (Al2O3), Sodium (Na2O), Magnesium (MgO), Potassium (K2O), Sulfur (SO3), Phosporus (P2O5) and Chlorine.

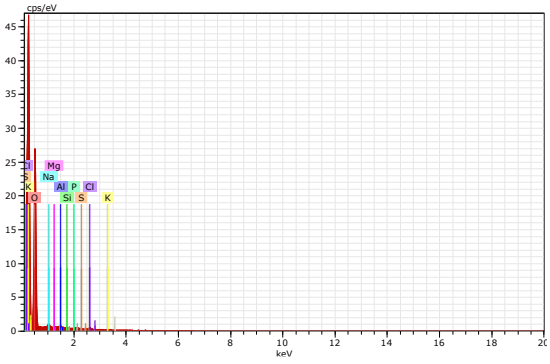

Figure 5. X-Ray Diffraction test results of bakau wood

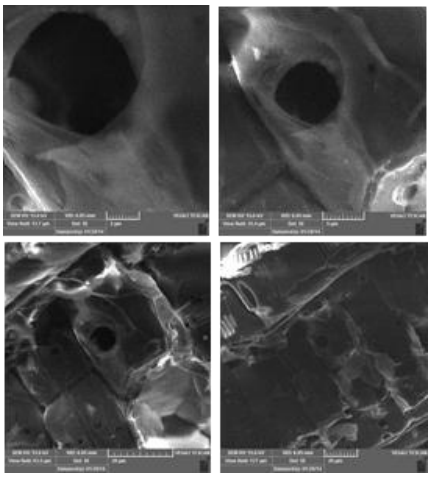

Figure 6. SEM (Scanning Electron Microscope) tes result bakau wood

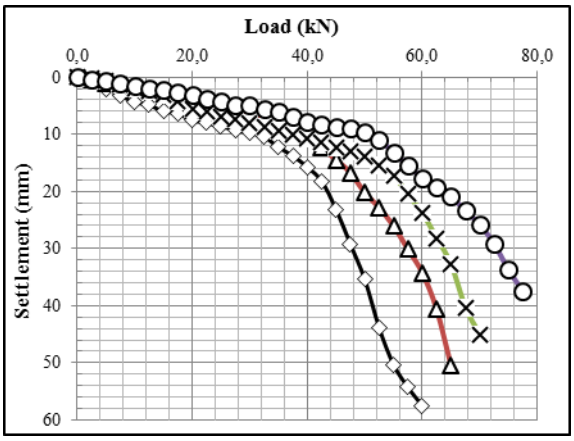

Figure 7. Load vs. settlement

From SEM (Scanning Electron Microscope) testing is a test used to view the microstructure that is formed, both for surface and transverse cross section. The SEM test result of bakau wood material is shown in Fig. 6.

4.3. Loading test result of foundation model

From the result of loading test of the foundation model in the laboratory obtained the graph of the load relationship vs. the decline of the foundation model as seen in Fig. 7.

The graph in Fig. 7 shows that at the beginning of the loading the decline is relatively small. This decrease is caused by elastic shape changes in the surrounding soil. If the load is added to the decrease that occurs faster until it reaches its maximum limit and the ground failure.

4.4. Ultimate bearing capacity analysis

In determine the value of ultimit bearing capacity (Q_{ult}) of each model of the loaded loaded foundation used Butler and Hoy method (1977). This method considers the load failure when the load occurs the intersection of two tangent lines against the relation curve between load vs. settlement at different points. The first tangent line is the initial straight line assumed as an elastic pressure line. For the second tangent line obtained is limited as a slope of 0.05 kN on the load vs. settlement graph [7].

- Soil model without reinforcement of pile foundation

To determine the ultimate bearing capacity (Q_{ult}) soil without foundation model, we create a graph of load vs. settlement as seen in Fig. 8. From the graph in Fig. 8 using the Butler and Hoy method, the value of ultimate support capacity (Q_{ult}) is 41.00 kN with ultimate settlement (δ_u) obtained at 14.00 mm.

- Soil model with pile foundation length 20 cm

To determine the ultimate bearing capacity (Q_{ult}) of the foundation model with a length of 20 cm pile then made the graph of load vs. settlement as seen in Fig. 9. From the graph of load vs. settlement in Fig. 9 using the Butler and Hoy method obtained the value of ultimate bearing capacity (Q_{ult}) of 52.00 kN with ultimate settlement (δ_u) obtained at 13.00 mm.

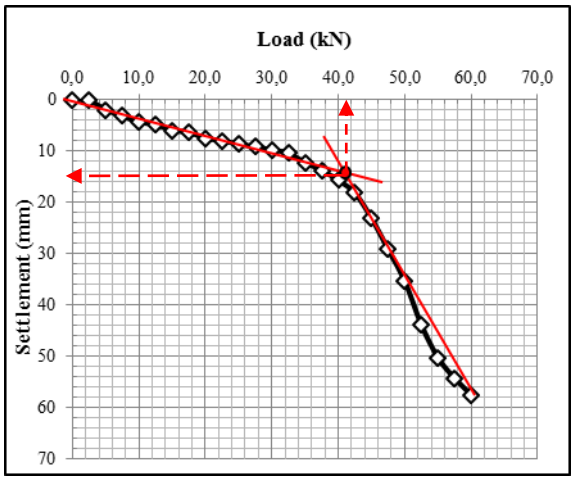

Figure 8. Ultimate bearing capacity determination of soil model without foundation

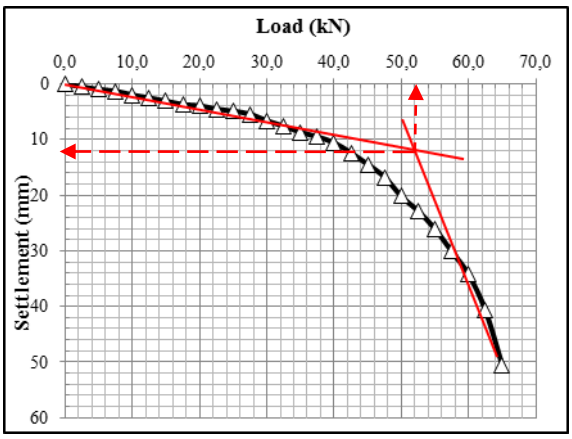

Figure 9. Ultimate bearing capacity determination of pile foundation model pile length 20 cm

- Soil model with pile foundation length 30 cm

To determine the ultimate bearing capacity (Q_{ult}) of the foundation model with a length of 30 cm pile then made the graph of load vs. settlement as seen in Fig. 10. From the graph of load vs. settlement in Fig. 10 using the Butler and Hoy method obtained the value of ultimate bearing capacity (Q_{ult}) of 54.00 kN with ultimate settlement (δ_u) obtained at 10.00 mm.

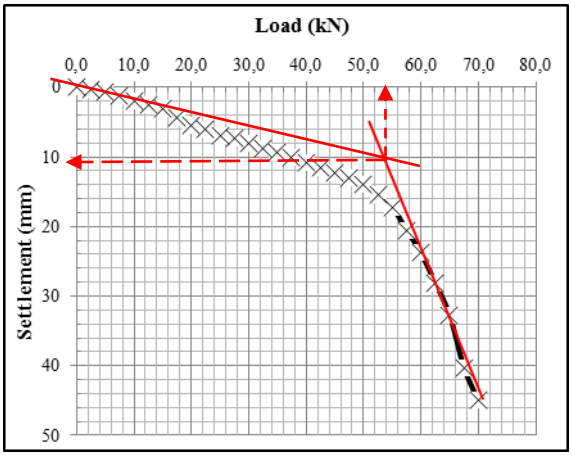

Figure 10. Graph of ultimate bearing capacity determination of pile foundation model length 30 cm

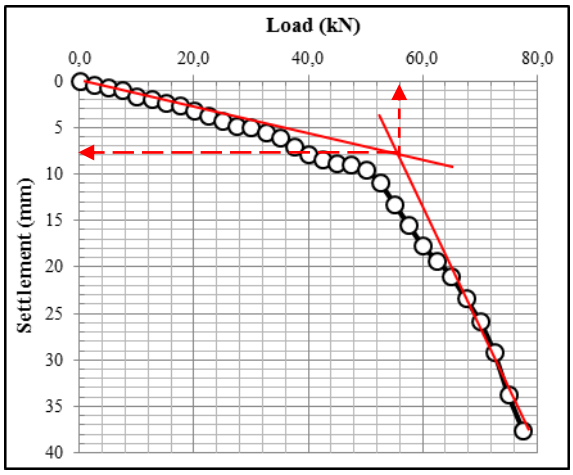

Figure 11. Ultimate bearing capacity determination of pile foundation model pile length 40 cm

- Soil model with pile foundation length 20 cm

To determine the ultimate bearing capacity (Q_{ult}) of the foundation model with a length of 40 cm pile then made the graph of load vs. settlement as seen in Fig. 11. From the graph of load vs. settlement in Fig. 11 using the Butler and Hoy method obtained the value of ultimate bearing capacity (Q_{ult}) of 56.00 kN with ultimate settlement (δ_u) obtained at 8.50 mm.

From the results of model testing in the laboratory capacity of foundation of bakau pile obtained foundation model of bakau pile wood with length of pile of 40 cm have the biggest capacity of support (Qult) compared to other foundation model.

5. Conclusion

Based on the test results and data analysis that has been implemented, the following conclusions can be drawn:

1. From the test of material characteristics, the soil used is organic clay type with medium plasticity with value of specific gravity (*Gs*) 2.75, liquid limit (*LL*) = 50.36% and plasticity index (*PI*) = 13.12%. While the result of dolken wood characteristic test obtained water content average 21.58%, tensile strength 18.51 MPa wood, compressive strength of wood parallel fiber 23.75 MPa and perpendicular fiber 14.10 MPa, wood bending strength 106.22 MPa, and wooden strength 29.91 MPa. Given a strong class of wood entering into a strong class of wood II.
2. From the result of load test of foundation model in laboratory get value of ultimate bearing capacity of model without foundation of 41.00 kN with decreasing ultimit 14.00 mm, model of 20 cm long pole foundation 52.00 kN with decreasing ultimit 13.00 mm, model of 30 cm long pole foundation 54.00 kN with a 10.00 mm ultimit decrease, a 40 cm long pole foundation model of 56.00 kN with an 8.50 mm ultimit decrease.

References

[1] Bowles, J.E., (1996), *Foundation Anaysis and Design*, McGraw-Hill, New York.

[2] Craig, R.F., (2004), *Soil Mechanics*, Erlangga, Jakarta.

[3] Das, Braja M., (1990), *Principles of Foundation Engineering*, PWS-KENT Publishing Company, Boston.

[4] Hardiyatmo, H.C., (2010), *Foundation Analysis and Design 1 dan 2*, Gadjah Mada University Press, Yogyakarta.

[5] Murthy, V.N.S., (2007), *Advanced Foundation Engineering*, CBS Publishers & Distributors, New Delhi Bangalore.

[6] Poulos, H.G. & Davis, E.H., (1980), *Pile Foundation Analysis and Design*, John Wiley & Sons, New York.

[7] Prakash, S., Sharma D., (1990), *Pile Foundation in Engineering Practice*, John Wiley & Sons, Inc., New York.

[8] Rahardjo, Paulus P., (2005), *The Use of Bamboo and Bakau Piles for Soil Improvement and Application of Pile Raft System for the Construction Embankments on Peats and Soft Soils*, Elsevier Geo-Engineering Book Series Volume 3, London.

[9] Standar Nasional Indonesia, (1994), *Methods of Testing Wood Tensile Strength in the Laboratory*, *SNI-03-3399-1994*, Badan Standardisasi Nasional.

[10] Standar Nasional Indonesia, (1995), *Methods of Testing Wood Compressing Strength in the Laboratory*, *SNI-03-3958-1995*, Badan Standardisasi Nasional.

[11] Standar Nasional Indonesia, (1995), *Methods of Testing Wood Bending Strength in the Laboratory*, *SNI-03-3959-1995*, Badan Standardisasi Nasional.

[12] Standar Nasional Indonesia, (2002), *Procedure for Measurement of Wood Water Content and Woody Material*, *SNI-03-6850-2002*, Badan Standardisasi Nasional.